EXPERIMENTAL INVESTIGATIONS ON WELDABILITY OF AUSTENITIC STAINLESS STEELS USED IN INDUSTRIAL BOILERS USING GAS TUNGSTEN ARC WELDING

Thesis Submitted by

SUBHODWIP SAHA

DOCTOR OF PHILOSOPHY (ENGINEERING)

DEPARTMENT OF POWER ENGINEERING
FACULTY COUNCIL OF ENGINEERING & TECHNOLOGY
JADAVPUR UNIVERSITY, KOLKATA-700032, INDIA

2025

JADAVPUR UNIVERSITY
KOLKATA-700 032

Index No. 49/18/E
Registration No. 1021814007

TITLE OF THE Ph.D. (ENGG.) THESIS:

EXPERIMENTAL INVESTIGATIONS ON WELDABILITY OF AUSTENITIC STAINLESS STEELS USED IN INDUSTRIAL BOILERS USING GAS TUNGSTEN ARC WELDING

NAME, DESIGNATION & INSTITUTION OF THE SUPERVISORS:

S Mondal 18/11/2025

DR. SUBRATA MONDAL

Assistant Professor,

Department of Power Engineering,

Jadavpur University,

Kolkata –700106, India.

Assistant Professor
Dept. of Power Engineering
Jadavpur University
Salt Lake, 2nd Campus
Kolkata-700 098

V Das 18/11/2025

DR. SANTANU DAS

Professor,

Department of Mechanical Engineering,

Kalyani Government Engineering College,

Kalyani – 741235, India

Dr. Santanu Das
Professor of Mechanical Engineering (WBCS)
Kalyani Govt. Engg. College, Kalyani, Nadia

LIST OF PUBLICATIONS

INTERNATIONAL JOURNALS:

(i) **Subhodwip Saha**, Barun Haldar, Hillol Joardar, Santanu Das, Subrata Mondal, Srinivas Tadepalli, "Supervised Machine Learning Models for Predicting SS304H Welding Properties Using TIG, Autogenous TIG, and A-TIG", **Crystals**, Vol. 15, No. 6, pp.529/1-28,2025. [ISSN:2073-4352], (DOI: https://doi.org/10.3390/cryst15060529), (Indexed in: SCIE, Web of Science, Scopus, EBSCO, J-Gate.)

(ii) **Subhodwip Saha**, Mainak Bandyopadhyay, Santanu Das, Subrata Mondal, Rafikul Islam, "Selection of Appropriate Process Parameters for Enhancement of Penetration in TIG Welding of 304H Stainless Steel Flats: An AHP Based Approach", **International Journal of the Analytic Hierarchy Process**, (revision one submitted after review). [ISSN:1936-6744]. (Indexed in: SCOPUS, DOAJ, Copernicus.)

NATIONAL JOURNALS:

(i) **Subhodwip Saha**, Santanu Das, Subrata Mondal, "Experimental Investigation on Autogenous TIG and A-TIG Welding for Enhanced Penetration in Austenitic SS304H Flats", **Indian Welding Journal**, Vol. 58, No. 1, pp. 75-82, 2025. [ISSN: 0046-9092], (DOI: https://doi.org/10.22486/iwj.v58i1.48809), (Indexed in: Indian Citation Index, EBSCO, Crossref, i-Scholar, J-Gate)

(ii) **Subhodwip Saha**, Santanu Das, Subrata Mondal. "Exploring the Weldability of Austenitic Stainless Steels in Advanced Ultra-Supercritical Power Plant Applications: An Extensive Review." **Indian Welding Journal**, Vol. 56, No. 4, pp.54-66, 2023. [ISSN: 0046-9092], (DOI: https://doi.org/10.22486/iwj.v56i4.223541), (Indexed in: Indian Citation Index, EBSCO, Crossref, i-Scholar, J-Gate)

INTERNATIONAL CONFERENCE:

(i) **Subhodwip Saha,** Santanu Das, Subrata Mondal. "The AHP-Based Evaluation of Welding Parameters for Optimized TIG Weld Bead Geometry of SS 304H Flats" Proceedings of the **10th International and 31st All India Manufacturing Technology, Design & Research Conference (AIMTDR 2025) Indore, India**, (communicated under review). Indian Institute of Technology-Indore (IIT-Indore), Indore, India.

NATIONAL CONFERENCES:

(ii) **Subhodwip Saha**, Santanu Das, Subrata Mondal. "Study of Weldability of 304H Austenitic Boiler Quality Steels by Gas Tungsten Arc Welding." Proceedings of the **Recent Advancements in Manufacturing Technology & Management (RAMTM-II 2025), Kolkata, India**, p. 234, 2025. Organized by Department of Production Engineering, Jadavpur University, Kolkata, India. ISBN: 978-81-986567-9-7.

(iii) **Subhodwip Saha**, Santanu Das, Subrata Mondal. "Exploring the Weldability of Austenitic Stainless Steels in Advanced Ultra-Supercritical Power Plant Applications: An Extensive Review." Proceedings of the **37th National Convention of Production Engineers, Kolkata, India**, p. 38, 2023. Organized by West Bengal State Centre, The Institution of Engineers (India), Kolkata, India. ISBN: 978-81-959819-6-0.

(iv) **Subhodwip Saha**, Mainak Bandyopadhyay, Gourab Biswas, Amlan Das, Soham Ghosh, Santanu Das, Subrata Mondal. "Optimization of Autogenous Butt Welded Joints of Austenitic Stainless Steels Using GTAW Process." Proceedings of the **37th National Convention of Production Engineers, Kolkata, India**, p. 39, 2023. Organized by West Bengal State Centre, The Institution of Engineers (India), Kolkata, India. ISBN: 978-81-959819-6-0.

(v) **Subhodwip Saha,** Santanu Das, Subrata Mondal. "Optimization of The Strength of Autogenous Butt Welded Joints of Austenitic Stainless Steels Using GTAW Process." Proceedings of the **Weld 2023, Kolkata, India**, p. 67, 2023. Organized by The Indian Institute of Welding, Kolkata Branch (Golden Jubilee Year Celebration), Kolkata, India.

(vi) **Subhodwip Saha,** Santanu Das, Subrata Mondal. "A Review on Weldability of Austenitic Stainless Steels Used in Advanced Ultra-Super Critical Power Plant Applications." Proceedings of the **National Welding Seminar (NWS) 2021, Baroda, India,** pp. 51-70, 2021. Organized by The Indian Institute of Welding, Baroda Branch in Hybrid Mode, Baroda, India.

LIST OF AWARDS: NIL

PATENTS: NIL

18/11/2025
Dr. Santanu Das
Professor of Mechanical Engineering (WBCS)
Kalyani Govt. Engg. College, Kalyani, Nadia

18/11/2025
Assistant Professor
Dept. of Power Engineering
Jadavpur Universi
Salt Lake, 2nd Ca
Kolkata-700 09

Statement of Originality

I, Subhodwip Saha registered on 26th June, 2018 do hereby declare that this thesis entitled "EXPERIMENTAL INVESTIGATIONS ON WELDABILITY OF AUSTENITIC STAINLESS STEELS USED IN INDUSTRIAL BOILERS USING GAS TUNGSTEN ARC WELDING" contains literature survey and original research work done by the undersigned candidate as part of Doctoral studies.

All the information in this thesis has been obtained and presented in accordance with existing academic rules and ethical conduct. I declare that, as required by these rules and conduct, I have fully cited and referred all the materials and results that are not original to this work.

I also declare that I have checked this thesis as per the "Policy on Anti Plagiarism, Jadavpur University, 2019", and the level of similarity as checked by iThenticate software is 4%.

Subhodwip Saha

Signature of the Candidate

(SUBHODWIP SAHA)

Date: 18.11.2025

Certified by Supervisors:

(Signature with date & seal)

1. Dr. Subrata Mondal

S Mondal 18/11/2025

Assistant Professor
Dept. of Power Engineering
Jadavpur University
Salt Lake, 2nd Campus
Kolkata-700 098

2. Dr. Santanu Das

18/11/2025

Dr. Santanu Das
Professor of Mechanical Engineering (WBCS)
Kalyani Govt. Engg. College, Kalyani, Nadia

JADAVPUR UNIVERSITY
FACULTY OF ENGINEERING AND TECHNOLOGY
DEPARTMENT OF POWER ENGINEERING

CERTIFICATE FROM THE SUPERVISORS

This is to certify that the thesis entitled "EXPERIMENTAL INVESTIGATIONS ON WELDABILITY OF AUSTENITIC STAINLESS STEELS USED IN INDUSTRIAL BOILERS USING GAS TUNGSTEN ARC WELDING" submitted by Mr. Subhodwip Saha, who got his name registered on 26th June 2018 for the award of Ph.D. (Engg.) degree of Jadavpur University is absolutely based upon his work under the supervision of Dr. Subrata Mondal and Dr. Santanu Das and that neither his thesis nor any part of the thesis has been submitted for any degree/diploma or any other academic award anywhere before.

S Mondal 18/11/2025

Dr. Subrata Mondal

(Signature of the supervisor

and date with official seal)

Assistant Professor
Dept. of Power Engineering
Jadavpur University
Salt Lake, 2nd Campus
Kolkata-700 098

18/11/2025

Dr. Santanu Das

(Signature of the supervisor

and date with official seal)

Dr. Santanu Das
Professor of Mechanical Engineering (WBCS)
Kalyani Govt. Engg. College, Kalyani, Nadia

ACKNOWLEDGEMENT

The author would like to take this opportunity to express his heartfelt gratitude to all those who have supported, encouraged, and guided him throughout his research journey. This work would not have been possible without their invaluable contributions.

First and foremost, the author would like to extend his sincere appreciation to his Ph.D. supervisors, Dr. Subrata Mondal, Assistant Professor, Power Engineering Department, Jadavpur University, and Dr. Santanu Das, Professor, Mechanical Engineering Department, Kalyani Government Engineering College. Their constant encouragement, insightful feedback, and expert guidance have played a crucial role in shaping the research. The author is truly grateful for their unwavering support and patience throughout this journey.

The author is also deeply thankful to the faculty members and research scholars of Department of Power Engineering, Jadavpur University, for their valuable discussions and technical inputs, which have helped him, gain a deeper understanding of his subject. In particular, the author likes to extend his sincere gratitude to Dr. Angshuman Roy of the Power Engineering Department, Jadavpur University, for his continuous support during the work.

The author likes to extend his sincere thanks to the administration and technical staff of the Power Engineering Department, Jadavpur University, and Mechanical Engineering Department, Kalyani Government Engineering College (KGEC), for providing the necessary infrastructure, resources and assistance for the experimental work. He would like to extend special thanks to Shri Susanta Barik (Welding Lab, KGEC), Shri Asish Kumar Bhattacharya (Metallurgy and Material Science Lab, KGEC) and Shri Susanta Das (Applied Mechanics Lab, KGEC) for their technical assistance and support during the experimentation. The author would like to acknowledge Dr. Dipankar Bose, Mechanical Engineering Department, National Institute of Technical Teachers' Training and Research, Kolkata, for his support to the author to use their Scanning Electron Microscope (SEM) for the research work. The author would also like to extend his sincere thanks to Safiul Anam, Lab Assistant, SEM Lab, NITTTR Kolkata, for his significant help in obtaining SEM images and conducting EDX analysis, which played a crucial role in the author’s study.

The author would like to express his sincere appreciation to Mr. Devasish Paul and Mr. Dipayan Paul of NextGen Plasma Ltd., Howrah, for kindly allowing a part of the experimentation to be conducted at their facility, which added substantial value to the research.

The author wishes to extend his heartfelt thanks to Dr. Barun Halder, Assistant Professor, Department of Mechanical and Industrial Engineering, College of Engineering, Al-Imam Mohammad Ibn Saud Islamic University, KSA, and Dr. Hillol Joardar, Associate Professor, Department of Mechanical Engineering, C. V. Raman Global University, Bhubaneswar, for their generous support, technical input and cooperation throughout the course of this work.

The author is also grateful to his students and colleagues at Techno Main Salt Lake, whose encouragement and cooperation have been a great source of motivation throughout this journey. In particular, the author would like to acknowledge the efforts and support of his students at

Techno Main Salt Lake—Arghya Samanta, Samriddho Sahoo, Krishnangshu Ghoshal, Arisudan Nandi, Akshita Singh, Ashutosh Mandal, Sagnik Ghosh, Mridul Acharya, Nabendu Dinda, Arnab Loha, Danish Kazi and Souradipta Sen—for their involvement in the research. He also extends his appreciation to the students of Kalyani Government Engineering College—Mainak Bandyopadhyay, Amlan Das, Soham Ghosh, and Gourab Biswas—for their contributions.

A special note of gratitude is reserved for the author's friend and former classmate from KGEC, Shri Bashab Chandra Pal, who has been an exceptional support throughout the research. His involvement in specimen preparation, experimentation and continuous technical assistance has been invaluable, and his generosity with time and expertise is deeply appreciated. The author would also like to acknowledge Shri Sudip Santra, fellow researcher from CSIR and Production Engineering Department, Jadavpur University, for his helpful inputs during certain post-welding experiments and for offering valuable research suggestions.

Above all, the author is profoundly grateful to his daughter Irshita Saha, wife Anuradha Saha (Roy), parents, family and friends specially Amar Sekh Mirja, Tonmoy Das and Zinia Mondal whose constant encouragement, patience and sacrifices have been his greatest source of strength. Their unwavering belief in him has kept him going through the challenges of this journey. Lastly, the author extends his sincere appreciation to all researchers and authors whose work has contributed to the foundation of this study. While every effort has been made to acknowledge contributions, any unintentional omissions are purely inadvertent.

Subhodwip Saha

Subhodwip Saha

18.11.2025, Kolkata

(Date, Place)

PREFACE

Welding is one of the important processes used to permanently join metals in industries like power generation, construction, manufacturing etc. To meet the growing demand for stronger and more reliable welded structures, especially in high-temperature and corrosive environment, industries are now turning to advanced welding techniques. These methods are developed to improve mechanical strength, durability and safety of components used in critical applications. However, traditional welding processes often face difficulties when working with modern, high-performance materials. Understanding how these materials behave during welding is important to ensure the joints to be strong and long-lasting. As industries use more advanced materials to meet strict performance standards, it becomes crucial to understand the details of how well these materials can be welded. Among various welding processes, Gas Tungsten Arc Welding (GTAW) has gained popularity due to its high precision and versatility.

The increasing need for improved power plant efficiency has prompted the evolution of thermal power plants from subcritical to Ultra Supercritical (USC) and Advanced Ultra Supercritical (AUSC) technologies. These advancements necessitate the use of high-performance materials such as Creep Strength Enhanced Ferritic (CSEF) steels, austenitic stainless steels and Ni-based superalloys. Austenitic stainless steels, particularly 304H grade, exhibit superior high-temperature strength and corrosion resistance, making them suitable candidates for elevated temperature applications. Weldability of such steels is of key importance, as achieving high-quality welds ensure structural integrity and enhances the long-term performance of components operating under extreme thermal and mechanical conditions.

Austenitic stainless steel of grade 304H is one of the critical materials extensively used in advanced boiler components such as fabricating terminal sections of superheaters and reheaters (as reported by the previous researchers) due to its excellent high-temperature strength and corrosion resistance. However, despite its significant role in such demanding environment, the weldability study of more than 5 or 6-mm thick SS 304H remains underexplored. Achieving full penetration and producing high-quality welds are crucial for ensuring the strength and durability of welded joints in critical applications. However, welding characteristics of thick SS 304H, particularly the interaction between various welding parameters, requires further investigation.

Employing Multi Criteria Decision Making (MCDM) tools like the Analytic Hierarchy Process (AHP) can enhance decision-making by systematically analyzing, prioritizing and optimizing various welding parameters that was not reported in the literature for welding of SS 304H. Also, application of Artificial Intelligence and Machine Learning in such weld joints of SS 304H flats was not found in the literature.

Also, the literature does not reveal the use of Activating Flux in the enhancement of penetration of TIG welded joints of SS 304H materials. Despite several advantages, this A-TIG welding is not yet broadly adopted in the welding industry worldwide. Further research and experimentation are necessary to validate its effectiveness for thick SS 304H flats, highlighting

the potential benefits of this method in industrial applications.

Use of SS 304H filler in enhancing depth of penetration was not reported in the published works while joining similar materials. Therefore, investigations may well be performed in this area.

The main objective of this work would be to investigate and optimize weldability while joining 8 mm-thick 304H austenitic stainless steel using TIG welding process. Achieving full penetration and producing high-quality welds are essential requirements. To accomplish this, a series of experiments and various post welding tests and analysis would be carried out.

In the initial phase of experimentation, autogenous TIG welding is planned to be conducted using butt joints prepared from 8 mm thick SS 304H specimens on a single side. To structure the experimental design effectively, Response Surface Methodology (RSM) is planned to employ in conjunction with Central Composite Design (CCD), allowing systematic variation of key welding parameters such as heat input, shielding gas flow rate and torch angle across three levels. It is tried to evaluate the combination of these parameters that would facilitate maximum weld penetration while minimizing weld bead reinforcement and overall bead width.

Building upon the findings from the initial investigation, a second set of experiments is planned with the optimal parameter combinations derived from the global matrix of a widely used Multi-Criteria Decision-Making (MCDM) technique known as the Analytic Hierarchy Process (AHP). In this phase, welding is planned to perform on both sides of the specimen aiming at achieving full penetration.

Experiment Set 3 is planned wherein the same process parameters identified in the second set would be retained, but with the application of Activated Flux (A-TIG) on the faying surface of the specimens. This approach is intended to enhance arc constriction and increase penetration depth further due to the reverse Marangoni effect, thereby improving the effectiveness of the TIG welding process under the optimized conditions. Together, these sequential experimental stages are planned to be done to build a comprehensive understanding of how process modifications and enhancements influence weld quality and penetration characteristics in high-performance austenitic stainless steels.

Extending the investigation further, a fourth phase of experimentation is planned to focus on non-autogenous TIG welding by incorporating SS 304H filler material under conditions comparable to the previous experiment sets. 1.2 mm diameter SS 304H filler wire is planned to use to better understand the influence of filler addition on weld penetration and joint quality. A structured Design of Experiment is again planned to be developed using Response Surface Methodology (RSM) with a Central Composite Design (CCD), facilitating the optimization of welding parameters specific to filler-assisted TIG welding. Key process parameters, such as, heat input, root gap and shielding gas flow rate are planned to be varied across three levels to examine their combined effect on weld characteristics.

To further strengthen the findings, investigation into the microstructural features, tensile tests to determine ultimate tensile strength and percentage elongation of the welded joints, hardness and micro-hardness measurements across the weld cross-sections and Scanning Electron Microscopy (SEM) and optical microscopy to understand the microstructural features are planned to be performed to gain deeper insights into the weld morphology. Finally, standard Machine Learning algorithms are planned to apply to the entire experimental dataset to evaluate the predictive capability of weld quality parameters such as bead geometry, tensile strength, elongation and hardness based on the selected input process variables.

To address the objectives mentioned above, the work has been executed and documented in the subsequent chapters of this thesis.

Chapter 1 outlines the motivation behind the study and underscores the importance of investigating the weldability of SS 304H stainless steel using the Gas Tungsten Arc Welding (GTAW) process. The aim and scope of the research are clearly defined, followed by a summary of how the thesis is organized.

Chapter 2 presents a thorough examination of existing literature relevant to welding processes, with emphasis on GTAW applied to austenitic stainless steels, especially in boiler component manufacturing. It explores the influence of welding parameters on weld quality, discusses experimental design methods like Response Surface Methodology (RSM), and delves into decision-making frameworks such as the Analytic Hierarchy Process (AHP). Additionally, the use of predictive algorithms for modelling welding outcomes is also reviewed.

Chapter 3 provides a detailed account of the materials selected and experimental procedures adopted for the study. It describes the execution of four different TIG welding configurations autogenous, A-TIG, and filler-assisted on SS 304H plates to examine the effect of key variables on weld performance. Post-welding evaluation methods including tensile testing, hardness measurement, microstructural analysis by Optical microscope and Scanning Electron Microscope and machine learning-based prediction models are also discussed.

In Chapter 4 results of the initial experiment involving autogenous TIG welding on 8 mm thick SS 304H specimens are presented and analyzed. The setup, including the weld joint configuration, shielding gas selection, and parameter levels, is described. A Central Composite Design (CCD) under the RSM framework is used for systematic experimentation. The effects of varying welding parameters on weld quality are interpreted through the presented data.

Chapter 5 focuses on the findings from the second and third experiment sets. Experiment Set 2 involves double-sided TIG welding based on parameter optimization using AHP, aiming to overcome the partial penetration issues found in Set 1. In Experiment Set 3, A-TIG welding is introduced with TiO_2-based activating flux to achieve deeper penetration via arc constriction. The results from both sets are critically compared to assess their impact on weld quality.

Chapter 6 discusses the fourth experimental phase, where TIG welding is performed with the addition of SS 304H filler wire. The experiment follows a CCD-RSM design and investigates

how factors such as heat input, gas flow rate, and root gap affect the welds. The use of a cold wire feeding mechanism is also explored. Results are analyzed to determine the influence of filler wire on penetration and mechanical properties.

Chapter 7 discusses the six standard machine learning models used in the weld dataset to predict welding outcomes based on experimental data. Multiple algorithms are employed to estimate output variables such as weld bead dimensions, tensile strength, and hardness. The performance of each algorithm is compared, highlighting their effectiveness in modeling the TIG welding process.

The final chapter, Chapter 8 summarizes the research outcomes across all four experimental sets and discusses how the integration of AHP and machine learning contributed to process optimization. Conclusions are drawn regarding weldability, penetration improvement, and predictive capabilities. The chapter concludes by outlining recommendations for future research on TIG welding of advanced stainless steels.

The thesis ends with the list of references.

VITA

The author, Subhodwip Saha, son of Sri Nabadwip Saha and Smt. Aparna Saha, was born on 15th September, 1990 in Kolkata, West Bengal, India. He studied in Sudhir Memorial Institute and passed the All-India Secondary School Examination (AISSE) in 2007. Then he continued his education in the same school and passed the All-India Senior School Certificate Examination (AISSCE) in 2009.

The author graduated in Mechanical Engineering in 2014 from Kalyani Government Engineering College under West Bengal University of Technology (WBUT). After that, he completed his Master of Technology with specialization in Production Engineering from the Department of Mechanical Engineering, Kalyani Government Engineering College, under Maulana Abul Kalam Azad University of Technology, West Bengal (Formerly WBUT), during the period 2015–2017.

The author has registered as a Ph.D. student on 26th June, 2018 in the Department of Power Engineering, Jadavpur University, Kolkata. He has carried out his research work in the area of Welding of SS 304H Austenitic Stainless Steel using Tungsten Inert Gas (TIG) Welding.

His research includes investigation of welding parameters and the influence of TIG, Autogenous TIG and Activated TIG welding on the mechanical properties of austenitic stainless steels. One of his notable works, titled "Supervised Machine Learning Models for Predicting SS304H Welding Properties Using TIG, Autogenous TIG, and A-TIG", was published in a SCI journal, Crystals, and was funded by the Deanship of Scientific Research at Imam Mohammad Ibn Saud Islamic University (IMSIU).

The author has published three research papers in national and international refereed journals, which include two UGC-approved journals and one SCI journal. He has also presented five papers in national-level conferences on advanced welding technologies and manufacturing.

DEDICATED TO MY DAUGHTER

AND TO ALL MY FAMILY

MEMBERS

CONTENTS

LIST OF FIGURES

LIST OF TABLES

CHAPTER 1

Introduction

1.1 Preamble

Welding plays a pivotal role in modern engineering, serving as a fundamental process for joining materials permanently in various industries, including power generation, construction and manufacturing. The advancement of welding technology is critical for enhancing the mechanical properties and longevity of welded structures, especially those subjected to extreme conditions such as high temperature and corrosive environment.

Traditional welding methods often face challenges in achieving optimal joint properties, particularly when dealing with high-performance materials. As industries use more advanced materials to meet strict performance standards, it becomes crucial to understand the details of how well these materials can be welded. Among various welding processes, Gas Tungsten Arc Welding (GTAW) has gained popularity due to its ability to produce high quality welded joints [1]. However, it has a limitation of having low productivity. A schematic diagram representing GTAW process is shown in Figure 1.1.

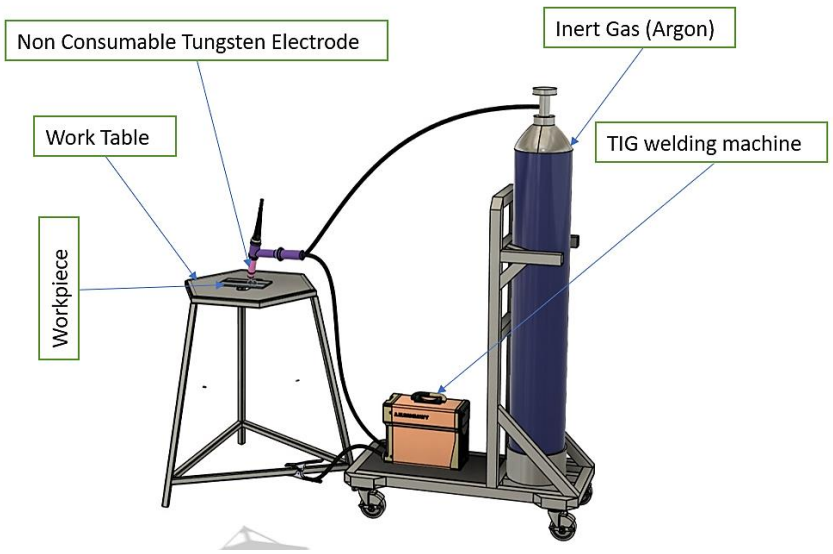

Figure 1.1. Schematic diagram of standard GTAW process

Efforts are ongoing to enhance the operational efficiency of power plants that rely on fossil fuels, particularly coal-fired facilities, with the aim of reducing the environmental impact caused by carbon emissions. For this, high operating temperature and pressure are required for boiler applications. This demands for development and utilization of advanced boiler materials. One of the key factors for selection of these materials depends on its ability to be welded easily for fabrication works. As a consequence, weldability plays a pivotal role in determining the suitable materials for modern coal-fired power plants.

Throughout a span of more than five decades, thermal power plants utilizing coal as a fuel source have undergone a remarkable evolution. They have transitioned from subcritical plants, characterized by an operating temperature of 540ºC, pressure of 16.5MPa, and efficiency of 35%, to the more advanced Ultra Supercritical Power plants. These newer plants operate at a higher temperature of 593ºC, pressure of 24.8MPa and achieve an improved efficiency of 42%. Continued initiatives are underway in the USA, Japan, and Europe to enhance power plant efficiency up to 45% by augmenting operating temperature and pressure. These specific parameters are being proposed for the implementation of Advanced Ultra Super Critical (AUSC) Boiler technology. To enhance overall efficiency, extensive efforts have been devoted to the advancement of alloys in USC power plants. Specifically, significant attention has been placed on optimizing Current Creep Strength Enhanced Ferritic (CSEF) alloys and modified Chromium-Molybdenum (Cr-Mo) steels. These materials [2-4] showcase remarkable physical and corrosion properties along with superior creep strength at an elevated temperature.

Through a quantitative methodology, Bhadeshia introduced [5] a range of new steels which are thermally resistive and welding consumables customised to meet the specific material demands of USC and AUSC power plants. To avoid weld cracking within the heat-affected zone (HAZ), it is essential to implement appropriate precautions during the welding process of Current Creep Strength Enhanced Ferritic (CSEF) steels.

During the welding process, thermal and solidification shrinkage induce stresses that can impact the performance of the weld. These stresses, if not addressed, can remain unchanged and have detrimental effects on the weldment. When exposed to a corrosive atmosphere, the presence of residual stresses can further increase the susceptibility to Stress Corrosion Cracking (SCC) [6-8]. Hydrogen-induced cracking can occur in CSEF materials when there is a combination of residual stress and insufficient preheating [9-12]. Moreover, in certain components like grade 23 (2.25Cr, 1.6W-V-Nb-B) compliant with ASME code, the presence of both residual stress and tri-axial stress can lead to the occurrence of reheat cracking [13-16].

CSEF steels exhibit satisfactory performance up to a maximum temperature of 650ºC. However, when it comes to corrosion resistance, they fall short beyond 620ºC. Furthermore, the maximum allowable stresses of CSEF steels are comparatively lower when compared to austenitic stainless steels and nickel base alloys. In contrast, austenitic steels typically have a composition of 18% Cr and 8% Ni, but they can be modified to contain 25% Cr and 20% Ni for enhanced corrosion resistance and improved strength. These modifications make austenitic steels excellent candidate materials for temperatures above 650ºC, offering superior corrosion resistance, higher strength and thermal stability at elevated temperatures [9-12].

Nickel base super alloys are commonly utilized for an operating temperature exceeding 700ºC. Nevertheless, the notable drawback of utilizing nickel and other alloying elements in their composition is the substantial increase in cost, rendering them considerably more expensive than ferritic and austenitic steels. In the United States, various nickel-based alloys are under consideration for implementation in advanced ultra-supercritical (AUSC) power plants. Particularly, Haynes 282 and Inconel 740/740H stand out for their exceptional mechanical properties in comparison to other alloys. [10-16].

As found in the literature, different process parameters, such as heat input, weld current, voltage, torch travel speed, and type of metal transfer, have a significant impact on bead geometry. Factors such as reinforcement form factor (RFF) and penetration shape factor (PSF) are crucial in determining the quality of weld bead geometry [17]. Mathematical models are used to predict weld bead geometry when depositing 316L stainless steel onto structural steel IS 2062 using a five-level factorial technique [18]. The impacts of various factors, such as flux type, weld current, voltage and torch travel speed on penetration, bead width, and reinforcement, have been analyzed [19,20].

Optimization techniques such as the Image Analysis Technique (IAT) have been employed to analyze weld bead geometry in the autogenous Tungsten Inert Gas (TIG) welding process. Weld voltage and vertex angle pairs were identified as crucial factors while developing neural network models for predicting bead size [21]. The influence of different variables, including the use of pulse current on weld characteristics, has also been explored in another research [22].

The design of experiments is achieved using Response Surface Methodology (RSM) [23], where authors integrate mathematical and statistical analyses through empirical models. In one work [24], mathematical models generated from the data effectively forecasted weld bead geometry, with optimized values achieved at a specific parameter setting. Steels such as austenitic stainless steels (ASS) and ferritic stainless steels (FSS) commonly use GTAW process for fabrication [25]. Heat input plays [26, 27] a crucial role in successful weld cladding and achieving desirable weld bead geometry. Researchers have employed several optimization techniques to enhance bead geometry and weld joint characteristics, with The Analytic Hierarchy Process (AHP) emerging as a simple yet powerful method. The AHP involves constructing a hierarchy that includes objectives, criteria, and alternatives, followed by pairwise comparisons using a ratio scale. The AHP has been successfully used

to optimize weld bead geometry parameters like reinforcement, penetration depth, and bead width [28-31]. The use of activated tungsten inert gas (A-TIG) welding with suitable fluxes, such as TiO_2, Fe_2O_3, Cr_2O_3, etc. significantly affects weld bead geometry in stainless steel welding, enhancing penetration and reducing bead width. Although A-TIG welding offers productivity advantages, its adoption remains limited. However, the process provides benefits like improved penetration and reduced welding time, particularly for butt joints of 10 mm-thick stainless-steel components [32-34]. A-TIG welding of aluminum alloys also enhances [35] joint strength while minimizing weld porosity. This method also introduces distinct morphological features in the weld zone and heat-affected zone compared to conventional TIG welding, providing superior penetration and mechanical properties. A-TIG welding, by reducing bead width, enhances penetration, resulting in significant improvements in weld quality and efficiency, especially in thicker materials and alloys such as stainless-steel components [36-39].

1.2 Aim of the Present Work

The aim of this research is to achieve optimal weld bead characteristics such as, bead width, height of reinforcement and depth of penetration, for 8 mm thick SS 304H austenitic stainless steel butt joints (50 mm × 50 mm). This steel is commonly used as high-temperature components like advanced boiler materials that are used for fabricating terminal sections of superheaters and reheaters commonly present in thermal power plants due to its excellent high-temperature strength and corrosion resistance. Selecting suitable input parameters, such as heat input, torch angle, root gap and shielding gas flow rate is the need. To meet this goal, a detailed investigation is planned to be carried out using different variants of TIG welding, including Autogenous TIG, A-TIG (Activated flux TIG) and filler-assisted TIG, with a focus on achieving full penetration and producing high-quality welds. Weldability of SS 304H is planned to be assessed by examining the resulting bead geometry and mechanical properties such as tensile strength, elongation, hardness and microstructure. The plan is to utilize suitable optimization technique to decide welding parameters and their levels for achieving optimized bead geometry and mechanical strength. It also plans to apply predictive algorithms to establish accurate correlations between input settings and weld outcomes, enabling consistent and high-quality welds.

1.3 Organisation of the Thesis

The whole thesis is divided into 8 chapters. The name of each chapter and its contents are briefly discussed in the following:

Chapter 1: Introduction

This chapter first introduces the background and significance of the research work on welding of SS 304H stainless steel using GTAW process. Aim of the work is discussed next. Organization of the thesis is also included at the end of the chapter.

Chapter 2: Literature Review

The second chapter presents a comprehensive review of the relevant literature on welding techniques, focusing on GTAW processes used in austenitic stainless steels mainly used in boiler applications, and the challenges involved in welding such steels. The impact of various welding parameters on bead geometry, penetration and joint quality is also discussed. This chapter also reviews design of experimentation techniques such as Response Surface Methodology (RSM) and Multi Criteria Decision Making processes such as the Analytical Hierarchy Process (AHP). Predictive algorithms which are widely used establish correlations between input variables and outcomes are also reviewed in this chapter.

Chapter 3: Materials and Method

This chapter details the materials used and the method employed in this work. The research investigates TIG welding variants on SS 304H stainless steel plates using four distinct sets of experiments to assess the impact of key process parameters on weld quality. Each set explores different welding configurations, such as autogenous, A-TIG and filler-assisted TIG to bead geometry parameters mainly focusing upon depth of penetration. Post-weld tests include tensile test, hardness and microstructural analysis, supported by SEM and predictive machine learning models. A summary of methodologies is provided inside the chapter.

Chapter 4: Results and Discussion on Experiment Set 1

This chapter presents the results obtained in the 1st set of welding experiment conducted using autogenous TIG welding on SS 304H stainless steel specimens and discussions on

them. It includes detail about the type of weld joint, shielding gas and other process parameters used. A structured design of experimentation using the Central Composite Design (CCD) under the Response Surface Methodology (RSM) is employed to systematically vary process parameters. The results of all these tests are represented, analysed and discussed in this chapter.

Chapter 5: Results and Discussion on Experiment Set 2 and 3

This chapter presents the results and discussion related to Experiment Sets 2 and 3 aimed at overcoming the lack of full penetration observed in Experiment Set 1. Experiment Set 2 involves double-sided autogenous TIG welding on SS 304H specimens using top-ranked parameters from Experiment Set 1, using the Analytical Hierarchy Process. Experiment Set 3 introduces A-TIG welding with TiO_2 flux to enhance penetration by altering heat flow in the weld pool. In both Experiment sets similar process parameters are set to ensure reliable comparison, and their outcomes are analyzed to evaluate improvements in weld quality and performance.

Chapter 6: Results and Discussion on Experiment Set 4

This chapter presents the 4th and final set of experiment involving filler-assisted TIG welding on SS 304H stainless steel plates. This chapter also utilizes the application of Design of Experimentation through Central Composite Design under Response Surface Methodology to plan and analyse welding runs. It highlights the use of a cold wire feeder for consistent filler deposition and explores the influence of key parameters such as heat input, gas flow rate and root gap on weld quality and performance.

Chapter 7: Results and Discussion on Predictive Modelling of Experimental Data Using Machine Learning Techniques

Chapter 7 presents the development and analysis of predictive models using machine learning techniques applied to the experimental data. The objective is to estimate key output parameters and to compare them with actual experimental results to evaluate the prediction accuracy. Four complete sets of experimental data containing input welding parameters and corresponding output responses are used for model training, testing and validation. Six widely used machine learning algorithms are employed to build these models and their

performances are comparatively assessed based on their predictive reliability for weld bead geometry and mechanical properties.

Chapter 8: Conclusion and Future Scope of Work

This chapter presents the conclusion drawn from the comprehensive research on variants of TIG based welding of 8 mm thick SS 304H stainless steel used in elevated temperature applications, aimed at achieving full penetration and optimal weld quality. The chapter summarizes the outcomes of four distinct sets of experiments involving autogenous TIG, A-TIG and filler-assisted TIG welding, alongside post-weld mechanical and metallurgical evaluations. The role of the Analytic Hierarchy Process (AHP) in ranking optimal welding conditions and the application of machine learning algorithms for predictive modelling are also highlighted. Finally, the chapter highlights possible future research areas.

The thesis ends with the list of references.

CHAPTER 2

Literature Review

2.1 Introduction

Welding is a fundamental joining process widely employed in industries such as power generation, construction and manufacturing. The demand for enhanced welded structures has led to the development of advanced welding techniques to improve mechanical properties and durability, particularly in high-temperature and corrosive environments. With growing industrial needs, especially in energy sectors, the role of welding has expanded beyond basic fabrication in becoming a critical factor in ensuring the long-term reliability of structural components.

Traditional welding methods often face challenges in achieving optimal joint properties, particularly when dealing with high-performance materials. As industries use more advanced materials to meet strict performance standards, it becomes crucial to understand the details of how well these materials can be welded. This becomes especially important when working with materials exposed to extreme environments, such as those found in thermal power plants. Among various welding processes, Gas Tungsten Arc Welding (GTAW) has gained popularity due to its versatility and widespread applicability in different materials and industries [1], providing high-quality welding. However, it has the limitation of low productivity, which restricts its use in mass-scale or high-deposition applications. Therefore, to meet the increasing demand for both quality and efficiency in modern power plant construction, industries are looking at both improved materials and welding techniques.

To enhance coal-based power plant efficiency and reduce emissions, researchers focused on increasing boiler temperature and pressure. This required strong, heat-resistant materials that could be effectively joined, making material selection crucial for USC and AUSC technologies [2–5]. Several countries, including the USA, Japan, and nations in Europe, had actively pursued power plant efficiencies above 45% by adopting advanced technologies [2–4], which demanded welding processes capable of delivering both precision and performance with minimal defects. Among the materials explored, Creep Strength

Enhanced Ferritic (CSEF) steels and modified Cr-Mo steels showed good strength and resistance to corrosion at high temperatures [2–4, 6–8]. However, they still faced welding issues like cracking, especially in the heat-affected zone (HAZ), when proper welding techniques and preheating were not used [5, 9–12]. While austenitic stainless steels performed better above 650°C due to their superior corrosion resistance and strength [9–12], nickel-based alloys like Haynes 282 and Inconel 740H were best suited for use above 700°C, though their high cost limited their widespread adoption [10–16]. As the demand for high-performance materials increases over the years in advanced thermal systems, it is essential to examine how different welding parameters influence joint quality.

As found in the literature, different process parameters, such as heat input, weld current, voltage, torch travel speed and type of metal transfer, were found have a significant impact on bead geometry. Factors such as reinforcement form factor (RFF) and penetration shape factor (PSF) were found crucial in determining the quality of weld bead geometry [17]. Mathematical models were used to predict weld bead geometry when depositing 316L stainless steel onto structural steel IS 2062 using a five-level factorial technique [18]. The influence of type of flux and composition, welding current, arc voltage and travel speed were found to have a strong impact on weld bead geometry parameters such as penetration depth, bead height, and bead width which were analyzed using Grey Relational Analysis (GRA). The multi-response optimization was achieved by converting these outputs into a single grey relational grade, which was then modeled through regression analysis for prediction and parameter optimization [19]. Weld bead geometry in autogenous TIG welding of P91 steel was evaluated using Image Analysis Techniques (IAT) based on pixel intensity from digital images. The results closely matched those from Leica-Q-win-V3 software, validating IAT as a reliable method for weld profile measurement [20]. In another work Image Analysis Technique (IAT) was effectively used in autogenous TIG welding to assess bead shape, where voltage and vertex angle significantly influenced the outcomes when neural networks were applied to predict bead geometry dimensions [21]. The influence of pulse currents on weld geometry and angular distortion in 3 mm thick SS- 304 autogenous butt joints was examined using the pulsed GTAW process. Peak and base currents were varied while keeping mean current and welding speed constant. Results indicated that pulsed GTAW produced wider beads and significantly lower angular distortion compared to continuous GTAW [22]. Statistical approaches, particularly Response Surface Methodology (RSM), were employed to develop empirical models that

described the influence of process parameters on bead formation [23]. Other investigations demonstrated that mathematical models derived from experimental data could reliably predict weld geometry, with optimal results achieved under specific parameter combinations [24]. Austenitic and ferritic stainless steels frequently employed the GTAW process for fabrication, owing to its high precision and adaptability across a range of materials [25]. Among the key variables, heat input remained a critical determinant in weld cladding and the formation of acceptable bead geometry [26, 27].

To further refine parameter selection, Multi Criteria Decision Making (MCDM) tools like the Analytic Hierarchy Process (AHP) gained popularity for their capacity to handle multi-criteria evaluations using structured pairwise comparisons [28–31]. The AHP was successfully implemented to optimize key geometrical attributes such as bead width, penetration depth and reinforcement. Additionally, the Activated Tungsten Inert Gas (A-TIG) welding technique, which incorporated activating fluxes such as TiO_2, Cr_2O_3, or Fe_2O_3, demonstrated considerable improvements in weld penetration and a reduction in bead width, particularly in thicker sections of stainless-steel weldments [32–34]. In the context of aluminum alloys, A-TIG process was reported to increase joint strength and reduce weld porosity [35]. Furthermore, A-TIG was found beneficial in producing desired morphological changes in both the weld zone and heat-affected zone, offering mechanical and structural advantages over conventional TIG welding techniques [36–39].

Using advanced welding methods effectively not only requires careful control of welding settings but also depends on how the material reacts to heat and changes in its structure during welding. This reaction is closely related to the concept of weldability, which is very important while choosing the right material and improving the welding process. As per the Handbook of the American Welding Society, weldability is characterized as the “ability of a material to be effectively welded under the given fabrication conditions, resulting in a well-designed structure that performs adequately in its intended service.” [40].

Weldability is influenced by multiple factors, including the composition properties, microstructure, process parameters and other relevant considerations. Extensive research and analysis led to the development of several weldability indicators that helped characterize the behaviour of different welding techniques [41-43]. Weldability of structural materials was examined such as stainless steels, and Ni- and Al-based alloys, detailing fabrication and service-related failures such as hot, warm, and cold cracking [42].

Various weldability tests like hot cracking tests were found to be done during fabrication and tests like toughness test, fatigue and corrosion resistance tests and tensile and ductility tests were found to be done during service [43].

Following paragraphs discuss welding and weldability related investigations corresponding to the materials used in boilers.

2.2 Welding and Weldability of Steels Employed in Coal Fired Power Plants

Power generation in India is still highly dependent on coal. Nevertheless, the combustion of coal for power generation is a major contributor to carbon dioxide emissions, which poses significant concerns in terms of climate change. In response, numerous clean coal technologies are being actively developed on a global scale. With the widespread adoption of advanced boiler technology all over the world, including in India, effort has been made to reduce the carbon dioxide emission as much as possible [44].

Previously, numerous welding experiments were carried out to determine the optimal combination of process parameters and filler material for welding various components of the predominantly steel boiler. Gas Tungsten Arc Welding (GTAW) was utilized for conducting these experiments [10].

For higher efficiency of power plants using fossil fuel as a source, materials are required to be developed with properties which can withstand higher operating temperature and pressure. A boiler carrying steam at higher pressure consists of tubes and pipes. Tubes typically possess a smaller outer diameter and thin walls, whereas pipes are characterized by larger outside diameters and thicker walls. Pipes can be further categorized into headers, that serve as passage for steam transportation to the turbine. Figure 2.1 depicts headers composed of thick-walled pipes that are penetrated by multiple tubes [45].

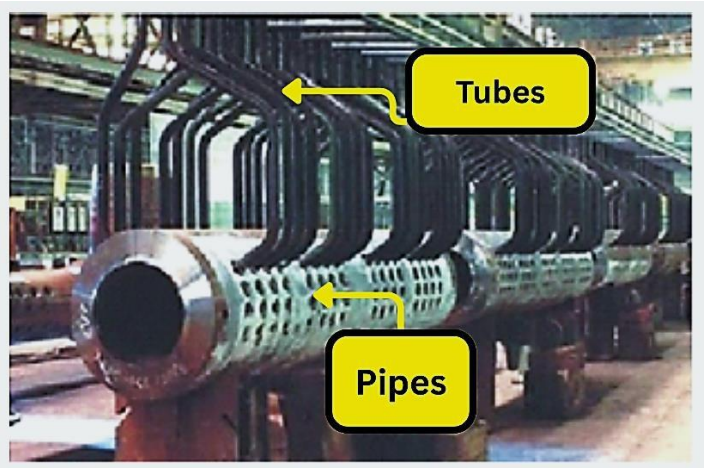

Figure 2.1. Headers consisting of pipes penetrated by tubes [45].

2.3. Application of Welding in Steam Generators

High temperature and continuous reaction with steam lead to corrosion in various boiler parts which have detrimental effects. Moreover, pipe channels and their bends used in steam generators and continuous joints are to be made of similar and dissimilar materials that require various welding processes to employ for their fabrication [45]. Repair welding is also often used to improve service life of these components mostly. Gas Tungsten Arc Welding (GTAW), is a widely employed welding technique in modern steam generators due to its effectiveness and suitability for the application [44,45].

2.3.1. Development of Advanced Boilers

In recent decades, the design and operation of fossil fuel-fired boilers have seen transformative advancements aimed at improving efficiency and reducing environmental impact. These developments are pivotal in addressing the dual challenges of growing energy demand and climate change mitigation. Boilers are now categorized based on their operational parameters, with "Subcritical," "Supercritical," and "Ultra-Supercritical" (USC) technologies representing progressively higher levels of temperature and pressure. Operating at elevated conditions allows these advanced boilers to generate more energy from the same amount of coal, reducing fuel consumption and lowering CO_2 emissions. Supercritical boilers, operating above the critical point of water where distinct liquid and vapour phases cease to exist, achieve superior thermal efficiency compared to their subcritical counterparts. USC boilers take this further, operating at temperatures exceeding 600°C and pressures above 30 MPa, necessitating the use of high-performance materials

such as austenitic stainless steels, nickel-based superalloys and creep-strength-enhanced ferritic steels. In addition to material innovations, advances in manufacturing and welding technologies have been critical to the successful deployment of these boilers. High-precision welding techniques such as Gas Tungsten Arc Welding (GTAW) ensure the structural integrity of critical components subjected to extreme operational conditions. These methods provide improved control over weld quality, minimize defects and enhance the durability of the welded joints. The use of suitable welding techniques with innovative materials ensures that modern boilers meet the demands for efficiency, reliability and sustainability while continuing to utilize coal as a primary energy source [44-46].

2.3.2. Material Requirements and Challenges in Modern Advanced Boilers

Modern advanced boilers, such as Advanced Ultra Super-Critical (AUSC) boilers require materials with high creep strength, weldability and corrosion resistance to withstand extreme conditions. Initiatives were taken globally with the aim to improve AUSC efficiency, with boiler steam temperatures exceeding 750°C for efficiencies above 45%. Materials like CSEF steels, austenitic stainless steels and nickel-based superalloys are key candidates. CSEF steels offered cost-effective options with superior creep resistance but face challenges like Type IV cracking in welds. Austenitic steels and nickel-based superalloys excel at temperatures above 650°C, making them ideal for modern power plants despite their higher costs. Efforts focus on optimizing welding parameters to ensure reliability in AUSC applications [47-62].

2.4. Austenitic Stainless Steels Used in Modern Boilers

Boiler parts such as pipes and headers are susceptible to thermal fatigue cracking. These parts were found to show lower thermal expansion and exhibit better thermal conductivity. However, despite the satisfactory performance of ferritic steels below 620°C with the aforementioned properties, they failed when exposed to temperatures exceeding this threshold [61-63]. Studies [64] have concluded that austenitic stainless steels were appropriate for applications at temperatures surpassing 650°C. These steels were derived from a ternary alloy system consisting of iron (Fe), nickel (Ni) and chromium (Cr), characterized by a fully austenitic structure and lacking transformation hardening capabilities [65]. In recent times, researchers have developed a range of heat corrosion-resistant and precipitation-hardenable austenitic steels [64, 66] that demonstrate outstanding

creep properties. To enhance high-temperature resistance and corrosion resistance, Chromium and Nickel percentages in austenitic stainless steels were typically increased to 25 and 20, respectively. Additional austenitic stainless steels with improved corrosion properties and higher creep strength were developed, though at a higher cost compared to high-performance austenitic stainless steels. Senba et al. [66] employed a combination of precipitation hardening and solid solution strengthening mechanisms to enhance the performance of these steels. On the other hand, the 304H grade of austenitic steel incorporates additions of Cu, N and Nb. It falls within the 18Cr-8Ni steel family and demonstrates enhanced strength and superior corrosion resistance [63, 65].

Stainless steel alloys belonging to the 18Cr-8Ni family commonly used include 304H, 316H, 321H and 347H. Stainless steel of grade 304H is known for its excellent combination of high-temperature strength and corrosion resistance, making it ideal for use in demanding environments. It offers outstanding resistance to oxidation, scaling and can withstand high-temperature conditions, typically up to 870°C (1600°F). The alloy also exhibits good weldability and fabricability, making it a popular choice for power plants, heat exchangers and other applications where thermal stability is crucial.

2.4.1. Solidification in Austenitic Weldments

Substantial progress had been made since 1970s in understanding the properties of austenitic stainless steels, including their solidification behaviour, segregation patterns and phase stability of weld characteristics. These factors were found to determine the structure, cracking tendency and overall performance of the steels and their weldments. Depending on the Chromium and Nickel content, austenitic stainless steels were either fully austenitic (γ) or a combination of austenitic and ferritic phases ($\gamma + \delta$), resulting in duplex microstructures. The residual δ ferrite in the weld referred to the portion remaining after the initial ferritic solidification and subsequent solid-state transformation to austenite. The amount of δ ferrite in the weld was commonly evaluated using the ferrite number (FN), which was based on magnetic properties such as magnetic permeability. However, it was important to note that FN did not directly correspond to the actual ferrite percentage. Typically, a Ferrite Number below 10 was considered indicative of a certain proportion of ferrite [67].

2.4.2. Ferrite in Austenitic Weldments

The presence of ferrite plays a crucial role in determining the properties and performance parameters of austenitic stainless steels. It was found to be both advantageous and potentially harmful effects when present in austenitic stainless steels. In welded joints, the presence of ferrite helped prevent hot cracking issues. Prolonged exposure to elevated and reduced temperatures caused spinodal decomposition, which in turn led to the loss of ductility and the embrittlement of the weld metal. It was well recognized that austenitic stainless steels were susceptible to hot cracking unless they contained a minimum percentage of 3 to 5% of δ ferrite. Conversely, an excessive presence of δ ferrite, exceeding 5–10%, negatively impacted the properties of the welded joints [68].

2.5. Problems of Weldability in Austenitic Stainless Steels

While austenitic stainless steels were commonly considered weldable with proper control over parameters, they remained prone to cracking problems, mainly attributed to the presence of impurities like sulphur, phosphorus, and other low melting point elements. Cracking failures manifested in different forms in austenitic stainless steels, including solidification cracking, liquation cracking, reheat cracking, and ductility dip cracking [65]. To assess the sensitivity of these materials toward weld cracking issues, several weldability tests were developed [35, 68, 69]. Lippold conducted a comprehensive review [64] on the development of testing procedures for weld cracking. In his analysis, he took into account various factors such as impurity levels, grain size, solidification mode, heat input and tried to evaluate the tendency and severity of these cracking phenomena. Additionally, attention had to be given to issues like sensitization observed in certain grades of austenitic stainless steels. As a result of sensitization, chromium carbide is formed along grain boundaries, degrading the chromium content in the matrix adjacent to the boundaries, causing intergranular corrosion.

2.5.1 Hot Cracking and Weld Penetration

Hot cracking, also known as solidification cracking, was the phenomenon where low penetration occurred in austenitic stainless steel during the GTAW process, resulting in cracking [57, 68]. It was predominantly observed in fully austenitic stainless steels and was less common in welds that contain a combination of γ and δ phases [57]. Consequently, it

was recommended to have a ferrite number ranging from 5 to 10 in the microstructure to mitigate the aforementioned failure. The most frequently accepted explanation for hot cracking suggested that low melting constituents segregated during the latter phases of weld solidification, resulting in the creation of a liquid phase with a lower melting point. This liquid phase infiltrated the grain boundaries and subsequently cracked under the influence of thermal and solidification stresses [68].

2.5.2 HAZ Liquation Cracking

Liquation cracking occured in the region of the fusion zone as a consequence of a liquid film forming along grain boundaries. This liquid film weakened the boundary strengths, leading to the occurrence of liquation cracking. The occurrence of these cracks was primarily attributed to the presence of tramp elements such as sulphur (S), phosphorus (P) and metal carbides like titanium carbide (TiC), niobium carbide (NbC), among others. An effective approach to address these cracks involved modifying the composition to encourage the formation of specific ferrite phases at the grain boundaries. Alternatively, reducing the impurity levels to the desired specifications could also help in reducing the likelihood of these cracking issues [70].

2.5.3 Stress Relief Cracking

These cracks exhibited an intergranular nature and was reported to occur specifically within the Heat Affected Zone (HAZ) of stainless steels that were strengthened through precipitation hardening, particularly grades that contained elements like niobium (Nb), titanium (Ti) and others [46]. In industries related to power generation, stress relaxation cracking was identified in weldments with thick sections, welds that connected stubs to headers, highly restrained weldments and cold-worked tube bends [71, 72].

2.6. Use of GTAW Process in Power Plant Technology

The GTAW process was found to be extensively employed as a key fabrication method in steam generators in recent times [73, 74]. Austenitic steels like modified 9 Cr-1Mo (P 91) steel were commonly used for the construction of components of power plants, and GTAW played a significant role in their joining process. However, there were several disadvantages to GTAW, including restricted penetration depth during single-pass welding operations, decreased productivity, and a high sensitivity of the weld bead to fluctuations in the

chemical composition of the parent metal. Nevertheless, these limitations were overcome by utilizing a multi-pass welding technique, which promoted surface treatment such as tempering of the weld after every pass. In recent times, there had been significant interest in the use of Activated Flux TIG (A-TIG) for joining power plant components. This welding process is known for its ability to achieve deep penetration and high productivity in a single pass, surpassing the conventional GTAW process. The A-TIG process used fluxes, where penetration was enhanced by reverse Marangoni flow [38]. In this process, a paste consisting of metallic oxides, such as a mixture of deoxidizers like Si and Ti in the correct proportions, was manually applied in a longitudinal direction along the weld. This application of flux aided in achieving the desired welding characteristics.

2.7. Material Selection for Welding of Boiler Steels Using GTAW Process

Selecting the right material for welding boiler components is critical due to the need for high-temperature strength, corrosion resistance and cost-effectiveness. While low-alloy ferritic steels such as Grade 91 and Grade 92 provided excellent creep resistance, they often suffered from Type IV cracking in the heat-affected zone (HAZ) and showed limited efficacy at temperatures beyond 600°C [75, 76]. On the other hand, nickel-based alloys offered superior high-temperature performance and oxidation resistance but were not economically viable for widespread use in large-scale boiler systems [77]. Among the available options, SS 304H austenitic stainless steel stood out as a highly favourable choice for advanced boiler applications. Elevated carbon content of this material enhanced its creep rupture strength, making it particularly suitable for use in ultra-supercritical (USC) and advanced ultra-supercritical (AUSC) boilers, where high pressure and temperature were prevalent [78]. Furthermore, chromium-nickel alloy composition of SS 304H provided exceptional resistance to oxidation and ensured that the material maintains its structural integrity during prolonged exposure to high temperature [79].

When employing Gas Tungsten Arc Welding (GTAW) for joining SS 304H, several notable benefits could be observed, including precise heat management, minimal defect formation and superior mechanical properties in the weld zone [80]. Studies indicated that weld metal of SS 304H displayed a well-balanced ferrite-austenite microstructure, which significantly reduced the risk of solidification cracking [81]. Enhanced GTAW techniques, such as Activated Flux GTAW (A-TIG), further improved the weld quality by increasing depth of penetration, particularly in thick sections [82]. Post-weld microstructural assessments

revealed that SS 304H weldments retained a stable carbide distribution, minimizing the risk of intergranular corrosion and sensitization [83]. These advantages made SS 304H an excellent choice for boiler components that could endure extreme operational conditions, ensuring both reliability and longevity [84]. Additionally, the research highlighted the importance of optimizing welding parameters, such as heat input and current, to improve the weld quality and address challenges like residual stress and distortion [85].

2.8. Weldability of SS 304H

SS 304H, a high-carbon variant of 304-grade austenitic stainless steel, is highly regarded for its excellent weldability, making it a key material for high-temperature applications, particularly in modern boiler systems. Its higher carbon content contributed to improved creep strength, enabling it to endure prolonged exposure to extreme operating temperatures and pressures. Additionally, its chemical composition, which included chromium and nickel, provided superior corrosion resistance and oxidation protection, both essential in intense operational environments such as power plants [75].

The welding characteristics of SS 304H were found notably advantageous due to its resistance to hot cracking during solidification. This was primarily achieved by maintaining a balanced microstructure with ferrite in the weld metal, which reduced cracking tendencies. Gas Tungsten Arc Welding (GTAW), known for its precise heat control, was found to be particularly suited to SS 304H, allowing the fabrication of thick-section components with minimal defects. Moreover, advanced techniques such as Activated TIG (A-TIG) welding, etc. were demonstrated to enhance weld penetration and improve joint integrity in this material. By optimizing welding parameters such as current and heat input, challenges like residual stresses and distortion could be effectively addressed, ensuring durable and reliable welds. These attributes established SS 304H as a versatile and dependable choice for high-performance welded components in demanding industrial applications [75, 76, 78, 81, 84].

2.8.1 Weldability of SS 304H using GTAW process

SS 304H exhibited good weldability owing to its balanced austenitic microstructure which ensured stability during the welding process. However, high carbon content increased the risk of sensitization and intergranular corrosion when exposed to elevated temperatures during welding. Research work showed that precise control over heat input was critical to

minimize these effects. The use of GTAW, with its controlled arc and inert shielding environment, helped mitigate formation of deleterious carbides, thus improving weld integrity [86-88]. The microstructure and mechanical behaviour of GTAW joints between P91 and SS304H was investigated using IN625 filler. Post-weld heat treatment improved tensile strength and ductility and a varied microstructure was observed across the weld zones [88].

One of the significant challenges associated with welding SS 304H is hot cracking, which arises due to the segregation of impurities like sulphur and phosphorus in the weld zone. It was demonstrated that maintaining a ferrite number (FN) between 5 and 10 could reduce susceptibility to hot cracking. This was achieved by controlling the composition and cooling rates during welding [89,90].

In another work Bayesian Neural Network model was used to predict the ferrite number in stainless steel welds. The model revealed that elements like chromium, nickel, titanium, and silicon had a major influence on ferrite content. It outperformed traditional constitution diagrams in accuracy and highlighted the nonlinear impact of individual element variations [91].

Moreover, the role of filler materials was explored extensively by various researchers to enhance joint strength [92-95]. Researchers investigated dissimilar GTAW joints of pure copper and AISI 304 stainless steel using various filler metals. Among the tested fillers, ER309L provided the best mechanical strength and impact energy with a more ductile fracture surface [92]. TIG welding of Ti-5Al-2.5Sn alloy was explored by using different fillers and was found that Ti-6Al-4V filler gave better tensile strength and hardness due to higher martensite formation. Welds with this filler also showed more compressive residual stress, improving surface properties [93]. Researchers also investigated dissimilar welding of SS304 and MS1020 using TIG and SMAW with various fillers and post-weld heat treatments (PWHT). They found TIG with mild steel filler and post welding heat treated at 600 °C gave the best mechanical and microstructural performance due to improved ductility and reduced hardness in the heat-affected zone [94]. A common approach involved using compatible filler wires which align with thermal expansion and metallurgical properties of the base material. In another work researchers examined dissimilar welding between T91 martensitic steel and Super 304H austenitic stainless steel using semi-automatic GTAW process with three different filler wires. The study revealed that appropriate filler selection

significantly influenced the microstructure and mechanical properties of the welds. The research focused on optimizing cost-effective joints for high-temperature boiler applications while ensuring performance through microstructural stability and mechanical integrity. [95].

2.8.2 Heat Input and Penetration of SS 304H using GTAW process

Achieving full penetration is a critical requirement in applications involving SS 304H, particularly for components subjected to high-pressure and high-temperature environment. GTAW process allows precise control over heat input, which is crucial for optimizing bead geometry and ensuring complete fusion without defects. Dissimilar welding of SS 304H was reported to be done using seven binary fluxes where weldments where 90% SiO_2–10% TiO_2 flux were used achieved ~290% higher penetration and ~58% narrower welds due to arc constriction and reverse Marangoni flow [96]. In another research hot wire TIG welding of 304HCu and P91 steels was done where higher heating currents, along with optimized wire feed rate, improved weld quality by enhancing heat input and deposition. The dissimilar joint achieved 664 MPa tensile strength, 398 HV hardness at the interface, and 220 J impact toughness, indicating strong metallurgical bonding [97]. Investigations employing autogenous GTAW and the addition of filler materials reported that parameters such as welding current, travel speed and shielding gas flow rate to greatly influence penetration depth and weld bead quality [98-99].

Additionally, Activated flux TIG (A-TIG) welding, a modification of the conventional GTAW process was explored for SS 304H. The application of surface-active fluxes like TiO_2 improved weld pool fluidity and penetration. This technique was particularly effective in reducing the need for multiple passes, thereby enhancing productivity while maintaining weld quality [100-103].

2.8.3. Microstructural and Mechanical Behaviour SS 304H Using GTAW Process

The microstructural stability of SS 304H during GTAW is a key factor influencing its weldability. The austenitic matrix may undergo delta ferrite formation in the weld metal, which provides crack resistance but can adversely affect toughness at an elevated temperature. Post-weld heat treatment (PWHT) is often recommended to restore ductility and relieve residual stresses in welded joints. Recent works emphasized the importance of

PWHT in enhancing the creep resistance of SS 304H, especially in applications involving prolonged thermal exposure [104-107].

From a mechanical perspective, welded SS 304H joints exhibit excellent tensile strength and ductility under optimized welding conditions. Proper shielding gas composition, typically pure argon or argon-helium mixtures were found to play a vital role in minimizing oxidation and ensuring weld surface quality [108-110].

2.9. Application of Response Surface Methodology in Welding with a Focus on Central Composite Design

Response Surface Methodology (RSM) is an effective statistical tool in optimization of weld joints using various techniques, including Gas Tungsten Arc Welding (GTAW), Gas Metal Arc Welding (GMAW), Friction Stir Welding (FSW), etc. Among various methods within RSM, the Central Composite Design (CCD) is one of the most frequently employed, primarily due to its efficiency in exploring quadratic relationships and generating accurate second-order response surfaces with minimal experimental runs [23,24, 111-117].

In the optimization of pulsed current GTAW for commercially pure titanium, Response Surface Methodology (RSM) combined with Central Composite Design (CCD) was utilized to determine the best input parameters such as peak current, pulse frequency and welding speed. This approach successfully identified the conditions that minimized bead width while improving mechanical properties like tensile strength and hardness. The findings demonstrated the capability of CCD to achieve these optimizations effectively [111].

A similar methodology was applied to submerged arc welding (SAW), focusing on key variables such as arc voltage and welding current. Optimization using RSM and CCD resulted in notable improvements in weld bead penetration, bead width and dilution. The accuracy of the CCD model was verified through confirmation experiments, which showed a strong correlation between predicted and actual results [112].

For friction stir welding of aluminum alloys, CCD was employed to examine how rotational speed, welding speed and axial force influenced tensile strength. The analysis offered a detailed understanding of the interplay between these factors, leading to the identification of optimal parameters that enhanced mechanical properties and surface finish [113]. In gas metal arc welding (GMAW) of AISI 304 stainless steel, the application of RSM and CCD

streamlined the experimental process, reducing the number of required trials while ensuring high-quality welds with minimal distortion and improved mechanical strength [114].

Further research demonstrated the advantages of using CCD in metal inert gas (MIG) welding to systematically analyze the nonlinear effects of welding variables. When coupled with confirmation tests, this approach provided reliable results and deeper insights into process optimization [115]. Combining CCD with other techniques, such as Artificial Neural Networks (ANN), further enhanced the predictive capabilities of models. This integration proved especially beneficial in optimizing complex welding conditions for microalloyed steels [116].

Overall, the application of RSM, particularly with CCD, has significantly improved welding process optimization. It has reduced the experimental workload while providing accurate predictions about the impact of welding parameters. This resulted in enhanced weld quality, reduced production costs and shorter development times, making this methodology invaluable for industrial practices [117].

2.10. Application of The Analytic Hierarchy Process in Optimization of Welding Parameters

The Analytic Hierarchy Process (AHP) is a structured approach designed to solve complex problems involving multiple criteria. It helps decision-makers systematically analyze and organize problems in a logical and quantitative way [118]. The main idea behind the AHP is to divide a complex problem into a hierarchy of smaller, easier-to-handle components, allowing each part to be evaluated individually. These smaller components typically represent criteria that are important in assessing various options. The AHP allows for a structured comparison of these options based on the importance of each criterion. The process involves three key steps. First, the problem is structured into a hierarchy, starting with the main goal, followed by criteria and alternatives. Next, pairwise comparisons are made to prioritize these elements using a scale of 1 to 9. Finally, a consistency check ensures the reliability of comparisons, leading to a priority ranking that identifies the best option. Its ability to integrate both qualitative and quantitative factors makes the Analytic Hierarchy Process highly valuable in fields such as engineering and management. In welding, it effectively balances key considerations like strength, cost and environmental impact, leading to more informed and effective decision-making [118-123].

In welding, the AHP was effectively used to optimize parameters by carefully assessing the importance of various factors that influence weld quality, cost and performance [119-123]. This method is especially useful for addressing multiple objectives commonly found in welding operations.

One major application of the AHP is in identifying the best settings for welding techniques such as Gas Tungsten Arc Welding (GTAW). Various works performed prioritized critical parameters like weld voltage, weld current, travel speed and filler material. These works showed that factors like weld voltage and weld current significantly affect the mechanical properties of welds, helping to make more informed decisions during parameter selection [119].

The AHP was also applied to compare the performance of different welding methods. For example, it was used to evaluate key factors like weld strength, thermal distortion and cost, useful in selecting the most appropriate welding technique for joining different materials. This was particularly useful to industries needing specific criteria to be met for various welding applications [120].

In the optimization of welding parameters for specific materials, the AHP could be integrated with other methodologies. For instance, combining the AHP with the Taguchi method allowed researchers to analyze factors like tensile strength and toughness more comprehensively when optimizing welding parameters for materials such as mild steel and stainless steel. This combined approach led to improvements in both weld quality and efficiency [121].

The AHP was utilized to evaluate the environmental sustainability of welding processes. By considering factors like energy use, emissions and material waste, the importance of including sustainability in welding parameter optimization was emphasized. This ensured welding practices were aligned with environmental goals while maintaining high-quality results [122].

In summary, the AHP was proven to be a versatile and effective tool in optimizing welding processes. By providing a clear and systematic framework for evaluating multiple factors, it improved selection of welding parameters, resulting in better weld quality, cost savings and sustainable practices [123].

In addition to the Analytical Hierarchy Process (AHP), several other Multi-Criteria Decision-Making (MCDM) techniques have been explored by researchers to address multi-objective optimization problems in welding. One investigation proposed a hybrid entropy-weighted GRA–TOPSIS method for optimizing Gas Tungsten Arc Welding of copper and SS304 stainless steel. Using a Taguchi L9 orthogonal array, the study optimized welding current, speed and gas flow rate to achieve enhanced tensile strength and hardness. The hybrid method effectively captured the influence of process parameters on weld quality, achieving superior corrosion resistance and mechanical performance compared to conventional optimization approaches [124].

In another work, the researchers evaluated the sustainability of key welding processes such as Friction Stir Welding (FSW), Gas Tungsten Arc Welding (GTAW), Gas Metal Arc Welding (GMAW) and Shielded Metal Arc Welding (SMAW). The assessment covered environmental, economic and social aspects, along with the physical performance of welds. Using the entropy weighting method and various MCDM techniques, the study objectively compared the processes and found FSW to be the most sustainable option due to its high energy efficiency, lower emissions and better weld quality [125].

A study optimized Gas Tungsten Arc (GTA) welding parameters for 15CDV6 aerospace steel using Multi-Criteria Decision-Making (MCDM) techniques such as Grey Relational Analysis (GRA) and the Technique for Order Preference by Similarity to Ideal Solution (TOPSIS). Experiments based on a Taguchi L9 array optimized current, voltage and travel speed to improve tensile strength, hardness and penetration. The results showed that TOPSIS provided superior mechanical and metallurgical properties, highlighting the effectiveness of MCDM methods in multi-response welding optimization [126].

Another group applied the MCDM-based TOPSIS optimization technique to compare conventional TIG and Activated TIG (A-TIG) welding of stainless steel 304L. Using Response Surface Methodology (RSM) with a central composite design, the researchers optimized welding current, gas flow rate and root gap to enhance tensile strength, hardness and penetration depth. The use of silicon dioxide (SiO_2) flux improved weld penetration, and ANOVA identified key influential factors. The TOPSIS approach effectively determined optimal parameters, showing that A-TIG welding achieved superior mechanical and metallurgical performance compared to conventional TIG [127].

A recent study evaluated the weldability and optimization of TIG welding parameters to maximize the yield strength of welded joints. The investigation analyzed how variations in

welding current, travel speed, and gas flow rate influence mechanical properties such as ultimate tensile strength and percentage elongation. Using the MCDM-based Grey Relational Analysis (GRA) technique, the optimal parameter combination was determined to be 100 A current, 100 mm/min travel speed, and 20 L/min gas flow rate. The optimized settings significantly enhanced weld quality and mechanical performance while minimizing material waste, energy consumption and process cost [128].

A recent study proposed an integrated MCDM-based framework for sustainable welding process selection, focusing on minimizing environmental impact, cost and health risks while ensuring joint strength. Using the Best–Worst Method (BWM), Sample Variance Analogy (SVA) and Correlation Coefficient (CC) adjustments for weighting, the MULTIMOORA method with BORDA rule ranked stainless steel 316LN welding alternatives. Laser Beam Welding (LBW) achieved the highest sustainability index, validated through sensitivity analysis and comparison with other MCDM methods [129].

A recent study applied the TOPSIS-based MCDM approach to optimize TIG welding parameters for super-martensitic stainless steel. Using a Taguchi L9 orthogonal array, key process parameters such as current, voltage, travel speed and shielding gas flow rate were optimized to improve bead geometry, penetration depth and hardness. Multi-response optimization confirmed that the TOPSIS method effectively enhanced weld quality, while metallographic analysis validated the improved mechanical properties of the optimized welds [130].

Another study investigated the optimization of TIG welding for dissimilar ferritic and austenitic stainless steels using a multi-criteria approach. Experiments were designed using a Taguchi L9 array, and weld quality was evaluated through visual inspection and X-ray radiography. Advanced analytical techniques, including Grey Relational Analysis (GRA), TOPSIS and Principal Component Analysis (PCA), were applied to optimize process parameters for multiple responses. The study found that PCA provided the most effective optimization for achieving superior weld quality, highlighting the utility of MCDM methods in handling complex, multi-objective welding scenarios [131]. Some important works employing MCDM techniques for optimizing welding parameters and evaluating welding process performance are summarized in Table 2.1.

Table 2.1: Overview of welding process optimization using MCDM techniques

Authors (Year)	Welding Process & Material	MCDM Technique(s)	Process Parameters & Ranges	Optimized Outcomes / Responses
Alam et al. (2025)	GTAW, Copper & SS304	Hybrid GRA–TOPSIS	Current: 80–120 A, Speed: 20–40 mm/min, Gas Flow: 8–12 L/min	Improved tensile strength, hardness, corrosion resistance
Saad et al. (2020)	FSW / GTAW / GMAW / SMAW – Aluminum plates	Entropy weighted multiple MCDM techniques	Current (A): 152–210–133; Voltage (V): 20–18.5–71.7;	FSW most sustainable: energy-efficient, low emissions, better weld quality
Srinivasan et al. (2018)	GTA Welding – 15CDV6 aerospace steel	GRA + TOPSIS	Current: 80–120 A, Voltage: 18–22 V, Travel Speed: 50–150 mm/min	Optimized tensile strength, hardness, penetration; TOPSIS best performance
Sutar & Jadhav (2021)	TIG / A-TIG – Stainless steel 304L	TOPSIS + RSM	Current: 80–120 A, Gas Flow: 10–20 L/min, Root Gap: 1–3 mm	A-TIG: higher tensile strength, hardness, penetration
Guambo Mondo et al. (2024)	TIG Welding – Not specified	GRA	Current: 80–120 A, Travel Speed: 80–120 mm/min, Gas Flow: 15–25 L/min	Maximized yield strength, improved UTS and elongation, reduced material waste
Saluja & Singh (2025)	GTAW, AGTAW, LBW, and FSW – Stainless steel 316LN	MULTIMOORA + BWM/SVA/CC	Current: 64–120 A; Voltage: 11–12.6 V; Speed: 50–1500 mm/min; Heat input: 0.63–1.33 kJ/mm;	Laser Beam Welding achieved highest sustainability index
Chellappan	TIG Welding –	TOPSIS	Current: 80–120	Optimized bead

et al. (2017)	Super-martensitic SS		A, Voltage: 18–22 V, Travel Speed: 20–40 mm/min, Gas Flow: 8–12 L/min	geometry, improved penetration depth and hardness
Roy et al. (2024)	TIG Welding – Dissimilar Ferritic & Austenitic SS	GRA + TOPSIS + PCA	Current: 80–120 A, Voltage: 18–22 V, Travel Speed: 50–150 mm/min	PCA best for multi-response optimization; improved weld quality, defect minimization

In addition to the above-mentioned Multi-Criteria Decision Making (MCDM) optimization techniques, some researchers have employed standard predictive algorithms using Machine Learning (ML) techniques to predict optimized weld parameters based on training and testing experimental datasets. The predicted values were then compared with experimental outcomes, and algorithms demonstrating close agreement with the observed data were considered suitable [132–138].

In one such study, a comparative evaluation of mechanical properties and defect detection was performed using ML techniques such as Adaptive Neuro-Fuzzy Inference System (ANFIS) and the Unified Convolutional Neural Network (UCNN) with Nd:YAG Laser and TIG welding processes. The tensile and microhardness predictions generated by the ANFIS model exhibited a high correlation with the Peak Signal Noise Ratio (PSNR) values from the UCNN model, indicating strong predictive consistency between the two approaches [132].

In another work, an AI-based TIG welding algorithm was developed using a fuzzy deep neural network combining fuzzy logic and deep learning. Trained and validated on data from 27 experiments, with current, arc length, and welding speed as control parameters, the model predicted weld bead width with a high accuracy of 92.59%, demonstrating its potential to improve weld quality and process efficiency [133].

Another investigation utilized an Artificial Neural Network (ANN) to predict penetration depth and weld bead width during A-TIG welding of 304 austenitic stainless steel. Experimental data with activating fluxes- SiO_2, TiO_2, and Fe_2O_3 in varying ratios- was used, and the ANN model effectively predicted bead geometry under different flux compositions and welding conditions [134].

In another study, predictive models were applied to estimate yield strength in welds using stainless steel filler metals for austenitic stainless steel base metal. With chemical composition and heat input as inputs, both multiple regression and ML models were evaluated. The multiple regression model achieved an R^2 of 0.8642 and MAPE of 3.75%, accurately predicting strength variations due to dilution and assisting in filler metal design [135].

Machine learning has also been employed to predict fatigue life in welded structures across industries such as shipbuilding and construction. Inputs like arc voltage, welding speed, and crack growth parameters were linked to outputs such as residual stress and fatigue life. High-strength and stainless steels were commonly used, particularly in bridges. Hybrid and random forest models showed strong potential for automating fatigue assessment and structural health monitoring [136].

A recent study applied ML to predict surface temperature in A-TIG welding of 304L stainless steel using thermal imaging. Supervised algorithms including decision tree, random forest, and XGBoost were trained on datasets with different activating fluxes. Random forest delivered the best accuracy, achieving the lowest root mean square error and mean square error, demonstrating effectiveness in thermal prediction during advanced welding processes [137].

Another study employed ML techniques to predict hot crack length and microhardness in ultrasonically assisted TIG (UA-TIG) welded Inconel 625 joints. Predictive models evaluated included Random Forest Regression (RFR), ANN, ANFIS, and Multiple Linear Regression (MLR). The RFR model exhibited the highest accuracy among all techniques [138].

2.11. Gap In The Literature

Austenitic stainless steel of grade 304H is one of the critical materials extensively used in advanced boiler components due to its excellent high-temperature strength and corrosion resistance. However, despite its significant role in such demanding environment, the weldability study of more than 5 or 6-mm thick SS 304H remains underexplored. Achieving full penetration and producing high-quality welds are crucial for ensuring the strength and durability of welded joints in critical applications. However, welding characteristics of thick SS 304H, particularly the interaction between various welding parameters, requires further investigation.

Employing Multi Criteria Decision Making (MCDM) tools like the Analytic Hierarchy

Process (AHP) can enhance decision-making by systematically analyzing and prioritizing the various welding parameters that was not reported in the literature for welding of SS 304H. Also, application of Artificial Intelligence and Machine Learning in such weld joints of SS 304H flats was not found in the literature.

Also, the literature does not reveal the use of Activating Flux in the enhancement of penetration of TIG welded joints of SS 304H materials. Despite several advantages, this A-TIG welding is not yet broadly adopted in the welding industry worldwide. Further research and experimentation are necessary to validate its effectiveness for thick SS 304H flats, highlighting the potential benefits of this method in industrial applications.

Use of SS 304H filler in enhancing depth of penetration was not reported in the published works while joining similar materials. Therefore, investigations may well be performed in this explored area.

2.12. Objective of The Work

The main objective of this work would be to investigate and optimize weldability while joining 8 mm-thick 304H austenitic stainless steel using TIG welding process. Achieving full penetration and producing high-quality welds are essential requirements. To accomplish this, a series of experiments would be carried out.

In the initial phase of experimentation, autogenous TIG welding is planned to be conducted using butt joints prepared from 8 mm thick SS 304H specimens on a single side. To structure the experimental design effectively, Response Surface Methodology (RSM) is planned to employ in conjunction with Central Composite Design (CCD), allowing systematic variation of key welding parameters such as heat input, shielding gas flow rate and torch angle across three levels. It is tried to evaluate the combination of these parameters that would facilitate maximum weld penetration while minimizing weld bead reinforcement and overall bead width.

Building upon the findings from the initial investigation, a second set of experiments is planned with the optimal parameter combinations derived from the global matrix of a widely used Multi-Criteria Decision-Making (MCDM) technique known as the Analytic Hierarchy

Process (AHP). In this phase, welding is planned to perform on both sides of the specimen to evaluate whether full penetration can be achieved.

Experiment Set 3 is planned wherein the same process parameters identified in the second set retained, but with the application of Activated Flux (A-TIG) on the faying surface of the specimens. This approach is intended to enhance arc constriction and increase penetration depth further due to the reverse Marangoni effect, thereby improving the effectiveness of the TIG welding process under the optimized conditions. Together, these sequential experimental stages are designed to build a comprehensive understanding of how process modifications and enhancements influence weld quality and penetration characteristics in high-performance austenitic stainless steels.

Extending the investigation further, a fourth phase of experimentation is planned to focus on non-autogenous TIG welding by incorporating SS 304H filler material under conditions comparable to the previous experiment sets. 1.2 mm diameter SS 304H filler wire is planned to use to better understand the influence of filler addition on weld penetration and joint quality. A structured Design of Experiment is again planned to be developed using Response Surface Methodology (RSM) with a Central Composite Design (CCD), facilitating the optimization of welding parameters specific to filler-assisted TIG welding. Key process parameters, such as, heat input, root gap and shielding gas flow rate are planned to be varied across three levels to examine their combined effect on weld characteristics.

To further strengthen the findings, investigation into the microstructural features, tensile tests to determine ultimate tensile strength and percentage elongation of the welded joints, hardness and micro-hardness measurements across the weld cross-sections and Scanning Electron Microscopy (SEM) are planned to be performed to gain deeper insights into the weld morphology. Finally, standard Machine Learning algorithms are planned to apply to the entire experimental dataset to evaluate the predictive capability of weld quality parameters such as bead geometry, tensile strength, elongation and hardness based on the selected input process variables.

CHAPTER 3

Materials and Method

3.1. Introduction

The present work is focused on selecting the key input welding parameters of TIG welding for SS 304H austenitic stainless steel, which is commonly utilized in the fabrication of components for advanced boiler systems that are used for fabricating superheater panels, vertical hanging tubes in reheaters, low temperature reheaters, etc. SS 304H is finding its applications in thermal power plants due to its excellent high-temperature strength and corrosion resistance [96] due to the presence of 12-18% Cr. It is typically employed in the temperature range of around 530^{o}C to 680^{o}C [45]. To accomplish this objective, four distinct sets of experiments are carried out. Each set is designed to explore different welding approaches and parameter combinations in order to evaluate their effects on weld quality and performance. A consolidated summary of all experiment sets and their respective methodologies is provided in Table 3.1.

Table 3.1. Experiments performed at a glance.

Sl. No	**Type of Experiment**	**Methodology**
1	Autogenous Single-Sided TIG Welding	• Welding Type: Autogenous single-sided TIG welding • Workpiece: SS304H stainless steel plate, Dimensions: 50 mm × 50 mm × 8 mm. • Electrode Details: 3.2 mm thoriated tungsten electrode • Electrode-to-work distance: 2 mm. • Welding Speed: 1.22 mm/s (constant). • Experimental Design followed Response Surface Methodology (RSM) using Central Composite Design (CCD). • Three input factors, each at three levels: ▪ Torch angle: 60°, 75° and 90° ▪ Heat input: 0.7679, 0.9434 and 1.1188 kJ/mm ▪ Shielding gas flow rate: 10, 12 and 14 L/min
		• MCDM Tool Used: The Analytic Hierarchy Process (AHP)

		• Ranking Criteria: Alternatives are assessed based on key weld quality parameters: ▪ Depth of Penetration ▪ Bead Width ▪ Reinforcement • Selection Basis: ▪ The top-performing alternatives, identified through Response Surface Methodology (RSM), are considered. ▪ These are ranked based on their weighted importance using the AHP model. • Final Selection: ▪ Top 5 ranked alternatives are selected for further testing
2	Double-Sided TIG Welding (Autogenous)	• Welding Type: Autogenous TIG is performed on both sides of the specimens using the top 5 alternatives from the AHP ranking. • Welding torch angle: 75° • All other parameters are kept the same as per the top 5 ranked settings.
		• The Analytic Hierarchy Process (AHP) is applied to rank the best welding conditions based on depth of penetration, bead width and reinforcement.
3	A-TIG Welding with TiO_2 Flux (Double-Sided Autogenous Welding)	• Activated TIG welding (A-TIG) is performed using the same methodology as Experiment Set 2 (Double-Sided TIG Welding), with the only difference being the application of a thin layer of flux. • Flux used: TiO_2 • The top 5 alternatives from the AHP ranking are tested, ensuring torch angle set at 75°, as per prior findings.
		• The AHP is applied to rank the best welding conditions based on depth of penetration, bead width and reinforcement.

4	GTAW with Continuous Filler Supply	• Gas Tungsten Arc Welding (GTAW) is performed on similar samples of 304H stainless steel using TIG welding machine with a MOGRA CWF 04 Cold Wire Feeder. • A 1.2 mm diameter filler wire is continuously supplied at 2 cm/s feed rate. The welding speed is set at 1.22 mm/s. • Experiments are conducted at a 75° torch angle with a constant arc gap of 5 mm. • The experiment is designed using Response Surface Methodology (RSM) with Central Composite Design (CCD), considering three factors at three levels: • The three factors (current, root gap and gas flow rate) are tested at three levels: Heat input – 1.337, 1.458, 1.520 kJ/mm.; Root Gap – 1.2mm, 1.6mm, 2.0mm; Gas Flow Rate – 10, 12, 14 L/min.
		• The AHP is applied to identify the optimal depth of penetration while maintaining productivity and determining the associated process parameters for TIG welding. • Welding experiments validate these findings by producing fully penetrated joints under specific conditions.

Despite the significant role of SS 304H, weldability study of more than 5 or 6 mm thick specimens remain underexplored [96]. Achieving full penetration and producing high-quality welds are crucial for ensuring strength and durability of welded joints in critical applications. Considering the above, work specimen used in the experiment is made of SS304H, with dimensions of length 50 mm, width 50 mm and height 8 mm that is used in several accessories of different industrial boilers, present in power plants, in particular. The specimen is cooled in open air after butt welding. The chemical composition of the austenitic stainless steel of 304H is given in Table 3.2 as detailed through spectrum analysis.

Table 3.2. Chemical composition of SS304H work specimen

Element	**C**	**Si**	**Mn**	**P**	**S**	**Cr**	**Ni**	**Fe**
Wt.%	0.055	0.477	1.398	0.028	0.03	18.11	8.477	Balance

A comprehensive series of post-weld tests is carried out to assess the mechanical and metallurgical characteristics of the welded joints across of all four experiment sets. Hardness test is performed using the Rockwell Hardness C (HRC) scale on polished cross-sections of each sample, with three readings taken per specimen and the average value is considered for analysis. Tensile strength and elongation are determined using a Universal Testing Machine (UTM), with specimens prepared as per ASTM 370a standard. For microstructural examination, metallographic samples from the highest-performing welds in each experiment set are sectioned, mounted, ground, polished, etched and examined under an optical microscope to study the structural features of the weld metal, heat-affected zone (HAZ) and base metal. Additionally, Vickers microhardness testing is conducted on selected specimens along a transverse line covering the base metal, HAZ and weld region to capture localized hardness variation. To supplement the microstructural analysis, Scanning Electron Microscopy (SEM) is also performed on selected specimens from each set to investigate grain refinement, phase transformations and features within the HAZ, offering deeper insights into the microstructural evolution influenced by different welding conditions.

The AHP is applied to all the Experiment Sets separately to obtain high ranking alternative corresponding to appropriate welding conditions.

Additionally, six standard machine learning algorithms are employed which aim to predict key input welding parameters which represent both the strength and favourable weld bead geometry of welded joints. These predictions are then compared with experimental results with the goal of establishing reliable correlations for tensile strength, hardness and bead geometry of welded joints, ensuring their strength and sound weld joint.

3.2. Detail of Experiment Set 1

The first set of autogenous TIG welding experiments are conducted at NextGen Plasma Ltd., Howrah, West Bengal, India using a model No. Qineo GLW 322 GTAW machine manufactured by CLOOS, Germany as shown in Figure 1(a-d). Welding torch carriage utilized in this experiment is the Promotech-Gecko made auto-magnetic carriage. The specific welding joint performed is an Autogenous Butt Joint using a 3.2 mm (diameter) non-consumable Thoriated tungsten electrode, accompanied by continuous flow of shielding Argon gas.

(a) (b) (c)

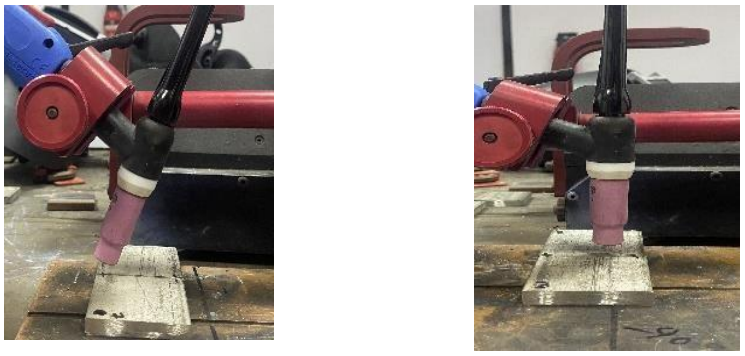

(d) (e)

Figure 3.1. (a) GTAW Machine used, (b) Torch Carriage, (c)Torch Angle set at 60°, (d) Torch Angle set at 75°, (e) Torch Angle set at 90°

The distance between the tungsten electrode tip and the base metal is maintained at 2 mm, and the torch travel speed is set at 1.22 mm/s. The experiment involves variations in torch angle, current range and gas flow rate. The torch angle is set at 60°, 75° and 90°, while the current is set at 110A, 130A and 150A. Gas flow rate is set at 10, 12 and 14 L/min.

The cross-sectional cuts of the welded specimens are polished and etched with Kalling's reagent 2 for measurement of bead geometry. The welded specimens are first polished using a polishing machine equipped with flat disk wheels. The specimens are progressively polished by fixing abrasive papers on the disk with finer grits one after the other to achieve a smooth, mirror-like finish. The specimens are then cleaned with water and alcohol. Kalling's reagent 2 is prepared by first mixing 50 mL of Hydrochloric Acid (HCl) with 50 mL of Ethanol in a beaker. To this solution, 2.5 mg of Cupric Chloride ($CuCl_2$) is added and stirred thoroughly until fully dissolved. Once the reagent is properly mixed and ready for use, it is applied to the weld cross-section and base metal zone after the specimen has been carefully polished. The reagent is applied by rubbing it onto the surface, ensuring even coverage, and is left to react for approximately 50 seconds. Following this, the specimen is rinsed under running water to remove any residual reagent and then allowed to air-dry.

Before proceeding with microscopic examination, the specimen is left undisturbed for about 4 to 5 minutes, ensuring that the etching process is complete and the microstructural features are well-developed.

A typical weld bead geometry is measured with the help of Tool Maker's Microscope on the basis of parameters such as weld bead width (W), reinforcement (R), depth of penetration (P). Heat input (HI) is calculated using equation (3.1).

$$HI = (V \times I \times \eta)/ (1000 \times S) \quad (3.1)$$

Heat input is considered in kJ/mm. V is the closed-circuit voltage in V, I is the closed-circuit current in A, S is the welding speed in mm/s and η is process efficiency (0.75 is considered for TIG based on literature).

Design of Experiment: In this first set of experimentation, the design of experiment is accomplished using the Central Composite Design (CCD), a widely used approach in Response Surface Methodology (RSM), to analyze the effects of three key process parameters on welding outcomes. CCD is a robust statistical technique that enables the development of a mathematical model to evaluate the relationship between independent variables and the response of interest. This approach facilitates optimization of welding parameters by systematically varying experimental conditions while minimizing the number of trials required for accurate prediction.

In this investigation, three key welding parameters—heat input, gas flow rate, and torch angle—are chosen as independent variables, each evaluated at three distinct levels: low, medium, and high. These parameters are selected due to their considerable impact on critical aspects of weld quality, such as depth of penetration, bead profile and overall joint performance. To systematically investigate their effects and interactions, 20 experimental runs are designed and conducted using the Central Composite Design (CCD) approach. Process parameters are varied at three different levels according to CCD is depicted in Table 3.3. The objective of this phase is to develop a structured understanding of how these parameters influence welding characteristics and to determine the most effective combination for achieving optimal welding performance.

Table 3.3. Process Parameters and Their Levels for CCD Experimentation

Parameter	Low Level (-1)	Medium Level (0)	High Level (+1)
Gas Flow Rate (L/min)	10	12	14
Torch Angle (°)	60	75	90
Heat Input (kJ/mm)	0.7679	0.9434	1.1188

3.3. Detail of Experiment Set 2

Experiment Set 2 is conducted using a KEMPI K2 TIG 200 ACDC machine as shown in Figure 3.2, and the experimental runs are conducted under the parameter conditions associated with the top 5 performing alternatives from the global matrix of the AHP optimization of Experiment set 1.

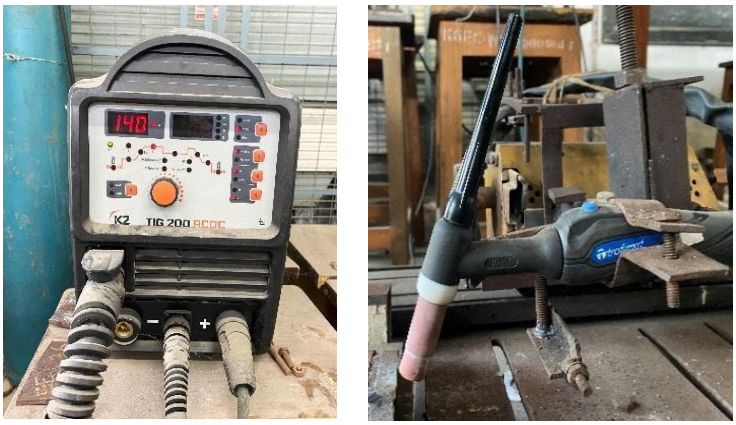

(a) (b)

Figure 3.2. (a) GTAW Machine used, (b) Torch angle set at 75°

In this phase, welding is carried out on both sides of the butt joints to ensure full penetration and improved joint quality. For this phase, the torch angle is set to 75°, as it is deemed more appropriate based on insights gathered from the literature review and established welding practices. All other process parameters, both fixed and variable, are maintained similarly as in Experiment Set 1, ensuring consistency in methodology and enabling meaningful comparison between the two sets of experimental results. The post welding specimen preparations like polishing and etching is similar to the experiment set 1.

3.4. Detail of Experiment Set 3

Experiment Set 3 is carried out using the same KEMPI K2 TIG 200 ACDC machine, as depicted in Figure 3.3. This phase employed Activated Tungsten Inert Gas (A-TIG) welding, in which a thin coating of titanium dioxide (TiO_2) activated flux is applied to the surface of the plates on both sides before welding. This technique is introduced to enhance weld penetration and improve bead characteristics by modifying the heat distribution at the weld zone.

Figure 3.3. Welding torch set above the TiO_2 flux coated sample before welding

The application of TiO_2 flux is intended to enhance heat concentration at the weld zone by promoting the reverse Marangoni effect and arc constriction effect which facilitate deep penetration by altering the fluid flow dynamics in the molten weld pool. All other process parameters in this set are kept similar to that used in Experiment Set 2 to ensure a valid comparison. Specifically, welding speed is maintained at 1.22 m/min, root gap is set to 0 mm, and arc gap is kept at 2 mm throughout the process.

A-TIG welding is specifically adopted to improve the depth of penetration in autogenous welding, which had been the objective throughout the first three sets of experiments. Post welding specimen preparations like polishing and etching is similar to the experiment Set 1 and 2.

3.5. Detail of Experiment Set 4

In the final set of experimentation filler assisted TIG welding is carried out using a KEMPPI K2 TIG 200 AC/DC machine (shown in Figure 3.5 a-c) on the same 304H stainless steel samples, each 8 mm thick and 50 mm x 50 mm in size. MOGRA CWF 04 Cold Wire Feeder is employed to ensure a constant supply of 1.2 mm diameter filler wire made of austenitic stainless steel of 304H grade, maintained at a consistent feed rate of 20 mm/s (feed rate is finalised based multiple trial runs). Experiments are conducted with the torch held at an angle of 75^{o}, maintaining a constant arc gap length of 5 mm and welding speed of 1.22 mm/s. Various welding current and welding voltage settings are tested in initial test runs to evaluate their impact on weld quality. The key varying input parameters are weld current, root gap and gas flow rate, each of these is evaluated at three different levels. Weld current values are set at 130 A, 140 A and 150 A, with the weld voltage noted accordingly. Root gap is varied at 1.2 mm, 1.6 mm and 2 mm and argon gas flow rate is controlled at 10, 12 and 14 L/min.

Each of the 20 samples is welded under these varying conditions. Joints are non-autogenous butt joints, welded with a 3.2 mm non-consumable thoriated tungsten electrode. After welding, specimens are air-cooled. To assess weld quality, welded specimens are polished and then etched with Kalling's 2 etchant. Polishing and etching procedures are similar to the previous set of experiments.

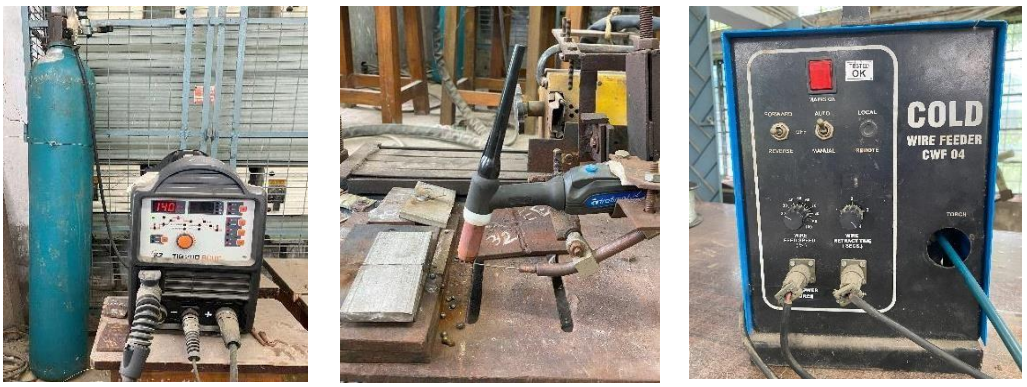

(a) (b) . (c)

Figure 3.5. (a) GTAW Machine used, (b) Torch set at 75°, (c) MOGRA CWF 04 Cold Wire Feeder used

Design of Experiment: In Experiment Set 4, filler-assisted TIG welding is carried out on SS 304H grade austenitic stainless-steel plates. The aim is to evaluate the effect of adding filler material on weld quality and to optimize the process parameters for achieving full penetration and desired bead geometry. To systematically plan experimental runs and to analyze the influence of variables, design of experiments is done using Response Surface Methodology (RSM), using Central Composite Design (CCD) approach.

Three critical process parameters are selected for investigation, such as heat input, gas flow rate, and root gap. Each of these factors is varied across three levels to assess their individual and combined effects on the welding outcome. Gas flow rate is maintained at 10, 12, and 14 L/min, which helped control shielding environment and arc stability. Root gap, an important variable influencing weld penetration and filler deposition, is adjusted at 1.2 mm, 1.6 mm and 2.0 mm. Heat input, a key parameter governing thermal behaviour and fusion characteristics, is set at 1.337, 1.458 and 1.520 kJ/mm. These values are derived from the heat input calculation formula of Equation 3.1, based on welding parameters such as weld voltage, weld current, and travel speed. This experimental setup is designed to explore the interrelationship between the selected parameters and to determine the most effective combination for achieving complete penetration and enhanced weld bead properties using filler material in TIG welding.

Table 3.3 presents the experimental details for all sets, highlighting the corresponding input and output parameters. Values in the parameters, 'Filler Used' and 'Flux Used', are represented as binary indicators, where '1' indicates the presence or usage of the specified parameter, and '0' indicates its absence or non-use. The sequence of experimental procedures has been illustrated in the schematic diagram provided in Figure 3.7.

Table 3.3. Experimental details of all the set of experiments

Autogenous TIG Experiment done on One side								
Set-1	**Input Parameters**							
Serial No.	**Gas flow rate**	**Torch Angle (Degree)**	**Filler Used**	**Welding Pass**	**Flux Used**	**Root Gap**	**Arc Gap (mm)**	**Heat input (kJ/mm)**
1	10	60	0	1	0	0	2	0.768
2	14	60	0	1	0	0	2	0.768
3	10	90	0	1	0	0	2	0.768

4	14	90	0	1	0	0	2	0.768
5	10	60	0	1	0	0	2	1.119
6	14	60	0	1	0	0	2	1.119
7	10	90	0	1	0	0	2	1.119
8	14	90	0	1	0	0	2	1.119
9	10	75	0	1	0	0	2	0.943
10	14	75	0	1	0	0	2	0.943
11	12	60	0	1	0	0	2	0.943
12	12	90	0	1	0	0	2	0.943
13	12	75	0	1	0	0	2	0.768
14	12	75	0	1	0	0	2	1.119
15	12	75	0	1	0	0	2	0.943
16	12	75	0	1	0	0	2	0.943
17	12	75	0	1	0	0	2	0.943
18	12	75	0	1	0	0	2	0.943
19	12	75	0	1	0	0	2	0.943
20	12	75	0	1	0	0	2	0.943
Autogenous TIG Experiment Done on Both Sides with best results of 1st Set								
Set-2	**Input Parameters**							
Serial No.	**Gas flow rate**	**Torch Angle (Degree)**	**Filler Used**	**Welding Pass**	**Flux Used**	**Root Gap**	**Arc Gap (mm)**	**Heat input (kJ/mm)**
21	10	75	0	2	0	0	2	1.18
22	14	75	0	2	0	0	2	1.18
23	10	75	0	2	0	0	2	1.18
24	14	75	0	2	0	0	2	1.18
25	12	75	0	2	0	0	2	0.964
A- TIG Experiment Done on Both Sides with best results of 1st set								
Set-3	**Input Parameters**							
Serial No.	**Gas flow rate**	**Torch Angle (Degree)**	**Filler Used**	**Welding Pass**	**Flux Used**	**Root Gap**	**Arc Gap (mm)**	**Heat input (kJ/mm)**
26	10	75	0	2	1	0	2	1.264
27	14	75	0	2	1	0	2	1.264
28	10	75	0	2	1	0	2	1.264
29	14	75	0	2	1	0	2	1.264
30	12	75	0	2	1	0	2	1.01

Filler TIG Experiment on Both Sides								
Set-4	**Input Parameters**							
Serial No.	**Gas flow rate**	**Torch Angle (Degree)**	**Filler Used**	**Welding Pass**	**Flux Used**	**Root Gap**	**Arc Gap (mm)**	**Heat input (kJ/mm)**
31	10	75	1	2	0	1.2	5	1.337
32	14	75	1	2	0	1.2	5	1.337
33	10	75	1	2	0	2	5	1.337
34	14	75	1	2	0	2	5	1.337
35	10	75	1	2	0	1.2	5	1.52
36	14	75	1	2	0	1.2	5	1.52
37	10	75	1	2	0	2	5	1.52
38	14	75	1	2	0	2	5	1.52
39	10	75	1	2	0	1.6	5	1.458
40	14	75	1	2	0	1.6	5	1.458
41	12	75	1	2	0	1.2	5	1.458
42	12	75	1	2	0	2	5	1.458
43	12	75	1	2	0	1.6	5	1.337
44	12	75	1	2	0	1.6	5	1.52
45	12	75	1	2	0	1.6	5	1.458
46	12	75	1	2	0	1.6	5	1.458
47	12	75	1	2	0	1.6	5	1.458
48	12	75	1	2	0	1.6	5	1.458
49	12	75	1	2	0	1.6	5	1.458
50	12	75	1	2	0	1.6	5	1.458

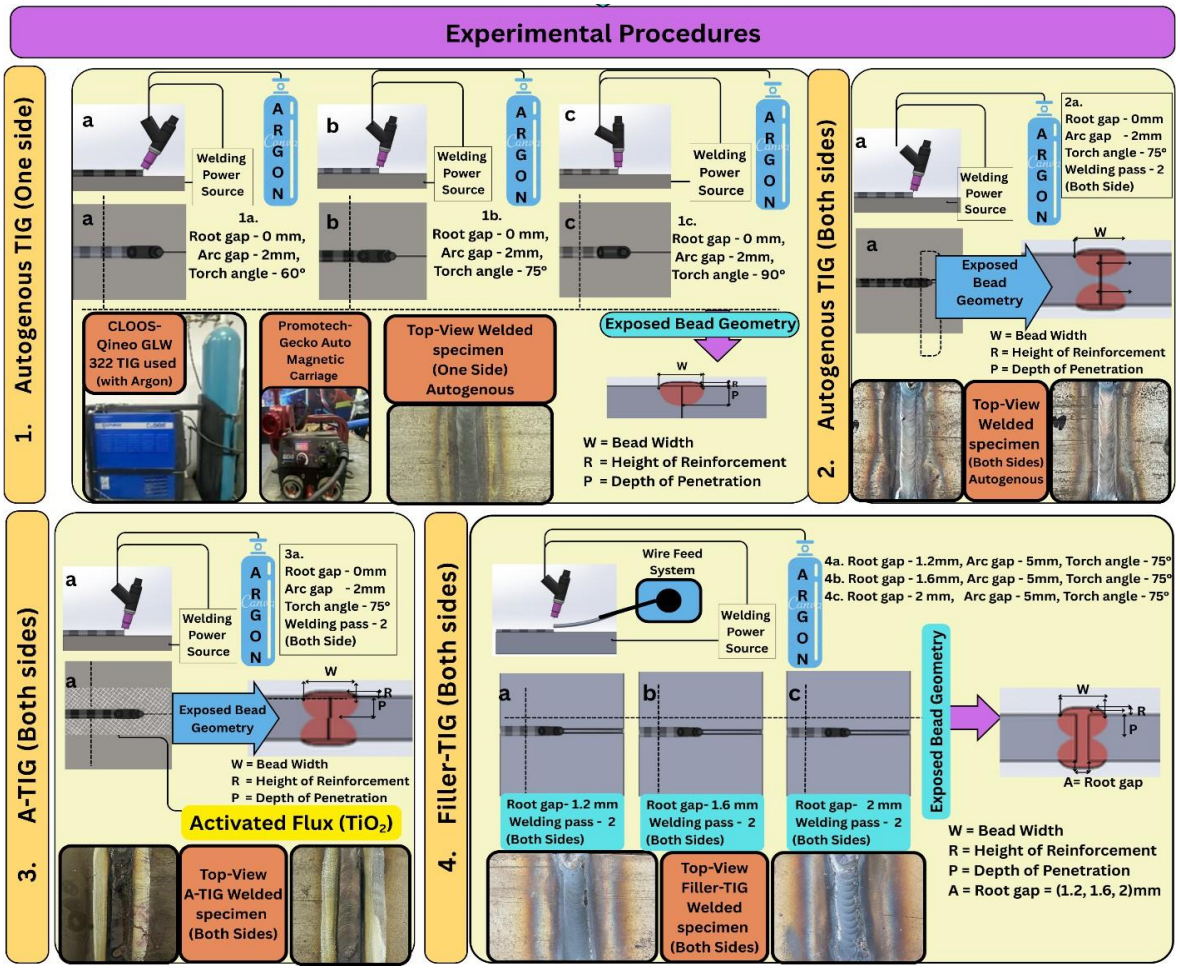

Figure 3.7. Schematic representation of sequence of Experimental procedures performed.

3.6 Post-Weld Testing and Analysis

Various post-weld tests are carried out to comprehensively evaluate the properties of the welded joints. These assessments are aimed at determining mechanical strength, hardness, and microstructural characteristics. Tensile testing is performed to assess the joint strength, while hardness measurements—including Rockwell and microhardness tests—are used to examine variations in hardness across the weld and heat-affected zones. In addition, microstructural analysis and Scanning Electron Microscopy (SEM) are employed on some typical specimens to study grain boundary features and metallurgical transformations in the weld region. A schematic representation showing all the post welding processes performed on the welded specimen is provided in Figure 3.8.

Following paragraphs discuss the detailed procedure of the tests performed.

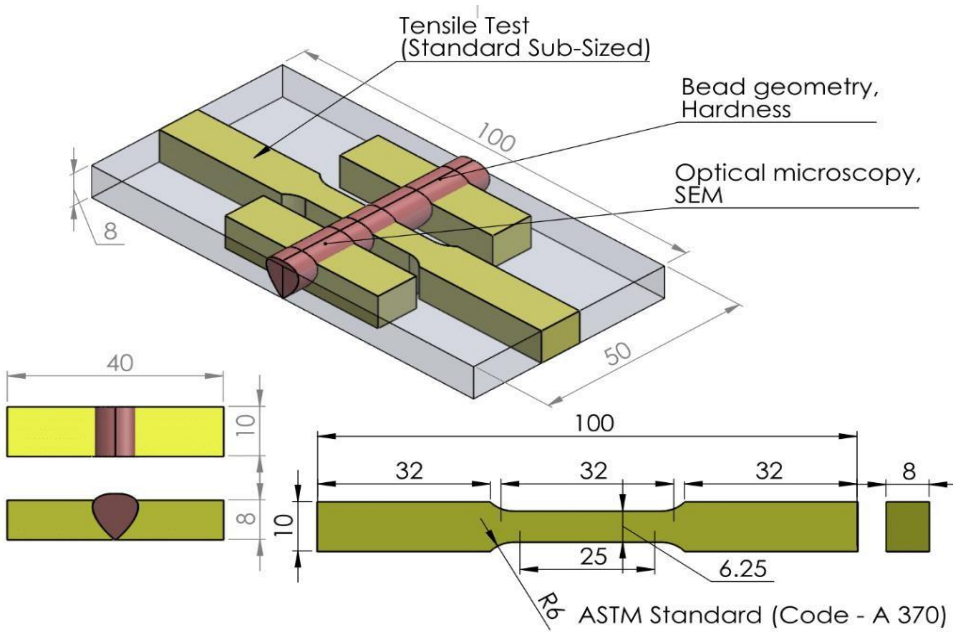

Figure 3.8. Schematic diagram representing all the post welding processes performed on the welded specimen.

3.6.1. Tensile Test

Tensile testing is carried out on all welded specimens in accordance with ASTM 370a standards, with the cut outs of the specimen along with the dimensions illustrated in Figure 3.7. Samples are made from all four experiment sets that includes autogenous TIG welding, Activated TIG (A-TIG) welding and filler-assisted TIG welding processes. This evaluation is aimed at determining the mechanical strength of the welded joints. The results indicate that the maximum tensile strength achieved by the welded specimens in this work is 676.126 MPa having % elongation value of 34.003, which is found to be more than the tensile strength of the base metal SS 304H (which is around 582 MPa), thereby validating effectiveness of the welding procedures in preserving the joint's load-bearing capacity. The tensile testing procedure is conducted using INSTRON 8862 universal testing machine and the setup utilized for this purpose is shown in Figure 3.9. Images of specimens prepared for Tensile test is shown in Figure 3.10.

Figure 3.9. Tensile test setup

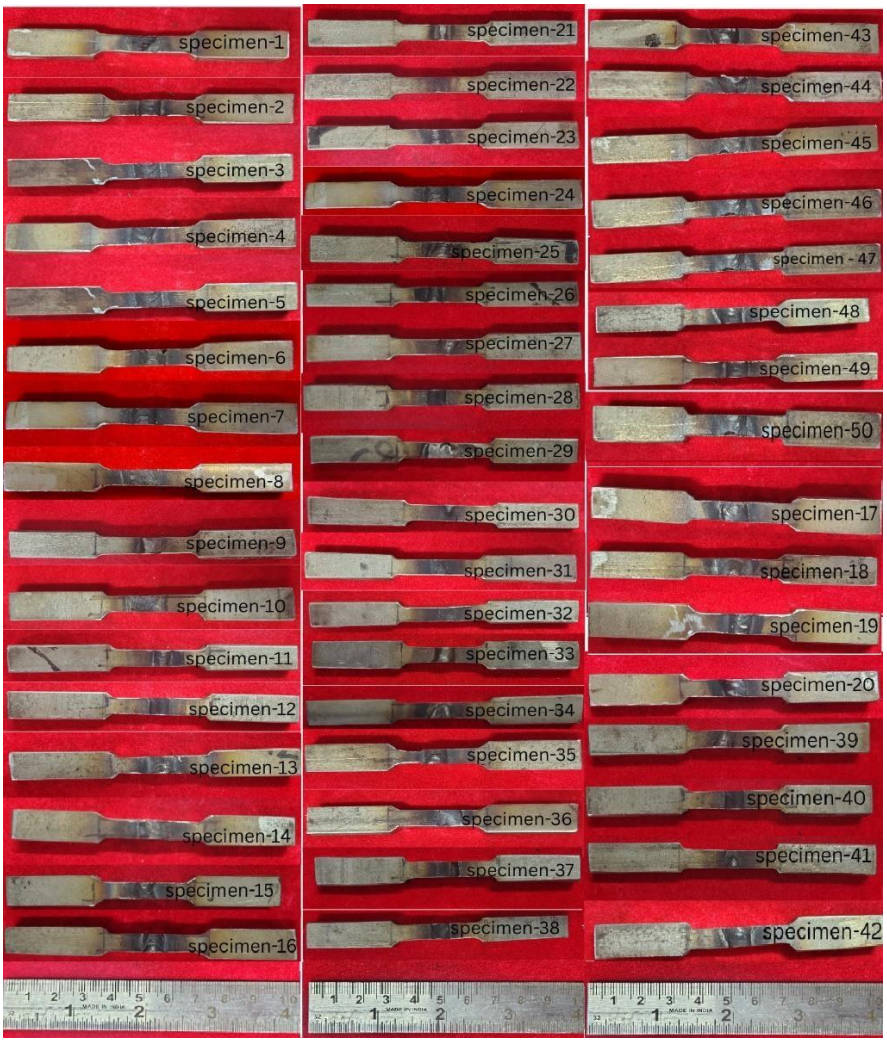

Figure 3.10. Images of specimens prepared for Tensile test

3.6.2. Rockwell Hardness Test

Rockwell Hardness test is carried out on the polished cross-sections of the welded samples from all four sets of experiment. Hardness values are recorded at three distinct points across the weld bead to determine an average reading for each specimen. The measured hardness values are found to be consistent with those of the base metal, indicating good weld quality. The highest hardness recorded in the weld zone is 36.33 HRC value. The Rockwell hardness testing machine used for the analysis is shown in Figure 3.11.

Figure 3.11. Rockwell Hardness test setup

3.6.3 Microhardness Test

Microhardness evaluation is carried out on some typical welded samples from the four sets of experiments using UHL-VMHT Vickers microhardness testing machine. Measurements are taken at five specific points along a straight line traversing the weld cross-section. These points include two locations in the base metal on either side, two within the heat-affected zones (HAZ), and one at the centre of the weld bead. This approach helped capture the hardness distribution across the welded joint. Noticeable variations in microhardness values are observed among different sets, reflecting the influence of welding parameters and techniques on material properties.

3.6.4 Microstructure Analysis

Microstructural analysis is carried out on selected representative specimens from each experiment set to assess the metallurgical characteristics present in the weld zone.

Specimens are initially prepared through a meticulous polishing process using a polishing machine fitted with flat disk wheels. A sequence of abrasive papers with progressively finer grits is employed to achieve a smooth, mirror-like finish on the cross-sectional surface. After polishing, the samples are thoroughly cleaned with water followed by alcohol to remove any surface contaminants.

For etching, Kalling's Reagent 2 is prepared by mixing 50 mL of Hydrochloric Acid (HCl) and 50 mL of Ethanol, to which 2.5 mg of Cupric Chloride ($CuCl_2$) is added and stirred until fully dissolved. The prepared reagent is then uniformly applied to the polished weld and base metal surfaces using a rubbing technique, allowing it to react for approximately 50 seconds. After the reaction time, the specimens are rinsed under running water and left to air-dry. To ensure the etching is fully developed, the samples are kept undisturbed for an additional 4 to 5 minutes prior to microscopic examination.

Etching process effectively reveals internal microstructural features, such as grain boundaries and phase transitions across the base metal, heat-affected zone (HAZ) and weld metal. Observations are conducted using the METSCOPE PRO optical microscope (Chennai METCO), which enables high-resolution imaging and accurate interpretation of the microstructural variations. Evaluation is conducted on the specimens with higher tensile strength values to gain deeper insights into the weld quality and associated metallurgical transformations. The optical microscope used for the analysis is shown in Figure 3.12.

Figure 3.12. METSCOPE PRO (Chennai METCO) optical microscope used for microstructural analysis

3.6.5 Scanning Electron Microscopy (SEM)

SEM analysis is performed on selected welded specimens to closely examine grain structure and surface morphology of the weld region. Samples are properly prepared to ensure clarity in imaging. Results show changes in grain structure across the weld bead, heat-affected zone

(HAZ) and base metal. Variations in grain boundaries and refinement are clearly visible, helping to understand the metallurgical changes caused by different welding conditions. Scanning Electron Microscope (SEM) used is shown in Figure 3.13.

Figure 3.13. The Scanning Electron Microscope (SEM) used

3.7. The Analytical Hierarchy Process (AHP)

The Analytical Hierarchy Process (AHP), a widely recognized multi-criteria decision-making tool, is employed in Experiment Set 1 through Set 4 to determine the optimal bead geometry characteristics and corresponding suitable input conditions. In this work, the Analytic Hierarchy Process (AHP) involves structuring the problem into a hierarchy, with the main goal at the top, followed by criteria and alternatives in subsequent levels as shown in Figure 3.14. The matrix used for pairwise comparisons is represented in Equation 3.2

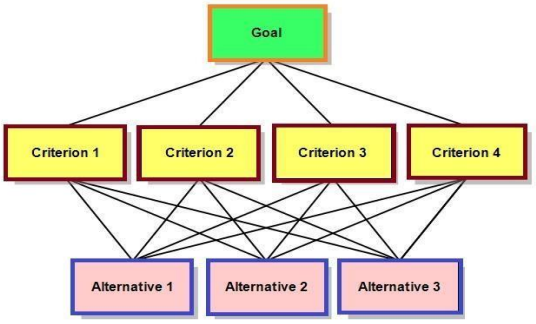

Figure 3.14. Basic hierarchy structure of the AHP

$$M=\begin{bmatrix} m_{11} & m_{12} & m_{13} \\ m_{21} & m_{22} & m_{23} \\ m_{31} & m_{32} & m_{33} \end{bmatrix} \text{----------(3.2)}$$

Here m_{ij} represents the strength of preferences of element m_i over m_j concerning a specific criterion ($m_{ij} = m_i/m_j$). The ratio scale of Saaty [28, 29] is employed to determine the values of m_i and m_j for pairwise judgments which is given in Table 3.4. A comparison matrix is considered consistent if $m_{ij} \times m_{jk} = m_{ik}$ for all values of i, j, and k. The random index values of different matrices are listed in Table 3.5.

Table 3.4. Ratio scale comparison matrix

Preference	Scale
Extremely Preferred	9
Very strongly to Extremely Preferred	8
Very strongly Preferred	7
Strongly to Very Strongly Preferred	6
Strongly Preferred	5
Moderately to strongly preferred	4
Moderately preferred	3
Equally to moderately preferred	2
Equally preferred	1

Table 3.5. Random index (RI) for different matrix order (n)

n	*2*	*3*	*4*	*5*	*6*	*7*	*8*	*9*	*10*
RI	*0*	*0.56*	*0.9*	*1.12*	*1.25*	*1.34*	*1.42*	*1.45*	*1.51*

In the Analytic Hierarchy Process (AHP), Consistency Index (CI) is used to evaluate how consistent the judgments are when elements are compared in pairs within a hierarchical structure. A higher CI indicates potential inconsistencies in the comparisons. If the CI value is too high, it suggests that the judgments made during the pairwise comparison might be unreliable, prompting a review and adjustment of the comparisons to improve consistency. The formula to find CI is shown in equation (3.3).

$$CI = (\lambda_{max} - n) / (n - 1) \text{ ----------} (3.3)$$

In addition to CI, Consistency Ratio (CR) is another important measure in the AHP. It compares consistency index (CI) with a pre-determined random index (RI), which is based on the size of the comparison matrix. The formula to find CR is shown in equation (3.4).

$$CR = CI/RI \text{ ----------} (3.4)$$

The local priority weights in the comparison matrix are determined based on the maximum eigenvalue (λ_{max}) of the normalized eigenvector. These local weights are then multiplied by the priority of each alternative and integrated with the pairwise comparison matrix criteria, referred to as the criteria weight. The global weight is computed by evaluating the total of these values. The alternative with the highest global weight is typically considered the most suitable choice in the decision-making process.

In each AHP analysis for all the experiment sets, the input alternatives are chosen from the top-performing results observed during the welding experiments. The AHP approach involves formulating the decision-making problem into a structured hierarchy placing the overall objective at the top, followed by selection criteria, and then the various input alternatives. The hierarchical representation for the process is illustrated in Figure 3.15.

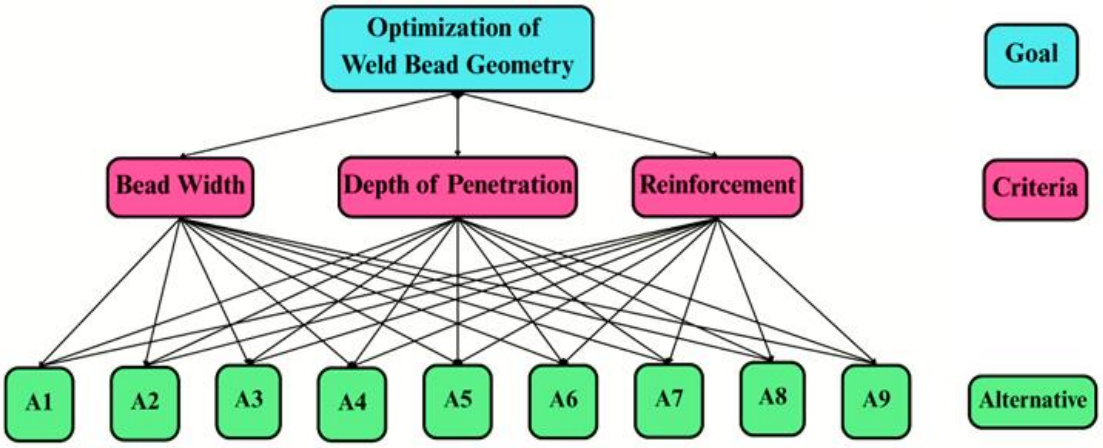

Figure 3.15 The hierarchical representation of the AHP performed

Priority weights for the AHP are calculated manually rather than use of any software after discussions with welding experts and academic guidance. Brainstorming sessions help to create more customized approach to it, ensuring that the weight assignments are based on expert comments and the unique complexities of the welding parameters.

3.8 Machine Learning-Based Predictive Modelling and Validation

The present research employed machine learning (ML) techniques such as ANN, KNN, SVR, RF, GBR (Also known as GBM) and XGBoost algorithms. The graphical representation is shown in Figure 3.15. Models have been established to forecast all the responses or outputs {Height of reinforcement (mm), Penetration (mm), Width (mm), Hardness (HRC), Ultimate tensile strength (UTS, MPa) and % Elongation} using each model. The aforementioned algorithms are employed due to their ability to generate highly accurate models within a short timeframe. For each developed model, performance evaluation metrics are established to assess its predictive capability on test data. In machine learning, the creation of reliable models and the generation of precise predictions require the use of both training and test datasets. Using Google Colab, data have been divided into two exclusive sets: a training set and a test set. The training dataset serves to construct and validate the ML models, whereas the test dataset is utilized to assess the performance of the models on new data. A common data splitting approach is applied, using 80% of data (40 data points) as training for the model and 20% of data (10 data points) for testing. To avoid overfitting problems and to establish more generalized models, 5-fold cross-validation is performed. The calculated training, test and validation data are applied for predicting all responses using the established machine learning algorithms. Figure 3.16 demonstrates the flow chart of the present work.

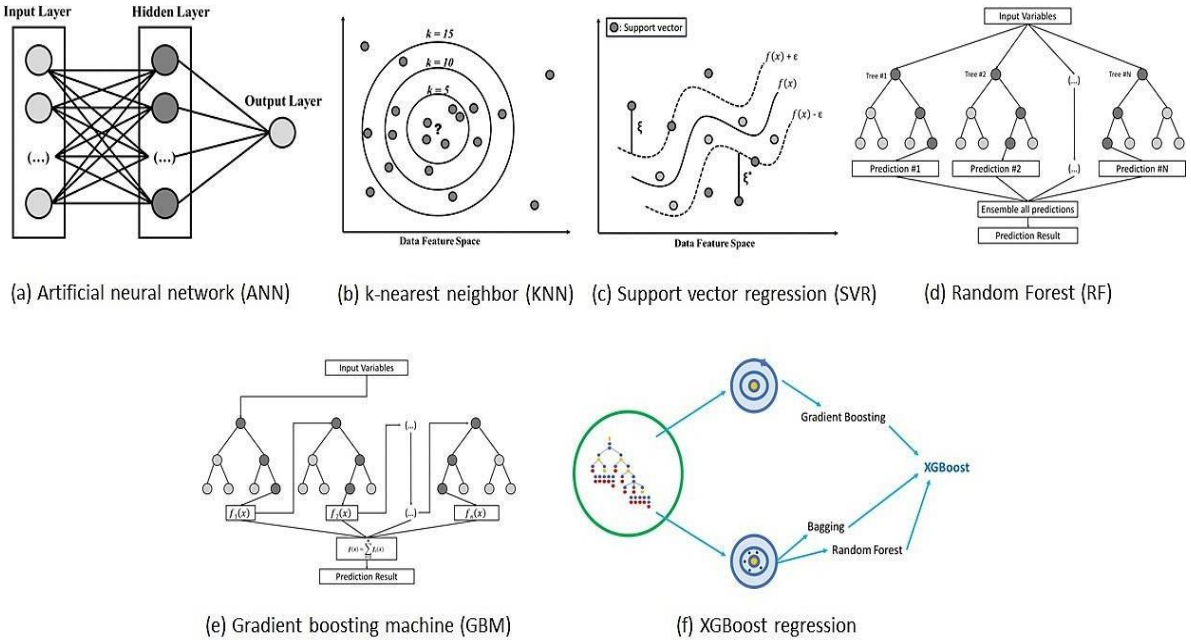

Figure 3.16. Graphical presentation of regression models: (a) ANN (b) KNN (c) SVR (d) RF (e) GBM and (f)

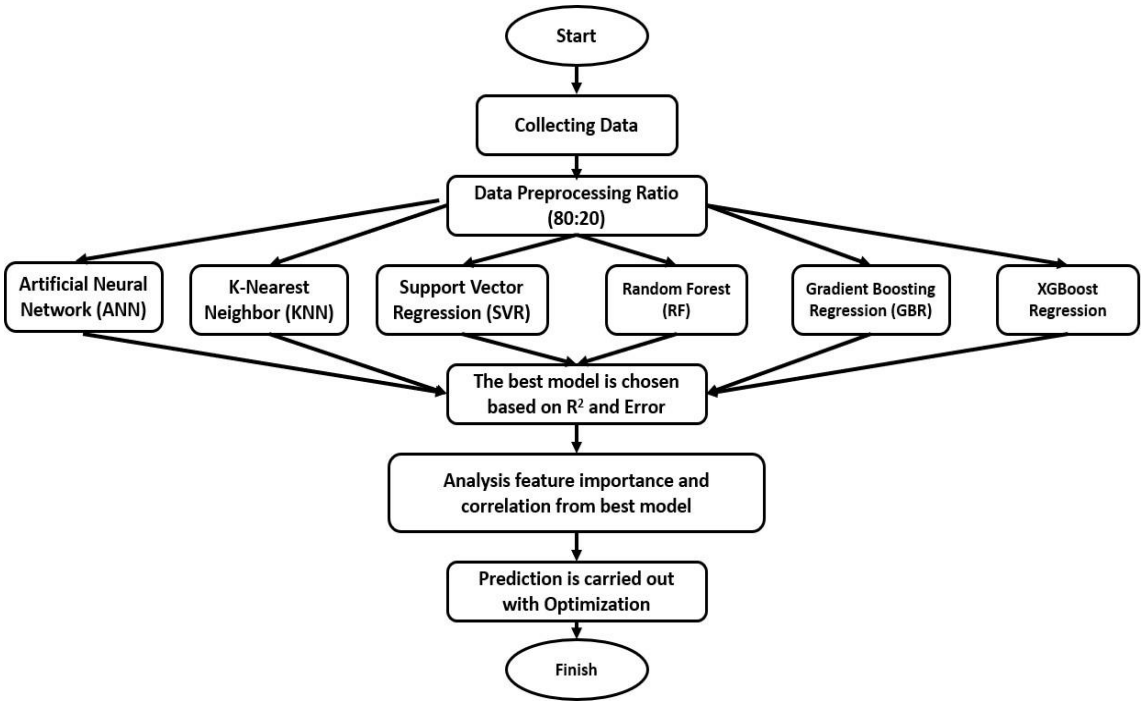

XGBoost

Figure 3.17. Flow chart of the present work

3.8.1. Artificial Neural Network (ANN)

ANNs represents a category of computational systems based on the architecture and processes of the human brain. They are made up of multiple layers of interconnected neurons which process input data and learn to recognize patterns through training. Primary components of an ANN include an input layer, several hidden layers and a final output layer as shown Figure 3.16 (a). Throughout the training process, the network modifies weights of connections according to the prediction error, employing techniques like back propagation. ANN is highly versatile and is capable of capturing intricate relationships within data, rendering them appropriate for various applications, including image and speech recognition, natural language processing and financial forecasting. Its ability to learn from data and improve over time enables it to perform well on tasks that involve large datasets and intricate patterns, but it requires careful tuning of hyperparameters and sufficient training data to achieve optimal performance. In Artificial Neural Networks (ANN), several parameters require optimization to enhance performance. Key parameters include the solver, which controls the weight adjustments based on the error through its line search procedure. The activation function transforms input signals and the number of hidden layers and neurons, which affects the model's learning capacity [126].

3.8.2. K-Nearest Neighbor (KNN)

KNN, as indicated by its name, predicts outcomes for a new data point by referencing the closest data points (neighbors) in the training dataset. The parameter "k" specifies how many closest data points are utilized in this prediction. The parameter "n" affects the intricacy of the KNN approach, making it crucial to select an appropriate "k" based on the characteristics of data and the difficulty of the problem to optimize performance. A schematic representation of KNN is depicted in Figure 3.16 (b). Moreover, it is important to determine whether to apply uniform weights or weights based on proximity to the neighboring data points in the KNN model [131].

3.8.3. Support Vector Regression (SVR)

SVR, an extension of Support Vector Machines (SVM), is a machine learning technique designed for predicting continuous values. Unlike conventional regression approaches that focus on minimizing the discrepancy between predicted and actual outputs, SVR seeks to determine a function that closely estimates the target while maintaining a predefined margin

of tolerance (ε). It ignores errors that fall within this ε-insensitive zone, focusing only on penalizing larger deviations, thereby increasing robustness of the model [131]. The solution is constructed using only the data points that lie outside the ε margin, known as support vectors, which influence the regression line or curve. Figure 3.16 (c) represents the SVR system schematically. SVR can handle both linear and nonlinear relationships through the use of kernel functions like linear, polynomial, or radial basis function (RBF), allowing it to model complex patterns effectively. The performance of SVR heavily depends on the choice of hyperparameters, particularly the penalty parameter C and the kernel parameter γ.

3.8.4. Random Forest (RF)

Random Forest serves as a supervised machine learning algorithm that utilizes decision trees to gain insights based on the training dataset. It is recognized for its ability to process large datasets and address problems with a wide range of input variables effectively [132]. The RF model or algorithm is composed of a collection of individual decision trees working together as an ensemble as shown in Figure 3.16 (d). The predictions from these individual trees are averaged, which enhances the predictive accuracy of RF. This approach helps mitigate the issue of overfitting that can occur with simple decision trees, making RF often superior to many other machine learning algorithms. To optimize Random Forest models, key parameters that require fine-tuning include the maximum features to assess at every split (max_features) along with the number of decision trees included in an ensemble (n_estimators). The predictive equation for RF algorithm is shown in Equation 3.5.

For regression, the prediction $\hat{y}$ from a Random Forest with M trees is the average of predictions from all individual decision trees $f(x)$:

$$\hat{y} = \frac{1}{M}\sum_{m=1}^{M} f_m(x) \qquad ------(3.5)$$

where $f_m(x)$ is the prediction from the m-th decision tree.

3.8.5. Gradient Boosting Machine (GBM)

GBM is a robust ensemble learning approach that constructs predictive models iteratively, with each subsequent tree trained to correct the residual errors from the preceding ones using gradient descent. This method integrates multiple weak learners—typically shallow

decision trees—to form a highly effective predictive model that adeptly captures intricate nonlinear relationships [133]. The network is represented in Figure 3.16 (e). Performance of GBM is largely governed by key hyperparameters: n_estimators, which determines the number of boosting iterations; learning_rate, which regulates contribution of each tree to mitigate overfitting; max_depth, which constrains tree depth to manage complexity; and subsample, which defines the proportion of training samples utilized per tree, introducing randomness to enhance generalization. The predictive equation for GBM algorithm is shown in Equation 3.6.

The model prediction $F_M\,(x)$ after M iterations (trees) is:

$$F_M\,(x) = F_0(x) + \sum_{m=1}^{M} \gamma_m h_m(x) \qquad ---------- (3.6)$$

where

$F_0\,(x)$ is the initial prediction (e.g., mean of y in regression); $h_m\,(x)$ is the decision tree at iteration m (trained on residuals); γ_m is the learning rate-adjusted weight for the m-th tree; M is the total number of boosting iterations (trees).

3.8.6. XGBoost (Extreme Gradient Boosting)

XGBoost is an efficient and scalable implementation of gradient boosting that delivers high predictive accuracy through a combination of advanced features like regularization, parallel processing, and optimized tree-building as shown in Figure 3.16 (f). Like traditional Gradient Boosting Machine (GBM), XGBoost builds trees sequentially to minimize prediction errors, but it enhances performance by including both L1 (alpha) and L2 (lambda) regularization [134] to control model complexity and prevent overfitting. Its key hyperparameters include n_estimators (number of trees), learning_rate (controls the contribution of each tree), max_depth (maximum depth of trees), subsample (fraction of samples per tree), colsample_bytree (fraction of features used per tree), and gamma (minimum loss reduction required for a split). These features make XGBoost a powerful choice for regression problems in scientific and engineering applications, such as predicting mechanical or thermal responses in material datasets.

The core objective function in XGBoost includes a training loss and a regularization term as shown in Equation (3.7):

$$Obj = \sum_{i=1}^{n} l(y_i, \hat{y}_i) + \sum_{k=1}^{K} \Omega(f_k) \quad ------(3.7)$$

where

3.8.7. Cross-Validation

Cross-validation is an essential method for measuring the effectiveness of machine learning models and determining their ability to adapt to new, unseen data. It is particularly useful when dealing with limited datasets, as it helps gauge how well the model performs in real-world data scenarios [135]. In K-fold cross-validation, the dataset is partitioned into random subsets, with the model being trained and validated on each subset. This approach ensures that the model is tested on different sections of the data, providing a more reliable estimate of its performance compared to a single train-test split. By using cross-validation, issues like overfitting can be detected, model parameters can be fine-tuned, and various model types can be compared. For this study, a 5-fold cross-validation approach was chosen.

3.8.8. Performance Evaluation Metrics

The model training process incorporates 5-fold cross-validation to improve generalization and reliability. The dataset is divided, with 70% allocated for training. To evaluate the predictive performance of the model, a variety of error metrics are used to compare the predicted output values with their corresponding actual measurements. These metrics includes Mean Square Error (MSE), Root Mean Square Error (RMSE), Mean Absolute Error (MAE) and the Coefficient of Determination (R^2). Employing multiple metrics ensure a comprehensive and balanced evaluation of accuracy of each model. In general, smaller values of MSE, RMSE, MAE and MAPE signify better performance whereas an R^2 value close to 1 indicates a high degree of correlation between actual and predicted outputs. The

mathematical formulations of these performance indicators are outlined in Equation 3.8 to Equation 3.11.

$$MSE = \frac{1}{n}\sum_{i=1}^{n}(y_i - \hat{y}_i)^2 \quad ------ (3.8)$$

$$RMSE = \sqrt{\frac{1}{n}\sum_{i=1}^{n}(y_i - \hat{y}_i)^2} \quad ------(3.9)$$

$$MAE = \frac{1}{n}\sum_{i=1}^{n}|\, y_i - \hat{y}_i| \quad ------(3.10)$$

$$R^2 = 1 - \frac{\frac{1}{n}\sum_{i=1}^{n}(y_i - \hat{y}_i)^2}{\frac{1}{n}\sum_{i=1}^{n}(y_i - \bar{y})^2} ------(3.11)$$

CHAPTER 4

Results and Discussion on Experiment Set 1

4.1. Introduction

This chapter corresponds to the 1st set of welding experiments conducted using autogenous TIG welding on SS 304H stainless steel specimens. It includes details about the type of weld joint used, the shielding gas and the process parameters used. Each experiment is performed using a different set of parameter combinations, which are listed in a table. Results of all these tests are represented and analysed in this chapter. Post-welding evaluations such as tensile test and hardness test are conducted and thoroughly analyzed. Additionally, microhardness tests are also performed on best performing specimens. MCDM tool such as the AHP is used also used to optimize the output parameters.

4.2. Detail of Setup and Conditions of Experiment Set 1

The initial phase of experimentation is carried out on austenitic stainless-steel plates, each measuring 50 mm x 50 mm with a thickness of 8 mm. For this study, autogenous butt welds are created using a standard Tungsten Inert Gas (TIG) welding setup. A non-consumable thoriated tungsten electrode with a diameter of 3.2 mm is employed and Argon gas is supplied through annular collar of the torch as the shielding medium. The TIG welding is using a Qineo GLW 322 GTAW machine by CLOOS, Germany as shown in Figure 3.1(a-d). The welding torch carriage utilized in this experiment is the Promotech-Gecko made auto-magnetic carriage. Details of Experiment Set 1 is given in Section 3.2.

4.3. Observations Made in Experiment Set 1

The results from the first set of welding experiments are carefully studied to understand how the selected process parameters—heat input, gas flow rate and torch angle—affect the weld quality of SS 304H welded specimens. The weld joints are examined based on their overall appearance, surface condition and continuity. Observations are made to find any visible issues that could affect strength, performance, or reliability.

4.3.1. Visual Inspection

Visual inspection for any weld defect is an important step for the experiment to be done. Presence of welding defects creates variation in mechanical characteristics. Table 4.1 shows

the non-presence of defects, namely uniformity, crack, blowhole, pinhole, undercut and spatter formation by visual inspection. Figure 4.1. shows the top view of some typical autogenous weld samples taken for visual inspection.

Table 4.1. Visual observations made in experiment set 1

Sl. No	**Gas flow rate (L/min)**	**Torch Angle (Degree)**	**Heat input**	**Spatter**	**Weld Uniformity**	**Crack**	**Blowhole -Pinhole**	**Undercut**
1	10	60	0.768	✓	✓	Nil	Nil	Nil
2	14	60	0.768	✓	✓	Nil	Nil	Nil
3	10	90	0.768	✓	✓	Nil	Nil	Nil
4	14	90	0.768	✓	✓	Nil	Nil	Nil
5	10	60	1.119	✓	✓	Nil	Nil	Nil
6	14	60	1.119	✓	✓	Nil	Nil	Nil
7	10	90	1.119	✓	✓	Nil	Nil	Nil
8	14	90	1.119	✓	✓	Nil	Nil	Nil
9	10	75	0.943	✓	✓	Nil	Nil	Nil
10	14	75	0.943	✓	✓	Nil	Nil	Nil
11	12	60	0.943	✓	✓	Nil	Nil	Nil
12	12	90	0.943	✓	✓	Nil	Nil	Nil
13	12	75	0.768	✓	✓	Nil	Nil	Nil
14	12	75	1.119	✓	✓	Nil	Nil	Nil
15	12	75	0.943	✓	✓	Nil	Nil	Nil
16	12	75	0.943	✓	✓	Nil	Nil	Nil
17	12	75	0.943	✓	✓	Nil	Nil	Nil
18	12	75	0.943	✓	✓	Nil	Nil	Nil
19	12	75	0.943	✓	✓	Nil	Nil	Nil
20	12	75	0.943	✓	✓	Nil	Nil	Nil

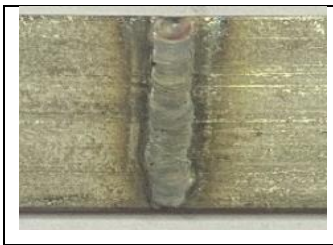

a) Serial No. - 3

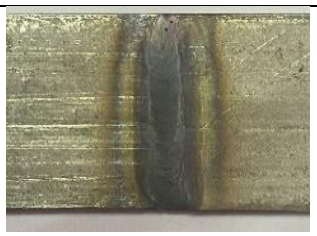

b) Serial No. - 6

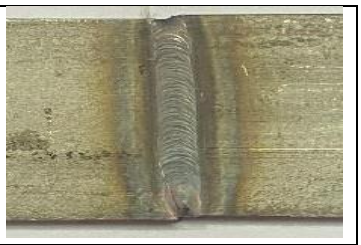

c) Serial No. - 9

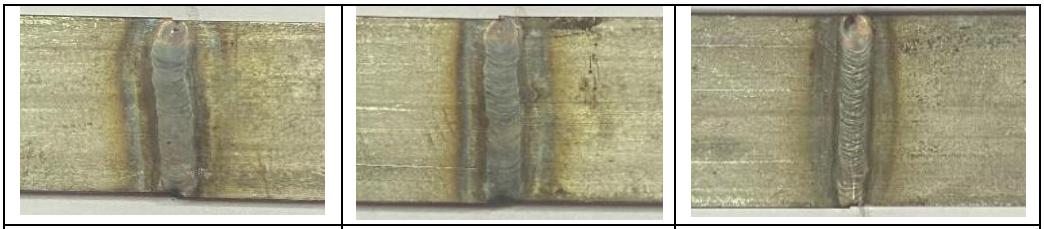

d) Serial No. - 13	e) Serial No. - 14	f) Serial No. - 2

Figure 4.1(a-f). Some typical images of visual inspected welded specimens of Experimental Set 1

It is found by visual inspection that all the welded specimens are uniformly welded with visible small spatter on the surface. Neither of the specimens are found with visible defects such as crack, undercut, blowhole and pinhole, etc. The overall bead appearance is smooth and continuous, indicating stable arc performance during the welding process.

4.3.2. Influence of Process Parameters on Bead Geometry

The bead geometry parameters such as depth of penetration, bead width, height of reinforcement, for the twenty welded specimens are presented in Table 4.2. It is observed that the depth of penetration ranges between approximately 1.6 mm to 3.5 mm, with corresponding variations in bead width and height of reinforcement.

Table 4.2. Bead Geometry Parameters for Autogenous Welded (single sided) Specimens with Varying Gas Flow Rate, Torch Angle, and Heat Input

Sl. No	**Gas flow rate (L/min)**	**Torch Angle (Degree)**	**Heat input**	**Penetration (mm)**	**Width (mm)**	**Reinforcement (mm)**
1	10	60	0.768	2.326	5.932	-0.1
2	14	60	0.768	2.156	6.045	0
3	10	90	0.768	1.674	7.531	-0.16
4	14	90	0.768	1.735	6.639	0
5	10	60	1.119	3.369	7.869	-0.14
6	14	60	1.119	3.058	8.422	0.12
7	10	90	1.119	3.459	9.375	0.11
8	14	90	1.119	2.908	6.609	-0.1
9	10	75	0.943	1.826	8.264	0.1
10	14	75	0.943	2.924	6.244	0
11	12	60	0.943	1.822	6.014	0.11
12	12	90	0.943	2.884	6.424	0
13	12	75	0.768	2.787	6.548	0
14	12	75	1.119	2.707	7.121	0

15	12	75	0.943	2.807	6.311	-0.19
16	12	75	0.943	2.607	7.029	0
17	12	75	0.943	2.747	7.162	0
18	12	75	0.943	2.968	7.008	0.08
19	12	75	0.943	2.618	7.118	0.11
20	12	75	0.943	2.712	6.582	0

The maximum penetration of 3.459 mm is achieved in Specimen 7, which is welded using a gas flow rate of 10 L/min, torch angle of 90° and heat input of 1.119 kJ/mm. Results show the influence of increased heat input and vertical torch alignment on achieving deeper weld penetration. In terms of bead width, this condition also lead to a larger bead width of 9.375 mm, indicating that higher heat input contributes to not just deeper penetration but also wider bead formation. Reinforcement, on the other hand, varies with different welding conditions. At this optimal setting, reinforcement is 0.11 mm, suggesting that while the penetration is maximized, reinforcement is relatively modest compared to other conditions with different heat inputs and torch angles. Images of bead geometry of few typical welded specimens of Experiment Set 1 are shown in Figure 4.2.

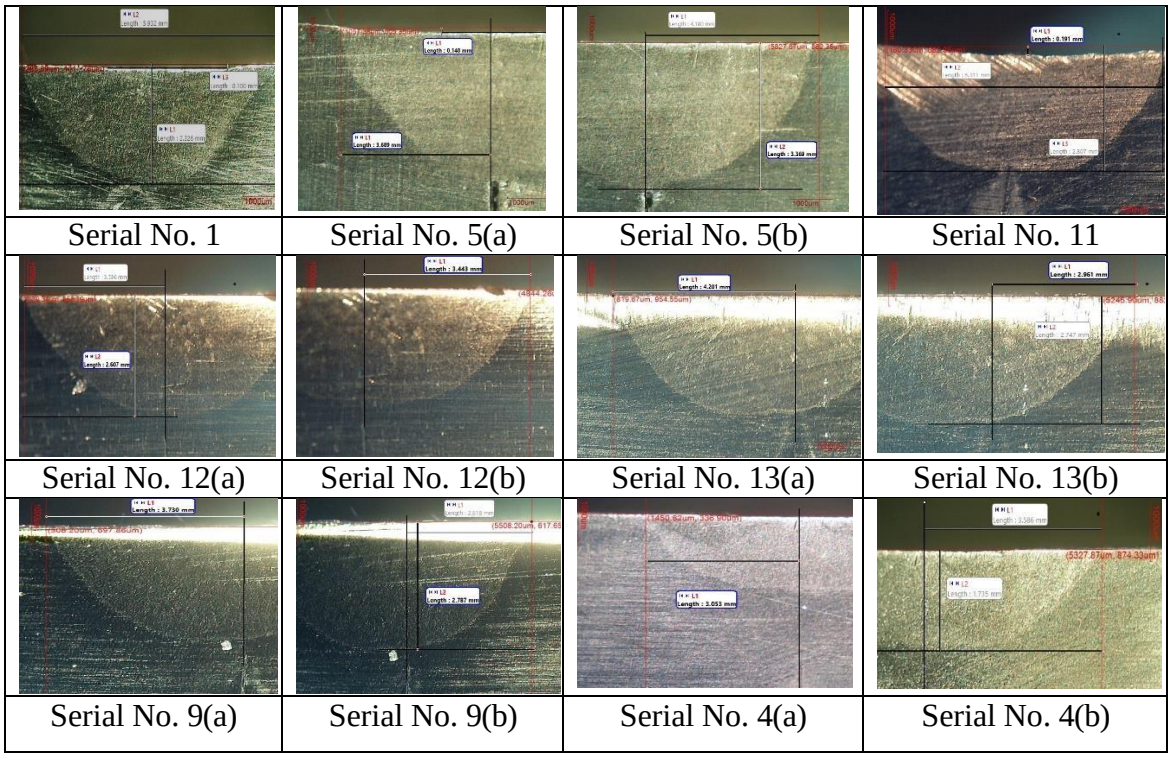

Figure 4.2. Bead Geometry of few typical specimens of Experiment Set 1

4.3.3. Analysis of Bead Geometry Parameters

In a contour plot or a surface plot, variation of a bead geometry parameter (such as P, R or W) is represented against the change of two factors keeping the third factor to a fixed value, commonly known as a hold value. Therefore, there would be three hold values for the 3rd factor would be three hold values for the 3rd factor corresponding to a low value (coded as '-1'), middle value (coded as '0') and high value (coded as +1). After observing the nature of contour or surface plots against two factors at three hold values of the 3rd factor, maximum variations of respective bead parameters are tried to detect. Corresponding hold value is noted and those contour and surface plots are included in this discussion. All the contour and surface plots are meant to represent variation of a bead geometry parameter with change in two independent variables keeping the third variable constant at its highest level (i.e., with a hold value of positive 1)

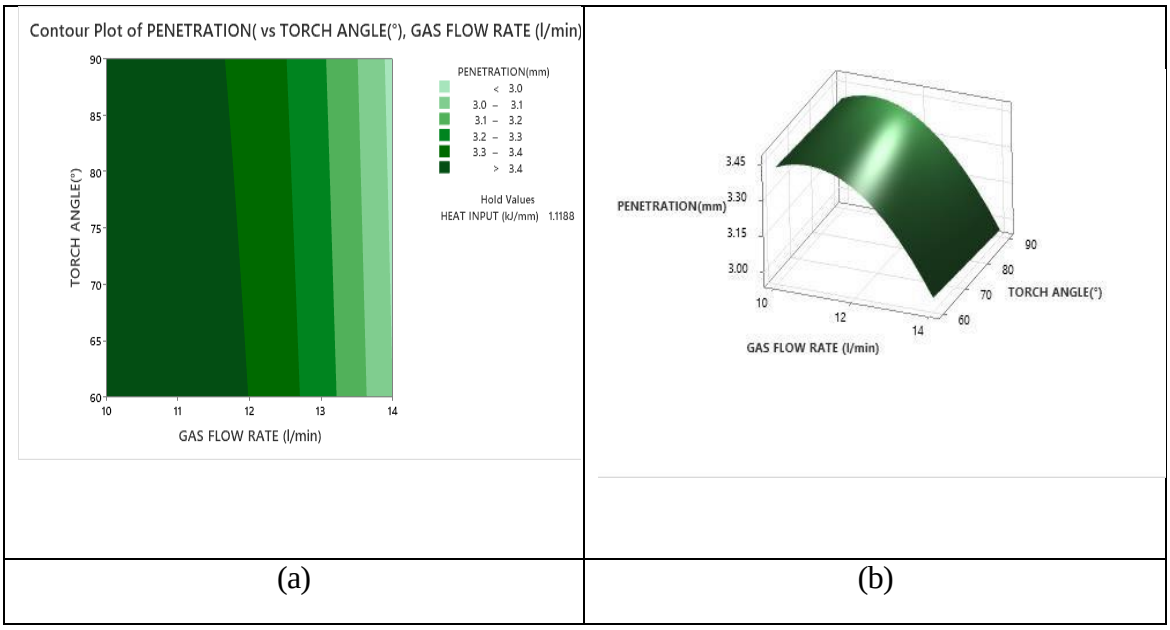

(a) (b)

Figure 4.3. (a) Contour plot and (b) surface plot of penetration with change in torch angle and gas flow rate at a hold value of heat input '+ve', i.e., 1.188kJ/mm.

Figure 4.3 is drawn at a '+1' hold value of heat input (1.1188kJ/mm). At this heat input of 1.1188kJ/mm, penetration is maximum when gas flow rate is between 10-12 L/min and it decreases as the gas flow rate increases. No such variation is observed with torch angle as shown in Figure 4.3 (a, b). Penetration is decreasing with the increasing value of gas flow rate but it remains almost the same with increasing rate of torch angle. Higher shielding gas

flow rate may have taken away comparatively more amount of heat resulting in decreasing depth of penetration to a small extent.

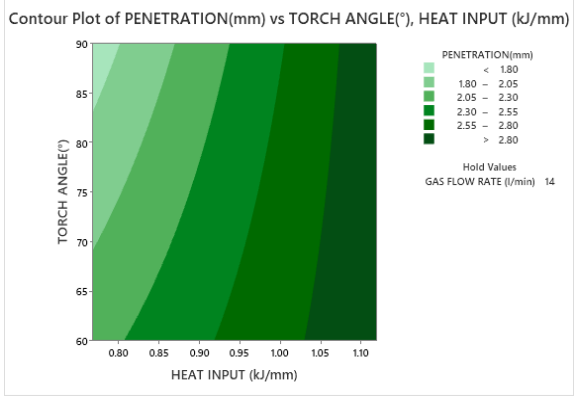

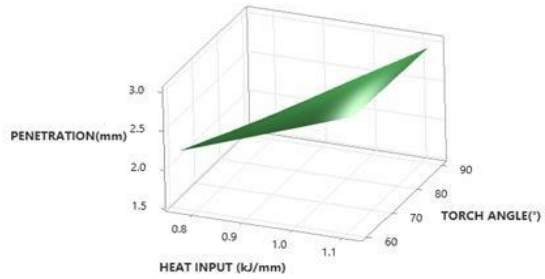

(a) (b)

Figure 4.4. (a) Contour plot and (b) surface plot of penetration with change in torch angle and heat input at a hold value of gas flow rate as '+ve', i.e. 14 L/min.

Penetration shows an increasing trend with Heat Input when gas flow rate of 14 L/min is the hold value. No much variation in penetration is observed with torch angle at higher heat input as shown in Figure 4.4 (a, b), Whereas at lower range of heat input, small amount of reduction in depth of penetration can be observed. Penetration is increasing with the increasing value of heat input at any torch angle.

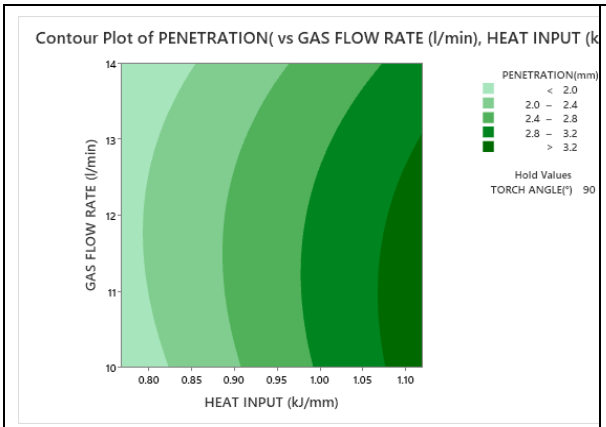

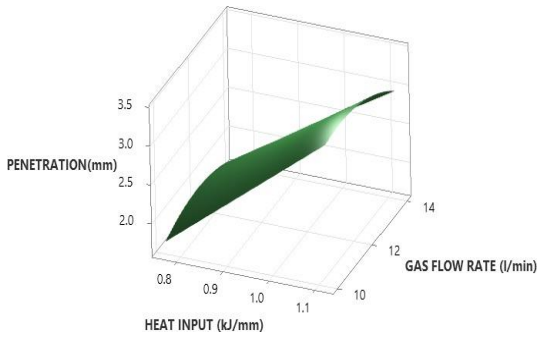

(a) (b)

Figure 4.5. (a) Contour plot and (b) surface plot of penetration with change in gas flow rate and heat input at a hold value of torch angle '+ve', i.e. 90°.

Penetration is remarkably increasing with an increase in Heat input when hold value of torch angle is 90° (coded value '+1'). High Heat Input causes large melt volume resulting in increasing in 'P' and 'W', and sometimes 'R' to some extent as expected. Penetration shows only small variation with increasing gas flow rate (shown in Figure 4.5 a,b) at any heat input indicating its marginal influence on 'P'.

From Figure 4.3 through 4.5, it is found that at high Heat Input ranging between 1.05-1.11 kJ/mm and gas flow rate between 11-13 L/min and at a torch angle of 90° maximum penetration is achieved.

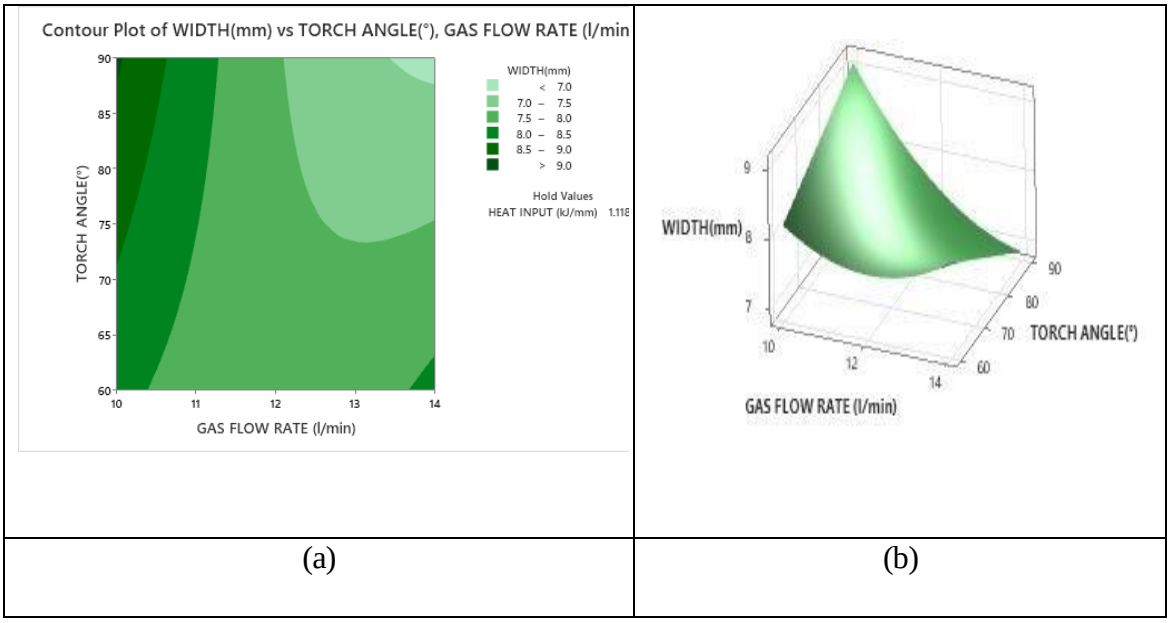

(a) (b)

Figure 4.6. (a) Contour plot and (b) surface plot of bead width with change in torch angle and gas flow rate at a hold value of heat input '+ve', i.e. 1.1188kJ/mm.

Maximum bead width is observed at a torch angle between 72-90° and gas flow rate between 10-10.5 L/min as shown in Figure 4.6 (a,b). Bead width is decreasing with increase in value of gas flow rate but marginal variation of bead width is found with change in value of torch angle.

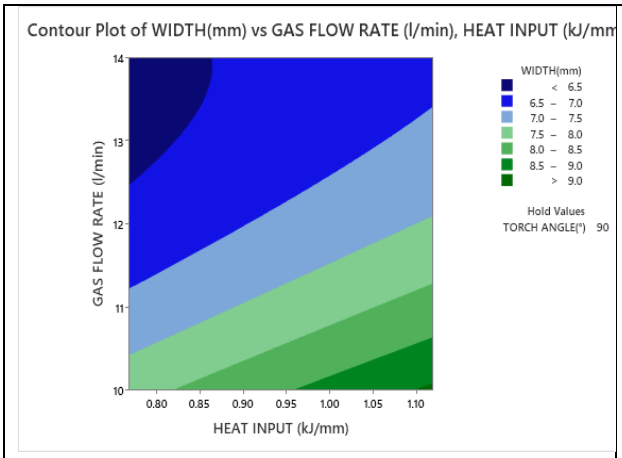

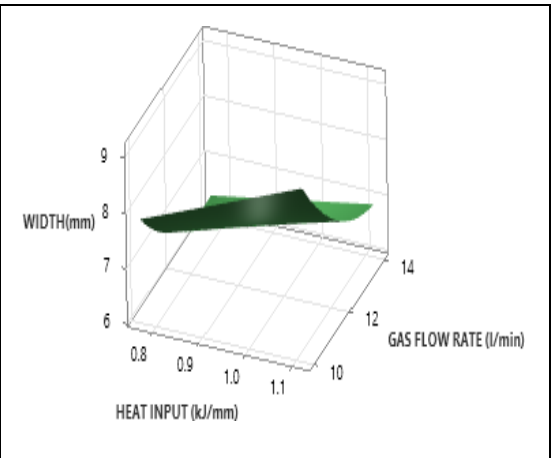

(a) (b)

Figure 4.7. (a) Contour plot and (b) surface plot of bead width with change in gas flow rate and heat input at a hold value of torch angle '+ve' i.e. 90 °

Bead width is found to be high significant at high heat input of 1.10kJ/mm and gas flow of 10 L/min where torch angle is set at '+1' hold value of 90° (shown in Figure 4.7). Bead width keeps on increasing at a low rate with the increasing value of heat input but it has marginal change with the increasing value of gas flow rate.

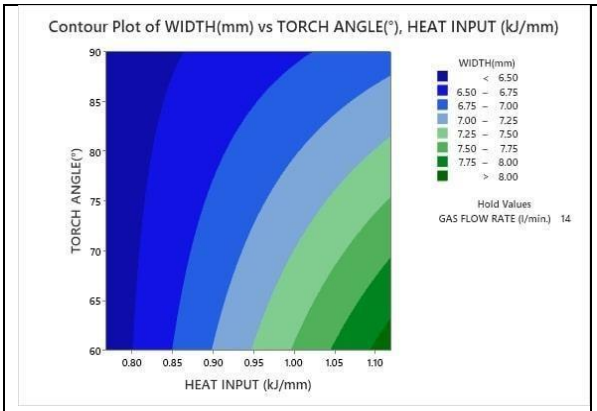

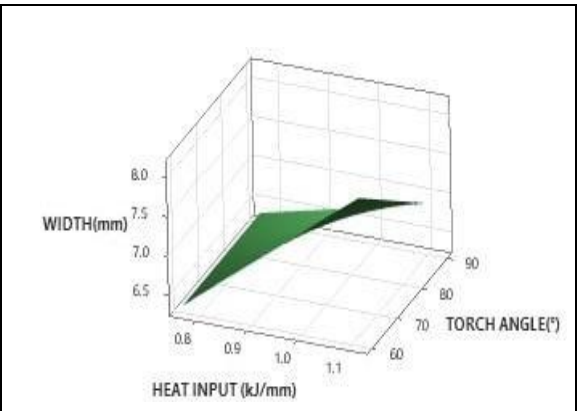

(a) (b)

Figure 4.8. (a) Contour plot and (b) surface plot of bead width with change in torch angle and heat input at a hold value of gas flow rate '+ve', i.e. 14 L/min

Bead width increases with hike in Heat Input and becomes maximum at a maximum Heat Input of 1.1kJ/mm. Marginal changes in bead width is found with variation in torch angle at low Heat Input. However, it decreases with torch angle at higher Heat Input (shown in Figure 4.8.).

The analysis of Figures 4.6 to 4.8 indicates that heat input has the most significant effect on bead width, while torch angle and gas flow rate show relatively lesser influence. Bead width reaches its maximum at higher torch angles (72–90°) and moderate gas flow rates (10–10.5 L/min) when heat input is kept at 1.1188 kJ/mm. When the torch angle is held constant at 90°, increasing heat input leads to a steady rise in bead width, though gas flow rate contributes minimally. At a fixed gas flow rate of 14 L/min, bead width continues to increase with heat input, but shows slight decrease with increasing torch angle, particularly at higher heat input levels.

Thus, heat input is the dominant factor, while torch angle and gas flow rate influence bead width through secondary or interactive effects, with minor or localized variations.

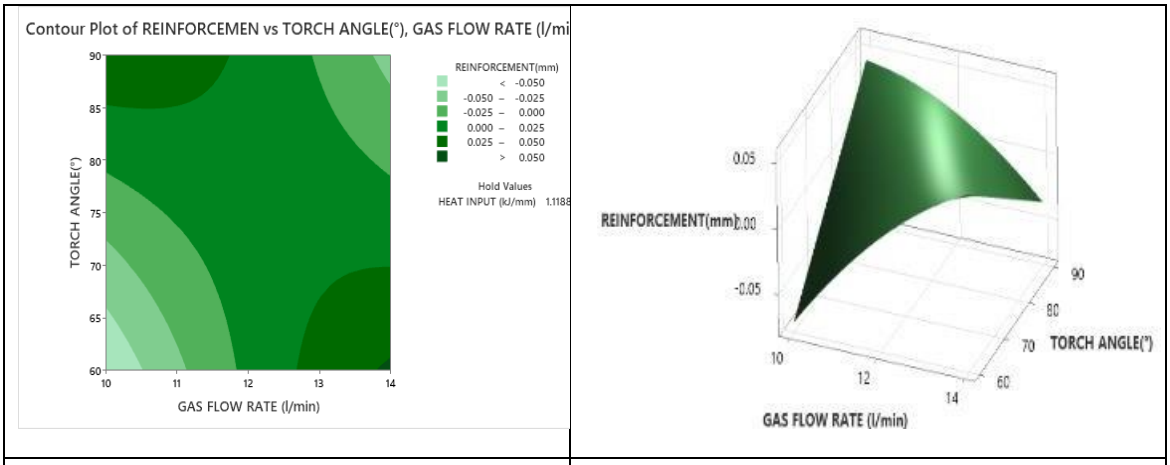

(a) (b)

Figure 4.9. (a) Contour plot and (b) surface plot of reinforcement with change in torch angle and gas flow rate at a hold value of heat input '+ve', i.e. 1.1188kJ/mm

Maximum reinforcement of 0.12mm is observed at a gas flow rate 10 L/min and torch angle of 90°. Again, higher reinforcement is observed at torch angle of around 65° and gas flow rate of 13 L/min as shown in Figure 4.9 (a,b).

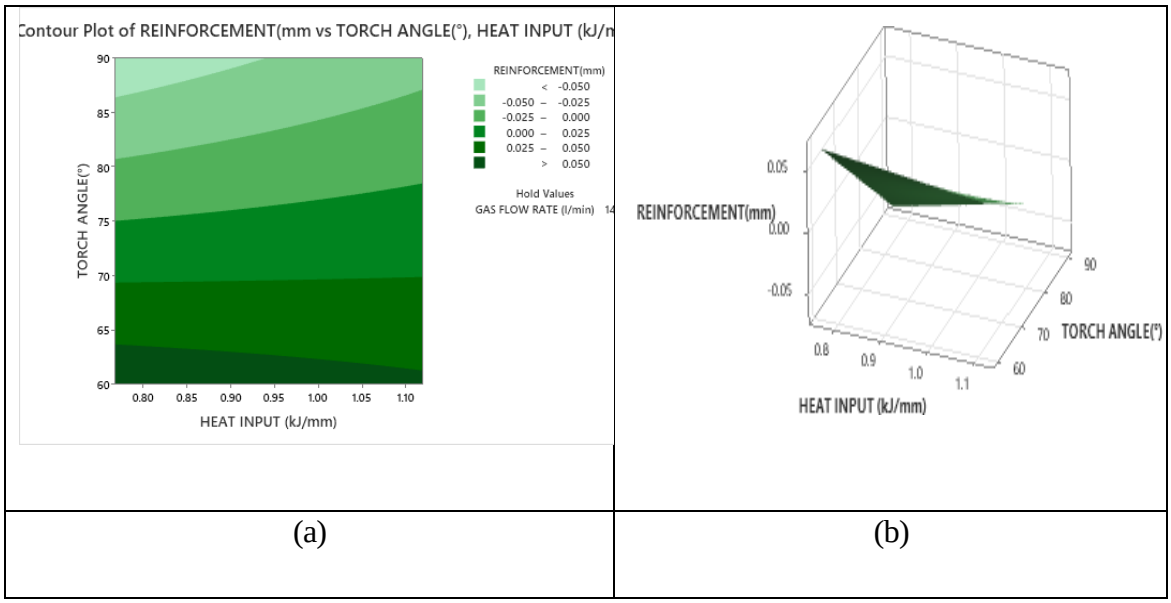

(a) (b)

Figure 4.10. (a) Contour plot and (b) surface plot of reinforcement with change in torch angle and heat input at a hold value of gas flow rate '+ve', i.e. 14 L/min

Reinforcement is maximum at a torch angle of 60°. Not much significant variation is found with heat input as shown in Figure 4.10 (a,b). Reinforcement value keeps decreasing with the increasing value of torch angle. With high Heat Input and torch angle, higher melt volume causes deeper penetration 'P' as well as width 'W', and it leaves less effect on reinforcement 'R'.

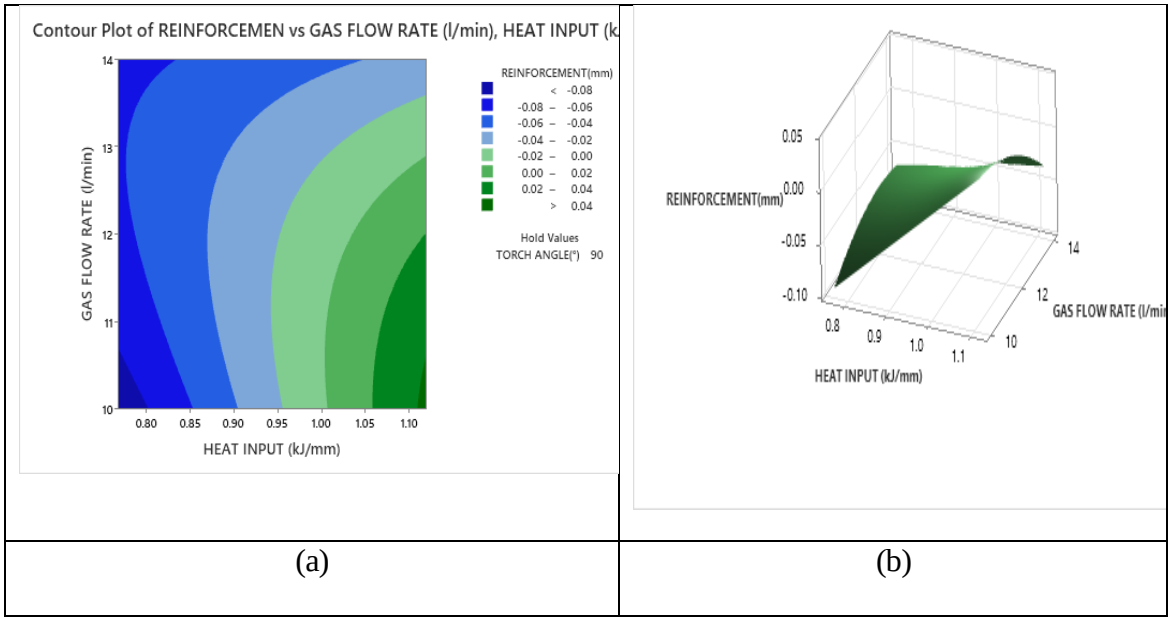

(a) (b)

Figure 4.11. (a) Contour plot and (b) surface plot of reinforcement with change in gas flow rate and heat input at a hold value of torch angle '+ve', i.e. 90°

Reinforcement increases with high heat input and is found maximum at a heat input of 1.10 kJ/mm with gas flow rate between 10-12 L/min as shown in Figure 4.11 (a,b). While reinforcement increases with the increasing value of heat input but marginal variation is found with the increasing value of gas flow rate.

From Figures 4.9, 4.10 and 4.11, it can be concluded that maximum reinforcement occurs at specific torch angles and gas flow rates, notably at 90° and 10 L/min, and higher reinforcement is observed at torch angles around 60°-65°. Additionally, reinforcement increases with higher heat input, peaking at 1.10 kJ/mm with gas flow rates between 10-12 L/min, while gas flow rate has a marginal effect compared to heat input.

4.3.4. Summary of Observation Made in Experiment Set 1

- In experiment set 1, design of experiments done by Response Surface Methodology (RSM) technique. Outcomes show that maximum penetration with considerable amount of reinforcement, and bead width are achieved with high Heat Input of 1.1188 kJ/mm, low gas flow rate of 10 L/min, and high torch angle of 90°. These parameters are used in obtaining optimal weld bead geometry but full penetration of bead specimen cannot be achieved that is the main goal to achieve in this work.
- This configuration yields penetration of 3.459 mm. At this condition bead width and reinforcement values of 9.375 mm and 0.11 mm are obtained respectively.

4.4. Observations Made in Tensile Test for Experiment Set 1

The tensile test results of Experimental Set 1 as presented in Table 4.3, revealed that the tensile strength of the welded joints varied between 206.29 MPa and 424.5 MPa, with the highest value recorded in Serial No. 7 and the lowest in Serial No. 9 (shown in Figure 4.12.). Although many samples exhibited strengths exceeding 300 MPa, the values remained significantly lower than the base material strength of approximately 580 MPa. This disparity suggests that the welded joints did not achieve sufficient strength, primarily due to incomplete penetration, which is observed to reach a maximum of only around 3.46 mm. To ensure the welded joints attain mechanical strength equivalent to that of the base metal, achieving full penetration is essential. This may require modification of the welding process, such as adjustments in heat input, welding technique, or the adoption of alternative welding methods to enhance fusion depth and overall joint integrity. Figure 4.13 illustrates the Tensile Stress vs. Elongation graph for Specimen Serial No. 7, which records the highest Ultimate Tensile Stress among the tested samples for Experiment Set 1.

Table 4.3. Tensile Strength Results of Welded Joints for Experimental Set 1

Serial No.	**Tensile Strength (MPa)**
1	284.32
2	274.86
3	212.62
4	218.67
5	349.4
6	334.96
7	424.5
8	346.06
9	206.29
10	370.22
11	231.54
12	351.62
13	328.31
14	332.86
15	352.36
16	331.42
17	339.82
18	311.691
19	326.61
20	331.42

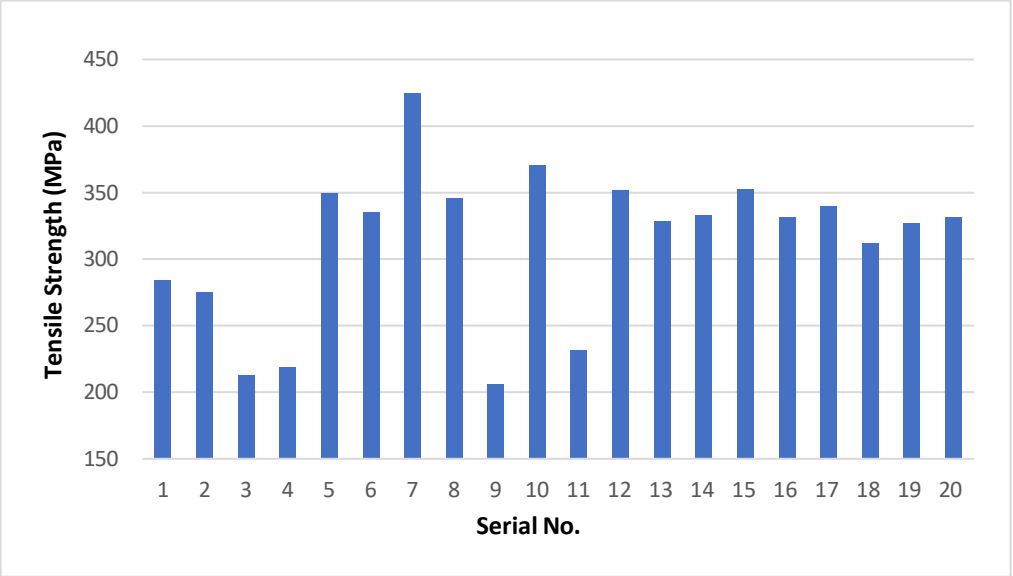

Figure 4.12. Variations in Tensile strength found in Autogenous TIG welding of SS 304H specimens

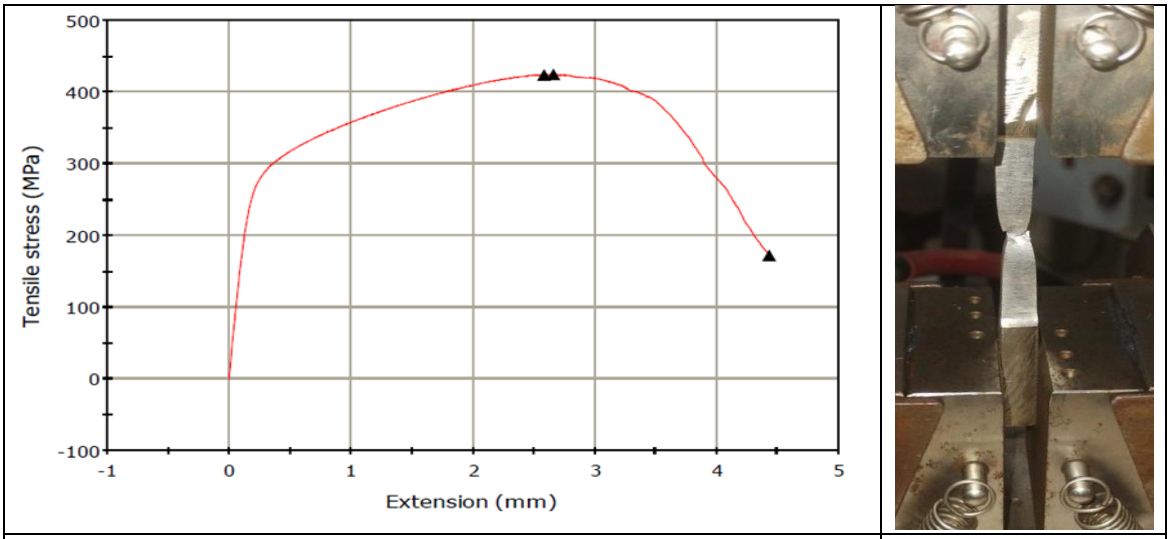

(a) (b)

Figure 4.13. (a) The maximum Tensile strength achieved of Specimen 7 of Experiment Set 1 (424.5 MPa), (b) Test specimen after test

4.5. Observations Made in Rockwell Hardness Test for Experiment Set 1

In Experimental Set 1 the average Rockwell hardness across the samples ranged from 25.33 HRC to 34.33 HRC, as shown in Table 4.4. The highest hardness value of 34.33 HRC is

recorded for Sample of Serial No. 11, indicating a comparatively harder weld region, potentially due to favourable thermal cycles or refined grain structure. In contrast, lower hardness values like 25.33 HRC observed in Samples of Serial Nos. 10 and 13 could be attributed to softer microstructures formed due to lower heat input or slower cooling rates. Most samples showed hardness values in the 27–32 HRC range, suggesting a consistent and moderate level of weld zone hardening. Figure 4.14. represents the variations in hardness values of the weld zone found for the autogenous welded specimens of Experimental Set 1.

Table 4.4. Rockwell Hardness (HRC) Test Results for Autogenous welded Joints of experimental set 1

Serial No.	**HRC1**	**HRC2**	**HRC3**	**Avg HRC**
1	26	31	26	27.67
2	29	32	28	29.67
3	31	33	33	32.33
4	29	27	31	29
5	26	31	27	28
6	32	29	33	31.33
7	32	31	28	30.33
8	25	29	28	27.33
9	29	33	31	31
10	25	25	26	25.33
11	32	37	34	34.33
12	28	28	32	29.33
13	27	25	24	25.33
14	27	28	27	27.33
15	26	32	27	28.33
16	29	27	32	29.33
17	30	33	31	31.33
18	32	34	31	32.33
19	28	28	27	27.67
20	31	28	27	28.67

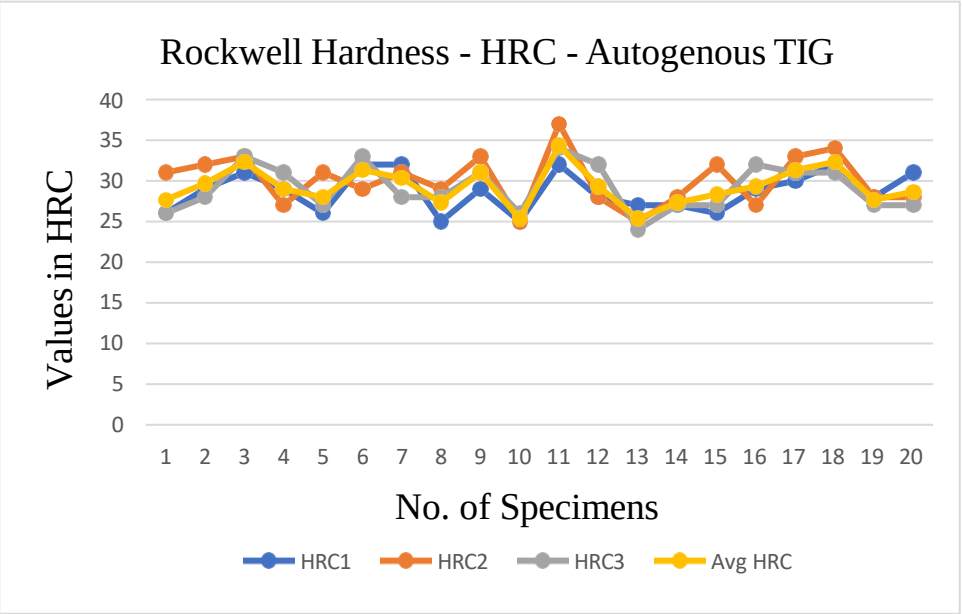

Figure 4.14. Variations in hardness values of weld zone found for welded specimens of Experiment Set 1

4.6. Observations Made in Microhardness Test

To assess the variation in hardness across different zones of the welded joints, microhardness testing is carried out using a Vickers Microhardness Tester (UHL VMHT). Typical specimens are selected for this test, and indentations are made at five different regions along a straight line, spanning from the base metal (BM) through the heat-affected zone (HAZ) to the weld centre (WC) and back across the HAZ to the base metal on the opposite side. This line profile is allowed for a detailed understanding of the hardness gradient caused by thermal cycles during welding. In experimental set 1, the test is conducted on typical samples from eight different Serial Nos. (Serial Nos. 14, 11, 18, 7, 4, 3, 9, and 19). The distance is measured in millimetre from the weld centre, ranging from –10 mm (left base metal) to +10 mm (right base metal). Results show that hardness values typically peak near the HAZ and vary across the weld zone depending on the thermal input and cooling rates, indicating microstructural transformations in different regions of the weldment. Vickers microhardness values at each location are provided in Table 4.5. Figure 4.15 presents the hardness plot for the autogenous TIG specimens welded on a single side.

Table 4.5. Vickers microhardness values of some typical specimens of Set 1 at various locations from weld centre

Distance from Weld Centre (mm)	**Serial No. 14**	**Serial No. 11**	**Serial No. 18**	**Serial No. 7**	**Serial No. 4**	**Serial No. 3**	**Serial No. 9**	**Serial No. 19**
-10	227	256	266	260	228	262	252	237
-8	238	259	269	262	232	259	259	239
-6	263	243	242	253	260	243	253	253
-4	253	253	240	256	254	245	245	253
-2	249	239	248	242	245	241	253	252
0 (Weld Center)	246	248	237	231	248	239	249	247
+2	251	254	229	228	246	231	241	248
+4	234	244	251	233	238	248	249	236
+6	226	249	248	235	233	248	238	235
+8	230	247	267	261	226	268	258	232
+10	224	252	261	256	222	264	254	234

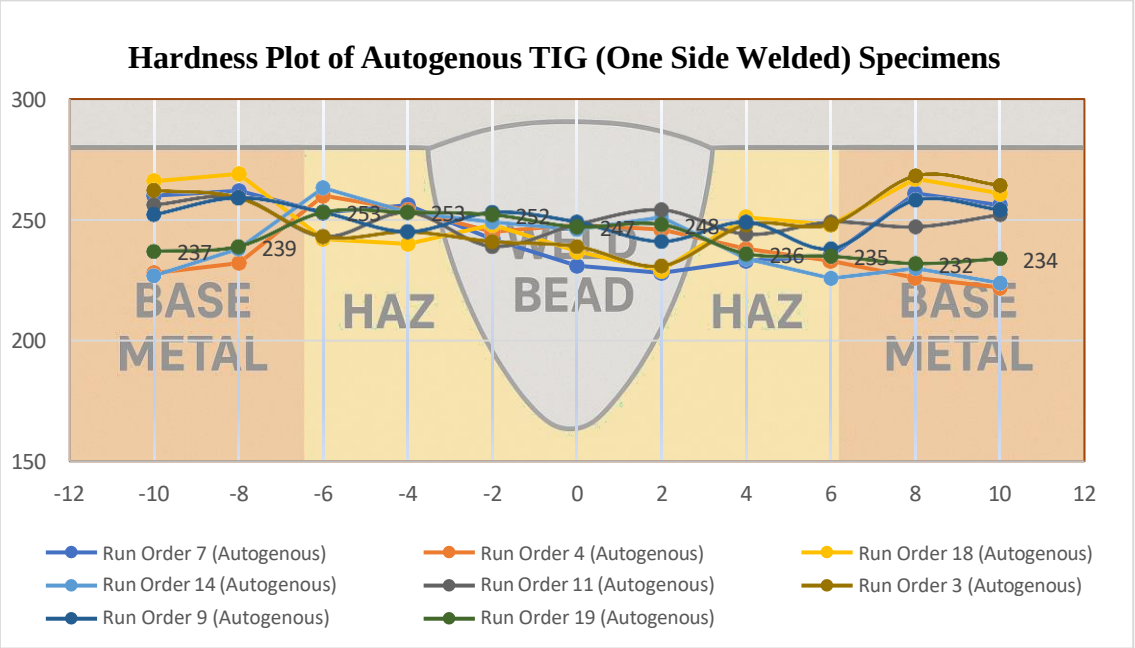

Figure 4.15. Hardness plot of some typical autogenous TIG one-side welded specimens (Set 1)

4.7. Observations Made in Microstructure Analysis

In Experiment Set 1, Serial No. 7 (424.50 MPa), Serial No. 10 (370.22 MPa), Serial No. 15 (352.36 MPa), and Serial No. 12 (351.62 MPa) are observed under the optical microscope (shown in Figure 3.11) for microstructural study. These samples exhibit the highest mechanical strength, suggesting superior weld quality and metallurgical bonding. Micrographs are captured under 50x, 100x, and 200x magnifications, covering the base metal, heat-affected zone (HAZ) and weld zone. Observations reveal a finer grain structure in the weld zone of high-strength specimens, attributed to optimal heat input and cooling rates that promote grain refinement. Microstructures of typical specimens of Experiment Set 1 having higher tensile strength seen under optical microscope are depicted in Figure 4.16.

		
a) Serial No. 7 - 50x	b) Serial No. 7 - 100x	c) Serial No. 7 - 200x

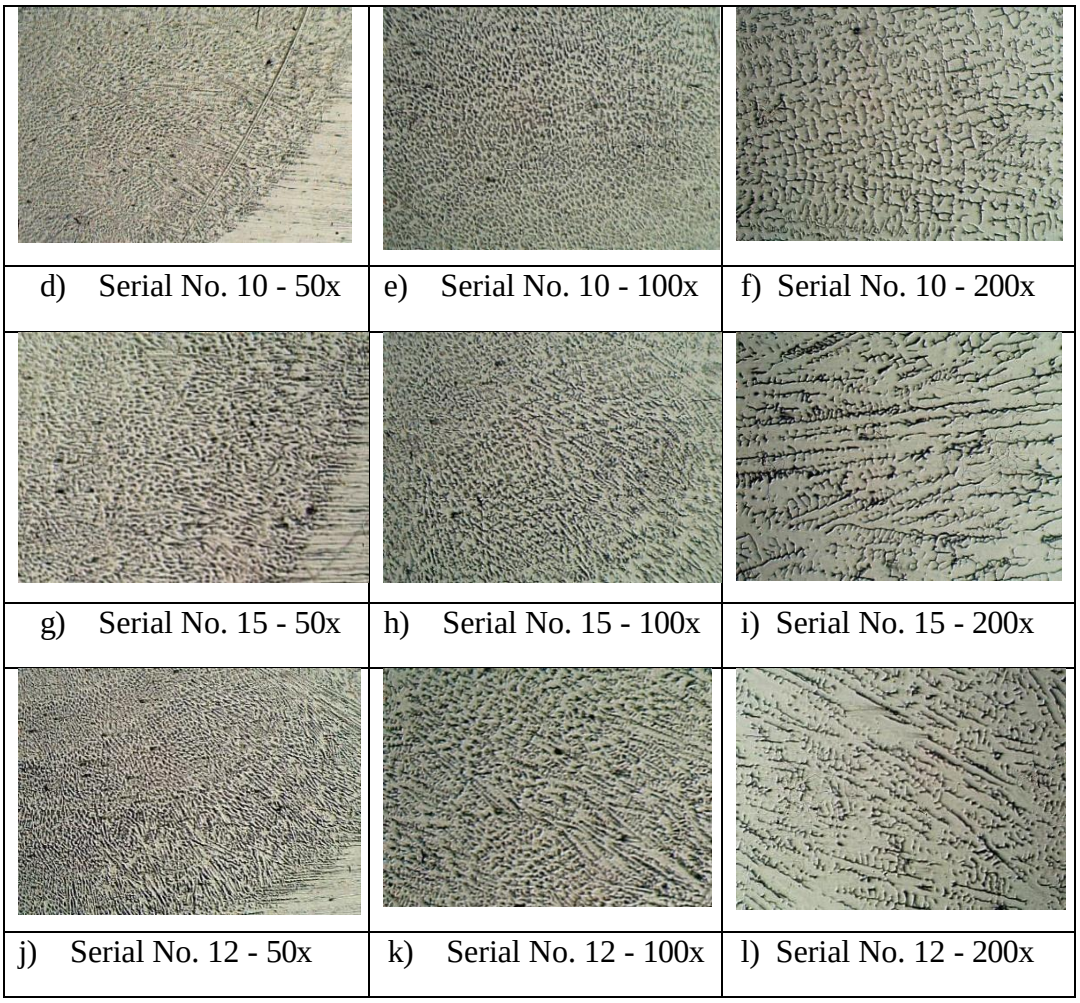

d) Serial No. 10 - 50x	e) Serial No. 10 - 100x	f) Serial No. 10 - 200x
g) Serial No. 15 - 50x	h) Serial No. 15 - 100x	i) Serial No. 15 - 200x
j) Serial No. 12 - 50x	k) Serial No. 12 - 100x	l) Serial No. 12 - 200x

Figure 4.16. Microstructures of typical specimens of Experimental Set 1 having higher tensile strength seen under optical microscope.

4.8. Observations Made in Scanning Electron Microscopy

The SEM micrographs of typical samples from Set 1 reveal well-refined and uniformly distributed dendritic structures, indicating effective thermal control during solidification. The grain boundaries appear continuous with minimal signs of cracking or porosity, suggesting strong metallurgical bonding and stable phase formation. As found from the images, the microstructure is relatively free from defects such as voids or shrinkage cavities, which is indicative of a controlled welding environment and optimized heat input. Overall, these microstructural characteristics correlate well with improved mechanical properties and successful autogenous welding outcomes. Figure 4.17 represents micrographs of typical specimens of Experimental Set 1 and Set 2 having higher tensile strength seen under Scanning Electron Microscope (SEM).

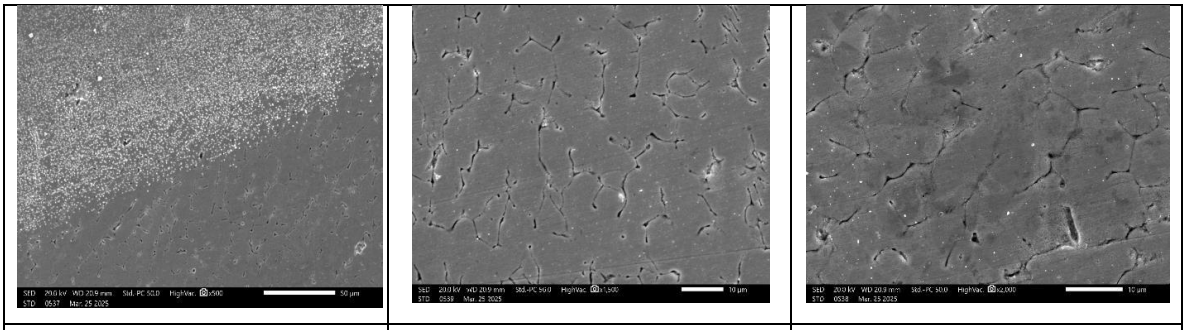

a) Serial No. 7 - 500x	b) Serial No. 7 - 1500x	c) Serial No. 7 - 2000x

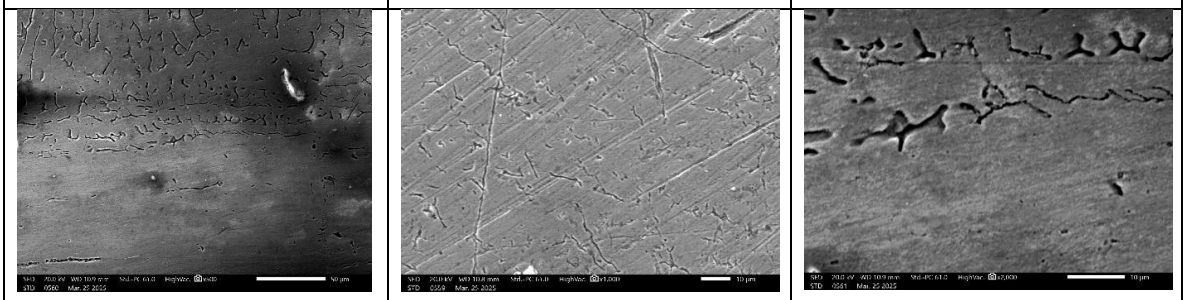

e) Serial No. 10 - 500x	f) Serial No. 10 - 1000x	g) Serial No. 10 - 2000x

Figure 4.17. Microstructures of typical specimens of Experimental Set 1 having higher tensile strength seen under Scanning Electron Microscope (SEM).

4.9. Outcomes of the Analytical Hierarchy Process applied to the results of Experiment Set 1

The pairwise comparison matrix for criteria is developed using the operating conditions from Serial numbers 1 to 9 from Experimental Set 1. These are selected based on unique parameter combinations, as several other experimental runs shared identical settings and are therefore excluded from the matrix to avoid redundancy.

The priority weights for the AHP are determined manually through extensive discussions with welding experts and academic supervisors. Instead of relying solely on software-generated values, brainstorming sessions are conducted to integrate expert judgment and practical welding experience. This approach ensured that the assigned weights accurately reflected the real-world significance and interdependence of parameters such as depth of penetration, bead width, and reinforcement, thereby providing a more customized and realistic decision-making framework. A similar methodology was also reported by Acharya et al. (2022, 2023) [28, 29] and Bhatti & Tharwat (2018) [123].

Table 4.6 represents the AHP model, where weights of various criteria are chosen based on the goal of optimizing weld parameters for all four Experiment Sets. Then maximum Eigen value is calculated from 3 × 3 matrix. It is calculated as λmax = 3.103 and finally consistency ratio (C.R.) is calculated. This value is calculated as 8.8% and it is less than 10%. So, it is accepted.

Table 4.6. Pair wise comparison matrix for criteria

Optimization of Weld Bead Geometry	**Depth of penetration**	**Bead width**	**Reinforcement**	**Geometric mean**	**Local weight**
Depth of penetration	1	4	3	2.27	0.62
Bead width	0.25	1	2	0.79	0.21
Reinforcement	0.33	0.5	1	0.55	0.15

λmax= 3.103, C.R.= 0.088

Now, in Table 4.7. the comparison matrix between alternatives for criterion 1 (Depth of penetration) is calculated keeping in mind the goal i.e. optimization of weld parameter. Now maximum Eigen value is λ_{max}= 9.36 is calculated from 9×9 matrix and consistency ratio is calculated as 4.3%. It is below 10% and is accepted.

Table 4.7. Pair wise comparison matrix for alternatives for depth of penetration

Depth of Penetration	**A1**	**A2**	**A3**	**A4**	**A5**	**A6**	**A7**	**A8**	**A9**	**Geometric mean**	**Local weight**
A1	1	2	3	3	1/4	1/3	1/4	1/3	1/3	0.70	0.0613
A2	1/2	1	3	2	1/4	1/3	1/4	1/3	1/3	0.577	0.0505
A3	1/3	1/3	1	1/2	1/5	1/4	1/5	1/4	1/4	0.322	0.0282
A4	1/3	1/2	2	1	1/5	1/4	1/5	1/4	1/4	0.393	0.0344
A5	4	4	5	5	1	2	1/3	2	2	2.15	0.188
A6	3	3	4	4	1/2	1	1/3	2	2	1.65	0.144
A7	4	4	5	5	3	3	1	2	2	2.86	0.250
A8	3	3	4	4	1/2	1/2	1/2	1	2	1.48	0.129
A9	3	3	4	4	1/2	1/2	1/2	1/2	1	1.273	0.112

C.R.= 0.043, λ_{max}= 9.36

Now, in Table 4.8. the comparison matrix between alternatives for criterion 2 (Bead Width) is calculated keeping in mind the goal i.e., optimization of weld parameter. Now maximum Eigen value is λ_{max} = 9.432 is calculated from 9×9 matrix and consistency ratio is calculated as 5.4 %. It is below 10% and is accepted.

Table 4.8. Pair wise comparison matrix for alternatives for bead width

Bead Width	A1	A2	A3	A4	A5	A6	A7	A8	A9	Geometric mean	Local weight
A1	1	2	4	3	4	5	5	3	3	2.99	0.269
A2	1/2	1	3	2	3	4	4	2	2	2.01	0.181
A3	1/4	1/3	1	1/2	2	3	3	1/2	1/2	0.830	0.074
A4	1/3	1/2	2	1	2	3	3	2	2	1.416	0.128
A5	1/4	1/3	1/2	1/2	1	3	3	1/2	1/2	0.713	0.064
A6	1/5	1/4	1/3	1/3	1/3	1	2	1/4	1/4	0.396	0.035
A7	1/5	1/4	1/3	1/3	1/3	1/2	1	1/4	1/4	0.340	0.031
A8	1/3	1/2	2	1/2	2	4	4	1	2	1.29	0.116
A9	1/3	1/2	2	1/2	2	4	4	1/2	1	1.112	0.10

C.R.= 0.054, λ_{max} = 9.432

Now, in Table 4.9 the comparison matrix between alternatives for criterion 2 (Reinforcement) is calculated keeping in mind the goal i.e., optimization of weld parameter. Now maximum Eigen value is λ_{max}= 10.27 is calculated from 9×9 matrix and consistency ratio is calculated as 10% so it is acceptable.

Table 4.9. Pair wise comparison matrix for alternatives for reinforcement

Alternative	A1	A2	A3	A4	A5	A6	A7	A8	A9	Geometric mean	Local weight
A1	1	1/3	2	1/3	2	1/2	½	1	3	0.884	0.0823
A2	3	1	3	1	3	2	2	3	1	1.88	0.175
A3	1/2	1/3	1	1/3	1/2	1/3	1/3	1/2	1/4	0.419	0.039
A4	3	1	3	1	3	2	2	3	1	1.88	0.175
A5	1/2	1/3	2	1/3	1	1/2	½	1/2	1/4	0.535	0.0498
A6	2	1/2	3	1/2	2	1	½	3	1/4	1.01	0.094
A7	2	1/2	3	1/2	2	2	1	2	1/4	1.128	0.105
A8	1	1/3	2	1/3	2	1/3	½	1	1/3	0.662	0.061
A9	3	1	4	1	4	4	4	3	1	2.34	0.217

C.R.= 0.10, λ_{max} = 10.27

In Table 4.10. the local weights for each parameter are considered and global weights are calculated for all individual alternatives. The maximum global weight of 0.177 for Alternative No. 7 represents the suitable alternative, which may be considered as the optimized condition.

Table 4.10. Local and global weights for alternatives and local weights for criteria

Alternative No.	Local Weights			Global Weights
	Depth of penetration	Bead Width	Reinforcement	
	0.62	0.21	0.15	
A1	0.0613	0.269	0.082	0.106
A2	0.0505	0.181	0.175	0.095
A3	0.0282	0.074	0.039	0.038
A4	0.0344	0.128	0.175	0.074
A5	0.188	0.064	0.049	0.137
A6	0.144	0.035	0.094	0.110
A7	0.250	0.031	0.105	0.177
A8	0.129	0.116	0.061	0.113
A9	0.112	0.100	0.217	0.123

In this work, the analytical hierarchy process is applied to explore favourable depth of penetration maintaining productivity and the related process conditions employing Tungsten Inert Gas welding. Global weight of each alternative is calculated and the highest global weight of 0.177 corresponding to alternative 7 is evaluated as the optimal condition (shown in Table 4.10).

4.10. Summary of Experiment Set 1

Experimental Set 1 focuses on autogenous TIG welding using the Response Surface Methodology (RSM) to optimize process parameters for 8 mm thick SS304H stainless steel specimens. The objective is to maximize penetration while maintaining desirable bead geometry. Results indicate that a high heat input of 1.1188 kJ/mm, a low gas flow rate of 10 L/min, and a high torch angle of 90° produces the most favourable weld profile (Serial No. 7). However, full penetration is not achieved, with the maximum penetration limited to approximately 3.46 mm. This insufficient depth of fusion resulted in tensile strengths significantly below the base metal strength (580 MPa), with values ranging from 206.29 MPa to a peak of 424.5 MPa.

Hardness analysis of the welds shows Rockwell hardness values between 25.33–34.33 HRC, with the highest hardness observed in Serial No. 11, potentially due to grain refinement and favourable thermal cycles. Most samples exhibit moderate hardness values, indicating a consistent weld profile. Vickers microhardness tests conducted on selected specimens show typical hardness gradients, with peaks near the heat-affected

zone (HAZ), reflecting the influence of thermal input during welding.

Microstructural investigations, using both optical and scanning electron microscopy (SEM), reveal dendritic structures with refined grains in high-strength specimens. The weld zones are largely free from common defects such as voids, cracks and porosity, suggesting effective thermal control during the solidification phase. The microstructural characteristics correlates well with the mechanical performance, particularly in samples with optimal welding conditions.

Additionally, the Analytical Hierarchy Process (AHP) identifies Serial No. 7 as the optimal welding condition with the highest global weight of 0.177, emphasizing the significance of parameter optimization. While acceptable weld quality is achieved in many cases, the limited depth of penetration and resulting low tensile strength highlight the need for improved techniques, such as using flux or alternative welding methods to meet the mechanical requirements of thick-section stainless steel joints.

Chapter 5

Results and Discussion on Experiment Set 2 and 3

5.1. Introduction

This chapter focuses on the second and third phase of welding experiments (Experiment Set 2 and 3), which aims at overcoming the limitations of incomplete penetration observed in the first phase. In Experiment Set 1, autogenous TIG welding is performed on only one side of the butt joints and complete fusion through the thickness of the plate is not achieved. To address this, Experiment Set 2 is undertaken involving autogenous welding on both sides of selected SS 304H specimens targeting full penetration and improving the mechanical property of the welded joint. Activating flux is also applied on the faying surface in Experiment Set 3 in autogenous TIG welding done on both sides of the specimens. Post-welding evaluations such as tensile test and hardness test are conducted and thoroughly analyzed. Additionally, microhardness tests are also performed on best performing specimens. MCDM tool such as the AHP is used also used to optimize the output parameters.

5.2. Detail of Setup of Experiment Set 2 and Experiment Set 3

The second set of experiments is conducted using a KEMPI K2 TIG 200 ACDC welding machine, as illustrated in Figure 3.2. Process parameters applied during these experiments are taken directly from the top five performing alternatives of Experiment Set 1 identified through the Analytic Hierarchy Process (AHP). In this Experiment Set 2, a torch angle of 75° to the horizontal is uniformly applied for all specimens, as supported by findings in the relevant literature and practical welding standards. It is commonly used for such welding applications and produced superior welded joints. Importantly, all other process parameters including current, travel speed, gas flow rate are kept identical to those used in Experiment Set 1 to ensure consistency across both sets of experiments and to facilitate direct comparison. Post-welding procedures such as surface preparation, polishing and etching for metallographic analysis are carried out in the same manner as described for Experiment Set 1. Based on initial experimentation, a gas flow rate range of 10–14 L/min and an arc gap of 2 mm are finalized. Accordingly, the selected parameters for this phase include a torch angle

of 75°, gas flow rates of 10, 12 and 14 L/min, and heat input of 0.9434 kJ/mm and 1.1188 kJ/mm.

Experiment Set 3 has employed Activated Tungsten Inert Gas (A-TIG) welding process, in which a thin coating of titanium dioxide (TiO_2) activated flux is applied to the faying surface of the plates on both sides before welding. This technique is introduced to enhance weld penetration and improve bead characteristics by modifying the heat distribution at the weld zone. The application of TiO_2 flux is intended to enhance heat concentration at the weld zone by promoting the reverse Marangoni effect, which facilitates deeper penetration by altering the fluid flow dynamics in the molten weld pool. All other process parameters in this set are kept consistent with those used in Experiment Set 2 to ensure a valid comparison. Specifically, the welding speed is maintained at 1.22 m/min, the root gap is set to 0 mm, and the arc gap is kept at 2 mm throughout the process. The selected parameters for this phase include a torch angle of 75°, gas flow rates of 10, 12 and 14 L/min, and heat input of 1.010 kJ/mm and 1.264 kJ/mm.

5.3 Observations Made in Experiment Set 2

This section first presents the observations made using visual inspection of the welds. It also tries to explore the influence of process parameters on weld bead geometry and the insights gained from the experimental observations. The results aim at validating the effectiveness of selected parameters in producing quality weld joints and to highlight limitations where further improvements may be necessary.

5.3.1 Visual Inspection

Visual examination of the welded specimens reveals uniform bead formation with minimal spatter and absence of surface defects. No undercut, blowhole, pinhole and cracks are observed in any of the weld runs. These findings suggest that selected welding parameters lead to stable arc performance and efficient shielding gas coverage. The visual results for each Serial No. are summarized in Table 5.1. A top view of the welded specimens is shown in Figure 5.1. This confirms that the chosen combinations of gas flow rate and heat input are capable of producing visually acceptable welds under consistent torch angle and travel speed.

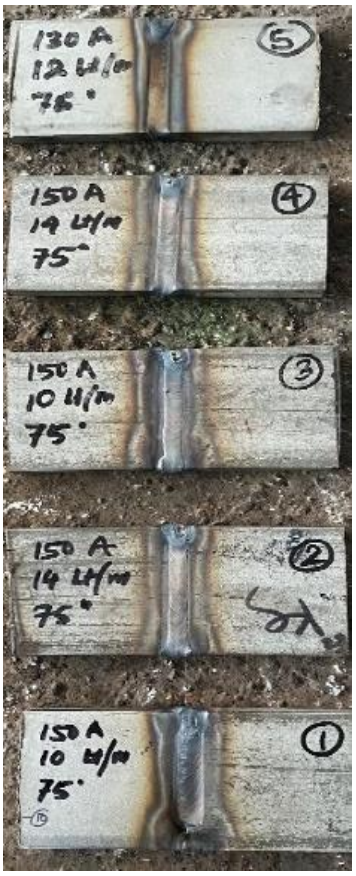

Figure 5.1. Top view of welded specimens of Experiment Set 2

Table 5.1. Visual observations made in Experiment Set 2

Sl. No.	Gas Flow Rate (L/min)	Heat Input (kJ/mm)	Weld Uniformity	Spatter	Crack	Blowhole-Pinhole	Undercut
21	10	1.1188	✓	✓	Nil	Nil	Nil
22	14	1.1188	✓	✓	Nil	Nil	Nil
23	10	1.1188	✓	✓	Nil	Nil	Nil
24	14	1.1188	✓	✓	Nil	Nil	Nil
25	12	0.9434	✓	✓	Nil	Nil	Nil

5.3.2 Influence of Process Parameters on Bead Geometry

To evaluate how varying process parameters influence the morphology of weld beads, a detailed cross-sectional analysis is performed. Key attributes considered include total depth

of penetration (i.e., the combined penetration from both sides of the weld), average bead width and average reinforcement height, each calculated as the mean of values obtained from both welded sides.

The summarized data in Table 5.2 indicate that the specimens subjected to a lower gas flow rate of 10 L/min and a higher heat input of 1.180 kJ/mm (Serial Nos. 21 and 23) demonstrate significantly greater depth of penetration and bead width. In contrast, specimens welded at a higher gas flow rate of 14 L/min exhibit reduced penetration. This reduction is likely due to increased cooling or arc instability effects, which can occur at elevated gas flow rates. Serial No. 25, which has a comparatively lower heat input (0.964 kJ/mm) and a moderate gas flow rate of 12 L/min, produced a weld with balanced penetration and minimal reinforcement.

Figures 5.2 through 5.5 illustrate cross-sectional views of typical representative weld beads. Although welding is done on both sides of the 8 mm thick plates, none of the samples have achieved full penetration. This shows that further improvement in the process is needed to achieve full weld penetration.

Table 5.2. Experimental observations made in Experiment Set 2

Sl. No.	**Gas flow rate (L/min)**	**Torch Angle (Degree)**	**Heat input (kJ/mm)**	**Total Penetration (mm)**	**Avg. Width (mm)**	**Avg. Reinforcement (mm)**
21	10	75	1.180	6.530	5.839	0.109
22	14	75	1.180	5.368	5.59	0.144
23	10	75	1.180	6.000	6.066	0.121
24	14	75	1.180	5.022	5.307	0.00
25	12	75	0.964	5.174	6.64	0.177

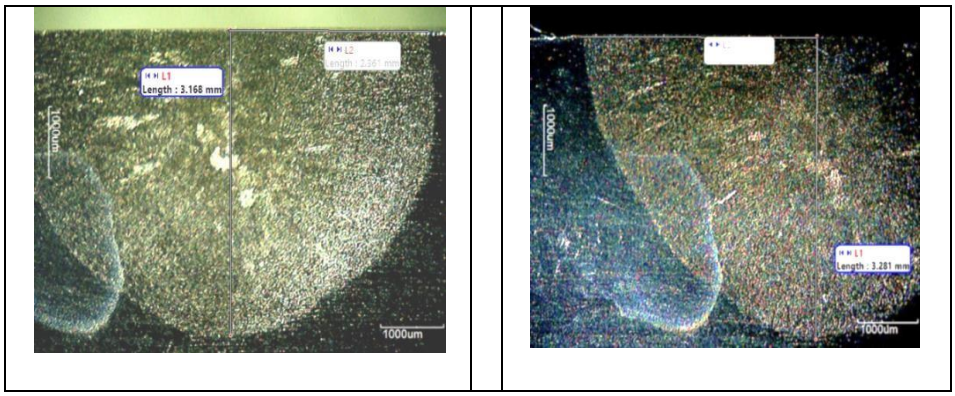

Figure 5.2. View of weld bead of Serial No. 21 (a) 1st pass and (b) 2nd Pass done on two sides

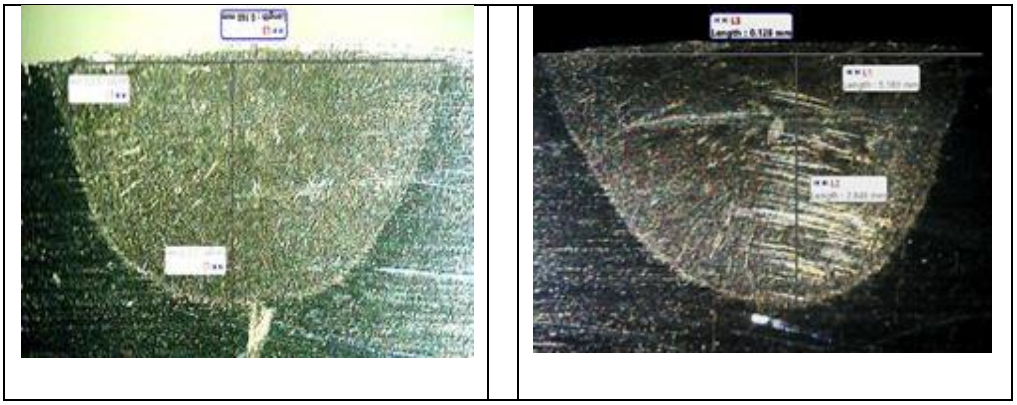

Figure 5.3. View of weld bead of Serial No. 22 (a) 1st pass and (b) 2nd Pass done on two sides

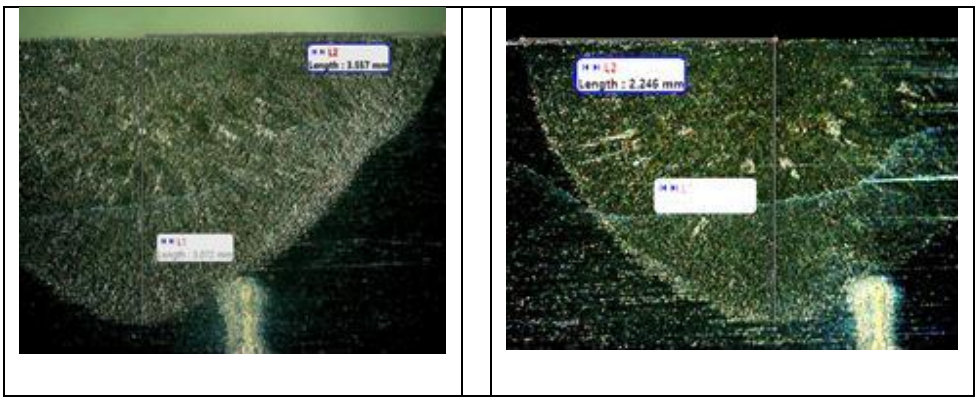

Figure 5.4. View of weld bead of Serial No. 23 (a) 1st pass and (b) 2nd Pass done on two sides

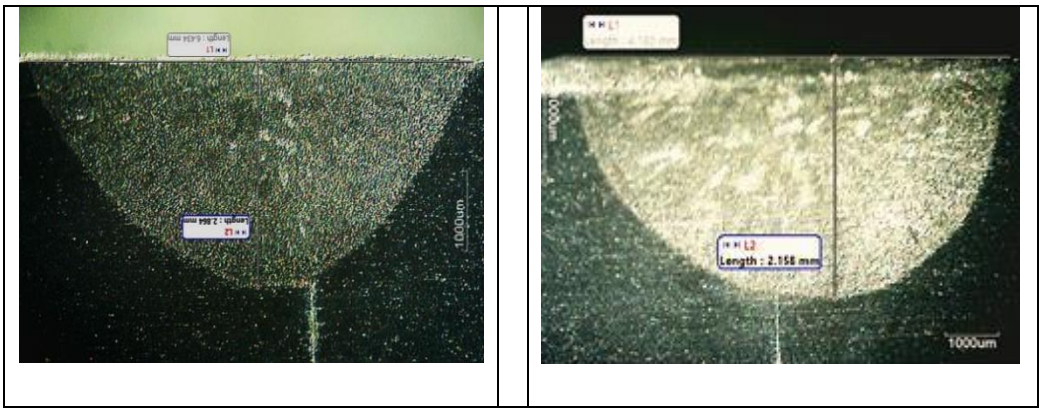

Figure 5.5. View of weld bead of Serial No. 24 (a) 1st pass and (b) 2nd Pass done on two sides

The observations from this set of experiments demonstrate a smooth and uniform deposition with minimal spatter and an absence of crack, undercut, blowhole and pinhole. These factors confirm the effectiveness of the selected welding parameters in producing high-quality weld joints. This autogenous welding on both sides of the specimen significantly improves penetration but does not lead to full joint penetration for 8 mm thick SS304H specimens. It is clear from the diagrams of bead geometry as shown in Figure 5.2 through Figure 5.5. This suggests that additional modifications, such as incorporation of activated flux, etc. may be necessary to enhance weld penetration.

5.4. Observations Made in Tensile Test for Experiment Set 2

In the second phase of experimentation, autogenous TIG welding is performed on both sides of the SS304H specimens using the optimal input parameters derived from the AHP-based global decision matrix. The tensile strength values obtained for the corresponding Serial Numbers (21 to 25) are presented in Table 5.3. The results demonstrated considerable variation in mechanical performance, with the highest tensile strength recorded at 481.73 MPa (Serial No. 21 shown in Figure 5.7), followed by 476.82 MPa (Serial No. 23). The lowest value is observed for Serial No. 24 at 416.83 MPa. These fluctuations indicate the sensitivity of weld quality to process parameter tuning, even under optimal conditions. The variations of Tensile strength values of second set are shown in Figure 5.6.

Table 5.3. Tensile Strength Results of Welded Joints for Experimental Set 2

Serial No.	Tensile Strength (MPa)
21	481.73
22	434.276
23	476.82
24	416.834
25	422.754

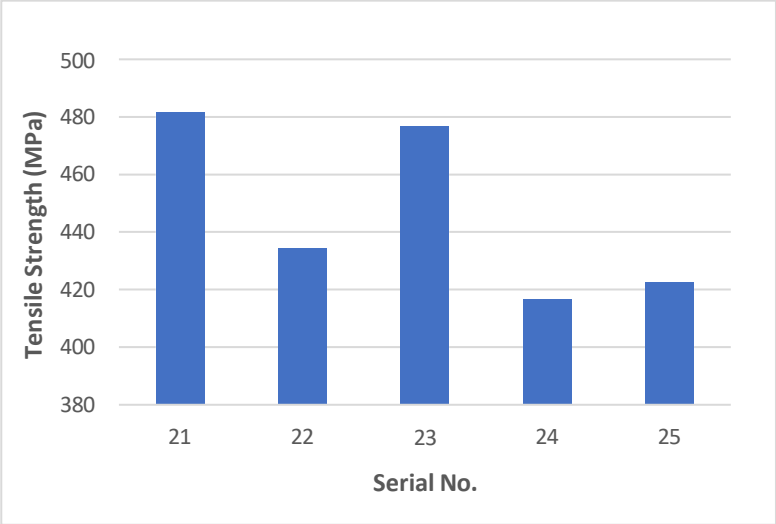

Figure 5.6. Variations in Tensile strength found in Experiment Set 2

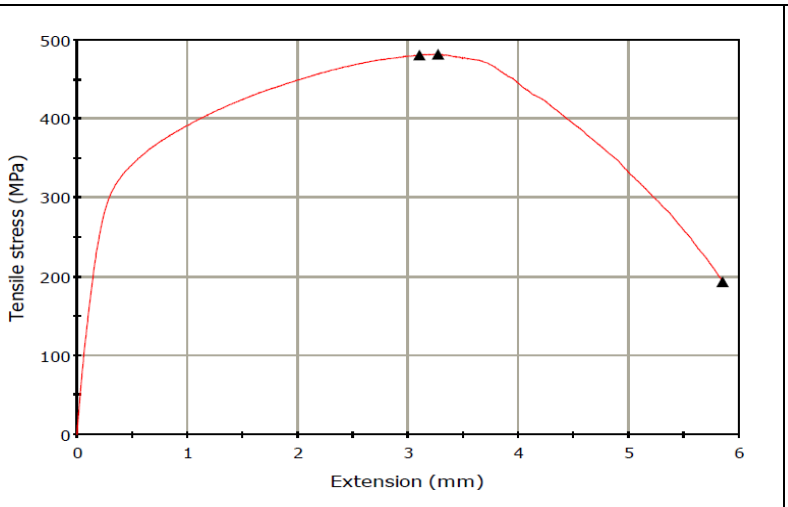

(a)

(b)

Figure 5.7. The maximum Tensile strength achieved of Specimen of Serial No. 21 of Experiment Set 2 (481.73 MPa), (b) Test specimen after test

5.5. Observations Made in Rockwell Hardness Test for Experiment Set 2

In Experimental Set 2, the average Rockwell hardness of the autogenous welded joints falls between 28.00 HRC and 31.67 HRC (Table 5.4). The highest hardness, 31.67 HRC in Sample 24, indicates a harder weld zone, probably due to good heat control and finer grains from the double-sided TIG weld. Conversely, the lowest average hardness of 28.00 HRC (Sample 21) points to a slightly softer microstructure that may stem from localized variations in heat input or cooling rate. Overall, most samples cluster in the 28–31 HRC range, indicating a fairly uniform and moderately hardened weld region throughout this experimental set. Figure 5.8 depicts the hardness variation for all autogenous welds (both side welded) in Set 2.

Table 5.4. Rockwell Hardness (HRC) Test Results for Autogenous welded Joints of Experimental Set 2

Sl. No	HRC1	HRC2	HRC3	Avg HRC
21	31	27	26	28
22	29	28	29	28.67
23	32	27	31	30
24	32	31	32	31.67
25	33	30	31	31.33

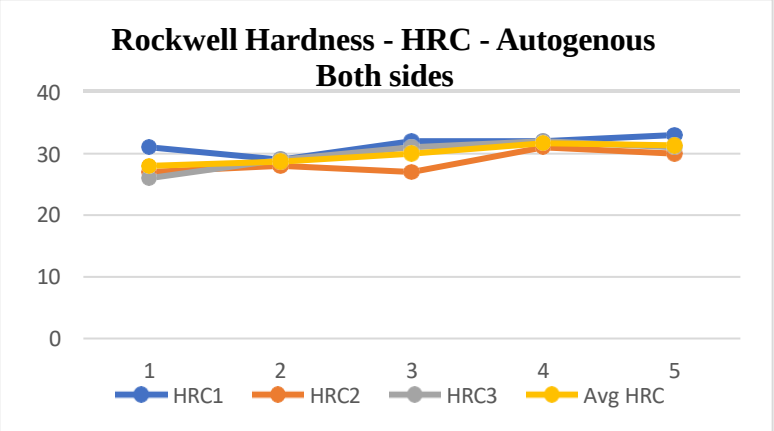

Figure 5.8. Variations in hardness values of weld zone found for Autogenous Welded (Both sides) specimens of Experiment Set 2

5.6. Observations Made in Microhardness Test

In Experimental Set 2, hardness testing is performed on typical specimens from four different Serial Nos. (Runs 21, 23, 24 and 25). Vickers microhardness measurements are taken at intervals ranging from –10 mm (left base metal) to +10 mm (right base metal) relative to the weld centre, covering both sides of the autogenous TIG weld zone. The hardness values exhibit variation across the weldment, generally peaking near the heat-affected zone (HAZ), reflecting the effects of thermal input and cooling rates on microstructural changes. The full set of Vickers microhardness data for each measurement location is presented in Table 5.5. The hardness distribution for these autogenous TIG both-side welded specimens is illustrated in Figure 5.9.

Table 5.5. Vickers microhardness values of some typical welded specimens of Set 2 at various locations from weld centre

Distance from Weld Centre (mm)	**Serial No. 21 (Autogenous both sides)**	**Serial No. 23 (Autogenous both sides)**	**Serial No. 24 (Autogenous both sides)**	**Serial No. 25 (Autogenous both sides)**
-10	240	245	238	242
-8	255	256	251	248
-6	263	268	266	261
-4	270	262	261	257
-2	265	259	257	255
0 (Weld Centre)	260	254	252	246
+2	268	264	258	252
+4	255	256	247	245
+6	250	248	245	243
+8	252	242	249	246
+10	245	246	242	239

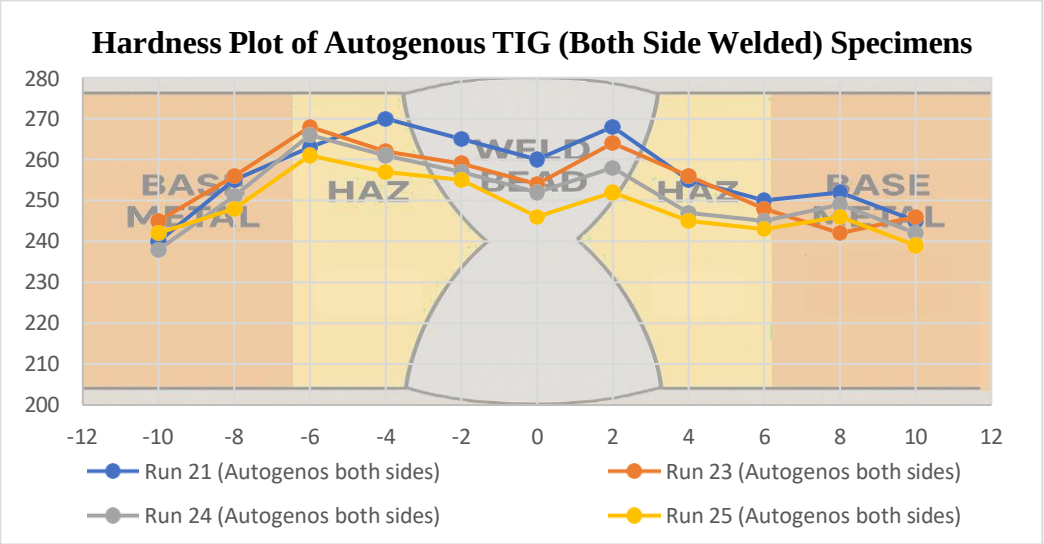

Figure 5.9. Hardness plot of some typical autogenous TIG both-side welded specimens (Experiment Set 2)

5.7. Observations Made in Microstructure Analysis of Experiment Set 2

In Experimental Set 2 specimens of Serial No. 21 (481.73 MPa) and Serial No. 23 (476.82 MPa), the two highest-strength welds in the set are selected for detailed microstructural examination. Optical micrographs are captured at 50x, 100x and 200x magnifications, encompassing the base metal, heat-affected zone (HAZ) and weld metal. Both high-strength samples display a noticeably refined grain structure within the weld zone, a feature attributed to the favourable heat input and cooling rates achieved during autogenous TIG welding. Representative microstructures of these high-strength specimens from Experimental Set 2 are presented in Figure 5.10.

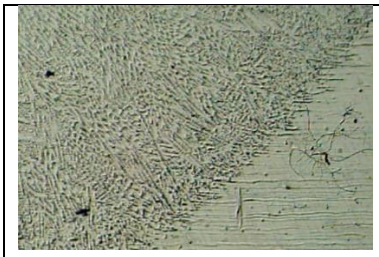		
a) Serial No. 21 - 50x	b) Serial No. 21 - 100x	c) Serial No. 21 - 200x

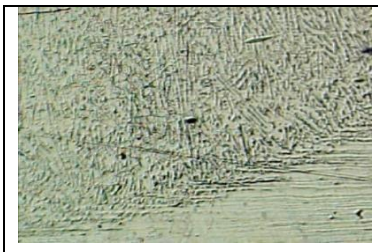		
e) Serial No. 22 - 50x	f) Serial No. 22 - 100x	g) Serial No. 22 - 200x

Figure 5.10. Microstructures of typical specimens of Experimental Set 2 having higher tensile strength seen under optical microscope.

5.8. Observations Made in Scanning Electron Microscopy of Experiment Set 2

The SEM micrographs of typical samples from Experiment Set 2 reveal well-refined and uniformly distributed dendritic structures, indicating effective thermal control during solidification. Grain boundaries appear continuous with minimal signs of cracking or porosity, suggesting strong metallurgical bonding and stable phase formation. In several images, the microstructure is relatively free from defects such as voids or shrinkage cavities, which is indicative of a controlled welding environment and optimized heat input. Overall, these microstructural characteristics correlate well with improved mechanical properties and successful autogenous welding outcomes. Figure 5.11 represents micrographs of typical specimens of Experimental Set 2 having higher tensile strength seen under Scanning Electron Microscope (SEM).

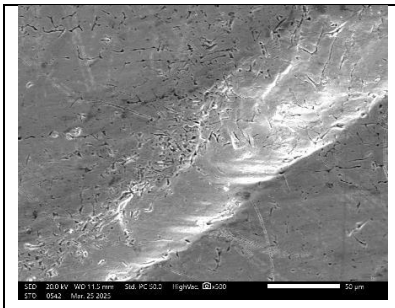		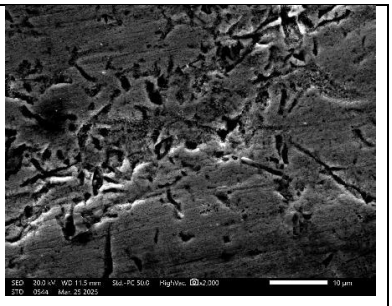
a) Serial No. 21 – 500x	b) Serial No. 21 - 1500x	c) Serial No. 21 - 2000x

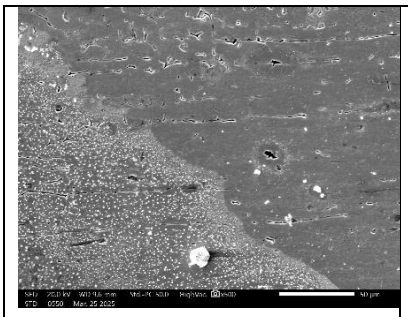

e) Serial No. 23 – 500x

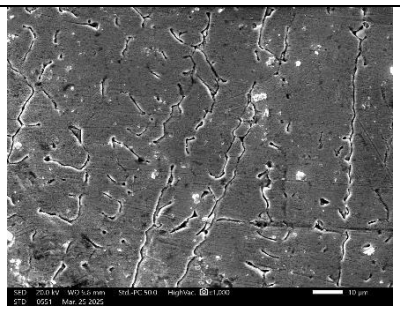

f) Serial No. 23 - 1500x

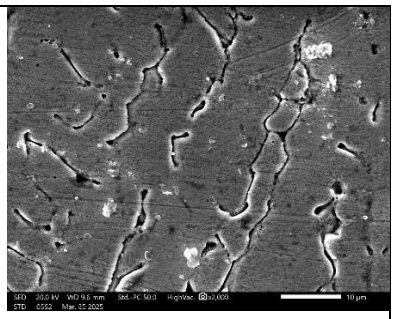

g) Serial No. - 2000x

Figure 5.11. Microstructures of typical specimens of Experimental Set 1 and Set 2 having higher tensile strength seen under Scanning Electron Microscope (SEM).

5.9 Outcomes of the Analytical Hierarchy Process Applied to the Results of Experiment Set 2

The pairwise comparison matrix for criteria for this Experiment Set 2 is identical to that Experiment Set 2 and it is shown in Table 4.6 of Chapter 4. These Serial numbers of the specimens 21 to 25 are represented as Alternatives 1 to 5 taken in the same order for Experiment Set 2. Now, in Table 5.6. the comparison matrix between alternatives for criterion 1 (Depth of penetration) is calculated keeping in mind the goal, i.e., optimization of weld parameter. Now maximum Eigen value is λ_{max}= 5.13 is calculated from 5x5 matrix and consistency ratio is calculated as 3.0%. It is below 10% and is accepted.

Table 5.6. Pair wise comparison matrix for alternatives for Depth of Penetration

Depth of Penetration	A1	A2	A3	A4	A5	Geometric mean	Local weight
A1	1	3	2	4	4	2.49	0.42
A2	1/3	1	1/3	2	2	0.84	0.14
A3	1/2	3	1	3	3	1.68	0.28
A4	1/4	1/2	1/3	1	1/2	0.46	0.07
A5	1/4	1/2	1/3	2	1	0.44	0.074

C.R.= 0.030, λ_{max} = 5.1348

Now, in Table 5.7. the comparison matrix between alternatives for criterion 2 (Bead Width) is calculated keeping in mind the goal i.e., optimization of weld parameter. Now, maximum Eigen value is λ_{max}= 5.324 is calculated from 5x5 matrix and consistency ratio is calculated as 7.22 %. It is below 10% and is accepted.

Table 5.7. Pair wise comparison matrix for alternatives for Bead Width

Bead Width	A1	A2	A3	A4	A5	Geometric mean	Local weight
A1	1	1/2	3	1/3	4	1.14	0.19
A2	2	1	3	1/2	4	1.64	0.27
A3	1/3	1/3	1	1/3	3	0.64	0.11
A4	3	2	3	1	3	2.22	0.37
A5	1/4	1/4	1/3	1/3	1	0.26	0.04

C.R.= 0.0722, λ_{max}= 5.3236

Now, in Table 5.8. the comparison matrix between alternatives for criterion 3 (Height of Reinforcement) is calculated keeping in mind the goal i.e., optimization of weld parameter. Now maximum Eigen value is λ_{max}= 5.168 is calculated from 5x5 matrix and consistency ratio is calculated as 3.79 %. It is below 10% and is accepted.

Table 5.8. Pair wise comparison matrix for alternatives for Height of Reinforcement

Height of Reinforcement	A1	A2	A3	A4	A5	Geometric mean	Local weight
A1	1	1/2	3	1/3	4	1.14	0.19
A2	2	1	3	1/2	4	1.64	0.27
A3	1/3	1/3	1	1/3	3	0.64	0.11
A4	3	2	3	1	3	2.22	0.37
A5	1/4	1/4	1/3	1/3	1	0.26	0.04

C.R.= 0.0379, λ_{max}= 5.168

In Table 5.9. the local weights for each parameter are considered and global weights are calculated for all individual alternatives. The maximum global weight of for Alternative No. 1 represents the suitable alternative which may be considered as the optimized condition.

Table 5.9. Local and global weights for alternatives and local weights for criteria

Alternative No.	Local Weights			Global Weights
	Depth of penetration	Bead Width	Reinforcement	
	0.62	0.21	0.15	
A1	0.42	0.19	0.32	0.348
A2	0.14	0.27	0.15	0.160
A3	0.28	0.11	0.23	0.231
A4	0.07	0.37	0.23	0.155
A5	0.074	0.04	0.07	0.064

In this work, the analytical hierarchy process is applied to explore favourable depth of penetration maintaining productivity and the related process conditions employing Tungsten Inert Gas welding. Global weight of each alternative is calculated and the highest global weight of 0.348 corresponding to Alternative 1 is evaluated as the optimal condition (shown in Table 5.9).

5.10. Observations Made in Experiment Set 3

In Experiment Set 3, welding trials are conducted using a single activated flux—titanium dioxide (TiO_2) applied as a thin, uniform layer on the faying surface of the specimens prior to welding. The selection of TiO_2 is based on preliminary trial runs involving various flux materials, where TiO_2 is found to produce the most favourable results in terms of bead quality and penetration. The flux layer is expected to intensify arc energy concentration in the weld zone, thereby facilitating deeper penetration and improved joint quality.

This process, referred to as Activated Flux Tungsten Inert Gas (A-TIG) welding is an advanced modification of the conventional TIG process wherein a thin layer of specially formulated flux is uniformly applied to the surface of the base metal prior to welding. Under the influence of high arc temperature, this flux alters the fluid flow dynamics within the weld pool, inducing a reverse Marangoni effect. This phenomenon causes the surface tension gradient to reverse, driving molten metal inward toward the centre of the weld pool rather than outward, thereby increasing depth of penetration. Activated flux not only improves heat concentration at the weld zone but also enhances arc stability, facilitates oxide removal from the weld metal. As a result, it becomes easier to achieve strong, defect-free weld joints with deeper and more consistent penetration.

All other welding conditions in this experiment set are kept consistent with the previous set to enable meaningful comparisons. The welding speed is fixed at 1.22 mm/s, with an arc gap of 2 mm and no root gap. Autogenous butt welding is carried out using a torch angle of 75°, as standardized earlier. Application of TiO_2 is done carefully to ensure uniform flux coverage. The main objective of this experiment is to evaluate whether A-TIG welding can produce full penetration while maintaining good weld strength and appearance.

5.10.1 Visual Inspection

Visual inspection of the A-TIG welded joints shows consistent and smooth bead formation across all specimens, indicating effective weld pool control with the TiO_2 flux. Minimal spatter is there, and no surface defects such as crack, undercut, blowhole, or pinhole are observed in any of the weld runs. This demonstrates that the applied flux and selected parameters maintain a stable arc and provide adequate gas shielding. Table 5.10 presents a summary of the visual observations for each run, confirming that A-TIG process produces welds with high surface integrity and uniformity under the fixed torch angle and travel speed. Top view of the A-TIG welded specimens is illustrated in Figure 5.12.

Table 5.10. Visual observations made in Experiment Set 3

Sl. No.	Gas Flow Rate (L/min)	Heat Input (kJ/mm)	Weld Uniformity	Spatter	Crack	Blowhole-Pinhole	Undercut
21	10	1.264	✓	✓	Nil	Nil	Nil
22	14	1.264	✓	✓	Nil	Nil	Nil
23	10	1.264	✓	✓	Nil	Nil	Nil
24	14	1.264	✓	✓	Nil	Nil	Nil
25	12	1.010	✓	✓	Nil	Nil	Nil

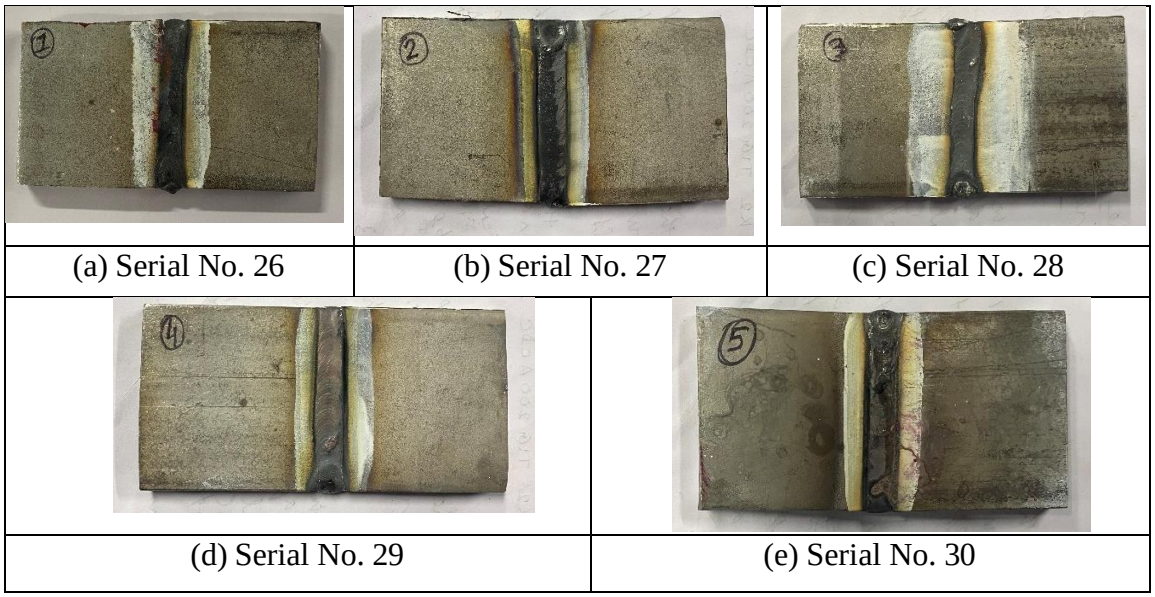

(a) Serial No. 26 (b) Serial No. 27 (c) Serial No. 28

(d) Serial No. 29 (e) Serial No. 30

Figure 5.12. Top view of welded specimens of Experiment Set 3.

5.10.2 Influence of Process Parameters on Bead Geometry

To evaluate how varying process parameters influence the morphology of weld beads, a detailed cross-sectional analysis is performed. Key attributes considered include the total depth of penetration (i.e., the combined penetration from both sides of the weld), average bead width and average reinforcement height, each calculated as the mean of values obtained from both welded sides.

The summarized data in Table 5.11. reveal that specimens welded at gas flow rates of 10 L/min and 14 L/min with a heat input of 1.264 kJ/mm (Serial Nos. 26 to 29) consistently achieved full penetration of 8 mm. However, bead width and reinforcement varies noticeably with changes in gas flow rate. Notably, Serial No. 29 (14 L/min) showed the highest average width of 5.881 mm and zero reinforcement, indicating stable arc behaviour and effective heat transfer at this setting. Conversely, Serial Nos. 26 and 28 (10 L/min) exhibited slightly lower bead widths (5.214 mm and 5.326 mm respectively) along with negative reinforcement, suggesting possible surface underfill. The specimen with intermediate gas flow and lower heat input (Serial No. 30, 12 L/min, 1.010 kJ/mm) failed to achieve full penetration, reaching only 6.640 mm. View of the cross-sections of the weld beads of typical welded specimens of Experiment Set 3 is shown in Figure 5.13.

Table 5.11. Experimental observations made in Experiment Set 3

Sl. No.	**Gas flow rate (L/min)**	**Torch Angle (Degree)**	**Heat input (kJ/mm)**	**Total Penetration (mm)**	**Avg. Width (mm)**	**Avg. Reinforcement (mm)**
26	10	75	1.264	8.000	5.214	-0.14
27	14	75	1.264	8.000	5.642	0.00
28	10	75	1.264	8.000	5.326	-0.11
29	14	75	1.264	8.000	5.881	0.00
30	12	75	1.010	6.640	6.314	0.00

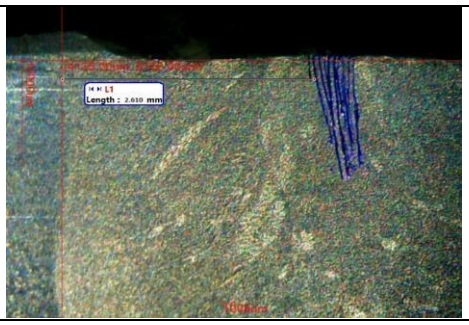

View of weld bead of Serial No. 26 - Left side

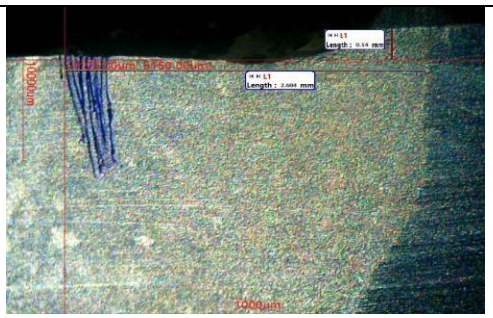

View of weld bead of Serial No. 26 - Right side

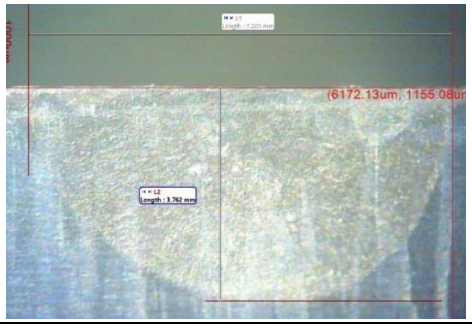

View of weld bead of Serial No. 30

View of weld bead of Serial No. 29

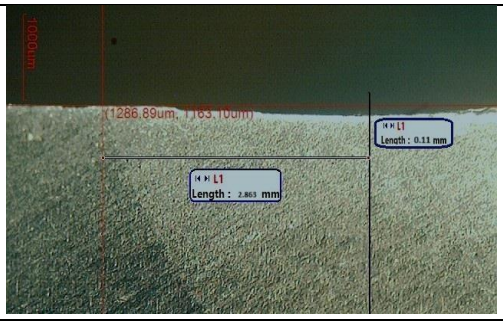

View of weld bead of Serial No. 28 - Left side

View of weld bead of Serial No. 28 - Right side

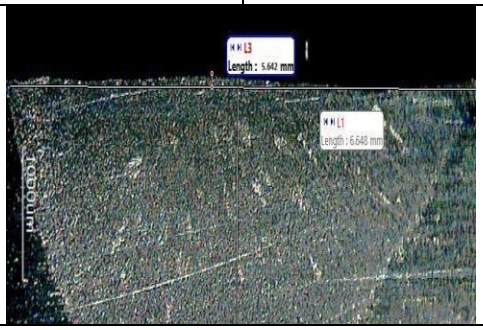

View of weld bead of Serial No. 27

Figure 5.13. View of weld bead geometry typical weld beads of Experiment Set 3

5.10.3. Inference Made from Experiment Set 3

Experiment results of Set 3, conducted using A-TIG welding, clearly demonstrate full penetration (8 mm) in most of the runs, confirming the significant improvement in weld depth over conventional TIG processes. Across Serial Nos. 26 to 30, uniform weld bead formation is observed with minimal surface defects, indicating stable arc characteristics and

efficient heat utilization. Notably, samples with higher gas flow rates and torch angles (e.g., Serial Nos. 27 and 29) exhibit broader bead width and neutral reinforcement profiles, which suggest a more controlled melt pool and effective shielding. Figure 5.6 illustrates the typical weld bead profiles for this set, supporting the conclusion that autogenous A-TIG welding process significantly enhances bead geometry and penetration as compared to Autogenous common TIG welding.

5.11. Observations Made in Tensile Test for Experiment Set 3

In the third set of experiments, the same optimized input parameters derived from the AHP global matrix are retained; however, a TiO_2 based activated flux is applied to the specimen surfaces prior to welding, aiming to enhance penetration through the A-TIG welding process. This modified setup, executed from Serial No. 26 to 30, led to a significant improvement in tensile strength compared to the autogenous welds. As summarized in Table 8.3 and depicted in the corresponding line graph shown in Figure 5.14., tensile strength values ranged between 602.08 MPa and 656.86 MPa, with the highest value observed in Serial No. 28. The graph of Tensile Stress vs Elongation of Specimen 28 and the specimen after test is shown in Figure 5.15. Notably, the ultimate tensile strength (UTS) in all five cases exceeded that of the base material, which is approximately 582 MPa—a promising indication of the effectiveness of this approach. The noticeable enhancement in mechanical performance is primarily attributed to the deeper penetration and improved weld pool dynamics caused by the reverse Marangoni effect induced by the flux.

Table 5.12. Tensile Strength Results of Welded Joints for Experimental Set 3

Serial No.	**Tensile Strength (MPa)**
26	648.64
27	628.94
28	656.86
29	636.41
30	602.083

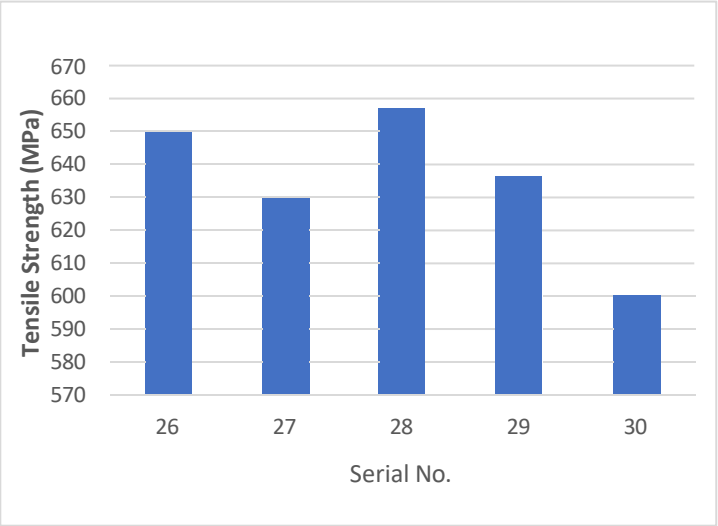

Figure 5.14. Variations in Tensile strength found in A-TIG (Both sides) welding of SS 304H specimens

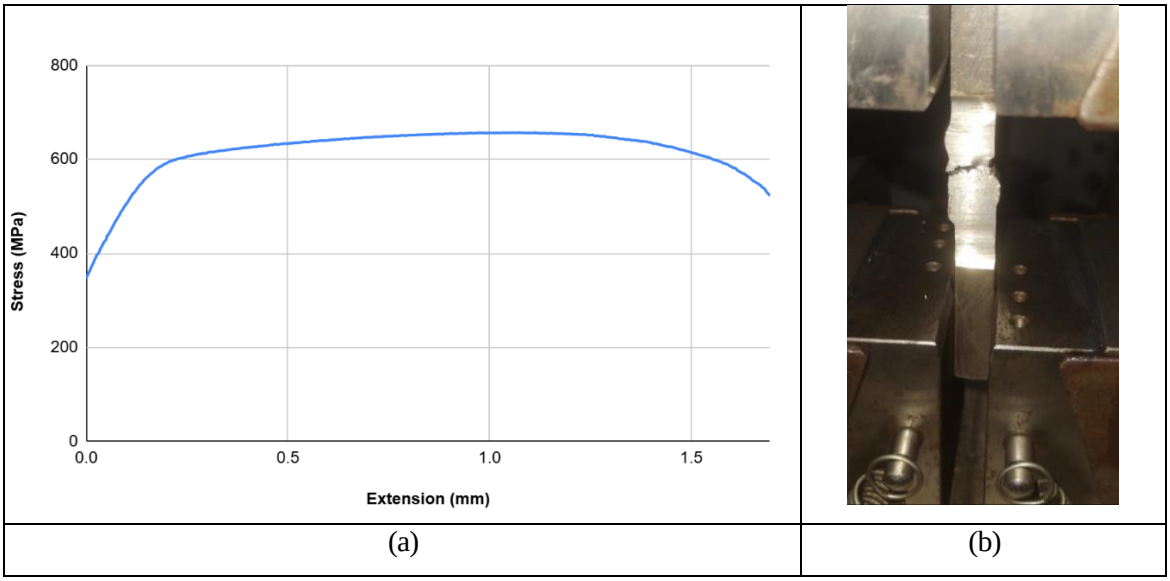

(a) (b)

Figure 5.15. The maximum Tensile strength achieved of Specimen of Serial No. 28 of Experiment Set 3 (656.86 MPa), (b) Test specimen after test

5.12. Observations Made in Rockwell Hardness Test for Experiment Set 3

For Experimental Set 3, where a TiO_2 activated-flux layer is introduced (A-TIG), hardness values show a clear upward shift, ranging from 32.33 HRC to 36.33 HRC as detailed in Table 5.13. The highest average hardness, 36.33 HRC (Sample 27), reflects the pronounced grain refinement and solid-solution strengthening typically associated with flux-assisted

deeper penetration and accelerated cooling. Even the lowest reading in this set, 32.33 HRC (Sample 30), exceeds the maximum recorded in Set 2, underscoring the beneficial influence of activated flux on weld-zone hardening. Figure 5.16 illustrates the corresponding hardness trend for the A-TIG welds in Set 3. Overall, these results show that using the TiO_2 flux in A-TIG welding makes the welds noticeably harder than those produced by standard autogenous TIG welding.

Table 5.13. Rockwell Hardness (HRC) Test Results for A-TIG welded Joints of Experimental Set 3

Sl. No.	HRC1	HRC2	HRC3	Avg HRC
26	34	35	34	34.33
27	36	37	36	36.33
28	35	36	36	35.67
29	36	34	32	34
30	32	31	34	32.33

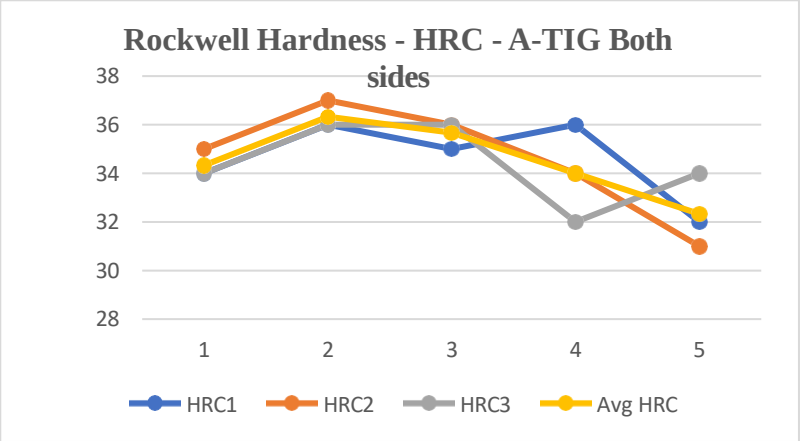

Figure 5.16. Variations in hardness values of weld zone found for the A-TIG welded (Both sides) specimens of Experimental Set 3

5.13. Observations Made in Microhardness Test for Experiment Set 3

In Experimental Set 3, hardness testing is carried out on typical specimens drawn from four different Serial Nos. (Runs 27, 29, 30 and 28). Vickers microhardness was recorded at positions from –10 mm (left-side base metal) to +10 mm (right-side base metal) with respect to the weld centre, thus capturing both sides of the A-TIG weld bead. The resulting hardness values vary across the weldment and, as expected, reach their maximum in the vicinity of the heat-affected zone (HAZ). This pattern shows the combined influence of heat input,

influence of activated-flux and subsequent rate of cooling on the evolving microstructure. The complete set of Vickers microhardness readings for every measurement location is compiled in Table 5.14. The corresponding hardness profile for these A-TIG welded specimens is depicted in Figure 5.17.

Table 5.14. Vickers microhardness values of some typical welded specimens of Set 3 at various locations from weld centre

Distance from Weld Centre (mm)	**Serial No. 27 (A-TIG)**	**Serial No. 29 (A-TIG)**	**Serial No. 30 (A-TIG)**	**Serial No. 28 (A-TIG)**
-10	289	273	264	281
-8	342	322	312	322
-6	323	342	324	316
-4	351	367	356	341
-2	348	364	346	322
0 (Weld Center)	378	340	338	348
+2	368	357	356	340
+4	342	311	298	352
+6	348	324	321	312
+8	322	298	267	322
+10	306	284	278	287

Figure 5.17. Hardness distribution for some typical A-TIG welded (both sides) specimens

5.14. Observations Made in Microstructure Analysis for Experiment Set 3

In Experiment Set 3, specimens from Serial No. 28 (656.86 MPa) and Serial No. 26 (648.64 MPa), the two highest-strength welds in the set are selected for detailed microstructural examination. Optical micrographs are captured at 50x, 100x, and 200x magnifications, encompassing the base metal, heat-affected zone (HAZ) and weld metal. Both high-strength samples display a noticeably refined grain structure within the weld zone, a feature attributed to the favourable heat input and controlled cooling achieved during A-TIG welding. This grain refinement correlates with their superior tensile performance, indicating sound metallurgical bonding and minimized weld defects. Representative microstructures of these high-strength specimens from Experimental Set 3 are presented in Figure 5.18.

		
a) Serial No. 26 - 50x	b) Serial No. 26 - 100x	c) Serial No. 26 - 200x

		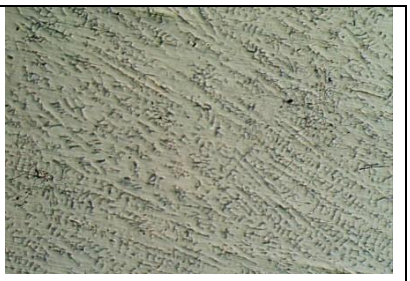
d) Serial No. 28 - 50x	e) Serial No. 28 - 100x	f) Serial No. 28 - 200x

Figure 5.18. Microstructures of typical specimens of Experimental Set 3 having higher tensile strength seen under optical microscope.

5.15. Observations Made in Scanning Electron Microscopy

The SEM images of the A-TIG welded specimens of Experimental Set 3 reveal a relatively smooth and refined surface morphology. The microstructure appears more uniform, with improved grain alignment and reduced irregularities, suggesting enhanced weld quality. The presence of well-defined features and orderly patterns across the surface indicates better thermal control and stable arc characteristics during welding. Overall, the surface shows signs of effective fusion and metallurgical bonding, which are desirable traits for improved mechanical performance and surface integrity of the welded zone. Figure 5.19. represents micrographs of typical specimens of Experimental Set 3 having higher tensile strength seen under Scanning Electron Microscope (SEM).

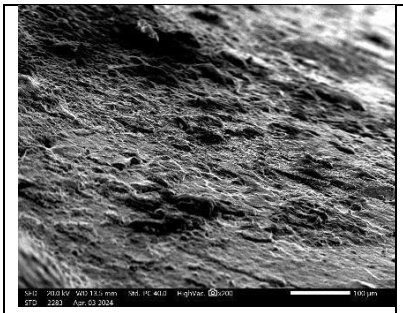	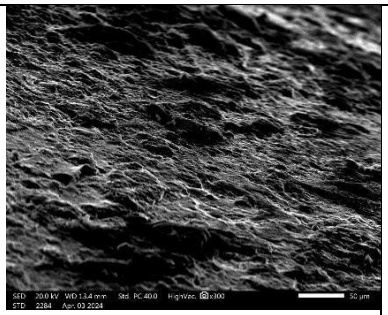	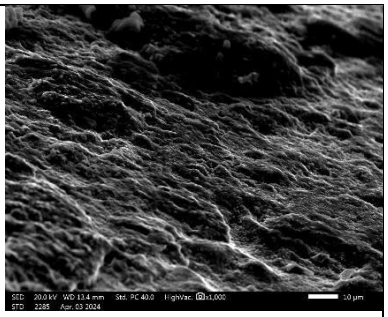
a) Serial No. 26 – 200x	b) Serial No. 26 – 500x	c) Serial No. 26 – 1000x

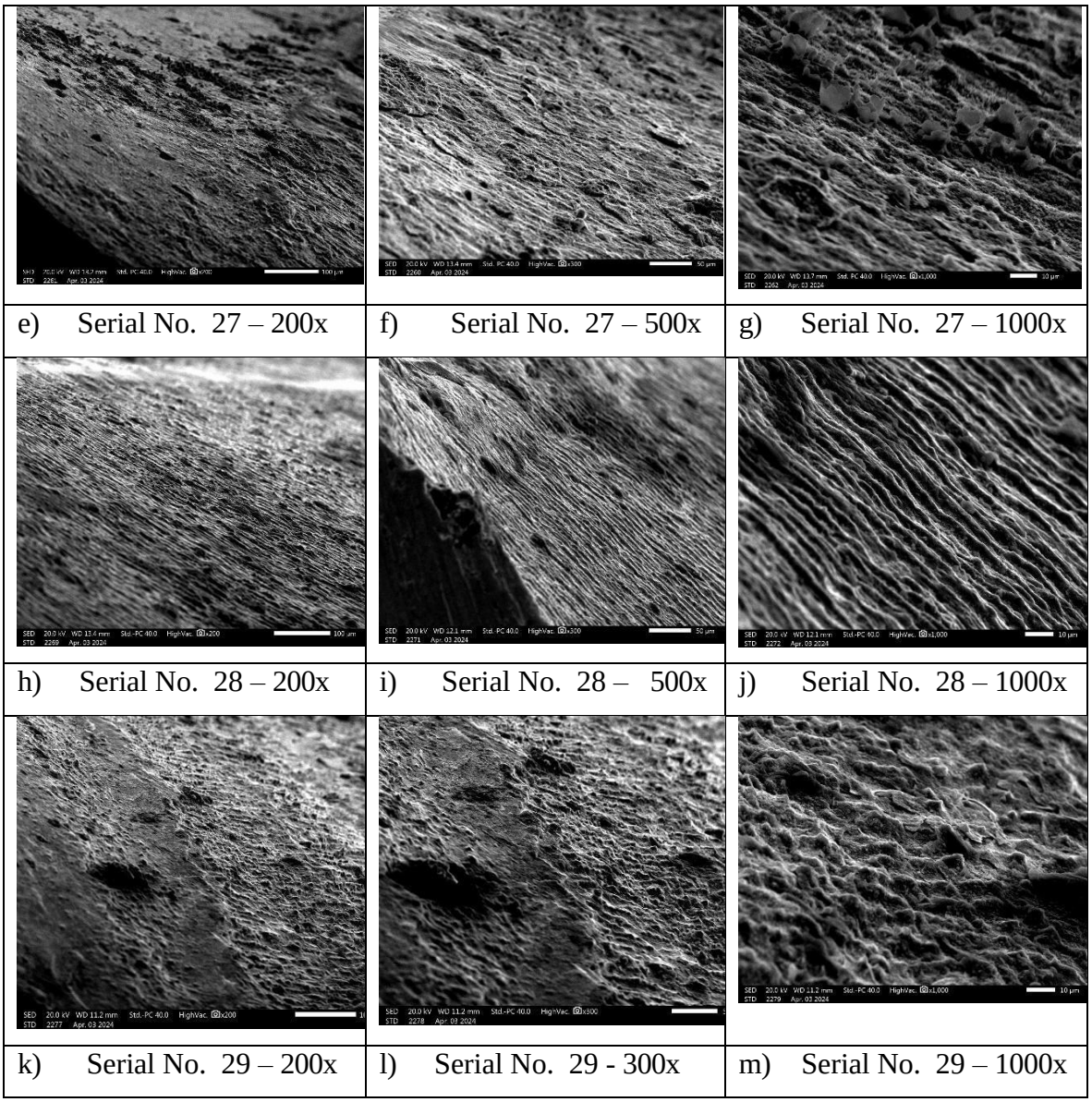

e) Serial No. 27 – 200x	f) Serial No. 27 – 500x	g) Serial No. 27 – 1000x
h) Serial No. 28 – 200x	i) Serial No. 28 – 500x	j) Serial No. 28 – 1000x
k) Serial No. 29 – 200x	l) Serial No. 29 - 300x	m) Serial No. 29 – 1000x

Figure 5.19. Microstructures of typical specimens of Experimental Set 3 having higher tensile strength seen under Scanning Electron Microscope (SEM).

5.16 Outcomes of the Analytical Hierarchy Process applied to the results of Experiment Set 3

The pairwise comparison matrix for criteria for this Experiment Set 3 is identical to that Experiment Set 1 and it is shown in Table 4.6 of Chapter 4. Serial numbers of the specimens 26 to 30 are represented as Alternatives 1 to 5 taken in the same order for Experiment Set 3. Now, in Table 5.15. the comparison matrix between alternatives for criterion 1 (Depth of penetration) is calculated keeping in mind the goal i.e. optimization of weld parameter. Now maximum Eigen value is λ_{max}= 5.13 is calculated from 5x5 matrix and consistency ratio is calculated as 3.0%. It is below 10% and is accepted.

Table 5.15. Pair wise comparison matrix for alternatives for Depth of Penetration

Depth of Penetration	A1	A2	A3	A4	A5	Geometric mean	Local weight
A1	1	1	1	1	4	1.31	0.23
A2	1	1	1	1	4	1.31	0.23
A3	1	1	1	1	4	1.31	0.23
A4	1	1	1	1	4	1.31	0.23
A5	1/4	1/4	1/4	1/4	1	0.32	0.057

C.R.= 0.030, λ_{max}= 5.1348

Now, in Table 5.16. the comparison matrix between alternatives for criterion 2 (Bead Width) is calculated keeping in mind the goal i.e., optimization of weld parameter. Now maximum Eigen value is λ_{max}= 5.288 is calculated from 5x5 matrix and consistency ratio is calculated as 6.4 %. It is below 10% and is accepted.

Table 5.16. Pair wise comparison matrix for alternatives for Bead Width

Bead Width	A1	A2	A3	A4	A5	Geometric mean	Local weight
A1	1	3	2	3	4	2.35	0.38
A2	1/3	1	1/2	3	4	1.14	0.18
A3	1/2	2	1	3	4	1.64	0.26
A4	1/3	1/3	1/3	1	3	0.64	0.1
A5	1/4	1/4	1/4	1/3	1	0.34	0.05

C.R.= 0.064, λ_{max}= 5.288

Now, in Table 5.17. the comparison matrix between alternatives for criterion 3 (Height of Reinforcement) is calculated keeping in mind the goal i.e., optimization of weld parameter. Now maximum Eigen value is λ_{max}= 5.208 is calculated from 5x5 matrix and consistency ratio is calculated as 4.6 %. It is below 10% and is accepted.

Table 5.17. Pair wise comparison matrix for alternatives for Height of Reinforcement

Height of Reinforcement	A1	A2	A3	A4	A5	Geometric mean	Local weight
A1	1	1/3	1/2	1/2	1/2	0.52	0.09
A2	3	1	2	1	1	1.43	0.26
A3	2	1/2	1	1/2	1/2	0.75	0.14
A4	2	1	2	1	1	1.31	0.24
A5	2	1	2	1	1	1.31	0.24

C.R.= 0.046, λ_{max}= 5.208

In Table 5.18. the local weights for each parameter are considered and global weights are calculated for all individual alternatives. The maximum global weight of for Alternative No. 1 represents the suitable alternative which may be considered as the optimized condition.

Table 5.18. Local and global weights for alternatives and local weights for criteria

Alternative No.	Local Weights			Global Weights
	Depth of penetration	Bead Width	Reinforcement	
	0.62	0.21	0.15	
A1	0.23	0.38	0.09	0.236
A2	0.23	0.18	0.26	0.220
A3	0.23	0.26	0.14	0.218
A4	0.23	0.10	0.24	0.199
A5	0.06	0.05	0.24	0.083

In this work, the Analytical Hierarchy Process is applied to explore favourable depth of penetration maintaining productivity and the related process conditions employing Activated Tungsten Inert Gas (A-TIG) welding. Global weight of each alternative is calculated and the highest global weight of 0.348 corresponding to Alternative 1 is evaluated as the optimal condition (shown in Table 5.18).

5.17. Summary of Experimental Set 2 and Set 3

Experimental Set 2 and Set 3 are conducted to evaluate and compare characteristics of bead geometry in particular, and weld penetration, under autogenous TIG and Activated TIG (A-TIG) welding processes, respectively.

In Experiment Set 2, autogenous TIG welding is performed on both sides of 8 mm thick SS304H specimens. The process resulted in smooth and uniform bead formation with

negligible defects such as crack, undercut, blowhole and pinhole. However, depth of penetration remains below full joint penetration levels, with a maximum penetration of 6.53 mm (Serial No. 21). Although the weld quality is acceptable, results indicate that conventional autogenous TIG welding is insufficient to achieve full depth of penetration for the selected material and thickness. Average bead width and height of reinforcement vary slightly across runs, suggesting relatively stable but limited fusion. In contrast, Experiment Set 3 utilizes Activated TIG (A-TIG) welding technique, where TiO_2 is used as the activating flux. This approach demonstrates a significant improvement in penetration and bead morphology. Most runs in this set, particularly Serial Nos. 26 through 29, achieve full penetration (8.0 mm), indicating superior heat concentration and arc efficiency facilitated by the use of flux. Bead formation is uniform and largely free of surface defects. Additionally, increased gas flow rates and optimized torch angles contribute to broader weld beads and stable reinforcement profiles. For instance, Serial Nos. 27 and 29, which use a gas flow rate of 14 L/min and a torch angle of 75°, yield balanced welds. The success of these parameters underlines the effectiveness of A-TIG process in achieving deep and defect-free welds in thicker stainless-steel sections.

The Tensile test results from Experiment Sets 2 and 3 reveal the impact of process modifications on weld strength. In Set 2, double-sided autogenous TIG welding using AHP-optimized parameters yielded tensile strengths ranging from 416.83 MPa to 481.73 MPa, highlighting how small variations in parameters still affect mechanical performance. In contrast, Set 3, which incorporated TiO_2-based activated flux for A-TIG welding, demonstrated a clear improvement in tensile strength, with values between 602.08 MPa and 656.86 MPa—surpassing even the base material strength of 582 MPa. This enhancement is primarily due to improved weld pool behaviour and deeper penetration enabled by the flux-induced reverse Marangoni effect.

In Experiment Set 2, autogenous TIG welds show Rockwell hardness between 28.00–31.67 HRC, with variations attributed to heat input and cooling rates. Vickers microhardness peaks near the HAZ, reflecting typical thermal effects during welding. In Set 3, A-TIG welds with TiO_2 flux exhibit higher hardness, ranging from 32.33–36.33 HRC. Vickers microhardness in this set also consistently records elevated values across the weld zone, especially near the HAZ, indicating enhanced grain refinement and accelerated cooling. Overall, the addition of flux in A-TIG welding significantly improves both Rockwell and Vickers hardness compared to autogenous TIG.

Microstructural analysis of the highest-strength welds from Experiment Sets 2 and 3 includes optical micrographs at 50x, 100x and 200x magnifications, which show refined grain structures across the base metal, HAZ, weld metal — suggesting effective heat input, and controlled cooling. SEM images further reveal uniform dendritic patterns, smooth surface morphology, improved grain alignment and minimal defects like cracks or voids, all confirming strong metallurgical bonding and stable weld formation.

Overall, a comparative analysis of these two sets confirms that autogenous A-TIG welding with TiO_2 flux is more effective than conventional autogenous TIG welding in enhancing bead geometry and achieving full penetration for 8 mm SS304H specimens.

CHAPTER 6

Results and Discussion on Experiment Set 4

6.1. Introduction

This chapter presents the 4th and final set of welding experiments conducted using filler-assisted TIG welding on SS 304H stainless steel specimens. While some parameters, such as torch angle and welding speed are kept constant based on earlier trials, others like weld current, gas flow rate and root gap are varied across three levels to study their effects. The setup includes a cold wire feeder to ensure a consistent supply of filler metal. Each welding trial is carried out under a unique combination of parameters according to a standardised Design of Experimentation. The chapter also presents visual inspection findings, bead geometry analysis and overall interpretation of weld quality based on the experimental observations. Post-welding evaluations such as tensile test and hardness test are conducted and thoroughly analyzed. Additionally, microhardness tests are also performed on best performing specimens. MCDM tool such as the AHP is used also used to optimize the output parameters.

6.2. Details of Setup and Conditions of Experiment Set 4

Experiment set 4 involves performing filler-assisted TIG welding on 304H grade austenitic stainless-steel plates using a KEMPPI K2 TIG 200 AC/DC machine shown in Figure 3.5 (a–c)). To facilitate controlled addition of filler material, a Mogra CWF 04 Cold Wire Feeder is employed as shown in Figure 3.5 (c), supplying 1.2 mm diameter 304H filler wire at a constant feed rate of 20 mm/s, determined through preliminary trials. During welding, the torch is positioned at a 75° angle, with an arc gap of 5 mm maintained throughout. A welding speed of 1.22 mm/s is fixed across all trials. Prior to the final runs, several test welds are performed to determine suitable current and voltage combinations. The main process variables investigated in this set are current (130 A, 140 A, and 150 A), root gap (1.2 mm, 1.6 mm, and 2 mm), and argon gas flow rate (10, 12, and 14 L/min). To systematically plan experimental runs and analyse the influence of variables, Design of Experiments using Central Composite Design (CCD) approach of Response Surface Methodology (RSM) is considered. Three critical process parameters are selected for investigation: heat input, gas flow rate, and root gap. Each of these factors is varied across three levels to assess their individual and combined effects on the welding outcome. Total

20 weld runs are performed. The filler wire is deposited in non-autogenous butt joint configurations using a 3.2 mm thoriated tungsten electrode. After welding, the plates are allowed to cool in ambient air.

The heat input, a key parameter governing thermal behaviour and fusion characteristics, is set at 1.337, 1.458 and 1.520 kJ/mm. These values are derived from the heat input calculation formula (Equation 3.1), based on actual welding parameters such as weld voltage, weld current and torch travel speed. This experiment is designed to explore the interrelationship between the selected parameters and to determine the most effective combination for achieving complete penetration and enhanced weld bead properties using filler material in TIG welding.

Table 6.1. Process Parameters and Their Levels for CCD Experimentation in Set 4

Parameter	Low Level (-1)	Medium Level (0)	High Level (+1)
Gas Flow Rate (L/min)	10	12	14
Root Gap (mm)	1.2	1.6	2.0
Heat Input (kJ/mm)	1.337	1.458	1.520

6.3. Observations Made in Experiment Set 4

The results from the fourth and final set of welding experiments are thoroughly analyzed to assess the impact of the selected parameters—heat input, gas flow rate, and root gap—on the weld quality of SS 304H plates when filler material is used. Weld joints are inspected primarily for surface condition, continuity, and evidence of any visible defects. The objective is to determine the influence of varying parameters on achieving full penetration, sound weld bead formation, and consistent weld integrity.

6.3.1. Visual Inspection

Visual inspection is conducted to identify any welding defects that may compromise mechanical properties. The primary focus is on detecting spatter formation, lack of weld uniformity, cracks, blowholes or pinholes, and undercuts. The presence or absence of these flaws is documented for all 20 weldments. Figure 6.1 represents top view of typical welded

specimens of Experiment Set 4. The consistent application of filler material and control of process parameters help maintain the integrity of the welds across different trials. Table 6.2 presents the visual inspection results.

Table 6.2. Outcome of the visual inspection of Experimental Set 4

Sl. No.	Gas Flow Rate (L/min)	Root Gap (mm)	Heat Input (kJ/mm)	Spatter	Weld Uniformity	Crack	Blowhole-Pinhole	Undercut
31	10	1.2	1.337	✓	✓	Nil	Nil	Nil
32	12	1.2	1.458	✓	✓	Nil	Nil	Nil
33	14	1.2	1.520	✓	✓	Nil	Nil	Nil
34	10	1.6	1.458	✓	✓	Nil	Nil	Nil
35	12	1.6	1.337	✓	✓	Nil	Nil	Nil
36	14	1.6	1.458	✓	✓	Nil	Nil	Nil
37	10	2.0	1.520	✓	✓	Nil	Nil	Nil
38	12	2.0	1.458	✓	✓	Nil	Nil	Nil
39	14	2.0	1.337	✓	✓	Nil	Nil	Nil
40	12	1.6	1.520	✓	✓	Nil	Nil	Nil
41	12	1.6	1.458	✓	✓	Nil	Nil	Nil
42	12	1.6	1.458	✓	✓	Nil	Nil	Nil
43	12	1.6	1.458	✓	✓	Nil	Nil	Nil
44	12	1.6	1.458	✓	✓	Nil	Nil	Nil
45	12	1.6	1.458	✓	✓	Nil	Nil	Nil
46	12	1.6	1.458	✓	✓	Nil	Nil	Nil
47	12	1.6	1.458	✓	✓	Nil	Nil	Nil
48	12	1.6	1.458	✓	✓	Nil	Nil	Nil
49	12	1.6	1.458	✓	✓	Nil	Nil	Nil
50	12	1.6	1.458	✓	✓	Nil	Nil	Nil

It is found by visual inspection that all the twenty welded specimens are uniformly welded with visible small spatter on the surface. None of the specimens exhibit visible welding defects such as cracks, undercut, blowholes, or pinholes. The overall bead appearance across all samples is smooth and continuous, suggesting that the arc during the welding process is stable and well-controlled. The consistency in surface finish further indicates good weld integrity and appropriate selection of parameters for achieving defect-free welds.

				
Serial No. 33	Serial No. 36	Serial No. 37	Serial No. 38	Serial No. 44

Figure 6.1. Top view of typical welded specimens of Experimental Set 4

6.3.2. Influence of Process Parameters on Bead Geometry

The bead geometry parameters such as Depth of Penetration, Bead Width and Height of Reinforcement are evaluated for all twenty specimens. These parameters provide important insight into weld quality and structural integrity. It is observed that most of the specimens achieve full penetration when welding is performed on both sides, indicating proper fusion and depth of weld metal. Minor variations in bead width and reinforcement are noted, reflecting the influence of parameter combinations on the surface morphology of the weld. Detailed measurements for bead geometry corresponding to each experimental condition are presented in Table 6.3. Images of bead geometry of few typical welded specimens of Experiment Set 4 are shown in Figure 6.2.

Table 6.3. Bead Geometry Measurements in Experiment Set 4

Sl No.	Gas flow rate (L/min)	Root Gap (mm)	Heat input (kJ/mm)	Depth of Penetration (mm)	Bead Width (mm)	Height of Reinforcement (mm)
31	10	1.2	1.337	2.825	8.105	1.61
32	14	1.2	1.337	4.63	8.61	1.18
33	10	2	1.337	8	8.295	1.14
34	14	2	1.337	8	7.755	2.455
35	10	1.2	1.52	8	8.99	1.315
36	14	1.2	1.52	8	9.65	0.665
37	10	2	1.52	8	9.705	0.51
38	14	2	1.52	8	9.135	0.485
39	10	1.6	1.458	8	8.32	1.16
40	14	1.6	1.458	8	7.564	0.621
41	12	1.2	1.458	3.34	9.632	0.34
42	12	2	1.458	8	9.224	0.56
43	12	1.6	1.337	8	8.19	1.045
44	12	1.6	1.52	8	8.615	-0.665
45	12	1.6	1.458	2.73	11.86	0.69
46	12	1.6	1.458	2.98	11.805	0.38
47	12	1.6	1.458	3.25	12.615	0.825
48	12	1.6	1.458	8	9.63	1.59
49	12	1.6	1.458	3.42	11.64	0.14
50	12	1.6	1.458	8	8.89	0.442

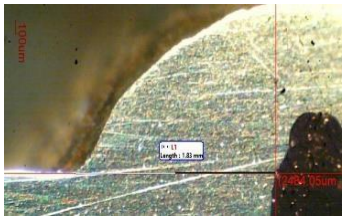		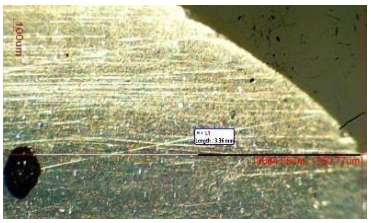
(a) Serial No. 33	(b) Serial No. 33	(c) Serial No. 33
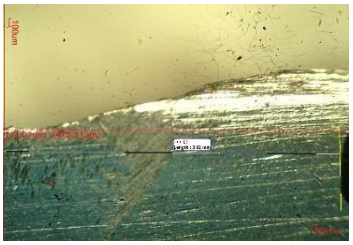		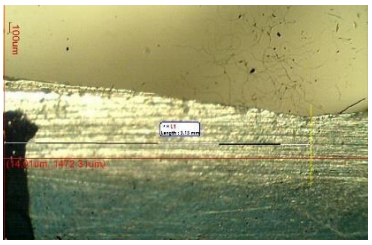
(a) Serial No. 36	(b) Serial No. 36	(c) Serial No. 36
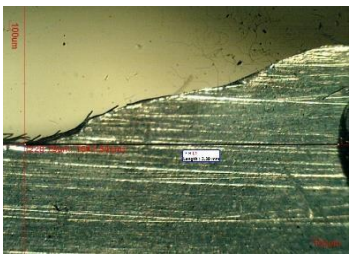	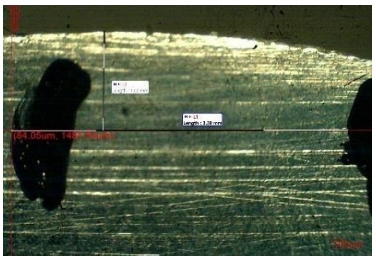	
(a) Serial No. 37	(b) Serial No. 37	(c) Serial No. 37
	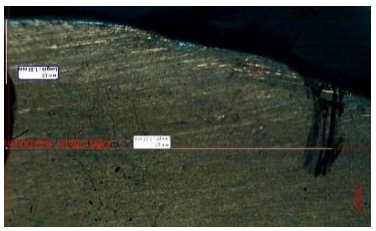	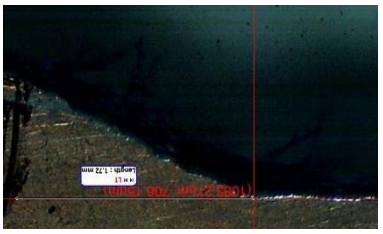
(a) Serial No. 39	(b) Serial No. 39	(c) Serial No. 39
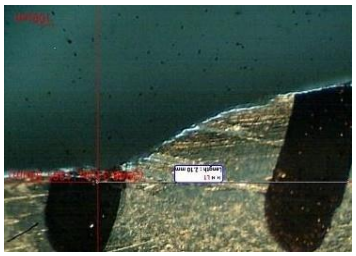		
(a) Serial No. 44	(b) Serial No. 44	(c) Serial No. 44

Figure 6.2. Images of Bead geometry of few typical specimens of Experiment Set 4

6.3.3. Analysis of Bead Geometry parameters

In a contour plot or a surface plot, variation of a bead geometry parameter (such as P, R or W) is represented against the change of two factors keeping the third factor to a fixed value, commonly known as a hold value. Therefore, there would be three hold values for the 3rd factor corresponding to a low value (coded as '-1'), middle value (coded as '0') and high value (coded as +1). After observing the nature of contour or surface plots against two factors at three hold values of the 3rd factor, maximum variations of respective bead parameters are tried to detect. Corresponding hold value is noted and those contour and surface plots are included in this discussion. All the contour and surface plots are meant to represent variation of a bead geometry parameter with change in two independent variables keeping the third variable constant at its highest level (i.e., with a hold value of positive 1).

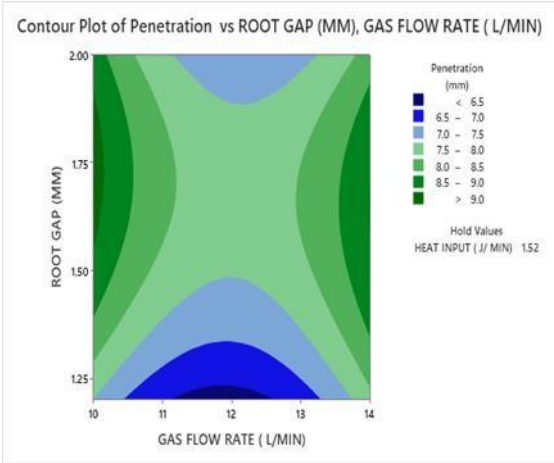

(a)

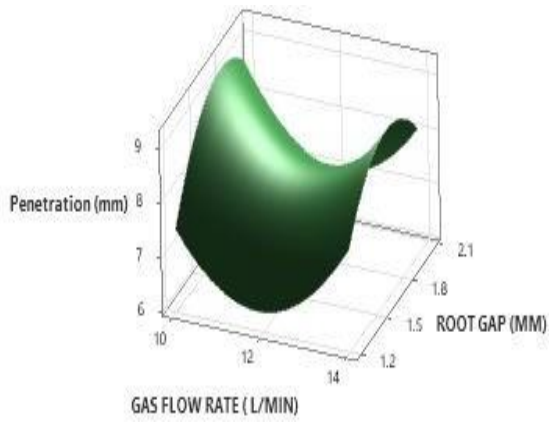

(b)

Figure 6.3. (a) Contour plot and (b) surface plot of penetration with change in root gap and gas flow rate at a hold value of heat input '+ve', i.e., 1.520 kJ/mm.

Penetration shows a dual-peak trend with respect to gas flow rate, as observed in Figure 6.3 (b). At a constant heat input of 1.520 kJ/mm, maximum penetration occurs at both low (10 L/min) and high (14 L/min) gas flow rates, while a notable dip in penetration is found at the intermediate gas flow rate (~12 L/min). With respect to root gap, penetration generally increases slightly up to a moderate value and then stabilizes. This behaviour suggests that the arc is more stable and the shielding is more effective at very low or very high gas flow rates. In the middle range of gas flow rate, penetration decreases, possibly due to some disturbance or weak shielding caused by turbulence or uneven gas flow.

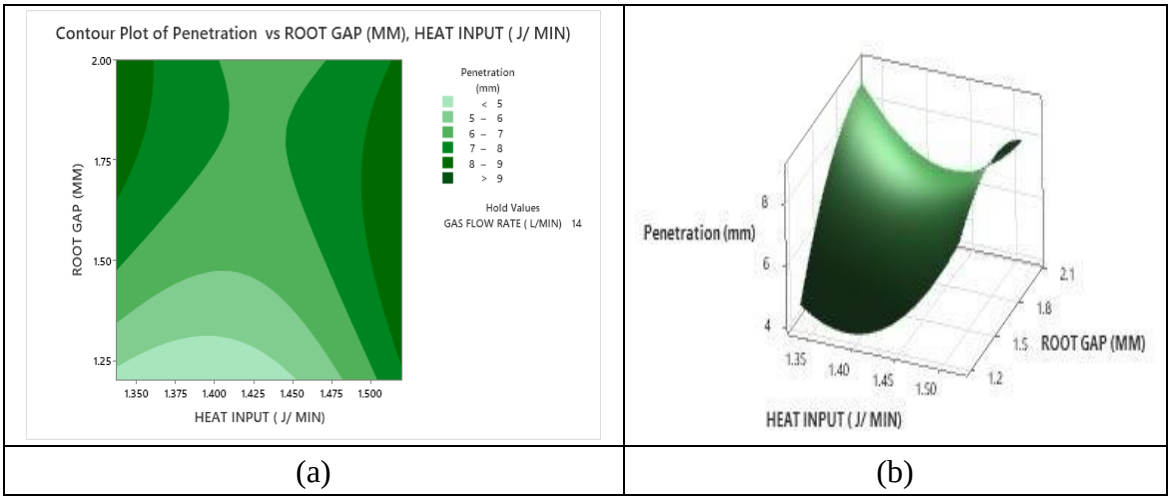

(a) (b)

Figure 6.4. (a) Contour plot and (b) surface plot of penetration with change in root gap and heat input at a hold value of gas flow rate as '+ve', i.e. 14 L/min.

Figure 6.4 (a, b) shows the variation in weld penetration with change in root gap and heat input at a fixed gas flow rate of 14 L/min ('+ve' hold value). Penetration shows an increasing trend with heat input across all levels of root gap. Penetration is found to be more at higher values of root gap, particularly beyond 1.75 mm, as seen in both the contour and surface plots. However, at lower root gaps, a slight reduction in penetration can be noted at the lower range of heat input. This is likely because higher heat input provides more energy for melting, and a larger root gap allows more molten material to accumulate and fuse effectively.

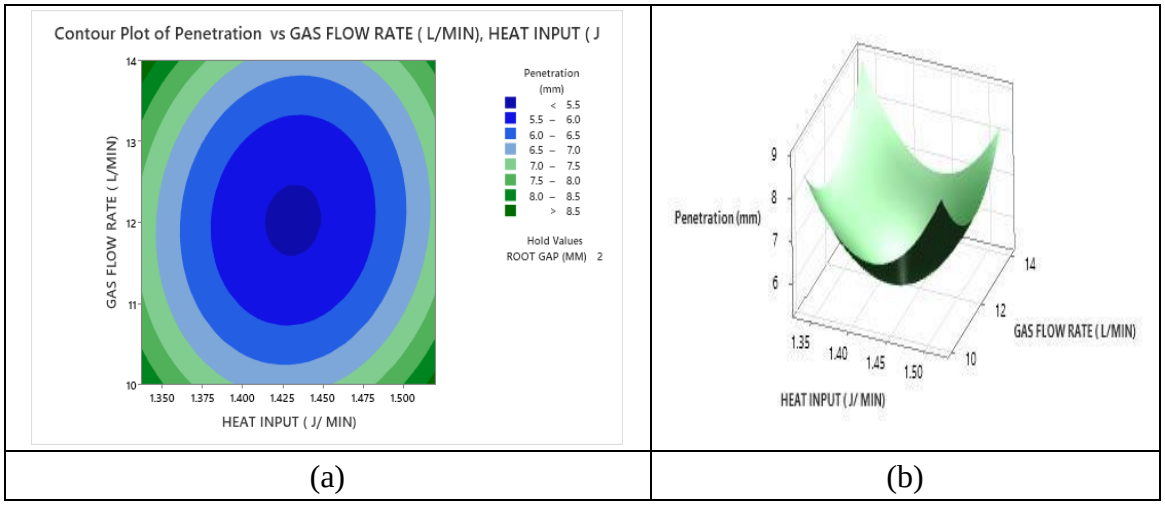

(a) (b)

Figure 6.5. (a) Contour plot and (b) surface plot of penetration with change in gas flow rate and heat input at a hold value of root gap '+ve', i.e. 2 mm.

Figure 6.5 (a, b) illustrates the variation in penetration with changes in gas flow rate and heat input at a fixed root gap of 2 mm ('+ve' hold value). Penetration is observed to be higher at both the lower and higher ends of the heat input range. A similar pattern is noted with gas flow rate, where penetration increases at the lower and higher extremes. However, when both heat input and gas flow rate fall within their mid-range values, the penetration tends to be relatively lower.

From Figures 6.3 through 6.5, it is observed that weld penetration is influenced by complex interactions between gas flow rate, heat input and root gap, with some multiple peak trends seen in gas flow rate, consistent increase with heat input, and enhanced penetration at higher root gaps, indicating that optimal penetration occurring at specific combinations of these parameters rather than at their mid-range values.

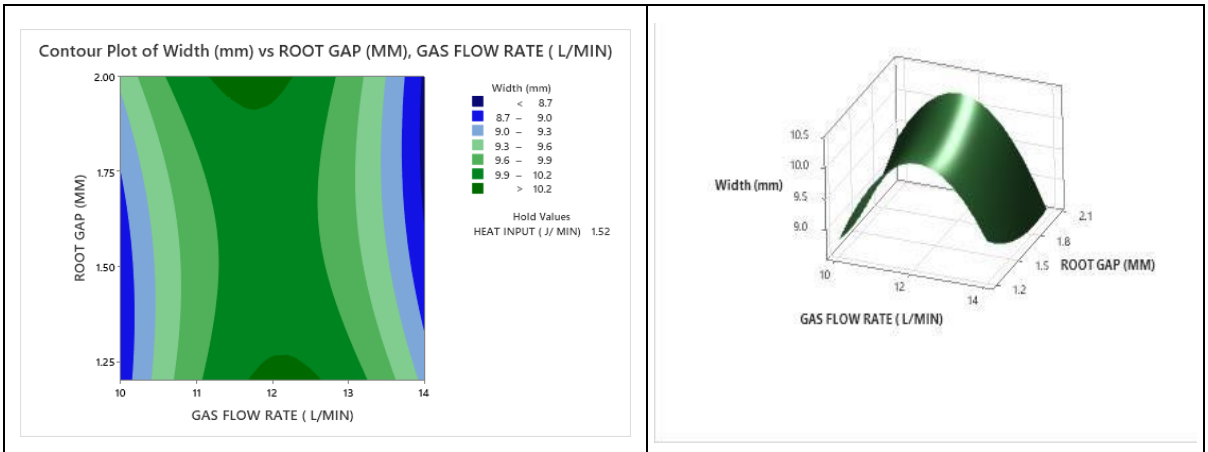

(a) (b)

Figure 6.6. (a) Contour plot and (b) surface plot of bead width with change in in root gap and gas flow rate at a hold value of heat input '+ve', i.e., 1.520 kJ/mm.

Maximum bead width is observed at a root gap between 1.75–2.00 mm and gas flow rate between 11.5–13 L/min as shown in Figure 6.6 (a, b). Bead width is found to be lower at lower gas flow rate of 10 L/min and also lower at higher gas flow rate of 14 L/min. It is found to higher at the midrange of gas flow rate at around 11.5–13 L/min. Bead width is found to increase steadily with root gap, suggesting that a larger gap allows more filler material to spread, resulting in a wider weld bead.

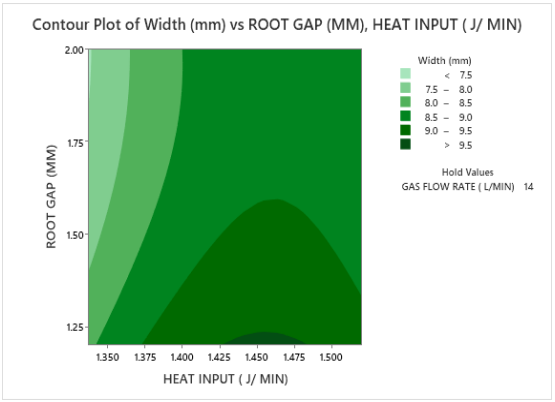

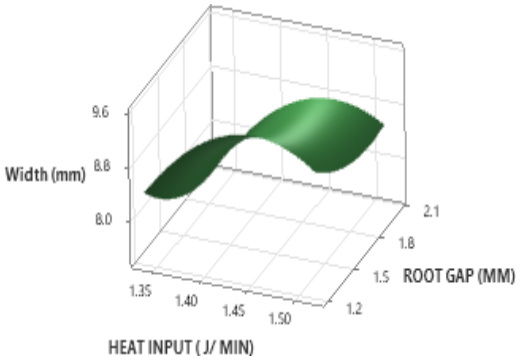

(a) (b)

Figure 6.7. (a) Contour plot and (b) surface plot of bead width with change in root gap and heat input at a hold value of gas flow rate as '+ve', i.e. 14 L/min.

Bead width is found to be significantly higher at a root gap of 1.25–1.50 mm and heat input near 1.48–1.50 kJ/mm, where gas flow rate is held constant at its '+ve' value of 14 L/min, as shown in Figure 6.7 (a, b). Bead width shows a gradual increase with increasing heat input, while the effect of root gap is moderately influential, especially in the lower range (1.25–1.5 mm), beyond which the change is marginal.

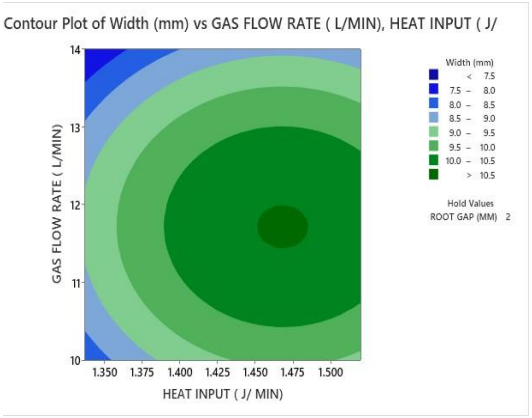

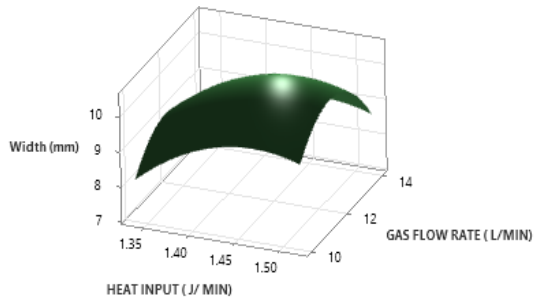

(a) (b)

Figure 6.8. (a) Contour plot and (b) surface plot of bead width with change in gas flow rate and heat input at a hold value of root gap '+ve', i.e. 2 mm.

Bead width increases progressively with rising heat input and reaches its maximum at around 1.48–1.50 kJ/mm, while the root gap is held at its '+ve' value of 2 mm, as depicted in Figure 6.8 (a, b). The effect of gas flow rate on bead width is minimal, with the width reaching its highest point around 12 L/min and staying mostly unchanged beyond that. The surface and contour plots confirm that heat input remains the primary influencing factor for bead width, while gas flow rate contributes subtle variations.

From Figures 6.6 through 6.8, it is observed that bead width is primarily influenced by heat input, showing a consistent increase as heat input rises. Root gap also plays a significant role, especially in the lower range, where bead width increases steadily before stabilizing. Gas flow rate has a smaller but noticeable effect, with bead width being widest at medium values (around 11.5–13 L/min) and becoming narrower at both lower and higher flow rates. Overall, the best bead width is achieved when the root gap is moderate, the gas flow rate is in the middle range, and the heat input is high.

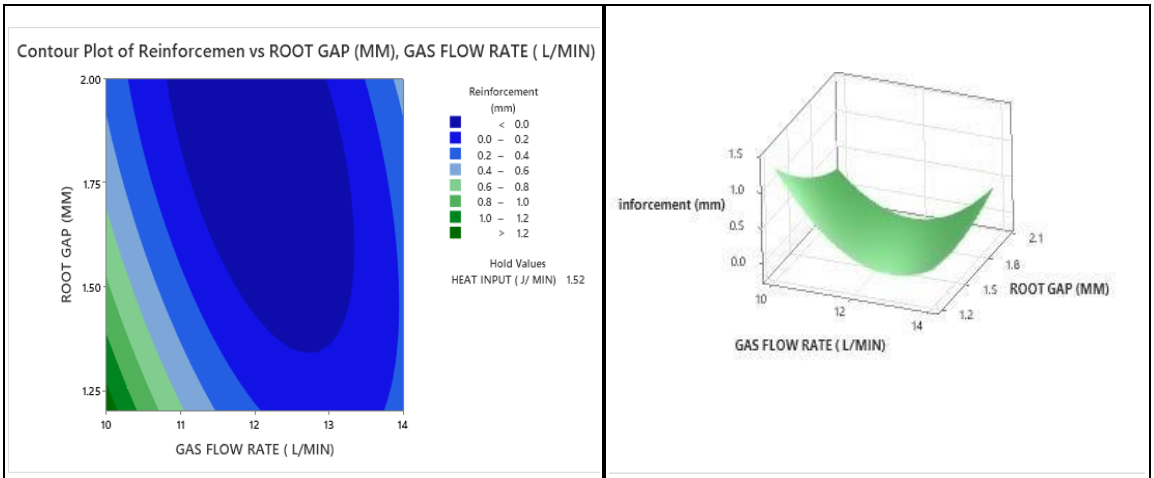

(a) (b)

Figure 6.9. (a) Contour plot and (b) surface plot of reinforcement with change in root gap and gas flow rate at a hold value of heat input '+ve', i.e., 1.520 kJ/mm.

Figure 6.9 (a, b) shows that reinforcement decreases as the root gap increases, while it first increases and then decreases with rising gas flow rate at a constant heat input of 1.520 kJ/mm. This trend suggests that a smaller root gap helps retain more molten material on the weld surface, and moderate gas flow provides stable shielding, whereas excessive gap or high gas flow may cause loss of reinforcement due to overflow or turbulence.

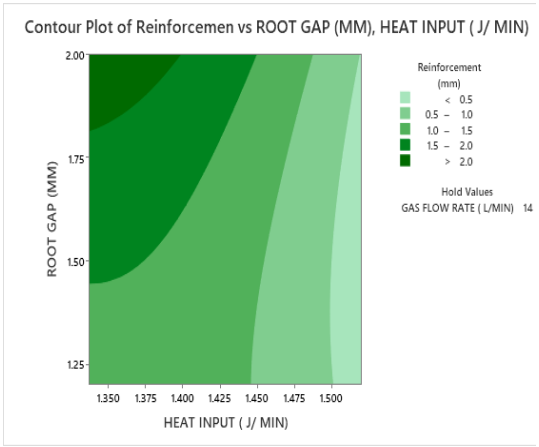

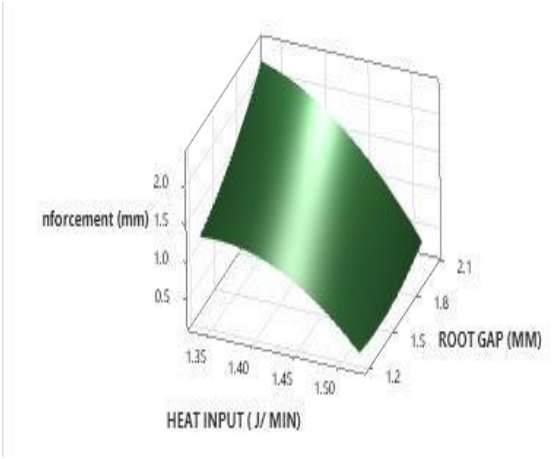

(a) (b)

Figure 6.10. (a) Contour plot and (b) surface plot of reinforcement with change in root gap and heat input at a hold value of gas flow rate as '+ve', i.e. 14 L/min

Reinforcement is found to be maximum at higher root gaps (close to 2 mm) and lower heat input values, as observed in Figure 6.10 (a, b). As heat input increases beyond 1.475 kJ/mm, reinforcement gradually decreases, particularly when combined with wider root gaps. The gas flow rate is held constant at its '+ve' level of 14 L/min in this analysis. The interaction between root gap and heat input shows that reinforcement is more sensitive to changes in root gap than to heat input in this case.

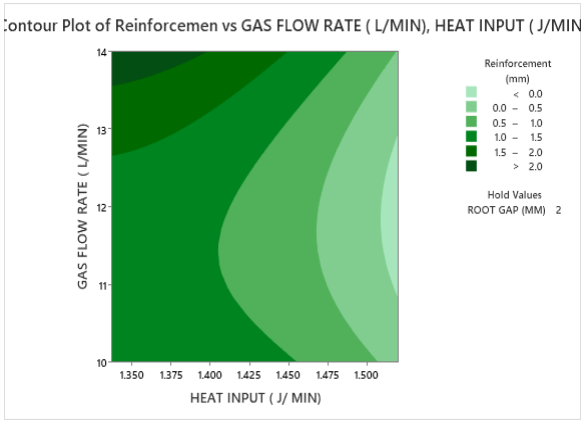

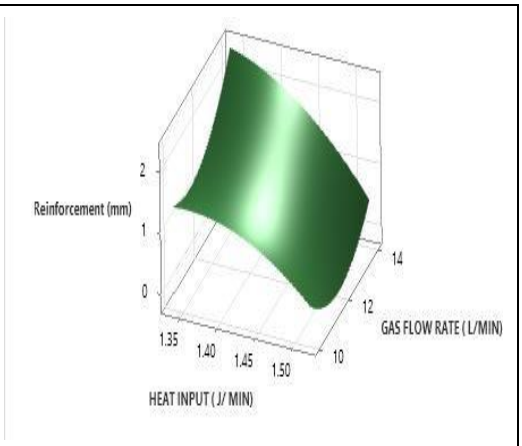

(a) (b)

Figure 6.11. (a) Contour plot and (b) surface plot of reinforcement with change in gas flow rate and heat input at a hold value of root gap '+ve', i.e. 2 mm.

From Figure 6.11 (a,b), it is found that reinforcement shows the highest peak at lower value of heat input at around 1.350 kJ/mm and having maximum gas flow rate of 14 L/min at a constant root gap of 2 mm. With the increase in heat input and lesser value of gas flow rate the reinforcement is found to be lower and minimum at around heat input of 1.520 kJ/mm and and gas flow rate of 10 L/min. This trend may be due to the fact that lower heat input helps retain more molten material on the surface, and higher gas flow provides better shielding, whereas higher heat input and lower gas flow may lead to excessive melting and poor arc stability, reducing reinforcement.

From Figures 6.9, 6.10 and 6.11, it can be concluded that reinforcement is influenced by a combination of root gap, gas flow rate and heat input, with the most favourable reinforcement occurring at lower heat input and higher gas flow rate. Reinforcement generally decreases with increasing root gap and heat input, while gas flow rate shows a non-linear effect—moderate to high values tend to enhance reinforcement, but excessive or insufficient flow can reduce it. Overall, lower heat input helps retain more molten material, and higher gas flow improves shielding, while wider root gaps and excessive heat may lead to reduced reinforcement due to overflow or excessive melting.

6.4. Observations Made in Tensile Test for Experiment Set 4

In the final phase of the study, denoted as Experiment Set 4, filler-assisted TIG welding is conducted on SS 304H grade austenitic stainless-steel plates (50 mm × 50 mm × 8 mm). This experimental set comprised 20 runs (Serial No 31–50), focusing on evaluating the effect of filler addition on weld penetration and bead geometry. The experiments are systematically designed using a Central Composite Design (CCD) under Response Surface Methodology (RSM) to analyze the influence of key process parameters. The tensile strength values, as shown in Table 6.4, ranged from 334.68 MPa to 676.13 MPa. Notably, several welded joints exhibit UTS values exceeding the base material strength of approximately 582 MPa, indicating a significant improvement in mechanical performance. The tensile strength trend is graphically represented in Figure 6.12. Figure 6.13 illustrates the Tensile Stress vs. Elongation graph for Specimen Serial No. 38, which records the highest Ultimate Tensile Stress among the tested samples for Experiment Set 4.

Table 6.4. Tensile Strength Results of Welded Joints for Experiment Set 4

Sl. No.	**Tensile Strength (MPa)**
31	361.34
32	468.69
33	622.243
34	642.536
35	656.172
36	634.562
37	664.239
38	676.126
39	616.362
40	621.643
41	416.631
42	616.263
43	618.472
44	671.473
45	334.682
46	346.732
47	364.862
48	628.02
49	386.793
50	621.462

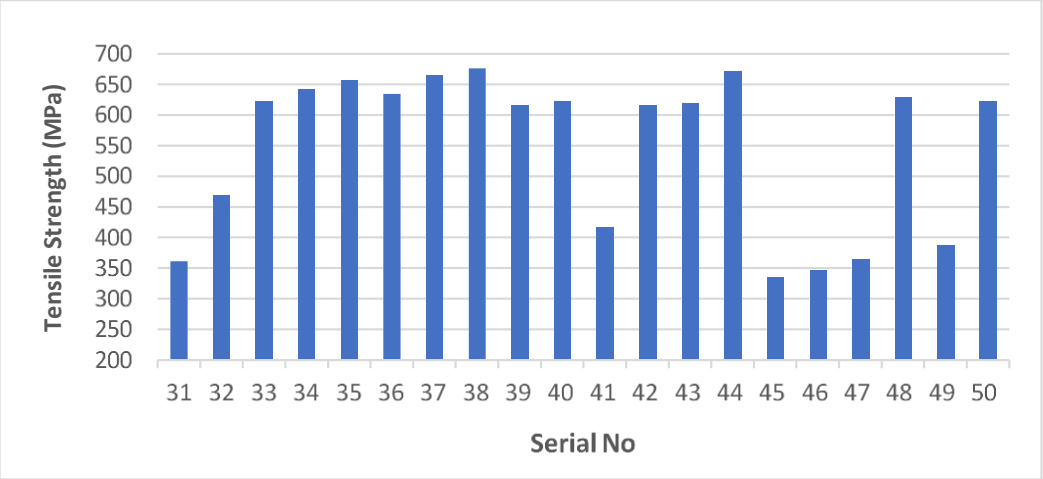

Figure 6.12. Variations in Tensile strength found in Filler assisted TIG welding of SS 304H specimens

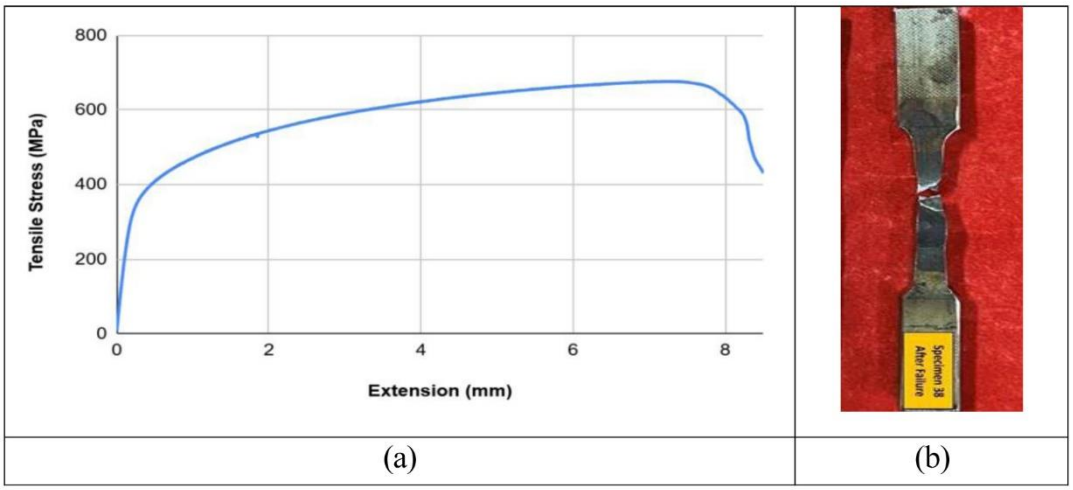

Figure 6.13. (a) The maximum Tensile strength achieved of Specimen Serial No 38 of Experiment Set 4 (676.126 MPa), (b) Test specimen after test

6.5. Observations Made in Rockwell Hardness Test for Experiment Set 4

In Experimental Set 4, which involve filler-assisted TIG welding, the Rockwell hardness (HRC) values show notable variation across the 20 welded samples. As seen in Table 6.5, the average hardness values ranged from a low of 25.33 HRC (Samples 40 and 43) to a peak of 34.33 HRC recorded for Sample 41. This peak value indicates a relatively harder weld zone, which may be attributed to enhanced filler material deposition and optimal thermal cycles during welding. Several samples such as 33, 36, 47, and 48 also exhibit

higher hardness values (above 31 HRC), indicating effective metallurgical bonding and possible refinement of grain structure. Figure 6.14 illustrates the variation in hardness values observed in the weld zones of the filler-assisted TIG welded specimens from Experiment Set 4.

Table 6.5. Rockwell Hardness (HRC) Test Results for Filler assisted TIG welded Joints of Experimental Set 4

Sl. No	**HRC1**	**HRC2**	**HRC3**	**Avg. HRC**
31	26	31	26	27.67
32	29	32	28	29.67
33	31	33	33	32.33
34	29	27	31	29
35	26	31	27	28
36	32	29	33	31.33
37	32	31	28	30.33
38	25	29	28	27.33
39	29	33	31	31
40	25	25	26	25.33
41	32	37	34	34.33
42	28	28	32	29.33
43	27	25	24	25.33
44	27	28	27	27.33
45	26	32	27	28.33
46	29	27	32	29.33
47	30	33	31	31.33
48	32	34	31	32.33
49	28	28	27	27.67
50	31	28	27	28.67

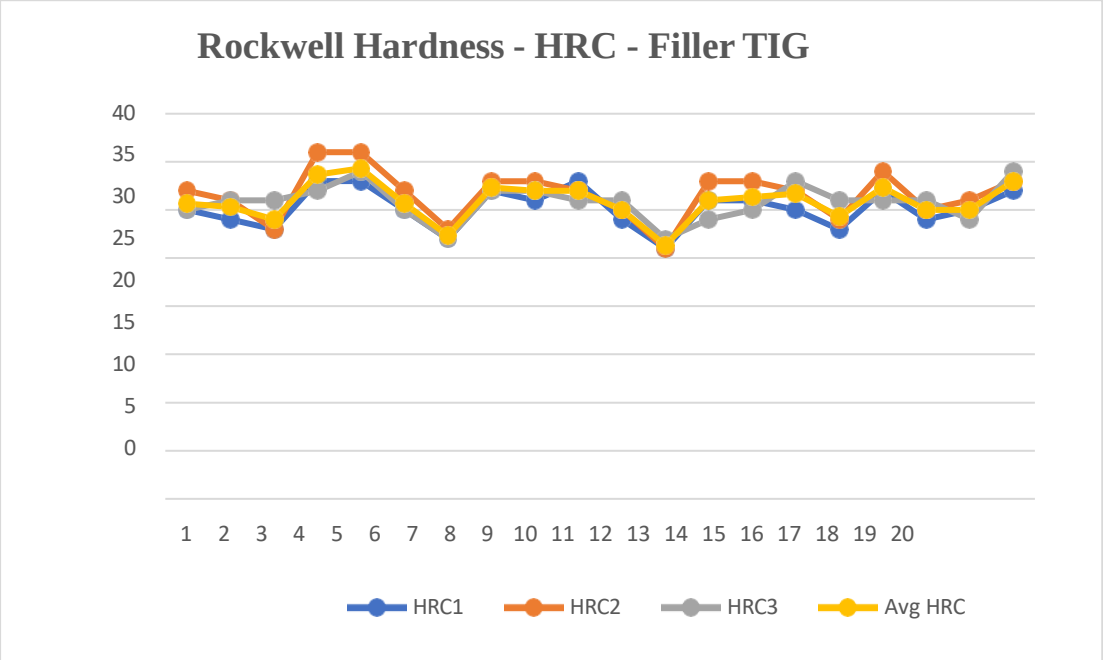

Figure 6.14. Variations in hardness values of weld zone found for the Filler assisted TIG welded (Both sides) specimens of Experimental Set 4

6.6. Observations Made in Microhardness Test of Experiment Set 4

In Experimental Set 4, hardness measurements are conducted on typical samples from eight different Serial Nos (43, 42, 33, 34, 35, 36, 48 and 40). The microhardness is measured at intervals ranging from –10 mm (left base metal) to +10 mm (right base metal) from the weld centre, covering both sides of the filler-assisted TIG weld zone. The Vickers microhardness results demonstrate that hardness values fluctuate across the weldment, typically peaking near the heat-affected zone (HAZ), which reflects the effects of thermal input and cooling rates on microstructural changes in different regions. Detailed Vickers microhardness values at various distances from the weld centre for all runs are presented in Table 6.6. Figure 6.15. illustrates the microhardness distribution for these filler-assisted TIG welded specimens.

Table 6.6. Vickers microhardness values at various locations from weld centre (Filler assisted welded specimens – both sides)

Distance from Weld Centre (mm)	**Serial No 43 (Filler TIG)**	**Serial No 42 (Filler TIG)**	**Serial No 33 (Filler TIG)**	**Serial No 34 (Filler TIG)**	**Serial No 35 (Filler TIG)**	**Serial No 36 (Filler TIG)**	**Serial No 48 (Filler TIG)**	**Serial No 40 (Filler TIG)**
-10	279	288	294	268	264	276	284	271
-8	301	312	284	298	334	341	334	286
-6	329	338	323	332	342	319	356	342
-4	345	352	336	348	354	331	342	356
-2	347	349	338	351	342	336	324	362
0 (Weld Center)	340	342	321	344	322	338	352	354
+2	339	347	341	346	340	344	358	334
+4	327	335	329	331	348	326	341	342
+6	318	328	335	324	334	322	346	348
+8	283	290	276	286	282	294	281	298
+10	270	280	316	272	278	284	264	274

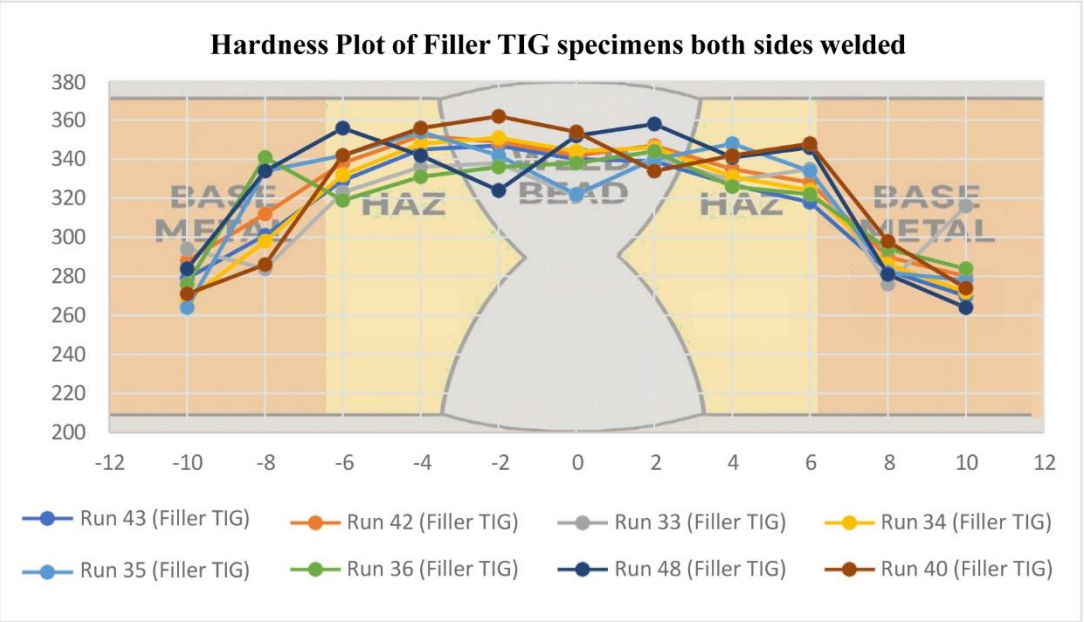

Figure 6.15. Microhardness distribution for some typical filler-assisted TIG welded specimens.

6.7. Observations Made in Microstructure Analysis of Experiment Set 4

In Experiment Set 4, specimens from Serial No 38 (676.13 MPa), Serial No. 44 (671.47 MPa), Serial No. 37 (664.24 MPa), and Serial No. 35 (656.17 MPa), the four highest-strength welds in the set are chosen for detailed microstructural study. Optical micrographs are taken at 50x, 100x and 200x magnifications, covering the base metal, heat-affected zone (HAZ), and weld metal. All four high-strength samples exhibit a finely refined grain structure within the weld region, a result of optimized heat input and controlled cooling during filler-assisted TIG welding. This grain refinement aligns with their excellent tensile performance, indicating robust metallurgical bonding and minimal weld defects. Representative microstructures of these top-strength specimens from Experimental Set 4 are shown in Figure 6.16.

	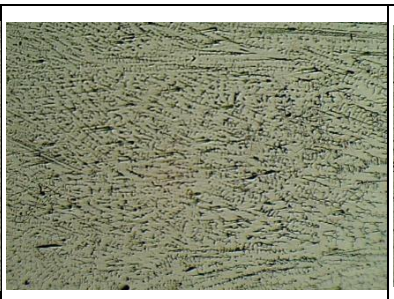	
a) Serial No 35 - 50x	b) Serial No 35 - 100x	c) Serial No 35 - 200x
	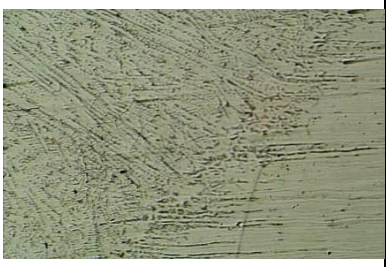	
d) Serial No 37 - 50x	e) Serial No 37 - 100x	f) Serial No 37 - 200x
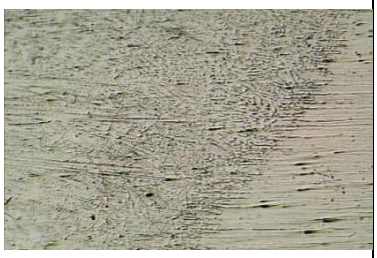	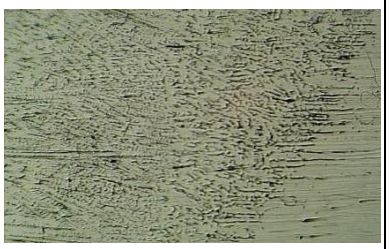	
g) Serial No 38 - 50x	h) Serial No 38 - 100x	i) Serial No 38 - 200x
		
a) Serial No 44 - 50x	b) Serial No 44 - 100x	c) Serial No 44 - 200x

Figure 6.16. Microstructures of typical specimens of Experimental Set 4 having higher tensile strength seen under optical microscope.

6.8. Observations Made in Scanning Electron Microscopy of Experiment Set 4

The SEM micrographs of Set 4 reveal a predominantly dendritic surface morphology. The uniform distribution of dendrites indicates consistent solidification and good metallurgical bonding. The use of SS 304H as the filler material has resulted in a homogenous weld structure with minimal surface irregularities, reflecting sound process stability and material compatibility. The presence of refined dendritic arms and reduced porosity points towards effective heat input and controlled cooling, which together contribute to the enhanced mechanical performance of the weldments. Figure 6.17. represents micrographs of typical specimens of Experimental Set 4 having higher tensile strength seen under Scanning Electron Microscope (SEM).

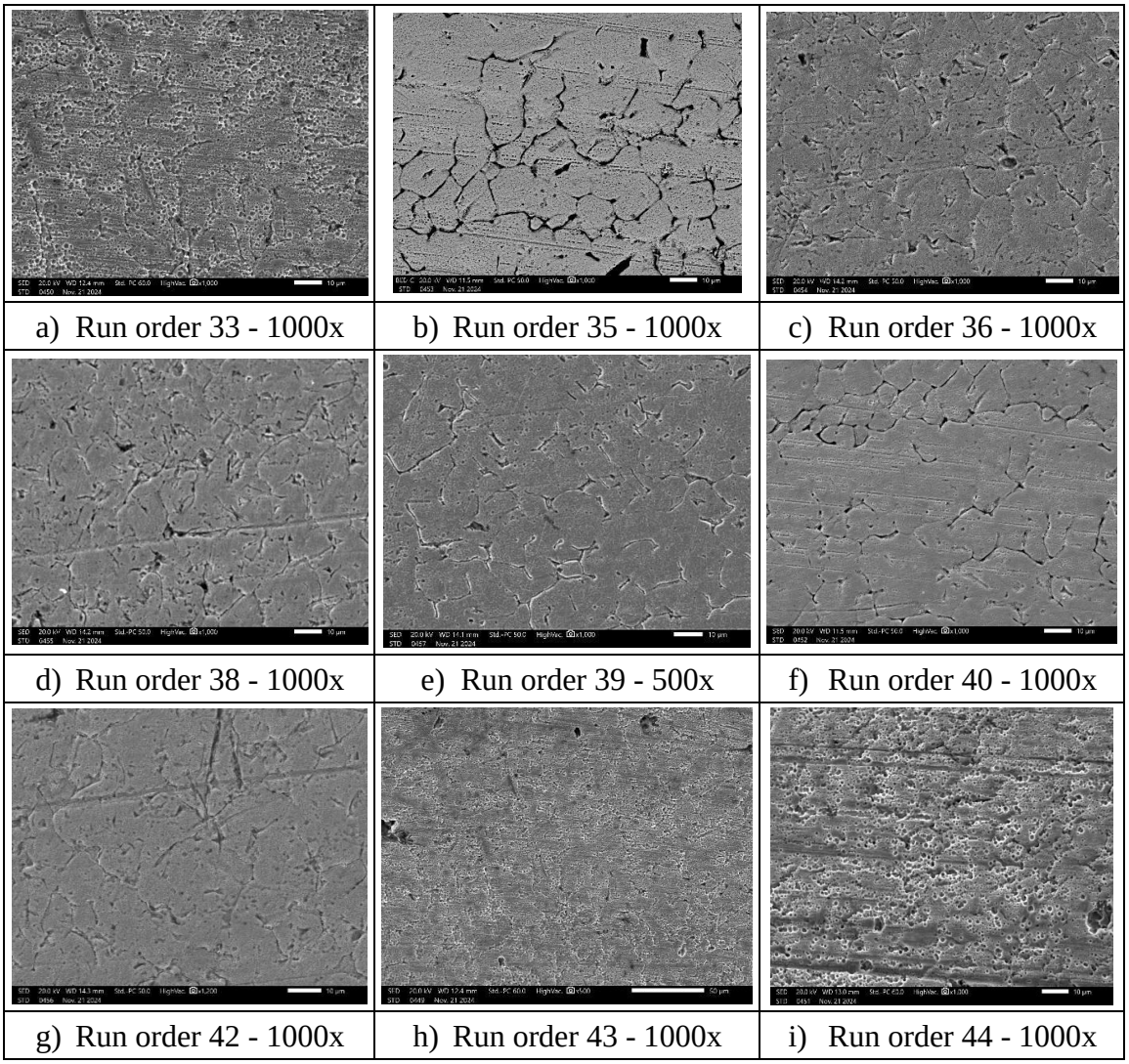

a) Run order 33 - 1000x | b) Run order 35 - 1000x | c) Run order 36 - 1000x

d) Run order 38 - 1000x | e) Run order 39 - 500x | f) Run order 40 - 1000x

g) Run order 42 - 1000x | h) Run order 43 - 1000x | i) Run order 44 - 1000x

Figure 6.17. Microstructures of typical specimens of Experiment Set 4 having higher tensile strength seen under Scanning Electron Microscope (SEM).

6.9. Outcomes of the Analytical Hierarchy Process applied to the results of Experiment Set 4

The pairwise comparison matrix for criteria for this Experiment Set 4 is identical to that Experiment Set 1 and it is shown in Table 4.6 of Chapter 4. Serial numbers of the specimens 31 to 39 are represented as Alternatives 1 to 9 taken in the same order for Experiment Set 4. The pairwise comparison matrix for alternatives is developed using the operating conditions from Serial No's 31 to 39 (denoted as Alternatives 1 to 9) from Experimental Set 4. These are selected based on unique parameter combinations, as several other experimental runs shared identical settings and are therefore excluded from the matrix to avoid redundancy.

Now, in Table 6.7. the comparison matrix between alternatives for criterion 1 (Depth of penetration) is calculated keeping in mind the goal i.e. optimization of weld bead geometry. Maximum Eigen value is λ_{max}= 9.0689 is calculated from 9×9 matrix and consistency ratio is calculated as 5.9%. It is below 10% and is accepted.

Table 6.7. Pair wise comparison matrix for alternatives for Depth of Penetration

Depth of Penetration	**A1**	**A2**	**A3**	**A4**	**A5**	**A6**	**A7**	**A8**	**A9**	**Geometric mean**	**Local weight**
A1	1	1/3	1/5	1/5	1/5	1/5	1/5	1/5	1/5	0.256	0.0246
A2	3	1	1/4	1/4	1/4	1/4	1/4	1/4	1/4	0.388	0.037
A3	5	4	1	1	1	1	1	1	1	1.39	0.134
A4	5	4	1	1	1	1	1	1	1	1.39	0.134
A5	5	4	1	1	1	1	1	1	1	1.39	0.134
A6	5	4	1	1	1	1	1	1	1	1.39	0.134
A7	5	4	1	1	1	1	1	1	1	1.39	0.134
A8	5	4	1	1	1	1	1	1	1	1.39	0.134
A9	5	4	1	1	1	1	1	1	1	1.39	0.134

C.R.= 0.059, λmax= 9.0689

Now, in Table 6.8. the comparison matrix between alternatives for criterion 2 (Bead Width) is calculated keeping in mind the goal i.e. optimization of weld bead geometry. Now maximum Eigen value is $\lambda_{max} = 9.657$ is calculated from 9×9 matrix and consistency ratio is calculated as 5.6 %. It is below 10% and is accepted.

Table 6.8. Pair wise comparison matrix for alternatives for Bead Width

Bead Width	**A1**	**A2**	**A3**	**A4**	**A5**	**A6**	**A7**	**A8**	**A9**	**Geometric mean**	**Local weight**
A1	1	3	2	1/2	3	4	4	4	3	2.270	0.19
A2	1/3	1	1/2	1/3	3	4	4	4	1/2	1.190	0.10
A3	1/2	2	1	1/3	3	4	4	4	1/2	1.462	0.13
A4	2	3	3	1	4	5	5	5	3	3.070	0.27
A5	1/3	1/3	1/3	1/4	1	3	4	2	1/3	0.747	0.06
A6	1/4	1/4	1/4	1/5	1/3	1	2	1/2	1/3	0.415	0.04
A7	1/4	1/4	1/4	1/5	1/4	1/2	1	1/2	1/3	0.345	0.03
A8	1/4	1/4	1/4	1/5	1/2	2	2	1	1/2	0.530	0.05
A9	1/3	2	2	1/3	3	3	3	2	1	1.415	0.12

C.R.= 0.056, λ_{max}= 9.657

Now, in Table 6.9. the comparison matrix between alternatives for criterion 2 (Reinforcement) is calculated keeping in mind the goal i.e. optimization of weld bead geometry. Now maximum Eigen value is λ_{max}= 9.445 is calculated from 9×9 matrix and consistency ratio is calculated as 3.8% which is below 10% so it is acceptable.

Table 6.9. Pair wise comparison matrix for alternatives for Height of Reinforcement

Height of Reinforcement	**A1**	**A2**	**A3**	**A4**	**A5**	**A6**	**A7**	**A8**	**A9**	**Geometric mean**	**Local weight**
A1	1	1/2	1/2	3	1/2	1/3	1/3	1/3	1/2	0.576	0.054
A2	2	1	1/2	3	2	1/3	1/3	1/3	1/2	0.782	0.073
A3	2	2	1	3	2	1/3	1/3	1/3	1/2	0.911	0.085
A4	1/3	1/3	1/3	1	1/3	1/4	1/4	1/4	1/3	0.343	0.032
A5	2	1/2	1/2	3	1	1/3	1/3	1/3	1/2	0.671	0.063
A6	3	3	3	4	3	1	1/2	1/2	2	1.750	0.164
A7	3	3	3	4	3	2	1/2	1/2	2	2.030	0.190
A8	3	3	3	4	3	2	1	1	2	2.370	0.220
A9	2	2	2	3	2	1/2	1/2	1/2	1	1.220	0.114

C.R.= 0.038, λ_{max}= 9.445

In Table 6.10. the local weights for each parameter are considered and global weights are calculated for all individual alternatives. The maximum global weight of 0.144 for Serial No. 4 represents the suitable alternative which may be considered as the optimized condition.

Table 6.10. Local and global weights for alternatives and local weights for criteria

Alternative No.	Local Weights			Global Weights
	Depth of penetration	Bead Width	Reinforcement	
	0.62	0.21	0.15	
A1	0.0246	0.19	0.054	0.063
A2	0.037	0.10	0.073	0.054
A3	0.134	0.13	0.085	0.123
A4	0.134	0.27	0.032	0.144
A5	0.134	0.06	0.063	0.105
A6	0.134	0.04	0.164	0.116
A7	0.134	0.03	0.19	0.117
A8	0.134	0.05	0.22	0.126
A9	0.134	0.12	0.114	0.125

In this work, the Analytical Hierarchy Process (AHP) is applied to identify the optimal depth of penetration while maintaining productivity and determining the associated process parameters for Tungsten Inert Gas (TIG) welding. Global weights of all alternatives are calculated, and the highest value of 0.144, corresponding to alternative 4, is identified as the optimal condition.

6.10. Summary of Experiment Set 4

Experimental Set 4 focuses on filler-assisted TIG welding of 8 mm thick SS 304H stainless steel plates, using Central Composite Design (CCD) within the Response Surface Methodology (RSM) framework. The objective is to evaluate the effects of filler addition and optimize process parameters such as heat input, gas flow rate, and root gap to achieve full penetration and improved bead geometry.

The results reveal that full penetration (8 mm) is successfully achieved in multiple runs, especially at high heat input levels (1.458–1.520 kJ/mm) combined with moderate to wide root gaps (1.6–2.0 mm). Gas flow rate plays a lesser role in penetration but influences reinforcement and bead shape. Notably, the highest reinforcement of 2.455 mm is recorded at a 2 mm root gap, 14 L/min gas flow, and 1.337 kJ/mm heat input, while negative

reinforcement (–0.665 mm) is observed under high heat and moderate root gap, indicating surface depression or excess melting. Bead width varies considerably, reaching a maximum

of 12.615 mm at 1.458 kJ/mm heat input and 1.6 mm root gap, demonstrating that bead spread is more responsive to heat than gas flow. Overall, optimal weld geometry featuring full penetration, balanced reinforcement, and bead width is achieved at 1.520 kJ/mm heat input, 1.6–2.0 mm root gap, and 12–14 L/min gas flow rate.

Tensile testing of the 20 welded samples (Serial Nos 31–50) shows strength values ranging from 334.68 MPa to 676.13 MPa, with several samples such as Serial Nos 38 (676.13 MPa), 37 (664.24 MPa) and 35 (656.17 MPa) exceeding the base material strength (about 582 MPa), signifying enhanced joint integrity and weld quality. These samples were selected for further microstructural analysis.

The Analytical Hierarchy Process (AHP) ranks Alternative 4 of Experiment Set 4 (Serial No 34) as the optimal condition with the highest global weight (0.144). This alignment with experimental observations confirms the effectiveness and reliability of AHP as a decision- making and optimization tool for welding parameter selection.

Microstructural examination under optical microscopy at 50×, 100×, and 200× magnifications reveal a refined grain structure in the weld zone of high-strength specimens, attributed to effective heat input and controlled cooling rates. The SEM micrographs (Figure 6.17) show uniform dendritic morphology, refined arms, minimal porosity, and smooth solidification fronts indicative of sound metallurgical bonding and filler compatibility.

Rockwell hardness (HRC) values in this set vary from 25.33 HRC (Samples 40 and 43) to a peak of 34.33 HRC (Sample 41), with several others (33, 36, 47, 48) above 31 HRC. This suggests localized hardening due to refined microstructures and optimal welding cycles. Vickers microhardness profiles measured from –10 mm to +10 mm across the weld zone show peaks near the HAZ, reflecting typical thermal influences.

In summary, Experiment Set 4 shows that by using filler-assisted TIG welding with the right combination of heat input, root gap, and shielding gas, full penetration can be achieved in several cases. This method leads to better mechanical strength and improved microstructure in SS 304H plates, making it more effective than autogenous TIG welding for thicker materials.

CHAPTER 7

Results and Discussion on Predictive Modelling of Experimental Weld Data Using Machine Learning Techniques

7.1. Preamble

This chapter focuses on the application of machine learning (ML) algorithms to develop predictive models based on experimental welding data. The goal is to forecast output parameters and assess their alignment with actual experimental results, thereby validating the predictive accuracy of the models. Four complete sets of experimental data are compiled and utilized in this analysis. Each dataset includes key process variables, and the corresponding output responses serving as target variables for model training and validation. A standard data-splitting approach is adopted, where 80% of the total dataset is used to train the models and the remaining 20% is reserved for testing and evaluation.

Six widely recognized machine learning algorithms commonly applied across multiple industrial domains are employed to build the predictive frameworks. The performance of each model is then comparatively analyzed based on its accuracy in predicting the experimental outcomes. The input and output parameters considered for training and testing are shown in Table 7.1.

Table 7.1 Experimental input and output parameters of this present work

Autogenous TIG Experiment done on One side														
	Input Parameters								Output Parameters					
Run Order	Gas flow rate	Torch Angle (Degree)	Filler Used	Welding Pass	Flux Used	Root Gap	Arc Gap (mm)	Heat input (kJ/mm)	Penetration (mm)	Width (mm)	Reinforcement (mm)	Tensile Strength (MPa)	% Elongation	Avg. Rockwell Hardness (HRC)
1	10	60	0	1	0	0	2	0.768	2.326	5.932	-0.1	284.32	3.96	27.67
2	14	60	0	1	0	0	2	0.768	2.156	6.045	0.00	274.86	3.61	29.67
3	10	90	0	1	0	0	2	0.768	1.674	7.531	-0.16	212.62	1.62	32.33
4	14	90	0	1	0	0	2	0.768	1.735	6.639	0.00	218.67	1.76	29
5	10	60	0	1	0	0	2	1.119	3.369	7.869	-0.14	349.4	4.95	28
6	14	60	0	1	0	0	2	1.119	3.058	8.422	0.12	334.96	4.58	31.33
7	10	90	0	1	0	0	2	1.119	3.459	9.375	0.11	424.5	17.696	30.33
8	14	90	0	1	0	0	2	1.119	2.908	6.609	-0.1	346.06	5.28	27.33
9	10	75	0	1	0	0	2	0.943	1.826	8.264	0.1	206.29	9.232	31
10	14	75	0	1	0	0	2	0.943	2.924	6.244	0.00	370.22	13	25.33
11	12	60	0	1	0	0	2	0.943	1.822	6.014	0.11	231.54	2.26	34.33
12	12	90	0	1	0	0	2	0.943	2.884	6.424	0.00	351.62	4.33	29.33
13	12	75	0	1	0	0	2	0.768	2.787	6.548	0.00	328.31	3.71	25.33
14	12	75	0	1	0	0	2	1.119	2.707	7.121	0.00	332.86	3.77	27.33
15	12	75	0	1	0	0	2	0.943	2.807	6.311	-0.19	352.36	4	28.33
16	12	75	0	1	0	0	2	0.943	2.607	7.029	0.00	331.42	3.76	29.33

17	12	75	0	1	0	0	2	0.943	2.747	7.162	0.00	339.82	4.17	31.33
18	12	75	0	1	0	0	2	0.943	2.968	7.008	0.08	311.691	6.781	32.33
19	12	75	0	1	0	0	2	0.943	2.618	7.118	0.11	326.61	4	27.67
20	12	75	0	1	0	0	2	0.943	2.712	6.582	0.00	331.42	4.05	28.67
Autogenous TIG Experiment Done on Both Sides with best results of 1st set														
	Input Parameters								**Output Parameters**					
Run Order	**Gas flow rate**	**Torch Angle (Degree)**	**Filler Used**	**Welding Pass**	**Flux Used**	**Root Gap**	**Arc Gap (mm)**	**Heat input (kJ/mm)**	**Penetration (mm)**	**Width (mm)**	**Reinforcement (mm)**	**Tensile Strength (MPa)**	**% Elongation**	**Avg. Rockwell Hardness (HRC)**
21	10	75	0	2	0	0	2	1.18	6.530	5.839	0.109	481.73	23.368	28
22	14	75	0	2	0	0	2	1.18	5.368	5.59	0.144	434.276	12.673	28.67
23	10	75	0	2	0	0	2	1.18	6.000	6.066	0.121	476.82	17.562	30
24	14	75	0	2	0	0	2	1.18	5.022	5.307	0.00	416.834	11.643	31.67
25	12	75	0	2	0	0	2	0.964	5.174	6.64	0.177	422.754	12.843	31.33
A- TIG Experiment Done on Both Sides with best results of 1st set														
	Input Parameters								**Output Parameters**					
Run Order	**Gas flow rate**	**Torch Angle (Degree)**	**Filler Used**	**Welding Pass**	**Flux Used**	**Root Gap**	**Arc Gap (mm)**	**Heat input (kJ/mm)**	**Penetration (mm)**	**Width (mm)**	**Reinforcement (mm)**	**Tensile Strength (MPa)**	**% Elongation**	**Avg. Rockwell Hardness (HRC)**
26	10	75	0	2	1	0	2	1.264	8.000	5.214	-0.14	648.64	26.884	34.33
27	14	75	0	2	1	0	2	1.264	8.000	5.642	0.00	628.94	26.224	36.33
28	10	75	0	2	1	0	2	1.264	8.000	5.326	-0.11	656.86	28.342	35.67
29	14	75	0	2	1	0	2	1.264	8.000	5.881	0.00	636.41	26.482	34
30	12	75	0	2	1	0	2	1.01	6.640	6.314	0.00	602.083	30.887	32.33
Filler TIG Experiment on Both Sides														
	Input Parameters								**Output Parameters**					
Run Order	**Gas flow rate**	**Torch Angle (Degree)**	**Filler Used**	**Welding Pass**	**Flux Used**	**Root Gap**	**Arc Gap (mm)**	**Heat input (kJ/mm)**	**Penetration (mm)**	**Width (mm)**	**Reinforcement (mm)**	**Tensile Strength (MPa)**	**% Elongation**	**Avg. Rockwell Hardness (HRC)**
31	10	75	1	2	0	1.2	5	1.337	2.825	8.105	1.61	361.34	11.342	30.67
32	14	75	1	2	0	1.2	5	1.337	4.63	8.61	1.18	468.69	16.546	30.33
33	10	75	1	2	0	2	5	1.337	8	8.295	1.14	622.243	22.643	29
34	14	75	1	2	0	2	5	1.337	8	7.755	2.455	642.536	26.892	33.67
35	10	75	1	2	0	1.2	5	1.52	8	8.99	1.315	656.172	31.342	34.33
36	14	75	1	2	0	1.2	5	1.52	8	9.65	0.665	634.562	26.472	30.67
37	10	75	1	2	0	2	5	1.52	8	9.705	0.51	664.239	31.573	27.33
38	14	75	1	2	0	2	5	1.52	8	9.135	0.485	676.126	34.003	32.33
39	10	75	1	2	0	1.6	5	1.458	8	8.32	1.16	616.362	24.346	32
40	14	75	1	2	0	1.6	5	1.458	8	7.564	0.621	621.643	24.63	32
41	12	75	1	2	0	1.2	5	1.458	3.34	9.632	0.34	416.631	16.583	30
42	12	75	1	2	0	2	5	1.458	8	9.224	0.56	616.263	23.064	26.33
43	12	75	1	2	0	1.6	5	1.337	8	8.19	1.045	618.472	24.664	31
44	12	75	1	2	0	1.6	5	1.52	8	8.615	-0.665	671.473	29.376	31.33
45	12	75	1	2	0	1.6	5	1.458	2.73	11.86	0.69	334.682	6.642	31.67
46	12	75	1	2	0	1.6	5	1.458	2.98	11.805	0.38	346.732	8.772	29.33
47	12	75	1	2	0	1.6	5	1.458	3.25	12.615	0.825	364.862	12.568	32.33
48	12	75	1	2	0	1.6	5	1.458	8	9.63	1.59	628.02	26.568	30
49	12	75	1	2	0	1.6	5	1.458	3.42	11.64	0.14	386.793	14.782	30
50	12	75	1	2	0	1.6	5	1.458	8	8.89	0.442	621.462	23.843	33

7.2. Optimization of Different ML Model's Parameters

A thorough refinement of various machine learning models is carried out to achieve optimal predictive performance. Essential hyperparameters for each model are outlined previously. Advanced techniques such as parameter tuning and cross-validation are applied to determine the most effective configurations for the forecasting models. During this process, different parameter ranges are explored, and the models are run multiple times to ensure robustness. The models include Artificial Neural Network (ANN), K-Nearest Neighbors (KNN), Support Vector Regression (SVR), Random Forest (RF), Gradient Boosting Machine (GBM) and Extreme Gradient Boosting (XGBoost). Among these, the most

suitable algorithm is recommended based on overall prediction accuracy and consistency across all response variables. Google Colab scripts are developed to implement the grid search method, which serves as an additional optimization tool alongside the core algorithms. By evaluating model performance across multiple parameter settings, grid search effectively identifies the configurations that deliver the most accurate results. The best-performing parameter sets are documented in Table 7.2.

Table 7.2. Optimization parameters for all the ML models

Model	**Particular parameters**
ANN	1st hidden layer (8), 2nd hidden layer (8), activation='tanh', solver='lbfgs', max_iter=10000, random_state=42
KNN	n_neighbors = 5; Weights= 'uniform'
RF	n_estimators = 100; max_features = 2, random_state=42
SVR	kernel='rbf', C=100
GBR	n_iestimators:100; Max depth:3; Learning rate: 0.1, random_state=42
XGBoost	n_estimators: 100, learning rate: 0.1, Max depth: 4

7.3. Results and Discussion

7.3.1. Model Performance Evaluation

Performance metrics provide a numerical assessment of how well machine learning models correspond to actual data. In supervised learning, particularly for regression problems, the coefficient of determination (R^2) is a fundamental evaluation measure. R^2 reflects the fraction of variance in the dependent variable that the model successfully explains. Its value ranges from 0 to 1, where 0 indicates that the model fails to capture any variation, suggesting no predictive capability. R^2 value less than 0.5 generally points to poor model performance. Values between 0.70 and 0.90 suggest that the model achieves a reasonably good fit, whereas values above 0.9 indicate excellent predictive performance. A perfect R^2 score of 1 implies that the model accounts for all variability in the dataset without any error, although this is rarely observed with experimental data. Alongside R^2, error metrics like Mean Absolute Error (MAE), Mean Squared Error (MSE), and Root Mean Squared Error (RMSE) are also critical for assessing model performance. Lower values of these errors correspond to higher model accuracy.

The bar charts Figure 7.1(a)(i–v) illustrate the R^2 values of six machine learning models: ANN, SVM, RF, GBR, XGBoost, and KNN and across six output parameters: penetration, width, reinforcement, hardness, tensile strength, and % elongation. For penetration, ANN achieves the highest R^2, nearing 0.95, while KNN shows the lowest performance around 0.65–0.70. In predicting width and reinforcement, GBR and XGBoost deliver superior results with R^2 values close to 0.95, while KNN again lags behind. For hardness, RF, GBR, and XGBoost perform notably better, with R^2 values around 0.85–0.90, whereas ANN and SVM show moderate results, and KNN remains the weakest. In tensile strength prediction, RF outperforms others with an R^2 exceeding 0.90, followed closely by GBR and XGBoost, while ANN shows relatively lower accuracy. For % elongation, all models except KNN demonstrate high R^2 values above 0.85, with GBR and XGBoost slightly ahead. Overall, GBR and XGBoost consistently deliver strong predictive performance across all output parameters, while KNN shows the least effectiveness.

Figure 7.1.(b)(i-v) represents the RMSE bar graph. For all parameters, KNN consistently shows the highest RMSE, indicating the poorest prediction accuracy. ANN and SVM exhibit higher RMSE values for penetration, width, reinforcement, and hardness compared to RF, GBR, and XGBoost. GBR and XGBoost models demonstrate the lowest RMSE values across almost all outputs, highlighting their superior prediction capabilities. Particularly for tensile strength and % elongation, GBR and XGBoost achieve significantly lower RMSE compared to other models. Overall, the error trends confirm that GBR and XGBoost provide more accurate predictions, while KNN performs the worst among all models.

The MAE bar graph is shown in Figure 7.1.(c)(i-v). Again, KNN shows the highest MAE values, indicating the poorest predictive accuracy among the models. ANN and SVM also show relatively higher MAE values compared to RF, GBR, and XGBoost, particularly for hardness, tensile strength, and % elongation. GBR and XGBoost consistently achieve the lowest MAE values across all parameters, confirming their superior performance in minimizing prediction errors. Specifically, for tensile strength and % elongation, GBR and XGBoost significantly outperform the other models, with much lower error margins. Overall, this comparison highlights that GBR and XGBoost offer the most accurate predictions, while KNN yields the least reliable results.

Another important performance metric is MSE which is shown in Figure 7.1.(d)(i-v). KNN shows the highest MSE values, indicating the poorest model performance with the largest

prediction errors. ANN and SVM also exhibit comparatively higher MSEs than RF, GBR, and XGBoost, particularly for hardness and tensile strength. GBR and XGBoost consistently achieve the lowest MSE values across all parameters, emphasizing their strong prediction capabilities. Especially for tensile strength and % elongation, GBR and XGBoost significantly outperform the others, showcasing much smaller error magnitudes. Overall, the results demonstrate that GBR and XGBoost provide more reliable and accurate predictions, while KNN consistently underperforms.

Based on the evaluation of R^2, RMSE, MAE, and MSE across all output parameters, XGBoost continuously deliver the highest prediction accuracy with higher R^2 values and lower error metrics compared to other models. Both models show excellent generalization and minimal prediction errors across penetration, width, reinforcement, hardness, tensile strength, and % elongation. Therefore, XGBoost is identified as the best-performing models for all cases. Table 7.3. summarizes the comparative performance of the models based on the results obtained from the test datasets.

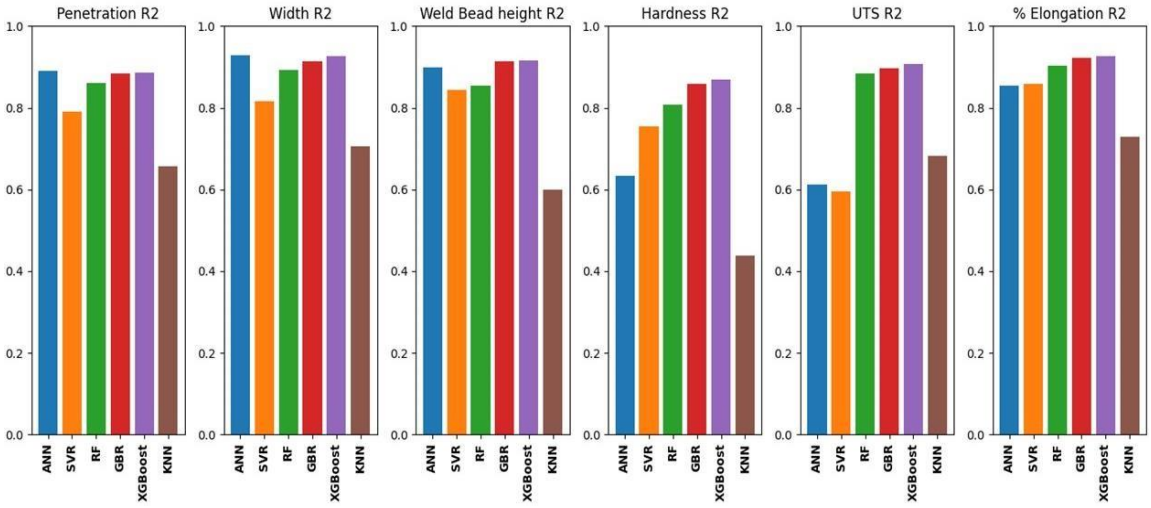

(i) (ii) (iii) (iv) (v)

(**a**)

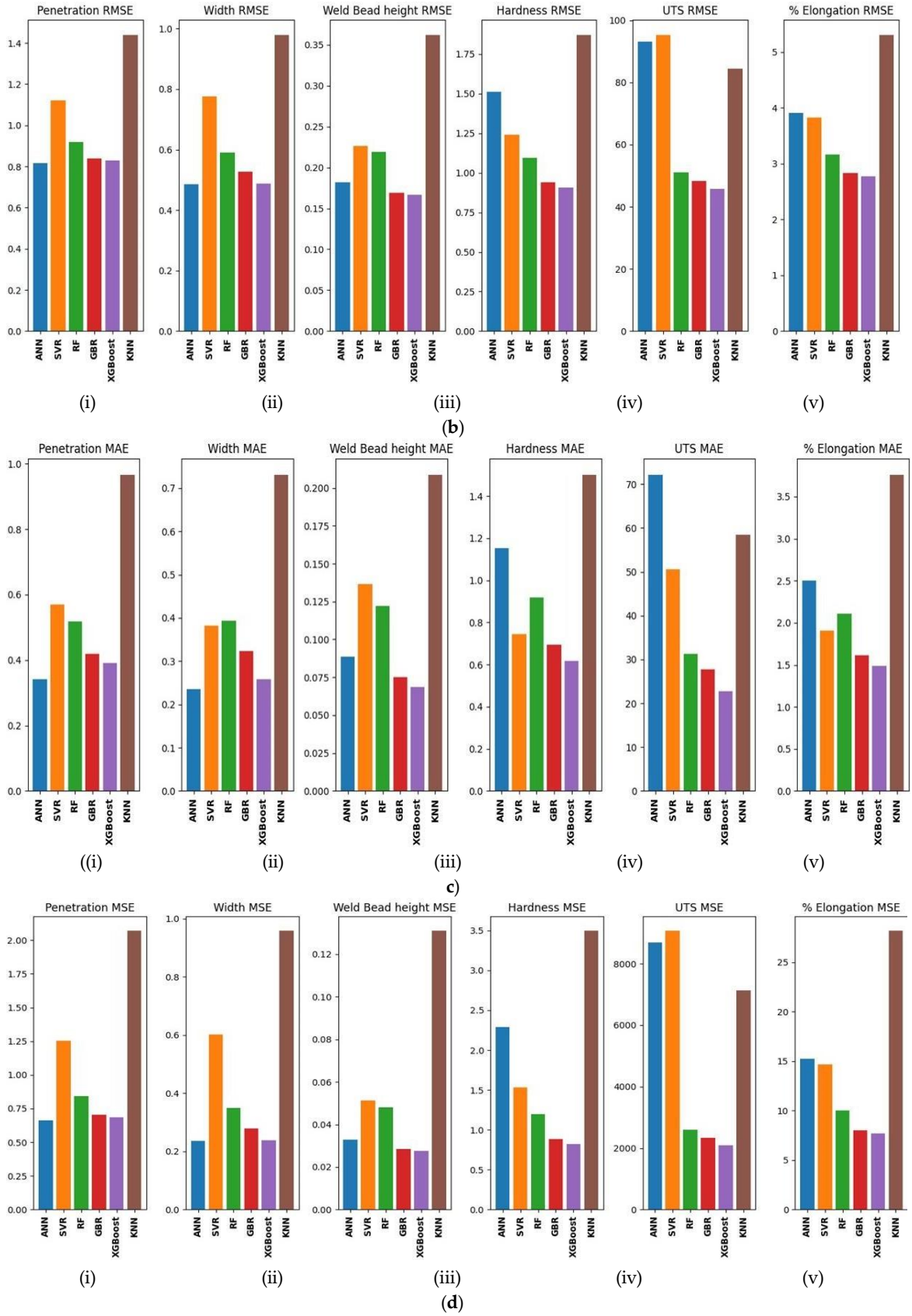

Figure 7.1. (a). Performance metrics—R^2 (Representing R2); (b) Performance metrics—RMSE; (c) Performance metrics—MAE; (d) Performance metrics—MSE.

Table 7.3. Performance comparison for all outputs

	Model	R^2	RMSE	MAE	MSE
Penetration	ANN	0.8898	0.8149	0.342	0.6640
	SVR	0.7916	1.1205	0.57	1.2555
	RF	0.8603	0.9173	0.5190	0.8414
	GBR	0.8833	0.8383	0.4196	0.7027
	XGBoost	0.8860	0.8286	0.3901	0.6866
	KNN	0.6561	1.4393	0.9668	2.0717
Bead Width	ANN	0.9251	0.4939	0.2593	0.2440
	SVR	0.8151	0.7762	0.3813	0.6025
	RF	0.8931	0.5903	0.3928	0.3484
	GBR	0.9147	0.5272	0.3236	0.2779
	XGBoost	0.9269	0.4882	0.2574	0.2384
	KNN	0.7057	0.9793	0.7312	0.9591
Reinforcement (Bead height)	ANN	0.8993	0.1818	0.0883	0.0330
	SVR	0.8440	0.2262	0.1365	0.0512
	RF	0.8539	0.2189	0.1222	0.0479
	GBR	0.9133	0.1686	0.0753	0.0284
	XGBoost	0.9155	0.1665	0.0685	0.0277
	KNN	0.6003	0.3621	0.2087	0.1311
Hardness	ANN	0.6270	1.5252	1.114	2.3261
	SVR	0.7540	1.2387	0.7454	1.5343
	RF	0.8082	1.0937	0.9188	1.1961

	GBR	0.8585	0.9395	0.6938	0.8827
	XGBoost	0.8686	0.9053	0.6177	0.8195
	KNN	0.4387	1.8709	1.5013	3.5004
Ultimate Tensile Strength (UTS)	ANN	0.6131	93.1933	72.1541	8685.0004
	SVR	0.5954	95.2976	50.5537	9081.6278
	RF	0.8838	51.0799	31.2737	2609.1608
	GBR	0.8959	48.3396	27.7642	2336.7174
	XGBoost	0.9064	45.8487	22.6831	2102.1067
	KNN	0.6819	84.5030	58.432	7140.7575
% Elongation	ANN	0.8605	3.8112	2.3766	14.5256
	SVR	0.8589	3.8330	1.91	14.6923
	RF	0.9038	3.1646	2.1117	10.0145
	GBR	0.9230	2.8324	1.6168	8.0223
	XGBoost	0.9261	2.7746	1.4849	7.6983
	KNN	0.7292	5.3104	3.7617	28.1998

7.3.2. Feature importance and correlation matrix

The feature importance analysis highlights the extent to which each input parameter affects prediction of the output. The input features considered for Feature Importance graphs are gas flow rate, torch angle, filler used, welding pass, flux used, root gap, arc gap, heat input, welding type 1 (representing Autogenous TIG on one side), welding type 2 (representing Autogenous TIG on both sides), welding type 3 (representing A-TIG welding on both sides), welding type 4 (representing filler-assisted TIG on both sides). According to the evaluation, the best-performing model is found to be XGBoost regression. A detailed breakdown of the feature's importance is presented in Figure 7.2(a-f).

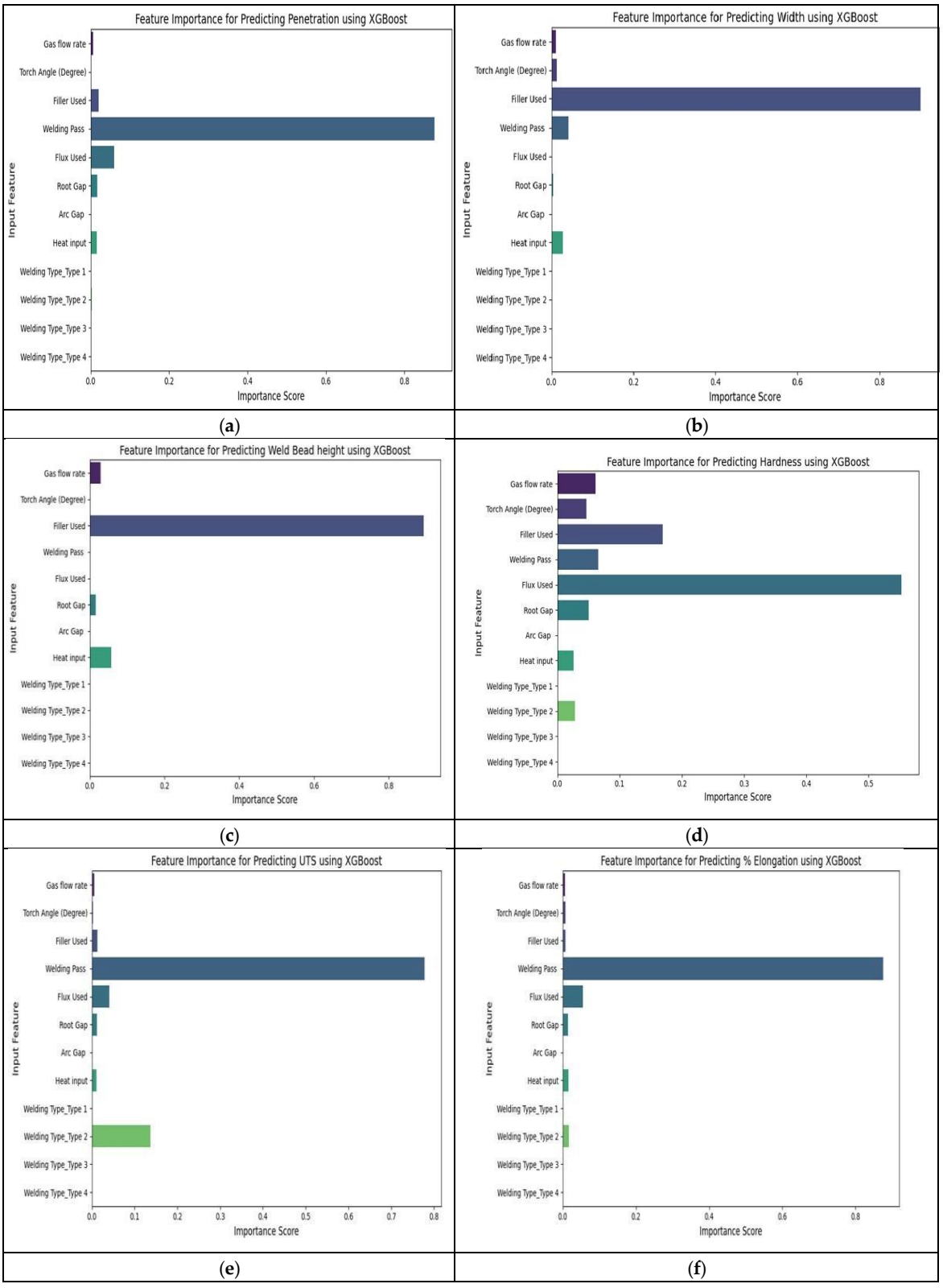

Figure 7.2. Feature importance of all the inputs in the XGBoost model where (a) represents Penetration, (b) represents Width, (c) represents Weld Bead height, (d) represents Hardness, (e) represents Penetration UTS, (f) represents % Elongation.

The feature importance analysis for predicting penetration {as shown in Figure 7.2(a)} using the XGBoost model reveals that “Welding Pass” has maximum influence, with an importance score nearing 0.9. In the present case, some experiments have been conducted with a single pass, where penetration is much smaller than the thickness of the plate. Other experiments have been carried out on both sides of the plate, meaning that two welding passes have been performed. In some of these cases, full penetration has been achieved. When single pass weld deposition is performed, the load withstanding capability of the butt-welded specimens is naturally quite smaller than the depth of penetration and hence, the area of the welded joint in these cases is considerably low. Expectedly, the strength of the welded joint is high when full penetration is achieved with weld deposition made from both sides, meaning two passes are undertaken. Considering welded butt joints, the number of welding passes is considered a parameter of the method of welding sequence. Other factors such as “Flux Used,” “Root Gap” and “Heat Input” show relatively less contribution in the present case on penetration. Parameters like “Gas Flow Rate,” “Torch Angle” and different “Welding Types” exhibit low importance scores, indicating minimal direct influence on penetration. On the whole, only when two welding passes are employed, desired full penetration has been achieved in most of the experimental runs indicating a high influence of the number of weld passes which is reflected in having a high importance score.

For predicting the weld bead width {as shown in Figure 7.2(b)}, the XGBoost model identifies “Filler Used” as the dominant factor, exhibiting a significantly higher importance score compared to other variables. The application of filler material results in the spread of the molten weld pool, thereby influencing the width of the weld. “Welding Pass” and “Heat Input” contribute marginally to bead width, while parameters like “Gas Flow Rate”, “Torch Angle,” and “Welding Type” show negligible impact, indicating that bead width is primarily governed by the application of filler material.

In the case of predicting the bead height {as shown in Figure 7.2(c)}, the use of filler stands out as the most critical factor within the present experimental domain, with an importance score close to 0.9. Other factors are found to have a quite low importance score, indi-cating their negligible influence on bead height.

For predicting hardness {as shown in Figure 7.2(d)}, the use of activating flux shows the highest importance, with a score of approximately 0.54, making it the most influential factor affecting the hardness of the weld. The use of filler has the next value of importance score

at around 0.18, indicating a secondary yet notable impact. “Welding Pass”, “Root Gap”, “Gas Flow Rate”, “Torch Angle” and “Heat Input” have minor effects, while “Welding Type” and “Arc Gap” show minimal contribution. This highlights that the use of activating flux influences hardness the most.

Figure 7.2(e) shows the feature importance for predicting ultimate tensile strength (UTS) using the XGBoost machine learning model. “Welding Pass” is found to be of the highest importance score (~0.77), indicating its high influence on UTS, whereas “Welding Type 2” (autogenous welding conducted on both sides) has a moderate in-fluence on UTS. Other features like flux used and heat input show minimal impact, possibly because their effects are either secondary or already captured through other correlated variables. Overall, this analysis helps prioritize key welding parameters for optimizing UTS.

Figure 7.2(f) illustrates the feature importance for predicting percentage elongation using the XGBoost model. “Welding Pass” is observed to have a high importance score of around 0.85. When the number of welding passes is one, full penetration is never obtained in this work. On the other hand, full penetration is obtained only when welding is performed at both sides and therefore, the welded joints with more area of weld exhibit more strength and elongation. Other features like Flux Used and Welding Type 2 show minor contributions, implying that although they may influence elongation, their effects are relatively less critical compared to the welding pass. Features like gas flow rate, torch angle and heat input have negligible importance, suggesting they have a minimal direct effect on elongation in the present case.

Figure 7.3 illustrates the correlation heatmap matrix illustrating the relationships between the parameters in the given dataset. The value approaching “1” signifies a strong positive relationship, meaning that when a specific feature varies, the other typically shifts expectedly: either rising or declining. The correlation value of “−1” reflects an ideal inverse relationship, wherein an enhancement in one variable directly leads to a reduction in the other. A correlation value near to “0” designates a lack of significant relationship be-tween the variables, suggesting that variations in one do not reliably correspond to variations in the others. This heatmap shows the correlation between various input parameters (such as gas flow rate, torch angle, filler used, welding pass, flux used, root gap, arc gap and heat input) and the output responses (weld bead height, penetration, width, hardness, ultimate tensile strength and % elongation) of a welded joint. The intensity of colour and correlation

values (spanning from −1 to 1) illustrate both the strength and direction of relationships. Shades of red signify positive correlations, while shades of blue indicate negative correlations. White areas, on the other hand, represent weak or negligible correlation. Depth of penetration exhibits a strong positive correlation with welding pass (0.77), heat input (0.69) and flux used (0.48) indicating their significant influence on depth of penetration. More than one weld pass enables more weld deposition resulting in more area of weld joint, thereby increasing in depth of penetration. An increase in heat input increases the melt volume. When heat input increases up to a level, the depth of penetration increases and, correspondingly, UTS increases due to the higher cross-sectional area of the weld. The use of activating flux is expected to increase the depth of penetration due to the reverse Marangoni effect and constriction effect. In this case, an insulating TiO_2 flux is used to coat the faying surfaces before TIG welding to obtain deeper penetration. Bead width shows positive correlations with filler used (0.76). The height of the bead has a moderate positive correlation with filler used (0.70) and heat input (0.52). Hardness is weakly correlated with most parameters but among them, flux used (0.54) has a moderate correlation. Ultimate tensile strength (UTS) shows strong positive relationships with welding pass (0.76), followed by heat input (0.73) and flux used (0.55). Similarly, % elongation shows high correlations with welding pass (0.79) and heat input (0.73).

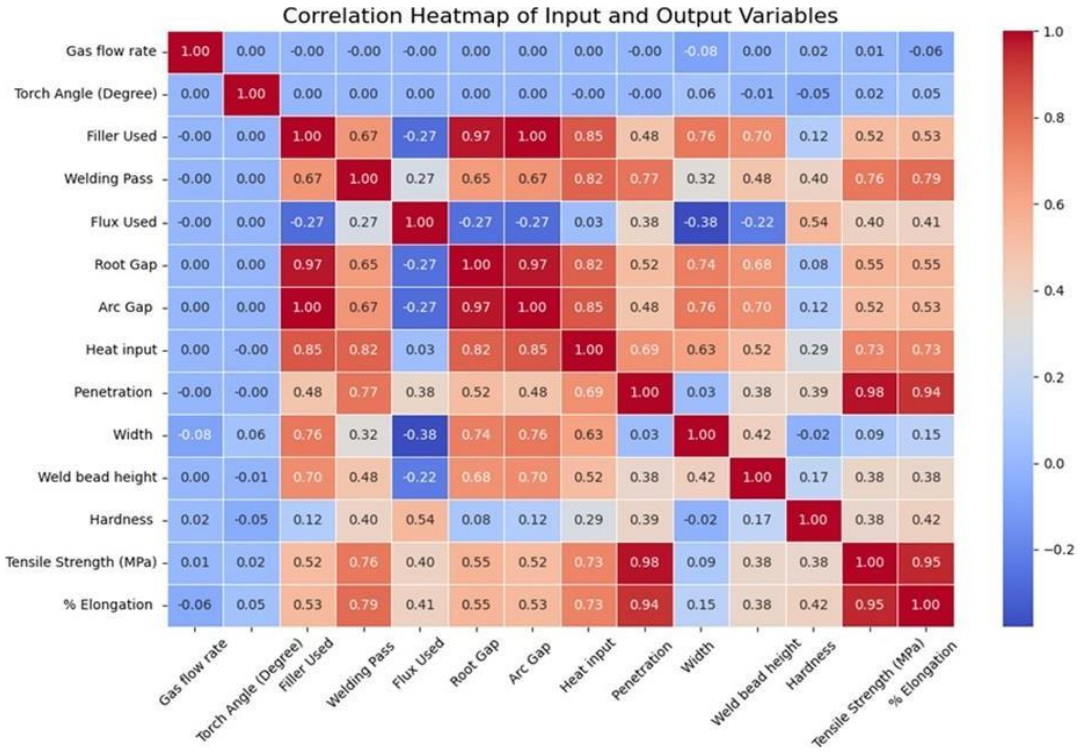

Figure 7.3. correlation heatmap matrix for XGBoost

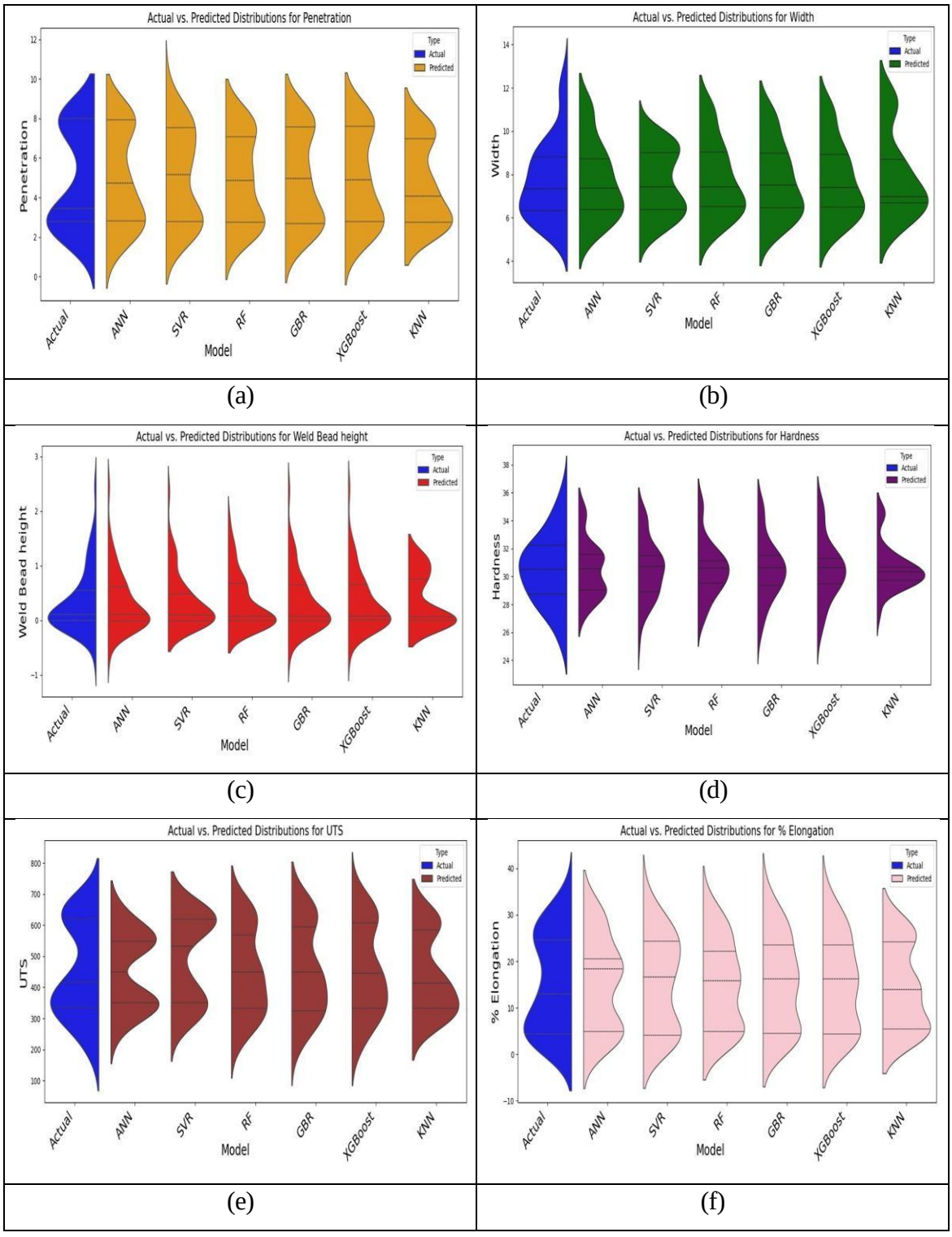

Figure 7.4. Prediction and validation with actual data with different models (a) Penetration (b) Width (c) Weld bead height (d) Hardness (e) UTS and (f) Elongation

This violin plot {in Figure 7.4 (a-f)} shows the comparison between the actual and predicted distributions of all the outputs for various machine learning models (ANN, SVR, RF, GBR, XGBoost and KNN). The blue distribution represents the actual measured output values, while the other colour distributions represent the different model predictions of different

outputs. Overall, the predicted distributions closely resemble the actual distribution in shape and spread, indicating that the models can capture the general behaviour of the output values. Among the models, XGBoost shows a particularly close match to the actual data, suggesting higher prediction accuracy, while slight deviations are observed in GBR, SVR and RF predictions at the extreme values. The plot highlights that a tree-based model like XGBoost is better at mimicking the actual output behaviour compared to others.

7.4. Inference and Key Insights from Machine Learning-Based Predictive Analysis

Based on the implementation of various machine learning techniques, a comprehensive predictive analysis is carried out to estimate key welding parameters and compare them with actual experimental data. The analysis reveals that most machine learning models are capable of accurately forecasting the welding outcomes. From this evaluation, several important conclusions are drawn, highlighting the effectiveness and reliability of these models in capturing complex welding behaviour.

- XGBoost regression emerges5 as the most effective model in predicting the welding outputs, exhibiting the highest R^2 values and the lowest error rates across all responses, including penetration, width, weld bead height, hardness, ultimate tensile strength and % elongation.

- The feature importance analysis using the XGBoost model highlights the pivotal role of specific input parameters in influencing key weld quality characteristics. Among all variables, the number of welding passes consistently emerges as the most influential factor, particularly in predicting penetration, ultimate tensile strength and percentage elongation, with importance scores nearing or exceeding 0.75. This underscores the critical role of double-sided welding in achieving full penetration and enhanced mechanical performance. The use of filler material significantly influences bead width and bead height, due to its influence on spreading molten pool and material deposition. Additionally, activating flux is identified as an impactful factor in determining weld hardness, primarily due to its role in modifying molten pool behavior through the reverse Marangoni effect, thereby improving penetration and weld quality.

- The filler-assisted both side TIG welding also shows satisfactory results in most of the cases, achieving good mechanical properties due to full penetration.

- Heatmap correlation analysis reveals that welding pass, heat input, and flux usage have strong positive correlations with key welding properties of the SS304H-welded joints.
- Prediction and validation analyses confirm that the established machine learning models and in particular, XGBoost, closely match the actual experimental results across all output parameters.
- The close alignment between predicted and experimental data highlights the effectiveness of machine learning in forecasting welding responses and optimizing process parameters.

CHAPTER 8

Conclusion and Future Scope of Work

8.1. Conclusion

This work has comprehensively investigated weldability and process optimization of 8 mm thick SS304H austenitic stainless-steel plates for high-efficiency boiler applications using Tungsten Inert Gas (TIG)-based welding techniques. The entire work has been designed with four distinct sets of welding experiments involving autogenous TIG welding, Activated flux TIG (A-TIG) welding using TiO_2 flux, and filler-assisted TIG welding. Primary objectives are to achieve full-depth penetration in single or double passes, enhance weld quality and mechanical properties through controlled variation of welding parameters and validate the experimental outcomes using machine learning techniques. Across all experimental sets, detailed measurements of weld bead geometry are performed focusing on bead width, height of reinforcement, and depth of penetration. In addition to bead geometry evaluation, a comprehensive set of post-weld tests has been conducted to assess the mechanical and metallurgical properties of the weldments. These included tensile strength testing, percentage elongation measurement and Rockwell hardness testing. Microstructural analysis using optical microscopy, Vickers microhardness testing and Scanning Electron Microscopy (SEM) have been also performed on selected specimens to gain deeper insight into weld quality, hardness distribution. Multi-Criteria Decision Making (MCDM) tool, such as the Analytic Hierarchy Process (AHP), is used to rank the output parameters based on their weighted priorities derived from the pairwise comparison matrix; which in turn, helped identify the most suitable input parameters for optimal welding performance.

To complement experimental evaluations, a data-driven predictive modelling framework is developed using Python programming in Google Collab. Various machine learning algorithms have been trained on the experimental dataset comprising of bead geometry, process parameters and mechanical test results. The predicted values for tensile strength, hardness, bead width, penetration and elongation are found to closely align with actual - measurements in most of the cases. The most suitable algorithm in this case amongst all are suggested for use.

Conclusion of the complete research work is broadly divided into following parts, such as

- Conclusion based on Outcomes of Bead Geometry.
- Conclusion based on Post Welding Tests and Analysis.
- Conclusion based on Multicriteria decision making tool used.
- Conclusion based on Predictive Modelling Using Machine Learning Algorithms.

➢ Conclusion based on Outcomes of Bead Geometry

Bead geometry parameters, namely depth of penetration, bead width, and height of reinforcement are critically assessed across four experimental sets to evaluate their influence on weld quality and effectiveness.

- In Experiment Set 1, the welds are produced using an autogenous TIG welding process on a single side with varying gas flow rates, torch angles, and heat inputs. The maximum penetration achieved is 3.459 mm with a bead width of 9.375 mm and reinforcement of 0.11 mm, under the condition of high heat input (1.119 kJ/mm), 90° torch angle and 10 L/min gas flow rate. However, despite these optimizations, full penetration is not being achieved, which remains a key limitation of single-sided autogenous TIG welding in this Experiment Set 1.
- Experiment Set 2 involves double-sided autogenous TIG welding. Welds have shown uniformity and minimal defects, but still fell short of full joint penetration. The best result is 6.530 mm penetration for an 8 mm thick plate, confirming that autogenous TIG welding even when applied from both sides is still insufficient for complete weld fusion in thicker stainless-steel sections.
- By contrast, Experiment Set 3, which has employed Activated TIG (A-TIG) welding with TiO_2 flux (welded from both sides), is found to significantly improve bead characteristics. Serial numbers 26 to 29 is found to successfully achieve full penetration (8 mm). The activating flux has enhanced arc concentration and heat transfer, resulting in deeper and cleaner welds. Optimal results are observed with increased gas flow (14 L/min) and torch angles of 75°, which has led to balanced bead width and stable reinforcement profiles.
- Finally Experimental Set 4 include double-sided welding with varied root gaps, heat inputs and gas flow rate assisted with continuous supply of filler wire at constant speed. Most specimens are found to reach full penetration, demonstrating good fusion across

the joint. Several welds have shown excellent fusion with penetration depths of 8 mm, widths up to 12.6 mm, and reinforcement values ranging from 0.34 mm to 1.6 mm, further verifying the effectiveness of optimized parameters in achieving sound bead geometry.

In summary, both Activated TIG (A-TIG) and filler-assisted TIG welding have proved themselves effective in achieving full penetration and good bead geometry in thicker stainless-steel sections. While A-TIG has enhanced penetration through arc concentration, filler-assisted TIG have also delivered uniform welds with proper control of gas flow, torch angle, root gap, and heat input. Both methods are found to offer reliable solutions depending on specific welding needs.

- **Conclusion based on Post Welding Tests and Analysis**

A comprehensive series of post-weld evaluations were carried out to assess the quality, performance of the welded joints. The key tests include Tensile testing, Rockwell and Vickers hardness measurements, and microstructural characterization using both optical and electron microscopy. Each of these techniques has provided critical insights into the mechanical robustness and metallurgical features of the weldments, allowing a comparative analysis across different experimental sets.

- Firstly, the tensile test being performed on the welded specimens is found to be pivotal in assessing the mechanical integrity of the welded joints. The test results have exhibited a significant variation across the four experimental sets. The first experimental set, employing autogenous welding without any flux or filler, has showed moderate tensile strengths ranging from approximately 206 MPa to 424 MPa. In contrast, the second set also autogenous (welded from both sides) but being optimized for better parameters, is found to exhibit higher strengths between 416 MPa and 481 MPa. Notably, the third set, which has employed Activated TIG (A-TIG) welding, is found to deliver the highest tensile strength values, with results peaking at around 656 MPa. The fourth set, where filler-assisted TIG welding is being used, is found to display a broad range of tensile strengths between 334 MPa and 676 MPa. These results clearly indicate that the incorporation of flux in A-TIG and filler in conventional TIG significantly improves the tensile properties, likely due to improved penetration, refined microstructure, and reduced porosity. Among the four experimental sets, the filler-assisted TIG welding is

found to exhibit the highest tensile strength, demonstrating its superior performance in enhancing mechanical properties.

- Secondly. Rockwell hardness testing (HRC scale) is carried out to determine the surface hardness of the weldments. For Set 1 (Samples 1–20), which involve autogenous TIG welding, the average hardness values ranged from approximately 25.33 HRC to 34.33 HRC, with a general average around 29.43 HRC. The hardness indicate moderate strengthening, with no filler material contributing to enhanced alloying or fusion characteristics. Set 2 (Samples 21–25), also using autogenous TIG but with improved thermal control on both sides, has demonstrated slightly better hardness, with an average hardness range of 28.0 to 31.67 HRC, and a mean of approximately 29.93 HRC. This improvement is likely due to better heat input balance and refinement of the weld pool during dual-sided welding. In Set 3 (Samples 26–30), the A-TIG welded specimens has exhibited the highest Rockwell hardness, ranging from 32.33 HRC to 36.33 HRC, with an average of approximately 34.13 HRC. This significant increase is attributed to grain refinement, deeper penetration, and improved weld metal properties induced by the activation flux. Set 4 (Samples 31–50), which use filler-assisted TIG welding on both sides, is found to show a wide distribution of hardness values ranging from 26.33 HRC to 34.33 HRC, with an average of approximately 30.89 HRC. While not exceeding the hardness levels of the A-TIG samples, the presence of filler material has helped to maintain consistent hardness and better metallurgical bonding. The peak hardness recorded in this set is 34.33 HRC, suggesting localized improvements due to enhanced heat distribution and filler-induced alloying effects.
- To evaluate localized hardness variations across the weldment, Vickers microhardness measurements are taken for some typical welded samples from all Experimental sets at various distances from the weld center line. The profiles reveal a symmetric distribution of hardness with distinct peaks near the heat-affected zone (HAZ). For autogenous welds (Set 1 and Set 2), peak hardness values near the HAZ ranged between 260–270 HV, while the weld center typically showed slightly lower values around 240–260 HV. A-TIG welds (Set 3) is found to have a higher hardness profile across all measured points, with peak values reaching up to 378 HV at the weld center, and consistently high values across the HAZ, signifying substantial grain refinement and thermal gradient control. In the fourth set (filler-assisted TIG), hardness values are also significantly elevated compared to autogenous welds, with the HAZ and weld center frequently exceeding 340 HV. These

findings show that both A-TIG and filler-assisted TIG welding improve the weld quality by enhancing metal mixing and creating more favourable solidification conditions.

- Microstructural studies using optical microscopy and Scanning Electron Microscopy (SEM) are performed on representative specimens from each set. These analyses provide visual and quantitative confirmation of grain boundary morphology, phase transformations, and segregation behaviour. In autogenous welds, the microstructure exhibit coarse dendritic growth in the weld metal with partial grain coarsening in the HAZ. A-TIG welds reveal refined dendritic and cellular microstructures with narrower grain boundaries, suggesting accelerated cooling rates and reduced residual stress. The filler-assisted TIG welds has exhibited columnar grains transitioning into equiaxed structures at the fusion boundary, indicative of favourable thermal gradients and enhanced metallurgical bonding. SEM imaging has further highlighted the absence of significant porosity and minimal inclusion formation in the A-TIG and filler-assisted welds, underscoring their superior structural integrity.

➢ **Conclusion based on Multicriteria decision making tool used**

- In the first experimental set involving autogenous TIG welding, the Analytical Hierarchy Process (AHP) is applied to determine the most suitable process parameters that would ensure adequate penetration while maintaining overall weld quality and productivity. The alternatives are evaluated based on three critical factors: penetration depth, bead width, and reinforcement. In autogenous TIG welding from one side, alternative 7 has emerged as the best choice with the highest global weight of 0.177, in autogenous TIG welding from both sides, alternative 1 has emerged as the best choice with the highest global weight of 0.348, also in A-TIG welding from both sides, alternative 1 has emerged as the best choice with the highest global weight of 0.236.
- Similarly, for the fourth experimental set, which has utilized filler-assisted TIG welding, the AHP method is used to analyze and rank multiple welding alternatives under the same evaluation criteria. After computing the global weights, Alternative 4 (A4) has achieved the highest score of 0.144, identifying it as the optimal welding setup in this set. This outcome further validate the capability of AHP to effectively guide multi-criteria decision-making in welding parameter optimization.

Overall, the AHP has proved to be a reliable and systematic tool in this research for evaluating diverse TIG welding conditions by effectively balancing multiple performance

parameters such as penetration depth, bead width, and reinforcement, thereby aiding in the identification of the most suitable input welding parameters.

- **Conclusion based on Predictive Modelling Using Machine Learning Algorithms**

This section emphasizes the successful implementation of Machine Learning (ML) techniques to develop robust predictive models for estimating various welding output responses. The analysis is performed using four complete sets of experimental data, where each set include essential process input variables and corresponding output responses such as weld bead height, penetration, width, hardness, ultimate tensile strength (UTS), and percentage elongation. An 80:20 train-test split along with 5-fold cross-validation has ensured the reliability and generalization of the models developed.

- Six different ML algorithms, Artificial Neural Networks (ANN), K-Nearest Neighbour (KNN), Support Vector Regression (SVR), Random Forest (RF), Gradient Boosting Regression (GBR), and Extreme Gradient Boosting (XGBoost) are employed. Among them, XGBoost regression has emerged as the most accurate and reliable model, demonstrating the highest R^2 values and the lowest prediction errors across all output responses. This signifies its strong capability to capture nonlinear relationships and complex patterns in welding behaviour.
- The feature importance analysis using the XGBoost model highlights the pivotal role of specific input parameters in influencing key weld quality characteristics. Among all variables, the number of welding passes consistently emerges as the most influential factor, particularly in predicting penetration, ultimate tensile strength and percentage elongation, with importance scores nearing or exceeding 0.75. This underscores the critical role of double-sided welding in achieving full penetration and enhanced mechanical performance. The use of filler material significantly influences bead width and bead height, due to its influence on spreading molten pool and material deposition. Additionally, activating flux is identified as an impactful factor in determining weld hardness, primarily due to its role in modifying molten pool behaviorbehaviour through the reverse Marangoni effect, thereby improving penetration and weld quality.
- The filler-assisted both side TIG welding also shows satisfactory results in most of the cases, giving achieving good mechanical properties due to full penetration.
- Heatmap correlation analysis reveals that welding pass, heat input, and flux usage have strong positive correlations with key welding properties of the SS304H-welded joints.

- Prediction and validation analyses confirm that the established machine learning models, and in particular, XGBoost, closely match the actual experimental results across all output parameters.

Thus, the close alignment between predicted and experimental data highlights the effectiveness of machine learning in forecasting welding responses and optimizing process parameters.

8.2. Future Scope of Work

The future scope of work may include the following key areas for further exploration and optimization:

- Key welding parameters such as arc gap, root gap, shielding gas flow rate, heat input, and welding speed can be systematically varied and optimized to identify the best possible combination for producing defect-free, structurally sound welds of SS 304H specimens.
- Dissimilar filler wires may be used to explore their effect on weld strength and quality; the outcomes may be verified through post-weld mechanical testing and microstructural analysis.
- Though the Analytical Hierarchy Process (AHP) is used as a decision-making tool in this work, advanced multi-layer AHP may be used in future to explore additional welding parameters and joint types for better weld quality improvement.
- Advanced machine learning algorithms may be applied in the future to develop stronger correlations between experimental results and predictions, improving the accuracy and reliability of weld quality assessment. While six standard ML algorithms are used in this work, exploring additional or more advanced models may further enhance the outcomes.

REFERENCES

1. Giridharan, P. K., & Murugan, N. (2009). Optimization of pulsed GTA welding process parameters for the welding of AISI 304L stainless steel sheets. International Journal of Advanced Manufacturing Technology, 40, 478-489
2. Masuyama F. (2001); History of power plants and progress in heat resistant steels. The Iron and Steel Institute of Japan International, 41(6), 612–625.
3. Abe F. (2008); Precipitate design for creep strengthening of 9% Cr tempered martensitic steel for ultra-supercritical power plants. Science and Technology of Advanced Materials, 9(1), 9-15.
4. Abe F., & Tabuchi M. (2004); Microstructure and creep strength of welds in advanced ferritic power plant steels. Science and Technology of Welding and Joining, 9(1), 22–31.
5. Bhadeshia H. (2001); Design of ferritic creep-resistant steels. The Iron and Steel Institute of Japan International, 41(6), 626–640.
6. Guidelines and specifications for high-reliability fossil power plants, Report no. 1023199, EPRI, Palo Alto, CA, USA, 2011.
7. T24 Experience: A Hitachi Power Europe Perspective, 38–40, Modern Power Systems, Kent, United Kingdom, 2012, 38–40.
8. Fishburn J.D., Henry J.F., & Zhou G. (2001); Proc. 9Cr Materials Fabrication and Joining Technologies, Myrtle Beach, SC, USA, July 2001, EPRI, 7–11.
9. Nevasmaa, P., Laukkanen, A., & Häkkilä, J. (2005); Assessment of hydrogen cracking risk in multipass weld metal of 2.25Cr-1Mo-0.25V-TiB (T24) boiler steel. Welding in the World, 49(7-8), 45-58.
10. Dobrzanski J., Pasternak J., & Zielinski A. (2006); Proceedings to the 8th Liege Conference on Materials for Advanced Power Engineering, 2006 (Liege, Belgium), Forschungszentrum Jülich GmbH, 390–399.
11. Perrin, I.J., & Fishburn, J.D. (2005); A perspective on the design of high temperature boiler components, Proceedings of the International Conference on Creep and Fracture in High Temperature Components in Design and Life Assessment Issues, EPRI, Keynote paper 4, Institute of Mechanical Engineers, Central London, UK.
12. Creep strength enhanced ferritic (CSEF) steel welding guide, Report No. 1024713, EPRI, Palo Alto, CA, USA, 2011.

13. DuPont J.N., Marder A.R., Nawrocki J.G., Puskar J.D., & Robino C.V. (2003); The mechanism of stress-relief cracking in a ferritic alloy steel. Welding Journal, 82(2), 25–35.
14. Auerkari P., Holmstrom S., Nevasmaa P., Rantala J., & Salonen J. (2010); Proceedings to the 9th Liege Conference on Materials for Advanced Power Engineering, Liege, Belgium, 229–238.
15. Fuchs R., Hahn B., & Heuser H. (2004); Proceedings of the Sixth International Conference on Welding and Repair Technology for Power Plants, EPRI/ASM International, 1–26.
16. Park K., Kim S., Chang J., & Lee C. (2012); Post-weld heat treatment cracking susceptibility of T23 weld metals for fossil fuel applications, Materials and Design, 34, 699–706.
17. Saha MK, Hazra R, Mondal A, Das S. Effect of heat input on geometry of austenitic stainless steel weld bead on low carbon steel. Journal of The Institution of Engineers (India): Series C, 2019, 100:607-615.
18. Murugan N, Parmar RS, Sud SK. Effect of submerged arc process variables on dilution and bead geometry in single wire surfacing. Journal of Materials Processing Technology, 1993, 37(1-4):767-780.
19. Bhattacharya AB, Batish A, Kumar P. Experimental investigation for multi-response optimization of bead geometry in submerged arc welding using grey analysis. Journal of The Institution of Engineers (India): Series C, 2012, 93(2):123-132.
20. Singh AK, Dey V, Rai RN, Debnath T. Weld bead geometry dimensions measurement based on pixel intensity by image analysis techniques. Journal of The Institution of Engineers (India): Series C, 2019, 100:379-384.
21. Ghanty P, Paul S, Mukherjee DP, Vasudevan M, Pal NR, Bhaduri AK. Modelling weld bead geometry using neural networks for GTAW of austenitic stainless steel. Science and Technology of Welding and Joining, 2007, 12(7):649-658.
22. Widyianto A, Baskoro AS, Kiswanto G. Effect of pulse currents on weld geometry and angular distortion in pulsed GTAW of 304 stainless steel butt joint. International Journal of Automotive and Mechanical Engineering, 2020, 17(1):7687-7694.
23. Khuri AI, Mukhopadhyay S. Response surface methodology. Wiley Interdisciplinary Reviews: Computational Statistics, 2010, 2(2):128-149.

24. Vidyarthy RS, Dwivedi DK, Muthukumaran V. Optimization of A-TIG process parameters using response surface methodology. Materials and Manufacturing Processes, 2018, 33(7):709-717.
25. Kutelu BJ, Seidu SO, Eghabor GI, Ibitoye AI. Review of GTAW welding parameters. Journal of Minerals and Materials Characterization and Engineering, 2018, 6(5):541-550.
26. Bose S, Das S. Experimental investigation on bead-on-plate welding and cladding using pulsed GTAW process. Indian Welding Journal, 2021, 54(1).
27. Khara B, Mandal ND, Sarkar A, Sarkar M, Chakrabarti B, Das S. Weld cladding with austenitic stainless steel for imparting corrosion resistance. Indian Welding Journal, 2016, 49(1):74-81.
28. Acharya S, Gonda D, Das S. Achieving favourable depth of penetration and productivity of ATIG welds utilizing The AHP. Indian Science Cruiser, 2022, 36(5):24-30.
29. Acharya S, Gonda D, Das S, Bose D, Islam R. Augmentation of depth of penetration and productivity benefits of ATIG welds using The AHP. International Journal of the Analytic Hierarchy Process, 2023, 15(3).
30. Sarkar A, Roy J, Majumder A, Saha SC. Optimization of welding parameters of submerged arc welding using analytic hierarchy process (AHP) based on Taguchi technique. Journal of The Institution of Engineers (India): Series C, 2014, 95:159-168.
31. Dasgupta S, Banerjee S, Hasan H, Das S. Application of the AHP for optimization of weld strength of Al-8% SiC composite using PCTIG welding. Indian Science Cruiser, 2022, 36(4):19-25.
32. Saha S, Das S. Effect of polarity and oxide fluxes on weld-bead geometry in activated tungsten inert gas (A-TIG) welding. Journal of Welding and Joining, 2020, 38(4):380-388.
33. Magudeeswaran G, Nair SR, Sundar L, Harikannan N. Optimization of process parameters of the activated tungsten inert gas welding for aspect ratio of UNS S32205 duplex stainless steel welds. Defence Technology, 2014, 10(3):251-260.
34. Saha S, Paul BC, Das S. Productivity improvement in butt joining of thick stainless steel plates through the usage of activated TIG welding. SN Applied Sciences, 2021, 3(4):416.

35. Li H, Zou JS, Yao JS, Peng HP. Uniform design and optimization of active agent and technology research for A-TIG welding of 2219 aluminum alloy. The International Journal of Advanced Manufacturing Technology, 2017, 92:3435-3446.
36. Pandya D, Badgujar A, Ghetiya N. A novel perception toward welding of stainless steel by activated TIG welding: a review. Materials and Manufacturing Processes, 2020, 35(8):877-903.
37. Cai Y, Luo Z, Zeng Y. Influence of deep cryogenic treatment on the microstructure and properties of AISI 304 austenitic stainless steel A-TIG weld. Science and Technology of Welding and Joining, 2016, 22(3):236-243.
38. Kulkarni A, Dwivedi DK, Vasudevan M. Microstructure and mechanical properties of A-TIG welded AISI 316L SS-Alloy 800 dissimilar metal joint. Materials Science and Engineering A, 2020, 790:139685.
39. Niagaj J. Effect of A-TIG welding on deformation of austenitic steel components. Welding International, 2013, 27(11):853-856.
40. Welding Handbook (1987), American Welding Society, 8th edition, 1, 111.
41. Messler Jr. R.W., (1999); Principles of Welding: Processes, Physics, Chemistry, and Metallurgy, New York, John Wiley & Sons.
42. Dupont, J.N., & Lippold, J.C. (2009); Welding Metallurgy and Weldability of Nickel Base Alloys, New York, John Wiley & Sons.
43. Stout, R.D. (1987); Welding and weldability of steels, 4th edition, New York, Welding Research Council.
44. Saha S, Das S, Mondal S. Exploring the weldability of austenitic stainless steels in advanced ultra-supercritical power plant applications: an extensive review. Indian Welding Journal, 2023, 56(4), 54–66.
45. Viswanathan R., Henry J., Tanzosh J., Stanko G., Shingledecker J., Vitalis B., & Purgert R. (2005); U.S. Program on Materials Technology for Ultra-supercritical Coal Power Plants, Journal of Materials Engineering and Performance, 14(3), 281–292.
46. Wu Q., Song H., Swindeman R., Shingledecker J., & Vasudevan V. (2008); Microstructure of long-term aged IN617 Ni-base super alloy. Metallurgical and Materials Transactions, 39(11), 2569–2585.
47. Dittrich F., Mayr P., & Siefert, J.A. (2019); Thermodynamic simulation of ferritic to ferritic dissimilar metal welds, Welding in the World, 64(1), 95-103.

48. Blum R., & Bugge J. (2010); Proceedings of 6th International Conference on Advances in Materials Technology for Fossil Power Plants, EPRI, ASM International, Santa Fe, NM, USA, August–September, 1–10.
49. Fukuda M., Saito E., Tanaka Y., Takahashi T., Nakamura S., Iwasaki J., Takano S., & Izumi S. (2010); Advanced USC technology in Japan. Proceedings of International Conference on Advances in Materials Technology for Fossil Power Plants, EPRI, ASM International, Santa Fe, NM, USA.
50. Masuyama F. (2010); Proceedings of 6th International Conference on Advances in Materials Technology for Fossil Power Plants, EPRI, ASM International, Santa Fe, NM, USA, August–September, 11–29.
51. Xie X., Chi C., Yu H., Yu Q., Dong J., & Zhao S. (2010); Structure stability study on fossil power plant advanced heat-resistant steels and alloys in China, Proceedings of 6th International Conference on Advances in Materials Technology for Fossil Power Plants, EPRI, ASM International, Santa Fe, NM, USA, August–September, 30–52.
52. Siefert, J.A., Thomson, R., & Parker, J. (2018); Microstructure features contributing to heat affected zone damage in Grade 91 steel feature type cross-weld tests. Proceedings of the ASME 2018 Symposium on Elevated Temperature Application of Materials for Fossil, Nuclear, and Petrochemical Industries, ETAM, April 2018.
53. Viswanathan R., Henry J.F., Tanzosh J., Stanko G., Shingledecker J., Vitalis B., & Purgert G. (2015); The design and research of a new low cobalt-molybdenum niobium-containing Ni-base superalloy for 700℃ advanced ultra-supercritical power plants, Procedia Engineering, 130, 617-627.

54. Shibli I.A., Holdsworth S.R., & Merckling G. (2005); Creep & Fracture in High Temperature Components-Design & Life Assessment Issues, Proceedings of ECCC Creep Conference, September 2005, UK.
55. Shibli I.A., & Le M.H.N. (2001); Creep crack growth in P 22 & P 91 welds-Over view from SOTA and HIDA projects, International Journal of Pressure Vessels and Piping, 78(11-12), 785-793.
56. David S.A., Siefert J.A., & Feng Z. (2013); Welding and weldability of candidate ferritic alloys for future advanced ultra-super critical fossil power plants, Science and Technology of Welding and Joining, 18(8), 631-651.
57. Viswanathan R., Gandy D., & Coleman K. (2004); Proceedings of The 4th International Conference on Advances in Materials Technology for Fossil Power Plants, EPRI, ASM International, Hilton Head Island, SC, USA.
58. Viswanathan R., Henry J.F., Tanzosh J., Stanko G., Shingledecker J., Vitalis B., & Purgert R. (2005); U.S. Program on Materials Technology for Ultra-Supercritical Coal Power Plants, Journal of Materials Engineering and Performance, 14(3), 281–292
59. Sourmail .T, & Bhadeshia H. (2005); Microstructural evolution in two variants of NF709 at 1023 and 1073 K, Metallurgical and Materials Transactions A, 36(1), 23–25.
60. Masuyama F. (2004); Effect of heat treatment on the microstructure and properties of cold worked Inconel 740H boiler tubes, Proceedings of 4th International Conference on Materials Technology for Fossil Power Plants, Hilton Head, SC, USA, EPRI/ASM International.
61. Masuyama F. (2010); R & D program for AUSC material development with creep strength degradation assessment studies. Proceedings of 6th International Conference on Materials Technology for Fossil Power Plants, Santa Fe, NM, USA, EPRI/ASM International, August, 11–29.
62. Lippold J., & Kotecki D. (2005); Welding Metallurgy and Weldability of Stainless Steels, New York, John Wiley and Sons Inc.
63. Senba H., Sawaragi Y., Ogawa K., Natori A., & Han T. (2002); Development of high strength 18-8 series super 304H steel pipe for high efficiency thermal power boiler. Materia Japan, 41(2), 120–125.
64. Matsuda F. (1989); Proceedings of 2nd International Conference on Trends in Welding Research, Gatlinburg, TN, USA, 1989, 127–136. ASM International.
65. Lippold J.C. (2005); Joining of Advanced and Specialty Materials VII, No. 05116G, 2005, Materials Park, OH, ASM International.

66. Dhooge A., & Vinckier (1992); Reheat cracking–Review of recent studies (1984–1990). Welding World, 30(3/4), 44–71.
67. Thakur P., & Chapgaon A. (2016); A review on effects of GTAW process parameters on weld, International Journal for Research in Applied Science & Engineering Technology, 4(1), 136-140.
68. Arivazhagan B., & Vasudevan M. (2014); A comparative study on the effect of GTAW processes on the microstructure and mechanical properties of P91 steel weld joints. Journal of Manufacturing Processes, 16, 305–311.
69. Sawaragi Y., Hirano S., Hayase Y., & Masuyama, F. (1991); Proceedings of 3rd International Conference on Improved Coal-fired Power Plants, San Francisco, CA, USA, EPRI, 14-1–14-15.
70. Siefert J.A., & David S.A. (2014); Weldability and weld performance of candidate austenitic alloys for advanced ultra-supercritical fossil power plants. Science and Technology of Welding and Joining, 19(4), 631-651.
71. Mathur A., Bhutani O.P., Jayakumar T., Dubey D.K., & Chetal S.C. (2013); India's National A-USC Mission-Plan & Progress. Proceedings from 7th International Conference on Advances in Materials Technology for Fossil Power Plants, USA.
72. Srinivasan G., Dey H.C., Ganesan V., Bhaduri A.K., Albert S.K., & Laha K. (2016); Choice of welding consumable and procedure qualification for welding of 304HCu austenitic stainless steel boiler tubes for Indian advanced ultra-super critical power plant. Welding World, 60(5), 1029-1036.
73. Rajasekar, R., Balasubramanian, V., & Vasudevan, M. (2014). "Optimizing Pulsed Current Gas Tungsten Arc Welding Parameters of Commercially Pure Titanium Using Response Surface Methodology." Materials and Design, 53, 120-130..
74. Sundar, M., & Purnachandran, R. (2017). "Experimental Investigation and Optimization of Submerged Arc Welding Process Parameters Using Response Surface Methodology and Particle Swarm Optimization." Procedia Engineering, 174, 81-90.
75. Choudhary, B. K., Saroja, S., & Vijayalakshmi, M. (2021). "High-Temperature Mechanical Behavior of SS 304H Austenitic Stainless Steel." International Journal of Pressure Vessels and Piping, 195, 104-115.
76. Zhang, Y., Wang, P., & Luo, J. (2020). "Weldability and Performance Analysis of SS 304H Using GTAW." Journal of Materials Engineering and Performance, 29(10), 6355-6365.

77. Kumar, S., Balaji, K., & Ramesh, T. (2021). "The Effect of Advanced TIG Welding Techniques on Austenitic Stainless Steels." Welding Journal, 100(6), 281-290.
78. Singh, R., Mehta, R., & Sharma, A. (2022). "Microstructural Stability of SS 304H in Elevated Temperature Applications." Materials Science and Technology, 38(4), 453-462.
79. Patel, R., Kumar, D., & Singh, S. (2020). "Evaluation of Creep Strength and Weldability of Boiler Steels." Journal of Manufacturing Processes, 54, 523-534.
80. Li, H., Zhao, J., & Chen, W. (2020). "Enhancement of Weld Quality Using Advanced A-TIG Techniques." Materials Today: Proceedings, 28(1), 157-163.
81. Xu, W., Zhou, Z., & Liu, H. (2019). "Analysis of Solidification Cracking in Austenitic Stainless Steel Welds." Metallurgical and Materials Transactions A, 50(11), 5301-5314.
82. Ravi, K., Kumar, V., & Das, R. (2021). "Performance Evaluation of A-TIG Welding for Thick-Section Stainless Steels." Journal of Manufacturing Science and Engineering, 143(7), 071003.
83. Suresh, P., Narayanan, R., & Jayakumar, T. (2020). "Post-Weld Microstructural Analysis of SS 304H for Power Plant Applications." International Journal of Advanced Manufacturing Technology, 109(11-12), 3393-3405.
84. Mishra, D., Ghosh, S., & Chakraborty, P. (2022). "Reliability and Durability of SS 304H Weldments Under USC Conditions." Welding in the World, 66(4), 809-820.
85. Yadav, S., Gupta, P., & Kumar, A. (2021). "Influence of Welding Parameters on Residual Stress in GTAW of Austenitic Steels." Journal of Materials Processing Technology, 294, 117116.
86. Smith, T. L., & White, J. R. (2016). Heat Input Control in Gas Tungsten Arc Welding of Stainless Steels. Journal of Welding Technology, 34(2), 125-130.
87. Liu, H., Zhang, H., & Zhang, Y. (2015). Effects of Heat Input on Weld Metallurgy in Austenitic Stainless Steels. Materials Science and Engineering, 88(5), 42-48.
88. Sirohi, S., Pandey, C., & Goyal, A. (2021). Role of the Ni-based filler (IN625) and heat-treatment on the mechanical performance of the GTA welded dissimilar joint of P91 and SS304H steel. Journal of Manufacturing Processes, 65, 174–189.
89. Tanaka, M., & Nakaoka, Y. (2014). Hot Cracking in Austenitic Stainless Steels: Influence of Impurities and Alloying Elements. Journal of Materials Science, 49(1), 62-70.

90. Zhi, H., & Li, X. (2018). Influence of Ferrite Number on Weld Cracking in Austenitic Stainless Steel. Journal of Manufacturing Processes, 25(4), 121-130.
91. Vasudevan, M., Bhaduri, A.K. & Raj, B. Prediction of Ferrite Number in Stainless Steel Welds using Bayesian Neural Network Model. Weld World 51, 15–28 (2007).
92. Rafiei, M., & Mostaan, H. (2019). The effect of filler metal and butter layer on microstructural and mechanical properties of pure Cu to AISI304 stainless steel dissimilar joint. Proceedings of the Institution of Mechanical Engineers, Part L: Journal of Materials: Design and Applications, 233(9), 1894–1905.
93. Iltaf, A., Khan, F. N., & Junaid, M. (2021). Influence of filler material on the microstructure, mechanical properties, and residual stresses in tungsten inert gas welded Ti-5Al-2.5Sn alloy joints. Proceedings of the Institution of Mechanical Engineers, Part L: Journal of Materials: Design and Applications, 235(8), 1952-1966.
94. Khan, M., Dewan, M. W., & Sarkar, M. Z. (2021). Effects of welding technique, filler metal and post-weld heat treatment on stainless steel and mild steel dissimilar welding joint. Journal of Manufacturing Processes, 64, 1307–1321.
95. Tigga, S. S., Verma, D. K., & Panneerselvam, K. (2021). Microstructure & mechanical properties of dissimilar material joints between T91 martensitic & S304H austenitic steels using different filler wires. Materials Today: Proceedings, 46(19), 9397–9404.
96. Sharma, P., & Dwivedi, D. K. (2021). Study on flux assisted-Tungsten inert gas welding of bimetallic P92 martensitic steel-304H austenitic stainless steel using SiO_2–TiO_2 binary flux. International Journal of Pressure Vessels and Piping, 192, 104423.
97. Sashank, S. S., Rajakumar, S., & Karthikeyan, R. (2025). Mechanical and metallurgical characteristics of hot wire TIG welded 304HCu austenitic stainless steel and P91 ferritic steel dissimilar tube joints. Welding International, 39(6), 452–461.
98. Yang, J., & Tan, S. (2016). Effect of Welding Parameters on Heat Input and Weld Penetration in GTAW of Stainless Steels. Materials and Manufacturing Processes, 31(8), 939-947.
99. Gupta, R., & Reddy, M. (2019). Influence of Welding Parameters on Weld Penetration in Gas Tungsten Arc Welding of Stainless Steels. Welding and Joining, 45(2), 54-61.
100. Zhang, C., & Zhang, X. (2017). Advanced-TIG Welding of SS 304H: Surface-Active Fluxes and Their Effects on Weld Penetration. Journal of Welding Technology, 90(5), 144-150.
101. Li, Z., & Liu, H. (2018). Study on Advanced-TIG (A-TIG) Welding of Austenitic Stainless Steels Using TiO_2 Fluxes. Journal of Manufacturing Science, 42(3), 212-220.

102. Park, J., & Kim, J. (2015). Advanced TIG Welding of Stainless Steel: The Role of Surface-Active Fluxes. Materials Science and Technology, 33(7), 789-795.
103. Sato, M., & Nakamura, Y. (2019). Improvement of Weld Pool Fluidity in Advanced TIG Welding of Stainless Steel Using TiO_2 Fluxes. Journal of Materials Processing Technology, 268(3), 123-128.
104. Kumar, P., & Raj, S. (2017). Effect of Post-Weld Heat Treatment on Microstructure and Mechanical Properties of SS 304H Weldments. Materials Science and Engineering, 61(5), 91-97.
105. Zhang, S., & Zhang, W. (2018). The Role of Post-Weld Heat Treatment in Enhancing Creep Resistance in SS 304H Welds. Welding Journal, 96(8), 60-67.
106. He, Y., & Shi, Z. (2019). Influence of Post-Weld Heat Treatment on Microstructure and Creep Properties of SS 304H. Journal of Materials Science and Engineering A, 75(6), 314-320.
107. Wang, F., & Guo, B. (2017). Post-Weld Heat Treatment of Austenitic Stainless Steel for Improved Creep Resistance. Journal of Creep and Fracture, 29(3), 175-180.
108. Li, D., & Wang, Q. (2015). Corrosion Resistance of Stainless Steel Welds in Chloride Environments. Corrosion Science, 59(2), 34-40.
109. Li, J., & Zhang, Y. (2016). Corrosion Resistance of Welded SS 304H in Marine Environments. Journal of Electrochemical Science, 48(4), 214-220.
110. Xu, W., & Sun, D. (2018). Minimizing Oxidation and Improving Surface Quality in Stainless Steel Welding Using Proper Shielding Gases. Journal of Welding and Joining, 49(1), 88-93.
111. Rajasekar, E., Ravisankar, V., & Vasudevan, M. (2014). "Optimization of pulsed current gas tungsten arc welding process parameters using response surface methodology." Materials and Manufacturing Processes, 29(7), 867–873.
112. Sundar, R., & Purnachandran, R. (2017). "Optimization of submerged arc welding parameters using response surface methodology." Journal of Manufacturing Processes, 25, 180–192.
113. Biswas, R. K., Bhowmick, B., Saha, S. C., & Singh, R. K. (2020). "Application of Response Surface Methodology and Central Composite Design for Friction Stir Welding of Aluminum Alloy." Materials Today: Proceedings, 26(4), 1814–1821.
114. Sharma, P., Yadav, R. K., & Kumar, V. (2015). "Optimization of Process Parameters of Gas Metal Arc Welding by Response Surface Methodology." International Journal of Advance Research and Innovation, 3(2), 170–174.

115. Yadav, R., Jain, R., & Srivastava, A. (2018). "Application of Response Surface Methodology for Predicting and Optimizing Welding Parameters in MIG Welding of Stainless Steel (AISI 304)." Materials Today: Proceedings, 5(2), 4868–4874.
116. Pandey, C., Mahapatra, M. M., Kumar, P., & Kumar, A. (2019). "Welding Parameter Optimization Using Response Surface Methodology and Artificial Neural Network Algorithm for Microalloyed Steel." Journal of Materials Research and Technology, 8(1), 1224–1236.
117. Rai, S., Singh, S., & Singhal, S. (2019). "Application of Central Composite Design and Response Surface Methodology for Welding Parameters Optimization in TIG Welding of SS304." Materials Today: Proceedings, 22(4), 1230–1234.
118. Saaty, T. L. (1980). The Analytic Hierarchy Process: Planning, Priority Setting, Resource Allocation. McGraw-Hill.
119. Kaur, M., Saini, R. K., & Sharma, M. (2021). "Optimization of Welding Parameters for TIG Welding of Mild Steel Using Analytic Hierarchy Process." Materials Today: Proceedings, 45, 7458–7463.
120. Gupta, R., Kumar, A., & Kumar, S. (2019). "Application of AHP in the Selection of Welding Processes for Dissimilar Material Joints." Journal of Manufacturing Processes, 46, 469–479.
121. Manohar, S. D., Reddy, P. V., & Kumar, K. S. (2020). "Optimization of Welding Parameters for Mild Steel and Stainless Steel Joints Using AHP and Taguchi Methods." Materials Today: Proceedings, 45, 2483–2489.
122. Prasad, M., Rao, M. A., & Kumar, A. (2021). "Environmental Assessment of Welding Processes Using Analytic Hierarchy Process." Journal of Cleaner Production, 288, 125614.
123. Bhatti, M. Y., & Tharwat, A. A. (2018). "Multi-Criteria Decision Making for Selecting Welding Parameters in Metal Inert Gas Welding Using AHP." International Journal of Advanced Manufacturing Technology, 96(9–12), 3733–3740.
124. Alam, Z., Panda, S. S., Tanmay, B., & Misra, J. P. (2025). "Process Optimisation of Multi-Response Characteristics of GTA Welding Joint for Copper–SS304 Using Multi-Criteria Decision-Making Method." Materials Today: Communications, 112637.
125. Saad, M. H., Darras, B. M., & Nazzal, M. A. (2020). "Evaluation of Welding Processes Based on Multi-Dimensional Sustainability Assessment Model." International Journal of Precision Engineering and Manufacturing–Green Technology, 8, 57–75.

126. Srinivasan, L., Chand, K. M., Kannan, T. D. B., Sathiya, P., & Biju, S. (2018). "Application of GRA and TOPSIS Optimization Techniques in GTA Welding of 15CDV6 Aerospace Material." Transactions of the Indian Institute of Metals, 71, 373–382.

127. Vaibhav J. Sutar and Baliram R. Jadhav. (2021) “Implementation of TOPSIS Optimisation Technique in Comparative Analysis of Conventional TIG and Activated TIG Welding of Stainless Steel 304L.” International Journal of Materials Engineering Innovation, 12(3).

128. Guambo Mondo, G., Moharana, B. R., Syed, S. A., & Muduli, K. (2024). "Evaluation of Weldability and Optimization of TIG Welding Process Parameters for Maximized Yield Strength." Recent Advancements in Product Design and Manufacturing Systems, 135–146.

129. Saluja, R. S., & Singh, V. (2025). "Achieving Sustainability Goals Through Process Selection Using a Robust Multi-Criteria Decision-Making Approach." Process Integration and Optimization for Sustainability.

130. Chellappan, M., Lingadurai, K., & Sathiya, P. (2017). "Characterization and Optimization of TIG Welded Supermartensitic Stainless Steel Using TOPSIS." Materials Today: Proceedings, 4(2), 1662–1669.

131. Roy, A., Ghosh, N., & Mondal, S. (2024). "Analysis of the Multi-Criteria Optimization Strategies for Determining the Weld Quality of Dissimilar TIG Welding Between Ferritic and Austenitic Stainless Steel." International Journal on Interactive Design and Manufacturing, 18, 1443–1457.

132. Varun Kumar A., Pradeep Krishna R., Masood Fakouri Hasanabadi, and Sathickbasha K., “Evaluation of Machine Learning Techniques for the Nd:YAG Laser & TIG Welded Stainless Steel 304,” Materials Today: Proceedings, vol. 72, Part 3, 2023, pp. 3263–3271. doi: https://doi.org/10.1016/j.matpr.2022.09.202

133. Kesse, M. A., Buah, E., Handroos, H., & Ayetor, G. K. (2020). Development of an Artificial Intelligence Powered TIG Welding Algorithm for the Prediction of Bead Geometry for TIG Welding Processes using Hybrid Deep Learning. Metals, 10(4), 451. https://doi.org/10.3390/met10040451

134. Acharya, S., Patra, S. & Das, S. Predicting A-TIG weld bead geometry of 304 stainless steel using artificial neural networks. Discov Mechanical Engineering 4, 12 (2025). https://doi.org/10.1007/s44245-025-00096-5

135. Park, S., Choi, M., Kim, D., Kim, C., & Kang, N. (2023). Modeling yield strength of

austenitic stainless steel welds using multiple regression analysis and machine learning. Metals, 13(1), 113. https://doi.org/10.3390/met13010113

136. Gbagba, S., Maccioni, L., & Concli, F. (2024). Advances in machine learning techniques used in fatigue life prediction of welded structures. Applied Sciences, 14(1), 398.

137. Chandra, M., Kumar, S., Ankit, K., et al. "A Machine Learning Approach for Prediction of Surface Temperature of the Weld Region in A-TIG Welding." Transactions of the Indian Institute of Metals, vol. 77, 2024, pp. 907–917.

138. A, D.; Nampoothiri, J., and K, S. "Leveraging Machine Learning to Predict Welding Quality in Ultrasonically Assisted TIG Welded Inconel 625 Joints." Journal of Materials Engineering and Performance, 2025.

139. Trinh, S.H.; Ly, H.-B. Enhancing compressive strength prediction of roller compacted concrete using machine learning techniques. Measurement 2023, 213, 113196.

140. Breiman, L. Random forests. Mach. Learn. 2001, 45, 5–32.

141. Freund, Y.; Schapire, R.E. Experiments with a new boosting algorithm. In Machine Learning, Proceedings of the Thirteenth International Conference, Bari, Italy, 3–6 July 1996; Morgan Kaufmann Publishers: San Francisco, CA, USA, 1996.

142. Agarwal, R.; Singh, J.; Gupta, V. An intelligent approach to predict thermal injuries during orthopaedic bone drilling using machine learning. J. Braz. Soc. Mech. Sci. Eng. 2022, 44, 320.

143. Vieira, J.T.; Pereira, R.B.D.; Lauro, C.H.; Brandão, L.C.; Ferreira, J.R. Multi-objective evolutionary optimization of extreme gradient boosting regression models of the internal turning of PEEK tubes. Expert. Syst. Appl. 2024, 238, 122372.

The Indian Institute of Welding
(IIW-India)

The Indian Institute of Welding
Baroda Branch

Certificate of Participation

Mr. Subhodwip Saha

presented a technical paper on

'*A Review on Weldability of Austenitic Stainless Steels Used in Advanced Ultra-Supercritical Power Plant Applications*'

Co-Authored by: ***Mr. Santanu Das and Mr. Subrata Mondal***

in National Welding Seminar 2020-21 organized on virtual platform by IIW-India, Baroda branch from 8th April to 10th April, 2021. The theme of seminar was

"Evolvement Of Digitalization And Automation In Welding - Industry 4.0."

Mr. Rajesh Madnani
Convener
NWS 2020-21

Mr. R. R. Chari
Vice Chairman
Technical Committee
NWS 2020-21

WELD 2023

Speaker

Certificate of Participation & Paper Presentation

This is to certify that ***Shri Subhodwip Saha*** *of Techno Main, Salt Lake, Kolkata and Kalyani Govt. Engineering College, Kalyani, West Bengal has presented a paper on* ***'Optimization of the Strength of Autogenous Butt Welded Joints of Austenitic Stainless Steels Using GTAW Process'*** *in the seminar 'WELD 2023-Welding Technology, the Present Status and Way Forward', being held at the Biswa Bangla Convention Centre, Newtown, Kolkata on 11th & 12th March 2023.*

Prof. G. L. Datta
Chairman, IIW-India, Kolkata Branch

Devasis Paul
Hony. Secretary, IIW-India, Kolkata Branch

The Institution of Engineers (India)

West Bengal State Centre

8 Gokhale Road, Kolkata - 700020, West Bengal, India

(Established in 1920, Incorporated by Royal Charter 1935) - A Scientific and Industrial Research Organisation

37th National Convention of Production Engineers

On

Recent Trends and Future Direction in Production Engineering and Management : Vision 2030

Certificate of Participation

This is to certify that **SUBHODWIP SAHA** *participated as a* Paper presenter

in the 37th National Convention of Production Engineers , Jointly organized by Production Engineering Division Board, WBSC, IEI and Department of Industrial and Systems Engineering, IIT KGP at Sir R. N. Mookherjee Hall, Kolkata on 18th & 19th August, 2023.

Dr. Nirmal Das	Prof. (Dr.) Pradip Kumar Ray	Prof. (Dr.) Bijan Sarkar	Prof. (Dr.) Goutam Sengupta	Prof. (Dr.) Raju Basak
Chairman, WBSC, IEI	Chairman, PE Division, WBSC, IEI	Convener, PE Division, WBSC, IEI	Member, PEDB, IEI	Honorary Secretary, WBSC, IEI

This is an approved CPD programme of The Institution of Engineers (India)

National Conference
on

Recent Advancements in Manufacturing Technology & Management
(RAMTM – II 2025), January 16-17, 2025

Organized By
Department of Production Engineering, Jadavpur University

Certificate of Presentation

Paper Title: Study of Weldability of 304H Austenitic Boiler Quality Steels by Gas Tungsten Arc Welding

Author(s) name: Subhodwip Saha, Santanu Das, Subrata Mondal

This is to certify that Dr./Mr./Ms. **Subhodwip Saha** has presented the above mentioned paper in RAMTM -II 2025 held during 16th - 17th January, 2025 at Jadavpur University, Kolkata, India.

Organising Secretary

Chairman

Exploring the Weldability of Austenitic Stainless Steels in Advanced Ultra-Supercritical Power Plant Applications: An Extensive Review

ORCID: Subhodwip Saha : https://orcid.org/0009-0004-0588-4076
ORCID: Santanu Das : https://orcid.org/0000-0001-9085-3450
ORCID: Subrata Mondal : https://orcid.org/0009-0001-0907-5709

DOI : 10.22486/iwj.v56i4.223541

Subhodwip Saha[1], Santanu Das[2] and Subrata Mondal[3]
[1,3]Power Engineering Department,
Jadavpur University, Kolkata- 700098.
[2]Mechanical Engineering Department,
Kalyani Government Engineering College,
Kalyani- 741235, West Bengal.
[1]Mechanical Engineering Department,
Techno Main Saltlake, Kolkata- 700091, West Bengal.
Email: [1]subhodwipsaha@gmail.com,
[2]sdas.me@gmail.com, [3]sub.mondal@gmail.com

Abstract

Despite continuous efforts to enhance the operational efficiency of power plants dependent on these fuels, fossil fuels are expected to remain a significant global energy source in the coming decades. India has initiated a mission program to establish Advanced Ultra Super Critical (AUSC) power plants operating at temperature and pressure exceeding 720°C and 30.4kPa respectively. These plants are anticipated to utilize specialized materials with high resistance to corrosion and deformation at elevated temperatures. Among the materials considered, Nickel-base alloys, Creep Strength Enhanced Ferritic (CSEF) Steels and Austenitic Stainless Steels have emerged as the primary candidates. The prime emphasis of this paper is directed towards examining the weldability of Austenitic Stainless Steels utilized in AUSC power plants. It encompasses various aspects such as the choice of filler materials, welding techniques, and the attributes of welds involving both similar and dissimilar metals. The paper provides a comprehensive review of weldability challenges encountered in Austenitic Stainless Steels, including issues like liquation cracking in the heat-affected zone (HAZ), hot cracking, and stress relaxation cracking induced by tramp elements. Additionally, it investigates the performance of different filler wires, namely ER304HCu, ERNiCrCoMo-1, and ERNiCrMo-3, in weld joints involving 304HCu SS tubes, as well as ERNiCrCoMo-1 in dissimilar tube weld joints between 304HCu Stainless Steel and Alloy 617M.

Keywords: Weldability, Austenitic Stainless Steel, AUSC, Advanced Ultra-Supercritical Power Plant.

Experimental Investigation on Autogenous TIG and A-TIG Welding for Enhanced Penetration in Austenitic SS304H Flats

ORCID: SUBHODWIP SAHA: https://orcid.org/0009-0004-0588-4076
ORCID: SANTANU DAS: https://orcid.org/0000-0001-9085-3450
ORCID: SUBRATA MONDAL: https://orcid.org/0009-0001-0907-5709

DOI : 10.22486/iwj.v58i1.48809

Subhodwip Saha[1], Santanu Das[2] and Subrata Mondal[3]
[1,3]Power Engineering Department, Jadavpur University, Kolkata- 700106.
[2]Mechanical Engineering Department, Kalyani Government Engineering College, Kalyani- 741235, West Bengal.
[1]Mechanical Engineering Department, Techno Main Salt Lake, Kolkata- 700091, West Bengal.
Email: [1]subhodwipsaha@gmail.com, [2]sdas.me@gmail.com, [3]sub.mondal@gmail.com

Abstract

Austenitic stainless steels, such as SS304H, find areas of applications in high-temperature power plants, chemical as well as aerospace industries. They have good corrosion resistance and hot strength. However, welding such material using conventional Tungsten Inert Gas (TIG) welding often presents challenges, such as limited penetration, susceptibility to hot cracking and potential solidification defects. This work investigates the effect of autogenous TIG welding and Activated-flux TIG (A-TIG) welding on penetration of SS304H stainless steel flats. The primary objective is to achieve full penetration while maintaining weld quality and integrity. In the first set of experiments, autogenous TIG welding is performed on both sides of the specimens, revealing that complete penetration was not attained under the selected parameters. To enhance penetration, a second set of experiments incorporates a coating of titanium dioxide (TiO_2) flux on SS304H flats to do A-TIG welding. The flux has facilitated a constricted arc and concentrated heat input to give improved penetration with smooth, uniform weld deposition. Key experimental parameters, including gas flow rate, torch angle, current, voltage and heat input have been analyzed to explore their influence on bead geometry and overall weld quality. The findings highlight the significant role of flux in optimizing penetration depth and structural integrity, making A-TIG a viable approach for welding austenitic stainless steel components in critical applications.

Keywords: Welding, TIG, A-TIG, SS304H, TiO_2, Weld penetration.

1. Introduction

Welding is an essential fabrication process practised in power plants, aerospace and automotive manufacturing installations. Among different welding techniques, Tungsten Inert Gas (TIG) welding finds its preference in the application areas needing high-quality welds with minimal defects. Weldability of such welding is influenced by multiple factors, including the composition properties, microstructure, process parameters and other relevant considerations. Extensive research and analysis led to the development of several weldability indicators that help characterize the behaviour of different welding techniques [1-3].

In applications requiring superior mechanical properties and corrosion resistance at an elevated temperature, austenitic stainless steels such as SS304H are extensively employed in various industrial applications such as industrial boilers. However, the weldability of these steels presents challenges due to their susceptibility to solidification cracking, segregation and residual stress development during welding [4].

Austenitic stainless steels have been recognized for their superior performance at elevated temperatures exceeding 650°C, making them suitable to employ in an Advanced Ultra-Supercritical (AUSC) power plant. However, their weldability is influenced by factors such as solidification behaviour,

crystals

MDPI

Article

Supervised Machine Learning Models for Predicting SS304H Welding Properties Using TIG, Autogenous TIG, and A-TIG

Subhodwip Saha [1], Barun Haldar [2,*], Hillol Joardar [3,*], Santanu Das [4], Subrata Mondal [1] and Srinivas Tadepalli [5]

[1] Department of Power Engineering, Jadavpur University, Kolkata 700106, India; subhodwipsaha@gmail.com (S.S.); sub.mondal@gmail.com (S.M.)
[2] Department of Industrial Engineering, College of Engineering, Imam Mohammad Ibn Saud Islamic University (IMSIU), Riyadh 11432, Saudi Arabia
[3] Department of Mechanical Engineering, C. V. Raman Global University, Bhubaneswar 752054, India
[4] Department of Mechanical Engineering, Kalyani Government Engineering College, Kalyani 741235, India; sdas.me@gmail.com
[5] Department of Chemical Engineering, College of Engineering, Imam Mohammad Ibn Saud Islamic University (IMSIU), Riyadh 11432, Saudi Arabia; stadepalli@imamu.edu.sa
* Correspondence: bhaldar@imamu.edu.sa (B.H.); joardar.2011@gmail.com (H.J.)

Abstract: This investigation explores the application of supervised machine learning regression approaches to predict various responses, including penetration, bead width, bead height, hardness, ultimate tensile strength, and percentage elongation in autogenous TIG-, A-TIG-, and TIG-welded joints of SS304H, which is considered as an advanced high-temperature resistant material. The machine learning (ML) models were constructed based on the data gathered from 50 experimental runs, considering eight key input variables: gas flow rate, torch angle, filler material, welding pass, flux application, root gap, arc gap, and heat input. A total of 80% of the collected dataset was used for training the models, while the remaining 20% was reserved for testing their performance. Six ML algorithms—Artificial Neural Network (ANN), K-Nearest Neighbors (KNN), Support Vector Regression (SVR), Random Forest (RF), Gradient Boosting Regression (GBR), and Extreme Gradient Boosting (XGBoost)—were implemented to assess their predictive accuracy. Among these, the XGBoost model has demonstrated the highest predictive capability, achieving R^2 scores of 0.886 for penetration, 0.926 for width, 0.915 for weld bead height, 0.868 for hardness, 0.906 for ultimate tensile strength, and 0.926 for percentage elongation, along with the lowest values of RMSE, MAE, and MSE across all responses. The outcomes establish that machine learning models, particularly XGBoost, can accurately predict welding characteristics, marking a significant advancement in the optimization of TIG welding parameters. Consequently, integrating such predictive models can substantially enhance the precision, reliability, and overall efficiency of welding processes.

Keywords: A-TIG; autogenous TIG; supervised machine learning; process parameter optimization

Academic Editor: Hongbin Bei

Received: 28 April 2025
Revised: 28 May 2025
Accepted: 29 May 2025
Published: 1 June 2025

Citation: Saha, S.; Haldar, B.; Joardar, H.; Das, S.; Mondal, S.; Tadepalli, S. Supervised Machine Learning Models for Predicting SS304H Welding Properties Using TIG, Autogenous TIG, and A-TIG. *Crystals* **2025**, *15*, 529. https://doi.org/10.3390/cryst15060529

1. Introduction

TIG welding is a widely adopted welding method across multiple industries, as it is efficient for welding a wide range of metals and alloys, including steels, magnesium, aluminum, titanium, and their alloys, super-alloys, bi-metals, etc., with high-quality welds [1,2]. This process utilizes an inert shielding gas, commonly argon, He, or a mixture of these, along with a non-consumable tungsten electrode to establish a highly stable arc

The AHP-Based Evaluation of Welding Parameters for Optimized TIG Weld Bead Geometry of SS 304H Flats

Subhodwip Saha
Department of Mechanical Engineering, Techno Main Salt Lake, Department of Power Engineering, Jadavpur University
Kolkata, West Bengal, India
subhodwipsaha@gmail.com

Santanu Das
Department of Mechanical Engineering, Kalyani Government Engineering College
Kalyani, West Bengal, India
sdas.me@gmail.com

Subrata Mondal
Department of Power Engineering, Jadavpur University
Kolkata, West Bengal, India
sub.mondal@gmail.com

***Abstract*— Austenitic stainless steels are extensively used in high-temperature and corrosive environments, such as in power plants, aerospace, and marine industries. Their superior mechanical properties, oxidation resistance, and weldability make them a preferred material for critical applications. Tungsten Inert Gas (TIG) welding finds wide application to join austenitic stainless steels because of its precise heat control and ability to produce high-quality welds. However, optimizing process parameters to achieve full penetration remains a challenge due to the material's susceptibility to solidification cracking and distortion. The Analytic Hierarchy Process (AHP) is applied to rank various welding runs to find out appropriate TIG welding parameters to have maximum penetration in 8mm thick SS 304H specimens. Process parameters considered include flow rate of gas, weld torch angle as well as heat input, which are varied during the experimental trials. The AHP is utilized to develop a 5×5 pairwise comparison matrix, assigning relative weights to the parameters to determine their significance in achieving optimal welding conditions. The results indicate that penetration is the most critical factor influencing weld integrity, with variations in gas flow rate and heat input playing a significant role in determining the final weld quality. The findings of this investigation provide a structured decision-making approach for selecting appropriate welding parameters, offering valuable insights for producing sound welding in industrial applications.**

Keywords*— *TIG, welding, AHP, SS 304H, Austenitic stainless steel.

I. Introduction

The Analytic Hierarchy Process (AHP) has been reported to be a less complicated multi-criteria decision-making technique which is prevalent all over the world as it is designed to simplify complex decision making problems. This method breaks down intricate problems into hierarchical components, allowing for systematic evaluation through pairwise comparisons [1,2,3]. By assigning relative importance to each criterion, the AHP facilitates informed decision-making, particularly in optimizing process parameters. In welding applications, selecting optimal parameters is crucial to ensuring high-quality welds. The AHP method proves particularly useful in addressing challenges related to weld strength, efficiency, and cost-effectiveness. By evaluating multiple influencing factors such as process parameters, environmental impact, and mechanical properties, the AHP enables an objective and structured selection process for welding optimization [1,3].

Application of the AHP was made to optimize TIG welding parameters for joining mild steel specimens successfully to enhance the quality of the welded joints [4]. Similarly, the AHP was utilised to compare welding processes for dissimilar materials, highlighting its effectiveness in evaluating weld strength, distortion, and cost [5]. Researchers integrated the AHP with the Taguchi method to optimize welding parameters for mild steel and stainless-steel joints [6]. In another research the AHP was utilised to assess the environmental sustainability of welding techniques, considering factors like energy consumption, emissions, and waste reduction [7]. The utility of the AHP in welding was also found to be applied to optimize parameters for MIG welding process where demonstration of multi-criteria decision-making resulting in enhancement of weld efficiency and quality was shown [8]. The AHP was effectively utilised to select suitable weld parameters in welding of aluminium and steel weldments [9,10].

The AHP was also employed to differentiate between judgment-based and quantitative decision-making approaches, as demonstrated by Saaty, thereby reinforcing its adaptability and robustness across diverse industrial and engineering applications [11]. The AHP was employed for selection of best suitable weld parameters in resistance spot welding [12]. It was also applied for selecting appropriate edge preparations aimed at improving the fatigue life of welded joints [13].

A hybrid approach integrating the AHP with the TOPSIS method was employed to optimize welding parameters for carbon steel storage tanks [14]. The AHP was further utilised to determine optimal welding conditions for high-carbon steel joints using the Gas Metal Arc Welding (GMAW) process by evaluating criteria such as penetration, deposition rate, and crack resistance [15]. In another work, the AHP was employed to optimize key input welding parameters such as penetration, reinforcement and bead width in GMAW process of austenitic stainless steel [16]. The AHP was also effectively applied to validate optimized A-TIG welding parameters, thereby confirming its practical relevance in welding process optimization [17].

Recent advancements in predictive analytics have further strengthened parameter optimization frameworks in welding. Supervised machine learning models have been employed to predict weld bead geometry, hardness and tensile strength for

Gmail **Subhodwip Saha <subhodwipsaha@gmail.com>**

Fwd: AIMTDR 2025 - Acknowledgement

1 message

Prof. Santanu Das <santanu.das@iiwindia.com> Sat, Oct 25, 2025 at 11:44 PM
To: Subhodwip Saha <subhodwipsaha@gmail.com>, Santanu Das <sdas.me@gmail.com>

Please note the submission confirmation of your paper. PFA the submitted paper.

Prof. Dr. Santanu Das
Chairman, Welding Education Committee, Ex-Chairman, Board of Examiners, ANB-India, Chairman, Kolkata Branch
and Chief Editor, Indian Welding Journal
The Indian Institute of Welding
IIW-India House, Plot No. 38, Geetanjali Park
200 Kalikapur Main Road, P.O. Mukundapur, Kolkata- 700099
Web: www.iiwindia.com
Alternative email ID for IWJ: iwj@iiwindia.com, iwj.iiw@gmail.com
Personal email ID: sdas.me@gmail.com
Mobile: 9433956050/ 8620884652

---------- Forwarded message ---------
From: **AIMTDR 2025, IIT Indore** <aimtdr2025@iiti.ac.in>
Date: Sat, Oct 25, 2025 at 11:40 PM
Subject: AIMTDR 2025 - Acknowledgement
To: <santanu.das@iiwindia.com>

Dear Sir/Madam,

Hope you are doing well.

You have Successfully Submitted Your Paper.

Your Paper ID is: AIMTDR_1761415715

Thank you for your contribution.

Best regards,

2 attachments

AIMTDR2025-Subhodwip Saha.doc
817K

AIMTDR2025-Subhodwip Saha.pdf
418K

Assistant Professor
Dept. of Power Engineering
Jadavpur University
Salt Lake, 2nd Campus
Kolkata-700 098

18/11/2025
Dr. Santanu Das
Professor of Mechanical Engineering (WBGS)
Kalyani Govt. Engg. College, Kalyani, Nadia

18/11/2025
Assistant Professor
Dept. of Power Engineering
Jadavpur University
Salt Lake, 2nd Campus